

**BIO-ENGINEERED PANCREAS WITH HUMAN EMBRYONIC STEM CELLS AND  
WHOLE ORGAN DERIVED EXTRACELLULAR MATRIX SCAFFOLDS**

by

**Saik Kia Goh**

B.S. in Genetics, Cell Biology and Development, University of Minnesota, 2006

Submitted to the Graduate Faculty of  
Swanson School of Engineering in partial fulfillment  
of the requirements for the degree of  
Doctor of Philosophy

University of Pittsburgh

2015

UNIVERSITY OF PITTSBURGH  
SWANSON SCHOOL OF ENGINEERING

This dissertation was presented

by

Saik Kia Goh

It was defended on

November 19, 2015

and approved by

Stephen F. Badylak, DVM, PhD, MD, Professor, Department of Surgery

Suzanne Bertera, PhD, Senior Scientist, Institute of Cellular Therapeutics, Allegheny Health

Network

George K. Gittes, MD, Professor, Department of Surgery

William R. Wagner, PhD, Professor, Department of Bioengineering

Dissertation Director: Ipsita Banerjee, PhD, Associate Professor, Department of Chemical

and Petroleum Engineering

Copyright © by Saik Kia Goh

2015

# **BIO-ENGINEERED PANCREAS WITH HUMAN EMBRYONIC STEM CELLS AND WHOLE ORGAN DERIVED EXTRACELLULAR MATRIX SCAFFOLDS**

Saik Kia Goh, PhD

University of Pittsburgh, 2015

According to Centers of Disease Control (CDC), 25.8 million Americans were diagnosed with diabetes in 2010, and more than 300 million people were affected worldwide. One potential future treatment for diabetes is transplantation of bioengineered pancreas capable of restoring insulin function. However, bioengineering of the complex pancreas function is a significant engineering feat. It calls for appropriate combinations of cells, with biomaterials that provide structural support and a suitable extracellular environment to maintain cell survival and function *in vitro* and *in vivo*.

The first objective of this work is to investigate a suitable 3D bioscaffold to support pancreatic cell types. Our result demonstrated that perfusion-decellularization of whole pancreas effectively removes cellular material but retains intricate three-dimensional microarchitecture and crucial extracellular matrix (ECM) components. To mimic pancreatic cell composition, we recellularized the whole pancreas scaffold with acinar and beta cell lines and cultured up to 5 days. Our result showed successful cellular engraftment within the decellularized pancreas, and the resulting graft gave rise to higher insulin gene expression over individual ECM proteins.

The second objective of this work is to evaluate the feasibility to repopulate the native organ-derived scaffolds with renewable cell types such as differentiating human pluripotent stem cells (hPSC). We developed an in-house bioreactor to support the regenerative reconstruction of pancreas. Our result demonstrated that hPSCs cultured and differentiated as aggregates are more

suitable than the parallel adherent cultures for organ repopulation. Upon continued culture with chemical induction in bioreactor, the seeded PP aggregates grow within the 3D organ scaffolds with homogeneity and mature *in situ* into monohormonal C-peptide positive cells.

The last objective of this work is to evaluate the matrix-specificity of organ-derived ECM. We evaluated this by developing a miniaturized ECM array composed of organ-specific matrices derived from decellularized pancreas, liver and heart. Interestingly, our result showed higher PP cell adhesion and differentiation on liver-ECM over pancreas- and heart-ECM, suggesting that the requirement for ‘like-to-like’ basis for tissue engineering approaches may not always be the case. Overall, the findings from this dissertation represent a notable step toward bioengineering of pancreas as an alternative therapeutic solution for diabetes.

## TABLE OF CONTENTS

<b>PREFACE.....</b>	<b>XVII</b>
<b>1.0 INTRODUCTION.....</b>	<b>1</b>
<b>1.1 THE PANCREAS .....</b>	<b>1</b>
<b>1.1.1 Pancreas development .....</b>	<b>2</b>
<b>1.1.2 Extracellular matrix components in developing pancreas.....</b>	<b>3</b>
<b>1.1.3 Extracellular matrix components in adult pancreas .....</b>	<b>5</b>
<b>1.2 PANCREATIC DISORDER.....</b>	<b>6</b>
<b>1.2.1 Exocrine pancreas disorder .....</b>	<b>6</b>
<b>1.2.1.1 Pancreatitis .....</b>	<b>6</b>
<b>1.2.1.2 Pancreatic cancer .....</b>	<b>7</b>
<b>1.2.2 Endocrine pancreas disorder .....</b>	<b>7</b>
<b>1.2.2.1 Type 1 diabetes.....</b>	<b>8</b>
<b>1.2.2.2 Type 2 diabetes.....</b>	<b>8</b>
<b>1.2.3 Current treatment.....</b>	<b>9</b>
<b>1.3 PANCREAS TISSUE ENGINEERING.....</b>	<b>11</b>
<b>1.3.1 Cells .....</b>	<b>12</b>
<b>1.3.1.1 Pancreatic differentiation from human embryonic stem cells (hESC).....</b>	<b>12</b>

1.3.1.2	<b>Pancreatic differentiation from human induced pluripotent stem cells (hiPS).....</b>	<b>13</b>
1.3.1.3	<b>Other cell types.....</b>	<b>13</b>
1.3.2	<b>Biomaterial scaffolds .....</b>	<b>14</b>
1.3.2.1	<b>Synthetic materials.....</b>	<b>14</b>
1.3.2.2	<b>Natural materials and decellularized ECM.....</b>	<b>15</b>
1.3.3	<b>Bioreactor .....</b>	<b>17</b>
1.4	<b>SPECIFIC AIMS .....</b>	<b>18</b>
1.4.1	<b>Specific Aim 1: To decellularize a whole-organ pancreas and analyze the potential of the natural 3D scaffold to support pancreatic tissue engineering.....</b>	<b>19</b>
1.4.2	<b>Specific Aim 2: To repopulate the decellularized pancreas with hPSCs and mature into insulin-expressing cell in whole organ bioreactor culture ..</b>	<b>20</b>
1.4.3	<b>Specific Aim 3: To evaluate the matrix-specificity of organ-derived ECM in human embryonic stem cell differentiation .....</b>	<b>21</b>
2.0	<b>PERFUSION-DECELLULARIZED PANCREAS AS A NATURAL THREE-DIMENSIONAL SCAFFOLD FOR PANCREATIC TISSUE AND WHOLE ORGAN ENGINEERING.....</b>	<b>22</b>
2.1	<b>INTRODUCTION.....</b>	<b>22</b>
2.2	<b>METHODS .....</b>	<b>24</b>
2.2.1	<b>Mouse Pancreas Harvest and cannulation .....</b>	<b>24</b>
2.2.2	<b>Perfusion Decellularization of Mouse Pancreas.....</b>	<b>24</b>
2.2.3	<b>Cell culture .....</b>	<b>25</b>
2.2.4	<b><i>In vivo</i> implantation of decellularized pancreas.....</b>	<b>25</b>
2.2.5	<b>Recellularization and culture of seeded-pancreatic construct.....</b>	<b>26</b>
2.2.6	<b>MIN-6 seeded on different ECM substrates and 2D thin slices of Decellularized Pancreas.....</b>	<b>27</b>
2.2.7	<b>Two-photon Microscopy.....</b>	<b>28</b>

2.2.8	Immunohistochemistry (IHC) .....	29
2.2.9	ECM Digestion and Proteomics Analysis .....	30
2.2.10	DNA Quantification.....	31
2.2.11	sGAG content characterization .....	31
2.2.12	Scanning Electron Microscopy (SEM) and Transmission Electron Microscopy (TEM).....	32
2.2.13	Preparation of Pancreatic Tissue for Atomic Force Microscopy (AFM) Measurement .....	33
2.2.14	AFM Measurement of Pancreatic Tissue Stiffness .....	33
2.2.15	Quantitative RT-PCR.....	34
2.2.16	Statistical Analysis .....	34
2.3	RESULTS .....	35
2.3.1	Perfusion-decellularization of whole organ pancreas.....	35
2.3.2	ECM characterization: Immunohistochemistry and Mass spectrometry-based proteomics analysis .....	37
2.3.3	Biophysical Characterization: structural and mechanical properties of decellularized pancreas .....	40
2.3.4	<i>In vivo</i> response to decellularized pancreas.....	43
2.3.5	Recellularization of Decellularized Pancreatic Scaffold .....	44
2.3.6	Modulation of $\beta$ -cell Insulin Gene Expression by Native Pancreatic ECM.....	49
2.4	DISCUSSION .....	50
2.5	CONCLUSION .....	54
3.0	DEVELOPMENT OF A PERFUSION BIOREACTOR FOR WHOLE ORGAN PANCREAS BIOENGINEERING .....	56
3.1	INTRODUCTION.....	56
3.2	METHODS .....	58

3.2.1	Organ isolation and preparation .....	58
3.2.2	Decellularization chamber design and components.....	59
3.2.2.1	Organ chamber .....	59
3.2.2.2	Detergent reservoir .....	60
3.2.2.3	Peristaltic pump .....	60
3.2.3	Corrosion casting of vascular and ductal conduits.....	61
3.2.4	Cell culture .....	61
3.2.4.1	MIN-6 $\beta$ cell culture.....	61
3.2.4.2	Human Embryonic Stem Cells (hESC) culture.....	61
3.2.4.3	Human ESC-Derived Definitive Endoderm (hESC-DE).....	62
3.2.5	Recellularization of decellularized pancreas with MIN-6 and hESC-DE cells.....	62
3.2.6	Cell labelling and LI-COR Whole Organ Imaging.....	62
3.2.7	Perfusion bioreactor design and components.....	63
3.2.7.1	Organ culture chamber .....	63
3.2.7.2	Air bubble trapper .....	63
3.2.7.3	Coiled silicone oxygenator.....	64
3.2.7.4	Peristaltic Pump .....	64
3.2.8	Static and perfusion culture conditions for recellularized pancreas..	64
3.2.9	Immunofluorescence and histology .....	65
3.2.9.1	TUNEL staining .....	65
3.2.10	Quantitative RT-PCR.....	66
3.2.11	Statistical Analysis .....	66
3.3	RESULTS .....	66

3.3.1	Design of a perfusion bioreactor system for whole organ decellularization .....	66
3.3.2	Recellularization and perfusion bioreactor development for organ culture .....	70
3.3.3	Perfusion bioreactor culture enhances $\beta$ -cell engraftment, viability and insulin expression over static culture.....	74
3.3.4	Perfusion bioreactor culture enhances proliferation and differentiation of hESC-DE repopulated pancreas over static culture.....	77
3.4	DISCUSSION .....	82
3.5	CONCLUSION .....	86
4.0	REPOPULATION OF DECELLULARIZED ORGAN SCAFFOLD WITH HUMAN EMBRYONIC STEM CELLS-DERIVED PANCREATIC PROGENITOR CELLS	87
4.1	INTRODUCTION.....	87
4.2	METHODS .....	89
4.2.1	Human pluripotent stem cells (hPSC) culture and two-dimensional (2D) pancreatic differentiation .....	89
4.2.2	Decellularization of pancreas and liver.....	90
4.2.3	Characterization of decellularized pancreas and liver.....	90
4.2.4	Differentiation of hPSC in alginate capsules .....	90
4.2.5	Seeding of hPSC derived PP cells and 3D PP aggregates in decellularized scaffolds.....	91
4.2.6	Bioreactor culture of repopulated pancreas and liver.....	91
4.2.7	Cell labelling and LI-COR Whole Organ Imaging.....	92
4.2.8	Flow cytometry analysis .....	92
4.2.9	Histology and immunofluorescence staining.....	93
4.2.10	Quantitative RT-PCR.....	93
4.2.11	Statistical analysis .....	93

<b>4.3</b>	<b>RESULTS .....</b>	<b>93</b>
4.3.1	hPSC-derived pancreatic progenitors (hPSC-PP) engraft in decellularized whole-organ scaffolds and maintain pancreatic phenotype...	93
4.3.2	hPSC-PP aggregates as an alternate candidate to repopulate decellularized scaffolds.....	98
4.3.3	An alternate, highly vascularized platform to allow reconstruction with cell aggregates: Decellularized liver scaffold .....	100
4.3.4	Pancreas regeneration in liver scaffold.....	106
<b>4.4</b>	<b>DISCUSSION .....</b>	<b>113</b>
<b>4.5</b>	<b>CONCLUSION .....</b>	<b>119</b>
<b>5.0</b>	<b>FABRICATION OF 2D AND 3D ORGAN-SPECIFIC ECM ARRAY FOR INVESTIGATING CELL-ECM INTERACTION DURING STEM CELL DIFFERENTIATION.....</b>	<b>120</b>
<b>5.1</b>	<b>INTRODUCTION.....</b>	<b>120</b>
<b>5.2</b>	<b>METHODS .....</b>	<b>123</b>
5.2.1	Organ decellularization and ECM extraction.....	123
5.2.2	ECM characterization and SDS-PAGE .....	124
5.2.3	Nitrocellulose coating of slides and dishes .....	124
5.2.4	2D organ-specific ECM array fabrication.....	125
5.2.5	Atomic Force Microscopy (AFM) surface roughness and stiffness measurement .....	125
5.2.6	Human embryonic stem cell culture and differentiation into pancreatic progenitor cells.....	126
5.2.7	Cell adhesion on 2D ECM arrays.....	126
5.2.8	Differentiation of PP aggregates in 3D ECM array.....	127
5.2.9	Cell viability assay: live/dead staining and quantification.....	128

5.2.10	On-chip immunofluorescence assay and LI-COR Odyssey scanner analysis.....	128
5.2.11	3D ECM array fabrication.....	129
5.2.12	Immunofluorescence staining and confocal imaging of 3D cultures	129
5.2.13	Array microscopy imaging and quantification .....	130
5.2.14	Statistical analysis .....	130
5.3	RESULTS .....	130
5.3.1	Preparation and characterization of decellularized organ ECM extracts.....	130
5.3.2	Fabrication of organ-derived ECM array .....	135
5.3.3	ECM array combined with quantitative imaging permits analysis of ECM composition of organ-derived ECMs .....	138
5.3.4	Organ-derived ECM array to probe cell–ECM adhesion.....	141
5.3.5	Fabrication and characterization of 3D organ-derived ECM array	145
5.3.6	Differentiation of hPSC-PP is responsive to organ-specific ECM, as detected in the 3D array .....	149
5.4	DISCUSSION .....	156
5.5	CONCLUSION .....	163
6.0	OVERALL CONCLUSIONS AND FUTURE WORK.....	164
6.1	TO DECELLULARIZE AN INTACT WHOLE PANCREAS AND CHARACTERIZE THE POTENTIAL OF THE NATURAL 3D SCAFFOLD TO SUPPORT PANCREATIC TISSUE AND WHOLE ORGAN ENGINEERING...	164
6.2	TO REPOPULATE THE DECELLULARIZED PANCREAS WITH HESCS AND MATURE INTO INSULIN-EXPRESSING CELL IN WHOLE ORGAN BIOREACTOR CULTURE.....	166
6.3	TO EVALUATE THE MATRIX-SPECIFICITY OF ORGAN-DERIVED ECM IN HUMAN EMBRYONIC STEM CELL DIFFERENTIATION.....	169
	APPENDIX A .....	173
	BIBLIOGRAPHY.....	192

## LIST OF TABLES

Table 2.1 Mass Spectrometry Composition Analysis.....	39
Table 6.1 Supplemental table for ECM proteins detected with mass spec analysis .....	174

## LIST OF FIGURES

Figure 1.1 General pancreas anatomy.....	2
Figure 2.1 Perfusion-decellularization of murine pancreas .....	36
Figure 2.2 ECM characterization of decellularized pancreas .....	38
Figure 2.3 Ultrastructural characterization of decellularized pancreas .....	41
Figure 2.4 Biomechanical properties of decellularization pancreas .....	42
Figure 2.5 Biocompatibility of perfusion-decellularized pancreas ECM .....	43
Figure 2.6 MIN-6 culture on 2D slice pancreatic matrix.....	45
Figure 2.7 Recellularization of decellularized pancreas .....	46
Figure 2.8 Dual recellularization strategy with $\beta$ - and acinar cell types .....	48
Figure 2.9 Comparison of ECM mediated insulin gene expression of MIN-6 cells.....	50
Figure 3.1 Perfusion bioreactor design for whole organ decellularization.....	67
Figure 3.2 Perfusion-decellularization of murine pancreas, liver and heart.....	69
Figure 3.3 Recellularization of decellularized pancreas .....	71
Figure 3.4 Perfusion bioreactor setup for reconstructed pancreas culture.....	73
Figure 3.5 Comparison between static and bioreactor culture for repopulated pancreas with pancreatic $\beta$ -cell, MIN-6.....	76
Figure 3.6 Differentiation of human embryonic stem cells (H1) to definitive endoderm .....	78

Figure 3.7 Comparison between static and bioreactor culture for repopulated pancreas with hESC-derived DE.....	81
Figure 4.1 Schematic summarizing the hPSC differentiation and decellularization-recellularization of pancreas. ....	97
Figure 4.2 Schematic summarizing the large scale differentiation of hESC in alginate capsules and repopulation into decellularized pancreas and liver.....	99
Figure 4.3 Decellularization and characterization of mouse liver. ....	102
Figure 4.4 Cell seeding and distribution comparison between repopulated pancreas and liver. ....	104
Figure 4.5 Engraftment and viability of repopulated pancreas and liver after 9 days bioreactor culture. ....	106
Figure 4.6 Characterization of 3D PP aggregates repopulated liver after 9 days bioreactor culture. ....	112
Figure 5.1 Fabrication and characterization of ECM extracts from decellularized pancreas, liver and heart.....	134
Figure 5.2 Surface coating and immobilization of ECM proteins to generate 2D ECM array... ..	138
Figure 5.3 On-chip, near IR Dye, immunofluorescence staining and LI-COR quantification... ..	140
Figure 5.4 hPSC-derived PP cells on 2D ECM array to investigate Cell-ECM adherence.....	144
Figure 5.5 Fabrication and characterization of 3D organ-specific ECM array.....	148
Figure 5.6 hESC-derived PP cells on 3D ECM array to investigate differentiation.....	154
Figure A.1 Decellularization of bovine pancreas. Panel images show progressive decellularization of bovine pancreas over the course of 65 hours. ....	173
Figure A.2 ProE schematic drawing of perfusion-decellularization set-up.....	180
Figure A.3 Perfusion system is compatible for scaling up .....	180
Figure A.4 Microbiological testing for bioreactor culture.....	181
Figure A.5 Cylindrical control volume used for the mass balance equation.....	182
Figure A.6 Average axial oxygen concentration. ....	185
Figure A.7 Decellularization of adult mouse pancreas.....	185

Figure A.8 Matrigel culture of 3D PP aggregates as control.....	186
Figure A.9 Co-seeding of endothelial and PP cells into decellularized liver. ....	187
Figure A.10 AFM images showing the surface roughness of 2D ECM array.....	187
Figure A.11 Sensitivity analysis of the on-chip IR Dye immunofluorescence staining with LICOR scanner. ....	188
Figure A.12 LICOR sensitivity for 2D and 3D analysis.....	189
Figure A.13 Spot breakage was observed when larger PP aggregates were cultured inside the 3D alginate microspots. ....	189
Figure A.14 AFM stiffness measurement of the 3D ECM array.....	190
Figure A.15 Single cells of MIN-6 beta cells exhibited good viability throughout 10 days culture inside 3D alginate microspots with and without matrigel. ....	191

## PREFACE

This dissertation work summarizes years of challenging but rewarding work spanning across multiple research teams and disciplines. It is these people to whom I am forever indebted, and it is with great pleasure and humility that I have the opportunity to thank them for their contributions to my development, both personally and professionally.

First and foremost, I owe my advisor, Dr. Ipsita Banerjee my sincerest gratitude for both taking me into her laboratory and providing me with her valuable time and mentorship. I would like to thank her for all the advice, knowledge, encouragement, and trust which she imparted in me for the past 5 years. I am truly appreciative of all of the opportunities she has given me and things I have learned from working in her lab. I would also like to thank my doctoral committee members: Dr. Suzanne Bertera, Dr. Stephen Badylak, Dr. George Gittes, and Dr. William Wagner for their support and guidance throughout my doctoral candidacy. Their valuable insights and criticisms have trained me to be a logical problem solver and critical scientist.

I would like to thank collaborators and members of Banerjee lab for their input and experimental expertise. Special thank-you to Dr. Suzanne Bertera whose organ harvesting specialty was critical to the implementation of the experiments described. Thank you to Dr. Willi Halfter for training me on biochemistry and extraction of ECM. I very much enjoyed his stories about traveling across South East Asia, where he once swam in a river full of snakes in Penang Island (my hometown). I am also thankful to my fellow colleagues: Dr. Maria Jaramillo, Dr.

Keith Task, Dr. Joseph Candiello, Shubin Mathew, Thomas Richardson, Hikaru Mamiya, and Vimal Vaidya for your peer support and camaraderie. I look forward to our continued friendship and to additional intellectual discussions. Phil Olsen and Mahalia Bradford were both excellent undergraduate researchers who contributed to the completion of this work.

I would not have developed the passion and skills to pursue a doctorate degree without the inspiration and guidance from my former research advisors, Dr. Harald Ott and Dr. Sunjay Kaushal. Thank you for instilling scientific curiosity and fostering my interest in pursuing a doctorate degree.

The Department of Bioengineering, Chemical Engineering and Swanson School of Engineering have given unrelenting support. I especially thank Dr. Sanjeev Shroff, Dr. Harvey Borovetz, Dr. Steve Little, and Dr. Vorp for their dedication to the institution and their continuing support of my endeavors. The administrative staffs were invaluable friends and colleagues who keep the gears turning: Patricia Park, Nicholas Mance, Lynette Spataro, Alicia Kemp, Glenn Peterson, Melissa Penkrot, Dan Cesnalis, Paul Kovach, Leslie Karon-Oswalt, and Nancy Donaldson.

Finally, I wish to acknowledge my friends and family, who have encouraged me through difficult times and provided me with love when I needed it most. To my fellow graduate students at the University of Pittsburgh's Department of Bioengineering and Fourth River Solutions, I extend an especially heart-felt thank-you. It's been an absolute pleasure learning and growing with you, and my time here would not have been nearly as enjoyable without you. To my beautiful and loving wife, Dr. Luye Chang, I am forever grateful for your love and support no matter the hour, dedication, and sacrifice. You encouraged me always to remain positive, to laugh, and to enjoy life. To my mother, Ean Hia Lee and my sisters, Shanny Goh, Shannen Goh

and Shalynn Goh, whose unconditional faith in me is humbling. Lastly, to my late father, Chong Chuan Goh, who unfortunately won't be here for my graduation, but whose love will forever be in my memory. I dedicate my thesis to you.

## **1.0 INTRODUCTION**

### **1.1 THE PANCREAS**

The pancreas is a critical glandular organ located beneath the liver and in between the stomach and spine. It has two functional components: the exocrine and endocrine portion, and is often referred to as two organs housed in one location. The exocrine portion of the pancreas is primarily responsible for secreting digestive juices in response to hormonal signaling from the digestive system. These hormones from the stomach and duodenum cause the basophilic cells of the pancreas to release inactive digestive enzymes including trypsinogen and chymotrypsinogen which are used for the digestion of lipids and proteins [1]. Though the production of digestive enzymes is the primary function of the exocrine pancreas there are also centroacinar cells which release bicarbonates in response to heightened acid levels in the stomach.

The endocrine pancreas, on the other hand, plays a vital role in maintaining blood glucose level by secreting hormones directly into the blood vessels. Endocrine functionality of the pancreas is isolated to cell clusters called Islets of Langerhans as illustrated in Figure 1.1. The predominant cell types within the Islets are glucagon-producing  $\alpha$  cells, insulin-producing  $\beta$  cells, somatostatin-producing  $\delta$  cells, pancreatic polypeptide-producing PP cells and ghrelin-producing  $\epsilon$  cells. These islet clusters are densely vascularized, allowing the cells of the Islets of Langerhans to distribute hormones directly into the blood stream. The endocrine hormones act in

harmony to regulate the glucose levels in the blood. When blood glucose levels begin to fall below the normal range (70-130 mg/dL, fasting), glucagon signals the liver to release glucose into the blood stream. In the opposite fashion, when blood glucose is high, insulin is produced to affect a number of cells, including muscle, red blood cells, and fat cells to absorb glucose out of the blood, thereby having the net effect of lowering the high blood glucose levels into the normal range [1].

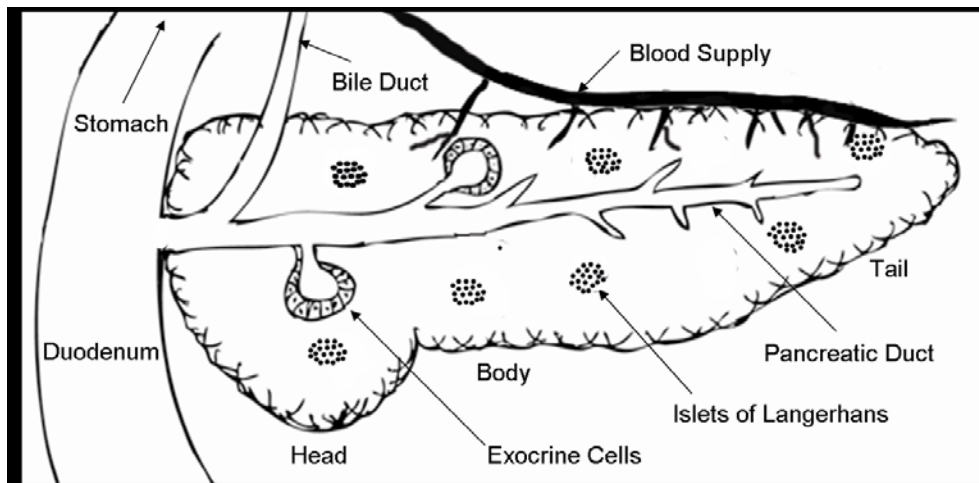


**Figure 1.1 General pancreas anatomy**

Exocrine cell interacts with the digestive system and endocrine cell (Islets of Langerhans) interacts with the blood stream.

### **1.1.1 Pancreas development**

The pancreas is a branching epithelial organ derived from endodermal germ layer. Pancreatic development occurs in a dynamic environment with active signaling from surrounding tissues. The dorsal and ventral portions of the pancreas undergo distinctly different developmental routine, although they are functionally similar in the mature organ. The dorsal pancreas results from budding of the dorsal endoderm upon receiving permissive signals from adjacent

notochord, aorta and pancreatic mesenchyme [2-4]. The ventral pancreas, on the other hand, buds out of the ventral endoderm, which is adjacent to the cardiac mesoderm. Cells of the ventral endoderm which escape inhibitory signals from cardiac mesoderm (FGF, BMP) results in the ventral pancreatic bud [5]. These epithelial buds subsequently branch and invade into the surrounding mesenchyme around embryonic day (E) 9.5 in the mouse embryo. As the pancreatic epithelium develops, the various hormone expressing cells appear from the common pancreatic progenitor and become apparent around E13.5. Around this time the dorsal and ventral pancreas are brought into proximity by the rotation of the gut tube. As organogenesis proceeds the pancreatic progenitor cells differentiate further to give rise to three distinct cell types by E18: acinar cell clusters which produce digestive enzyme; ductal cells which form a network which drains the digestive enzymes into the duodenum; endocrine cells which organize into islet clusters [6].

### **1.1.2 Extracellular matrix components in developing pancreas**

The branching epithelial morphogenesis of pancreas has been well investigated, and known to be associated with alterations in extracellular matrix (ECM) organization [7]. The ECM is primarily composed of high molecular weight molecules that include laminin, fibronectin, collagens [8-10] and a diverse array of proteoglycans and glycoproteins [11]. Pancreas development occurs in a transient environment – the ECM undergoes constant remodeling through its intimate interaction with surrounding cells. As the pancreas forms as an epithelial evagination into the surrounding mesenchyme, a specialized ECM termed the basement membrane (BM) develops in the epithelial-mesenchymal interface. The pancreatic BM is largely composed of laminins (80%) and collagen IV [8]. Laminin  $\alpha 1$  for instance, is detected in the BM of the developing mouse

pancreatic buds as early as E13.5 [12], but is down-regulated in adulthood [13, 14]. Importantly, Laminin  $\alpha 1$  has been shown to play a role early in gestation where it is present in the mesenchyme, then becomes focused to the epithelial–mesenchymal interface and then, through interactions with epithelial  $\alpha_6$ -containing integrins, mediates pancreatic duct formation [15]. Gittes et al. [16] verified this by overlaying isolated E11 mouse pancreatic epithelial cell with Matrigel, whose major component is laminin, where it induced duct formation. In addition, Laminin  $\alpha 1$  found in the mesenchyme was shown to mediate epithelial-mesenchymal interactions that lead to exocrine differentiation [17]. Laminin  $\alpha 1$  has also been shown to have a pro- $\beta$ -cell role slightly later in gestation. Specifically, laminin  $\alpha 1$  as a substrate enhanced  $\beta$ -cell differentiation in dispersed E13 mouse pancreatic epithelial cells, through binding to  $\alpha$ -dystroglycan [12, 18]. De Breuck, et al. [19] reported that netrin-1, a diffusible laminin-like molecule is present adjacent to E15-E18 pancreatic exocrine and endocrine cells, along with the netrin receptor neogenin [20]. Later Cirulli's group using embryonic pancreas as a model of developing epithelium, confirmed that netrin is localized to epithelial cells at their basal surface and binds  $\alpha_6\beta_4$  and  $\alpha_3\beta_1$  integrin during pancreatic epithelial adhesion and migration [21]. The integrin-ECM interactions in the developing human pancreas was demonstrated by Cirulli et al. by showing that  $\alpha_v\beta_3$  and  $\alpha_v\beta_5$  integrins mediates adhesion and migration on ECM [21]. Epithelial  $\alpha_v\beta_5$  and  $\alpha_v\beta_3$  integrins interacted with fibronectin, collagen-IV, and especially vitronectin to both maintain extracellular matrix anchorage ( $\alpha_v\beta_5$ ) and allow epithelial migration ( $\alpha_v\beta_3$ ). The expression pattern of these three matrix components was suggestive of their role in the migration of endocrine progenitor cells out of ducts to form islets. The same group further transplanted human fetal pancreas treated with RGD-blocking peptide 27O, which lead to a preferential loss of insulin-positive cells, or their precursors – this supports the vital role of

extracellular matrix components in guiding cell migration during early stages of islet morphogenesis [22]. The significance of vitronectin in early islet development was also demonstrated when upregulation of vitronectin receptor,  $\alpha_v\beta_1$ , in fetal compared to that of mature  $\beta$ -cells was observed [23].

### **1.1.3 Extracellular matrix components in adult pancreas**

The matrix composition of mature pancreas could vary significantly from developing pancreas. For example, while laminin plays a central role during pancreatic development, laminin  $\alpha 1$  was not detected extracellularly in the adult mouse pancreatic islets but found in the BM of acinar cells and duct epithelium [8]. Othonkoshi et al. [24] reported similar findings in human pancreas as well. Using antibodies specific for human laminin they showed that laminin  $\alpha 1$  is not expressed in the adult human pancreas but other isoforms of laminin were detected:  $\alpha 2$  is expressed only in the exocrine pancreas;  $\alpha 4$  is expressed in the blood vessel BMs;  $\alpha 5$  and  $\beta 1$  are expressed both in the endocrine and endothelial BMs in the islets. The other ECM protein reported to be most associated with adult pancreas is Collagen-IV, however fibronectin and Collagen-I, Collagen-III and Collagen-V and Collagen-VI have also been detected [9, 25]. In the endocrine “islet capsules”, the predominant ECM component are collagen types I, III, IV, laminin and fibronectin [25]. The laminin detected here have different isoforms than the one found in developing pancreas (laminin  $\alpha 1$ ). Studies in mouse islets have indicated the pancreatic islet cells interact with laminin associated with the pervading microvasculature, specifically laminin-2, laminin-8, and laminin-10 [23, 26-29]. Immunolocalization for laminin-V in rat and human islets demonstrated heterogeneous intracellular staining according to islet cell type, with stronger labeling on non-beta cells than beta cells, and negative labeling on the endothelial cells

or their associated basement membranes [30, 31]. Quantitative evaluation of the peripheral matrix composition of human islets demonstrated that the prevalence of collagen-VI was significantly greater than that of Collagen-I or Collagen-IV [32].

## **1.2 PANCREATIC DISORDER**

Due to the functional disparity between the exocrine and endocrine portion of the pancreas, pancreatic disorder is also specific to either exocrine or endocrine pancreas. The exocrine pancreas is the primary target of pancreatitis and pancreatic cancer while diabetes types I and II is caused by malfunction of the endocrine pancreas.

### **1.2.1 Exocrine pancreas disorder**

#### **1.2.1.1 Pancreatitis**

Pancreatitis is an inflammatory complication of the exocrine pancreas arising from early activation of the digestive enzymes produced by the exocrine pancreas before they exit into the duodenum. This results in the enzymes attacking the tissue of the pancreas itself. Pancreatitis is classified into two forms: acute and chronic. Symptoms of acute pancreatitis appear rapidly and can generally be relieved with a few days of therapy. Causes include gallstones blocking the pancreatic duct, abdominal trauma, or infection. Complications can range from severe pain to systemic problems such as low BP, kidney failure, or hypoxia. Treatment of pancreatitis generally involves resting the pancreas through fasting and antibiotics, or surgery to remove gallstones. Chronic pancreatitis, on the other hand, does not heal quickly and worsens over time

causing permanent damage to the pancreas. Common causes of chronic pancreatitis include prolonged alcohol abuse, cystic fibrosis, or hypercalcemia. Complications include severe pain, weight loss, and calcification of the pancreas requiring surgical intervention. Chronic pancreatitis can also lead to permanent damage of the insulin producing Beta cells of the pancreas, possibly leading to diabetes [33].

#### **1.2.1.2 Pancreatic cancer**

Pancreatic cancer, having a very high mortality rate, is the fourth leading cause of cancer death in the developed world. Risk groups include age, smoking, and chronic pancreatitis. The most common form of it is adenocarcinoma, which occurs in the exocrine portion of the pancreas [34]. While removal of the pancreas is a possible treatment, only 10% of diagnoses are discovered before the cancer has spread. If surgery is an option, either part or the entire pancreas is removed in addition to portions of the surrounding organs. While pharmacological treatment with gemcitabine has been used to increase quality of life and survival length, removal of part or whole of the pancreas is the only current option for cure making early detection key in the treatment of pancreatic cancer [35].

#### **1.2.2 Endocrine pancreas disorder**

The endocrine pancreas is composed of cluster of cells (islets of Langerhans) that are distributed throughout the exocrine pancreas. Insulin and glucagon, the two key hormones that orchestrate fuel storage and utilization, are produced by the islet cells in the endocrine pancreas. Diabetes mellitus is the most common disease associated with disordered secretion of hormones of the endocrine pancreas. It is a global disease with immense economic and social burden that affects

at least 285 million people worldwide [36]. It can be categorized into type 1 diabetes and type 2 diabetes according to their mechanism of action, even though type 2 diabetes itself is a whole family of disorders caused by an array of different factors [37].

#### **1.2.2.1 Type 1 diabetes**

Type 1 diabetes is a disease characterized by lack of insulin producing beta cells due to cell destruction via a person's own autoimmune response [38]. While there are various proposed models explaining the mechanism by which the immune cells infiltrate the Islets of Langerhans and destroy beta cells, the important aspect for treatment is that an alternate source of insulin must be adopted to maintain blood glucose level [39]. Hyperglycemia resulting from a loss of beta cell functionality can lead to blindness, cardiovascular complications, and kidney failure if left untreated [38]. While patients with type 1 diabetes lose pancreatic endocrine functionality, the pancreas maintains its ability to function as an exocrine organ as part of the digestive system [40].

#### **1.2.2.2 Type 2 diabetes**

Type 2 diabetes differs from type 1 diabetes in that the pancreas does produce insulin; however either in insufficient amounts or the body has developed a resistance to its effects. As a result hyperglycemia occurs with similar complications to type 1 diabetes if left untreated, although onset is more gradual [39]. Obesity is a major cause of type 2 diabetes, as fat interferes with the ability for insulin to be used properly; however other factors such as age, high blood pressure, and genetic history are also factors.

### 1.2.3 Current treatment

The major implication of diabetes is the loss of endocrine function of the pancreas. This results in a complete loss or severely diminished capacity to regulate blood glucose levels, which results in a variety of complications. For this reason, therapeutic approaches focus on restoring the body's ability to produce and regulate blood glucose level either through artificial introduction of insulin into the blood stream or regeneration/ transplantation of insulin producing cells.

The most prevalent pharmaceutical treatment for type 1 diabetes is to artificially introduce insulin to the blood stream. This approach involves careful monitoring of the blood glucose levels along with daily insulin injections [38]. Even with constant vigilance there is still a chance for hypoglycemic reactions leading to both minor and major complications [38]. Type 2 Diabetes can be effectively contained by either oral medications or injectable antidiabetic agents. Most of the pharmaceutical drugs for diabetes targets to maintain the blood glucose level by either (i) controlling glucose secretion by liver into the blood stream (ii) priming the body to respond better to insulin and (iii) inducing the pancreas to secrete more insulin. However in extreme cases Type 2 diabetes patients may also require to take insulin injection.

Alternate strategies for diabetes treatment include gene therapy, where islet like behavior is induced in non-islet cell types. The primary function of the pancreatic islet is to sense the glucose level in blood and secrete insulin in response to that. Hepatocytes of the liver have been a target of such therapy due to their already existing ability to sense changes in the blood glucose levels. Results so far have been limited in scope with precise control of insulin production in phase with blood glucose levels being problematic [41, 42].

Transplantation of donor islets has received considerable attention as an avenue for restoring insulin production in diabetic patients. The major breakthrough in Islet transplantation

came with the success of the Edmonton Protocol in 2000 [43], which established an effective immunosuppressive regimen. Ever since, Edmonton protocol has been adopted by many of the Islet transplantation clinics worldwide, however this procedure still requires a large supply of islets from donor pancreas. Currently the major roadblocks in cellular therapy for diabetes are the lack of sufficient quantities of donor tissue and the need for lifelong immunosuppressive therapy [38, 44]. There has been concentrated effort in addressing the issue of immune rejection by encapsulating donor islets in specific substrates designed to protect the donor islet from cellular immune attack while still allowing diffusion of insulin and glucose. Lack of sufficient donor islets has triggered investigation of alternate cell sources with the potential to generate fully functional pancreatic islet cells which can be transplanted to re-establish euglycemia in diabetic patients.

Pancreas transplantation remains the gold standard for patients who suffer from type 1 diabetes who do not respond to conventional therapy [45]. It involves implanting a healthy pancreas from a cadaveric donor into the diabetic patient. Since the pancreas is a dual-functioning organ also participating in the digestion process, the recipient's native pancreas is usually left in place, and the donated pancreas is placed in the right lower part of the patient's abdomen. The majority of pancreas transplantation (>90%) involve simultaneous transplantation of pancreas-kidney [46]. This treatment option is however limited by the low availability of donor pancreas [45] and other complications such as thrombosis, pancreatitis, infection, bleeding and rejection. The development of bio-engineered tissues/organs by regenerative medicine and tissue engineering strategies has the potential to provide alternative treatment avenues [47].

### 1.3 PANCREAS TISSUE ENGINEERING

In the past decade, pancreatic tissue engineering efforts have focused on recreating the natural the islet ‘niche’ to restore the critical signal loss between native islet cells and their ECM environment following islet isolation. The objective is to improve islet graft survival post transplantation, and making it immunologically compatible with the recipient. Microencapsulation and the addition of natural matrix substitutes such as collagen IV and laminin have provided an immuno-privileged islet niche while permitting waste and nutrient diffusion and improved islet function [48, 49]. More recently, combinations of cells, biomaterials and biologically active molecule have been integrated in an attempt to generate bioengineered pancreas to ameliorate type 1 diabetes and achieve complete insulin independence [50-52]. Many important milestones have been met toward the goal of generating bioengineered pancreas. Potential cell candidates have been derived from allogeneic or xenogeneic islets [53], trans-differentiation of adult cells [54] or differentiation of pluripotent stem cells into insulin-producing cells [55-58]. The construction of biomaterial scaffolds includes fabrication of synthetic and native biomaterials with the goal to rebuild the necessary microstructure and extracellular cues for cell attachment, differentiation, function and vascularization to enable formation of human size pancreatic constructs [59, 60]. Lastly, the development of bioreactor has facilitated the transport of biological signals to support the *in vitro* assembly, culture and maturation of bioengineered pancreas into functional tissue constructs [61].

### 1.3.1 Cells

Identifying a reliable source of mature cells is critical for regenerative medicine and tissue engineering studies. Early pancreas tissue engineering studies focused on the use of primary islets and immortalized endocrine  $\beta$  cell lines for demonstration of proof-of-concept [49-51, 62]. The use of human islets is limited by the scarcity of donor organs. While immortalized endocrine  $\beta$  cell lines are abundant, nevertheless they lack significant clinical application due to tumor formation concern as a result of gene transfection to immortalize the cells [63]. The production of a bioengineered pancreas from renewable cell source such as human pluripotent stem cells (hPSC), on the other hand, would be ideal due to their unlimited potential for self-renewal, expansion and differentiation. These cell types can be differentiated into any cell type including islet cells that respond to glucose stimulation and could function as beta-cell substitutes. Here we summarize some key findings of hPSC differentiation into pancreatic islet cells.

#### 1.3.1.1 Pancreatic differentiation from human embryonic stem cells (hESC)

Human embryonic stem cells (hESC) are pluripotent cells derived from the inner cell mass of the blastocyst, approximately 4-5 days after fertilization [64]. More than a decade ago, the first documented attempt to product insulin<sup>+</sup> cells from hESC was introduced by Lumelsky et al. [65] by following a protocol for neuronal differentiation, as the developmental pathways for the central nervous system and pancreas are similar. Since then, multiple groups [61, 66-68] including ours [69-71] have attempted to create cells that more closely resemble pancreatic  $\beta$ -cell development rather than insulin-positive neural-like cells. By recapitulating the early pancreatic developmental stage, step-wise *in vitro* differentiation protocols have successfully generated pancreatic progenitors and insulin-producing cells from hESC [57, 58, 67, 68, 72]. However,

overcoming the immunogenicity issue after allogeneic transplantation remains a major challenge for hESC to be an optimal cell candidate for clinical applications.

### **1.3.1.2 Pancreatic differentiation from human induced pluripotent stem cells (hiPS)**

hiPS cells can be engineered from somatic cells by the ectopic expression of four transcription factors (OCT4, SOX2, KLF4, and c-MYC) [73]. Virtually indistinguishable from ES cells, hiPS cells can be propagated indefinitely as undifferentiated cells and differentiated into practically any cell type. hiPS derived from patient's somatic cells opened the possibility of generating autologous cells, thus eliminating immune rejection concern. In 2009, Maehr et al. demonstrated the reprogramming of human skin fibroblast into hiPS from type 1 diabetic patients [74]. In addition to providing an immunologically matched autologous cell population, patient-specific hiPS derived cells make possible patient-specific disease modeling wherein the initiation and progression of type 1 diabetes can be studied. Several other groups have since derived their own hiPS lines and differentiated into pancreatic lineage and its successful *in vivo* maturation into functional insulin producing cells [66, 75-77]. Success with *in vitro* maturation was challenging until recently. In 2014, two groups have reported the *in vitro* differentiation and maturation of hPSC (both hESC and hiPS) into insulin-producing cells [78, 79]. The resulting hiPS derived islet cells secreted insulin in response to glucose stimulation *in vitro* and upon transplantation could restore glucose homeostasis in diabetic mouse model [78, 79].

### **1.3.1.3 Other cell types**

There is reported evidence to produce insulin<sup>+</sup> cells from cells that are developmentally close to  $\beta$ -cells. For instance, pancreatic acinar and ductal cells have been demonstrated to be potential cell populations that can be differentiated into  $\beta$ -cells [80-83]. Other attempts include the

feasibility of transdifferentiating common progenitors such as hepatocytes into pancreatic  $\beta$ -cells [84, 85]. To date, however, these cell populations have limited success in producing functional  $\beta$ -cell that reverse hypoglycemia *in vivo* [86]. It is still an active area of research, and if successful, would offer viable cell source of pancreatic tissue engineering. Islets from nonhuman source such as porcine islets have been investigated as alternative cell types. Several preclinical trials using macro and microencapsulation of porcine islets demonstrated efficacy for several years without the need for immunosuppressant [87]. Nonetheless, porcine islet transplantation remains an experimental procedure due to limited long-term viability and the current need for immunoprotection [88].

### **1.3.2 Biomaterial scaffolds**

Here we summarize various synthetic and natural biomaterial scaffolds have been used in pancreatic tissue engineering. The main objective in the use of biomaterial scaffold is twofold. The first is to provide structural support and restore the critical signal loss between native islet cells and their ECM environment following islet isolation. Secondly, it provides immunoprotection upon transplantation into host animal or patients.

#### **1.3.2.1 Synthetic materials**

Poly glycolic acid (PGA) is a highly biocompatible polymer which has a very low toxicity of byproducts when degraded. Rat islet cells cultured on PGA scaffolds modified with poly-L-lysine (PLL) exhibited both longer survival time and increased insulin production [89]. Self-assembling peptide nanofibers have been shown to increase both cell viability and function for rat islets when cultured in a 2D microenvironment [90], but cell viability and insulin secretion increased

further when cultured within a scaffold formed from self-assembling peptide nanofibers which demonstrates the preference of the islets for 3D culture configurations [91]. PLL induced aggregation of PDX1 transfected fetal hepatocytes showed matured islet functionality and glucose responsive insulin release within 24 hours of culture. Similar maturation could not be induced on parallel cultures on collagen [92]. Cells maintained on PLL also showed increase in NeuroD, Gck and Glut2 expression compared to collagen and tissue culture plastic [92]. These results were attributed to previous observations that PLL is able to activate insulin receptor kinase [93]. In addition to primary islets cells, rat pancreatic precursor cells have also been cultured on synthetic scaffold such as poly-ethylene-glycol (PEG) hydrogels. The dissociated rat pancreatic precursor cells were viable after 7 days of culture and showed an increase in insulin and MafA expression. In contrast, cells grown on 2-D plastic tissue culture plates were found to de-differentiate into mesenchymal phenotypes. Even though mature markers were sustained, these cells did not demonstrate mature functionality of glucose responsive insulin release, suggesting incomplete maturation [94]. While PEG alone failed to mature the pancreatic precursor cells, collagen entrapped in PEG was found to induce such maturation in subsequent studies [95]. Similarly, additional media supplementation by adding gamma secretase inhibitor to the pancreatic progenitors cultured in PEG hydrogels also resulted in adequate maturation with glucose responsiveness [96]. Taken together, 3D tissue culture configuration is deemed best suited for islet maintenance and function.

### **1.3.2.2 Natural materials and decellularized ECM**

Given the importance of scaffold design in islet function, there also has been a focused effort to investigate natural and purified ECM due to their closer resemblance to biological tissue microenvironment. Alginate is a chemically inert non-degradable natural polymer, and most

importantly it has the capability to immuno-isolate encapsulated cells. Due to its relatively high biocompatibility and gelation in the presence of a divalent cation it has been widely used for cell encapsulation. Lim and Sun in 1980 [97] first used an alginate complex to microencapsulate rat islets using syringe pump extrusion. Islets were first encapsulated in spherical alginate beads and then coated in poly-l-lysine. These encapsulated islets were found to be viable under culture conditions for up to 4 months, and transplantation into streptozotocin induced diabetic rats demonstrated an increase in islet viability and blood glucose level maintenance from 6 to 8 days to close to three weeks when compared to directly transplanted islets [97]. Other natural material such as rat-tail collagen I has been used to embed isolated human islets and was noted to hold their three dimensional spherical shape and maintained higher insulin producing capacity when compared to islets plated on cell culture treated plastic plates. In addition islets cultured on a collagen I 2-d layer regained spherical shape and insulin function when overlaid with an additional layer of collagen. In both the embedded and multilayer collagen I islet groups survivability and insulin production lasted more than 8 weeks, significantly longer than the 14 days maximum survival of islets cultured on uncoated cell culture treated plastic dishes [98]. Most of natural material scaffolds, however, use a purified single ECM protein and do not mimic the intricacy of the pancreatic ECM composition and ultrastructure. Recently there has been a shift towards multiple-matrix systems of purified proteins, which have been shown to improve stem cell proliferation and differentiation [99, 100] and promote isolated islet and  $\beta$ -cell survival and function [48, 49]. Alternatively, natural ECM derived from decellularized tissues and organs can provide physiologically relevant scaffold that recapitulates the complex *in vivo* microenvironment. Decellularization techniques allow us to extract this complex native ECM, and have been successfully demonstrated in various cells, tissues and organs [101]. Prior studies

have shown the positive effect of endothelial cell derived ECM for the enhancement of islet and  $\beta$ -cell attachment and proliferation [102, 103]. This is consistent with the previous finding from Nikolova et al. that demonstrated the vascular basement membrane is a niche for insulin gene expression and beta cell proliferation [27]. Other works have also shown improved islet functionality when cultured on decellularized matrices derived from small intestinal submucosa (SIS) [104, 105] and pancreatic slices [106, 107]. Decellularized pancreas work described by De Carlo et al. [106] and Mirmalek-Sani et al. [107] revealed the benefits of 2D decellularized pancreas slices to support and maintain islet functions. More recently, decellularized scaffolds have extended to more complex three-dimensional (3D) ECM scaffolds such as decellularized whole heart [108-110], lung [52, 111-114], liver [115-117], kidney [118], and pancreas from our group [50] based on a platform technology called perfusion-decellularization [119]. The reconstruction of 3D engineered tissue based of this technology relies heavily on perfusion bioreactor for adequate nutrient transport which will be demonstrated in the next section.

### **1.3.3 Bioreactor**

The basic requirement of a bioreactor is to facilitate media transport into and from 3D tissues by providing dynamic culture. The objective is to maintain the desired nutrient and gas concentration in the engineered 3D tissue constructs. The main components of a bioreactor apparatus usually include a temperature controlled sterile chamber to hold the cells and/or tissues, a perfusate pump and membrane oxygenator to provide a continuous supply of gases (e.g. oxygen, nitrogen, carbon dioxide) and nutrients for cell survival and growth. When possible, the nutrient supply of bioreactors is connected directly to existing vasculature of the engineered tissues. For instance, nutrient supply for recellularized heart is provided via

retrograde media perfusion through the aorta [108, 120]. For recellularized lung, it is flown antegrade via pulmonary artery [121] using a perfusion bioreactor. These bioreactor configurations limit dead zones and promotes mixing, as determined by mathematical modeling and experimentation [122]. Recently, a commercially available bioreactor was reported for decellularization, named Organ Regenerative Control Acquisition (ORCA) bioreactor (Harvard Apparatus Regenerative Technologies, HART) [123]. This bioreactor was demonstrated to efficiently decellularize multiple intact organs and also amenable to support the culture of recellularized lungs. In addition, these systems could also be modified to control critical environmental conditions and provide stimuli (e.g. electrical stimulation for cardiac regeneration), as well as incorporate data monitoring systems to record/adjust variables, such as temperature, perfusion flow rate, pressure and oxygen tension [47, 124]. Furthermore, specific sensors could also be incorporated to monitor organ growth and ensure a controlled culture environment. Recently, Uzarski et al. reported the monitoring recellularized kidney and liver by sampling of physical and biochemical markers such as hydrodynamic pressure and soluble biomarkers (e.g. albumin and kidney injury molecule-1) respectively [125]. To further customize these systems based upon need, custom-designed perfusates and artificial oxygen carriers can also be added [126].

#### **1.4 SPECIFIC AIMS**

The goal of this dissertation is develop a regenerative bioengineered pancreas for the treatment of diabetes. The central hypothesis is that decellularized organ scaffolds with preserved micro-environmental niche will act as a favorable 3D bioscaffold for the synthesis of a regenerative

bio-engineered pancreas using human embryonic stem cells (hESCs). The realization of this goal requires success in three challenging processes: i) adequate decellularization of the whole organ to obtain 3D ECM scaffold, followed by ii) its recellularization with relevant cell types and iii) subsequent phenotypic maturation to reconstruct organ specific function. To understand the contribution of decellularized organs, it is also critical to evaluate the matrix-specificity and how it affects stem cell fate commitment.

In the current dissertation, we will test our central hypothesis and address these critical challenges by pursuing the following **SPECIFIC AIMS**:

#### **1.4.1 Specific Aim 1: To decellularize a whole-organ pancreas and analyze the potential of the natural 3D scaffold to support pancreatic tissue engineering**

The objective of this aim is to generate a 3D bioscaffold from native pancreas and examine its potential to support pancreatic cell types. We achieved this by perfusion-decellularization of the whole pancreas, followed by a thorough characterization of the resulting bioscaffold. Upon recellularization, we evaluated its feasibility as a bioscaffold to support pancreatic tissue engineering.

In Chapter 2, we detailed the generation of 3D bioscaffold supportive of pancreatic cell types; and evaluated the potential benefit of using native organ derived multi-faceted ECM scaffold over single protein derived ECM scaffold. This result demonstrated the proof-of-concept of using decellularized pancreas as a biocompatible scaffold for pancreatic tissue engineering.

#### **1.4.2 Specific Aim 2: To repopulate the decellularized pancreas with hPSCs and mature into insulin-expressing cell in whole organ bioreactor culture**

The objective of this aim is to evaluate the feasibility of repopulating the native organ-derived scaffold with differentiating hPSCs and subsequent phenotypic maturation to reconstruct organ specific function in a bioreactor. This aim is spread across 2 chapters: Chapter 3 and Chapter 4.

The organ reconstruction step is critically dependent on the engineering of a perfusion bioreactor system. In Chapter 3, we report the development and assembly of a perfusion bioreactor to enable regenerative reconstruction of pancreas. The assembled bioreactor is versatile enough to efficiently decellularize multiple organs, as demonstrated by complete decellularization of pancreas, liver and heart in the same set-up. Further, the same system is amenable to support organ repopulation with diverse cell types such as MIN-6  $\beta$  cells and differentiating hPSCs. The second part of this aim, in Chapter 4, we demonstrated the reconstruction of bio-engineered pancreas with both hPSC-derived PP cells and PP aggregates by using our in-house bioreactor system. The engraftment of these PP aggregates required a more extensive vascular support; hence we investigated the possibility of using an alternate, highly vascularized platform: decellularized liver, to allow reconstruction with PP aggregates and further maturation into mono-hormonal insulin expressing cells in a whole-organ bioreactor setting.

### **1.4.3 Specific Aim 3: To evaluate the matrix-specificity of organ-derived ECM in human embryonic stem cell differentiation**

The objective of this aim is to evaluate the matrix specificity of organ derived ECM and its effect in inducing pancreatic differentiation of human embryonic stem cells. Toward this end, in Chapter 5, we developed 2D and 3D ECM array from solubilized whole-organ ECM extracts of pancreas, liver and heart. This array system permits rapid evaluation of the matrix protein profiles of different organ-derived ECM, along with the sensitive measurement of the cell-ECM interaction both in 2D adherent cultures of hESC-PP cells as well as 3D non-adherent culture of hESC-PP aggregates.

## **2.0 PERFUSION-DECELLULARIZED PANCREAS AS A NATURAL THREE-DIMENSIONAL SCAFFOLD FOR PANCREATIC TISSUE AND WHOLE ORGAN ENGINEERING**

### **2.1 INTRODUCTION**

In the first aim of this work, we investigate the development of a 3D native bioscaffold to support pancreas bioengineering. Our objective was to develop a bioscaffold that supports and enhances cellular function and tissue development. Perfusion-decellularized organs are a likely candidate for use in such scaffolds since they mimic compositional, architectural and biomechanical nature of a native organ. To this end, we investigate perfusion-decellularization of whole pancreas and the feasibility to recellularize the whole pancreas scaffold with pancreatic cell types.

Three-dimensional (3D) scaffold plays a critical role in regenerative medicine and tissue engineering. For example, cell-scaffold interactions are important for the regulation of cellular behavior, including pancreatic islet-cell survival and insulin production through integrin-mediated activation and downstream signaling events [127, 128]. Native tissues and organs are comprised of unique extracellular matrix (ECM) compositions, microstructures and biomechanical properties, which maintain distinct signals for resident cells [129, 130]. Ideally, a tissue engineered scaffold would provide the same or similar microenvironmental niche to the

seeded cells as that of a native ECM. Therefore, at present, the development of scaffolds for pancreatic tissue engineering have focused on recreating milieu similar to the native islet and surrounding ECM (summarized in review by Cheng et al. [62], Candiello et al. [131] and Tuch et al [132]).

The novel concept of whole organ perfusion decellularization has been described recently to generate native ECM scaffolds from complex organs such as heart [108, 133-135], liver [116, 117, 136, 137], lung [111-114, 121, 138], kidney [118, 139, 140] and more recently pancreas [52, 107, 141, 142]. Acellular matrices from whole organs provide an attractive scaffold for engineered tissue/organ because of the physiological resemblance with the original tissue, including intact 3D anatomical architecture, preserved spatial array of ECM components, vascular network, and biomechanical properties. These initial studies clearly motivate the need and indicate the potential benefits that can be attained by a whole organ 3D reconstruction of pancreas. The importance of 3D scaffold is well recognized for a better representation of the complex *in vivo* microenvironment and is important for proper regulation of cell behavior [143], yet recellularization of whole pancreas 3D scaffold remains to be demonstrated. We hypothesize that the optimal scaffold to support pancreatic tissue engineering may be the natural 3D ECM scaffold of the whole pancreas. To this effect, we propose that perfusion-decellularization of whole pancreas will yield an acellular scaffold suitable for pancreatic tissue and organ engineering.

This chapter presents the feasibility of generating an acellular whole pancreas scaffold by a perfusion decellularization technique and utilizing this scaffold to support whole organ pancreas regeneration. Toward this end, we characterized the resultant native pancreatic ECM-scaffold for preservation of ECM composition, 3D structural integrity, and biomechanical

properties. We then repopulated the decellularized pancreas with endocrine and exocrine cell types to demonstrate the feasibility of recellularization. Furthermore, the effects of pancreas derived ECM scaffold on modulating cell function such as insulin gene expression was determined.

## **2.2 METHODS**

### **2.2.1 Mouse Pancreas Harvest and cannulation**

All animal work performed was in accordance with animal welfare act, institutional guidelines and approved by Institutional Animal Care and Use Committee of the University of Pittsburgh). Female ICR mice (Taconic), between the ages of 6-12 weeks were euthanized by CO<sub>2</sub> inhalation followed by cervical dislocation. Sterile conditions were observed when removing the pancreas. A laparotomy was performed and a 24 G catheter was inserted approximately 1 cm into the anterior hepatic portal vein and sutured in place. The distal end of the superior mesenteric vein and large branches of splenic arteries and veins were carefully ligated to prevent leakage. The pancreas was then carefully dissected free from all adjacent structures including the stomach, intestine, spleen and mesenteric tissue.

### **2.2.2 Perfusion Decellularization of Mouse Pancreas**

The isolated pancreas was connected to a perfusion system to allow retrograde perfusion at 8ml/min, in which solutions flowed through the hepatic portal vein, into the splenic vein, and

throughout the vasculature of the pancreas. Next, ionic detergent, 0.5% SDS (Invitrogen) in deionized water was used as perfusate to rinse cells and cell debris out of the pancreas. After the tissues became translucent (about 325 min), subsequent steps of perfusion were 15 min of deionized water perfusion and 15 min of 1% Triton X-100 (Sigma Aldrich) in deionized water. A solution of benzonase (90U/ml, Sigma) was perfused for 15 min and a final washing step of 10% fetal bovine serum (FBS, Life Technologies) in PBS with Pen/Strep (100U/ml) perfused the pancreas for additional 48 hours to clear remaining cellular debris.

### **2.2.3 Cell culture**

The AR42J acinar cell line (CRL-1492, ATCC, VA, USA) was used at passage 18-25. AR42J was cultured in F-12K medium (ATCC, VA, USA) supplemented with 20% FBS (Life Technologies) and 100 U/ml penicillin/streptomycin (Life Technologies) on T75 tissue culture flasks. The MIN-6  $\beta$ -cell was used at passage 19-26. MIN-6 was cultured in Dulbecco's modified Eagle's medium (Life Technologies) supplemented with 15% FBS (Life Technologies) and 100 U/ml penicillin/streptomycin (Life Technologies) on T75 tissue culture flasks. Both cell types were cultured at 37°C and in a 95% air / 5% CO<sub>2</sub> atmosphere.

### **2.2.4 *In vivo* implantation of decellularized pancreas**

All animal work was approved by the Institutional Animal Care and Use Committee of the University of Pittsburgh. For preliminary biocompatibility studies, a 1 cm<sup>2</sup> perfusion-decellularized pancreas construct was surgically placed within a dorsal subcutaneous pocket of an adult mouse. Female C57BL/6 mice, age 6–8 weeks, were purchased from Jackson

Laboratories (Bar Harbor, ME). The mouse was anesthetized and maintained at a surgical plane of anesthesia with 1.5–2.5% isoflurane in oxygen and positioned in dorsal recumbency. The surgical site was prepared in sterile fashion by swabbing with 10% povidone-iodine solution followed by the placement of sterile drapes. For the subcutaneous surgical implantation: A central longitudinal incision measuring approximately 1.5 cm in length was made in the epidermis, dermis, and fascia to expose the underlying muscle tissue on the dorsal side. Dermal layers and underlying connective tissue was undermined to create a pocket with similar size to the implant construct. The decellularized pancreas construct was sutured to the underlying muscle with four non-absorbable marking sutures (3-0 prolene) and the skin was closed over the implant site in uninterrupted fashion. A minimal amount of suture material was placed only at the construct corners to avoid eliciting a host response to the suture that would obscure the host response to the implanted material. The incision was covered in betadine ointment after closure and assessed for signs of infection for 2 days post-surgery. The mouse received Buprenex (buprenorphine hydrochloride, 0.25 mg/kg) for analgesia, and Baytril (enrofloxacin, 20 mg) an antibiotic, for 3 days postoperatively. The animal survived the surgical procedure and its predetermined study period without complications. After 14 days the mouse was euthanized with 5% isoflurane in oxygen followed by an intracardiac injection of potassium chloride to induce cardiac arrest. Following euthanasia the implant along with the surrounding skin and muscle were harvested and fixed in 10% NBF for histologic evaluation.

### **2.2.5 Recellularization and culture of seeded-pancreatic construct**

MIN-6 cells ( $30 \times 10^6$ ) were trypsinized and diluted in 3mL of medium. The cell suspension was introduced into the decellularized pancreas by means of retrograde gravity perfusion via the

hepatic portal vein in 3 steps, 1mL each, with 20 min interval between each step. MIN-6 seeded pancreas was immersed and cultured in the same MIN-6 cell culture medium described above for 5 days. For co-recellularization strategy, AR42J was used as the second cell type for the recellularization. Similarly, AR42J ( $30 \times 10^6$  cells) were trypsinized and diluted in 3mL of medium. The AR42J cell suspension was inoculated into the pancreas by retrograde perfusion through the pancreatic duct but the MIN-6 cells were introduced through the vasculature. The two cell types were seeded in sequence, with the same multi-step repopulation mentioned for single-cell type seeding. Cells were allowed to attach for 2 hours before introducing a gentle rinse through both the hepatic portal vein and pancreatic duct in order to wash out any unattached cells. The cell-seeded pancreatic construct was left undisturbed and submerged in co-recell culture medium (DMEM/F12 supplemented with 15% FBS and 100 U/ml Pen/Strep). Both cannulation to the portal vein and pancreatic duct were kept intact to allow perfusion feeding of media every day. The seeded pancreas was cultured under static conditions at 37°C with a 95% air / 5% CO<sub>2</sub> atmosphere for 5 days.

## **2.2.6 MIN-6 seeded on different ECM substrates and 2D thin slices of Decellularized**

### **Pancreas**

Growth factor-reduced Matrigel (BD) was used as a thin coating according to manufacturer's instruction. Collagen IV (BD) and fibronectin (Milipore) were used at a concentration of 5 mg/ml. These ECM substrates were used for coating non-tissue culture-treated 12-well plates (BD). Collagen type I (BD) was used as 5 mm thick gels. Coated and untreated (UT) plates were blocked with 1% BSA (Sigma). Control culture was conducted on UT plates blocked with 1% BSA (Sigma). To prepare thin decellularized pancreata slices, decellularized

pancreata were filled with 1.1% alginate solution, and submerged in 100mM Calcium Chloride solution to crosslink the alginate. The solidified pancreas was sliced with a tissue slicer (Thomas Scientific) to yield thin, uniform, transverse sections. The alginate within the thin slices of pancreas were dissolved in a sterile dissolution buffer consisting of 50 mM tri-sodium citrate dihydrate (Sigma), 77 mM sodium chloride (VWR International, Leicestershire, UK), and 10 mM HEPES (Sigma) in PBS for 15–20 min while stirring gently at room temperature. Finally, the thin slices of pancreas were rinsed and covered with sterile PBS with Pen/Strep (100U/ml), and placed at 4°C until use. Cloning cylinder (Fisher) was applied and sealed with sterile silicone grease (Dow Corning) to the pancreatic slice to consolidate the seeded cells only to the pancreatic slice. MIN-6 cells (25,000 cells/cm<sup>2</sup>) were cultured on these various different ECM substrates for 5 days before harvest for qPCR analysis.

### **2.2.7 Two-photon Microscopy**

Two-photon microscopy was performed with an upright Olympus FV1000 MPE multi-photon microscope (Olympus, Central Valley, PA, USA) and a Mai Tai DeepSee femtosecond-pulsed laser (Spectra-Physics, Santa Clara, CA, USA) tuned at 800 nm. The pancreatic slice was line-scanned and fluorescence emission was captured by three non-descanned external photomultiplier tube (PMT) detectors coupled to the following long-pass dichroic mirrors and band pass emission filters: 505 nm mirror and 460–500 nm filter (blue channel), 570 nm mirror and 520–560 nm filter (green channel) and 575–630 nm filter (red channel). The pancreatic slice was placed on an imaging dish having a #1.5 coverslip and immersed in PBS. Fixed *xy* planes spanning 505 × 375 μm at a resolution of 0.994 μm/pixel and depth of 1–50 μm from the surface

of scaffold were imaged using a high numerical aperture (NA = 1.05), water-immersion 25X objective.

### **2.2.8 Immunohistochemistry (IHC)**

Native, decellularized and recellularized pancreas were fixed, sectioned and stained following protocol previously described[144]. Briefly, tissue samples were fixed with 4% formaldehyde (ThermoFisher), cryoprotected with 30% sucrose and cut into 7  $\mu\text{m}$  thick sections. For immunostaining, the following primary antibodies were used: rabbit anti-laminin, rabbit anti-collagen I, rabbit anti-collagen IV, rabbit anti-fibronectin (Abcam, 1:200), rabbit anti-Cpeptide (Cell signaling, 1:100) and rabbit anti- $\alpha$ -Amylase (Sigma Aldrich, 1:200). Secondary antibodies used were: donkey anti-rabbit Alexafluor 488 (1:500, Invitrogen) and donkey anti-rabbit Alexafluor 555 (1:500, Invitrogen). For co-labeling using antibodies from the same host species, sequential staining was conducted. After the first primary antibody staining, an additional blocking step was included prior to the addition of a second primary antibody. For actin staining, phalloidin rhodamine (Cytoskeleton, 1:200) was implemented and stained for 30 min in the dark. The slides were washed again three times with 1x PBS (5-10 min) each before being mounted with ProLong® Gold Anti-fade Reagent with DAPI (Invitrogen). Images were recorded with Metamorph 7.5.6.0 (Molecular Device) on an Olympus IX81 inverted microscope (Olympus, Central Valley, PA, USA).

## 2.2.9 ECM Digestion and Proteomics Analysis

The ECM pellet was digested for 2h with each of the following enzymes: 0.15 mU/ $\mu$ l heparan sulfate lyase and chondroitin ABC lyase from *Flavobacterium heparinum* and *Proteus vulgaris*, respectively (Seikagaku Corporation, Japan) and washed in PBS. The ECM proteins were dissolved in 8M urea and 1x reducing SDS sample buffer. The proteins from the ECM preparation were separated on 3.5-15% gradient SDS PAGE under reducing conditions [145]. The gel lane was divided into 11 slices and taken through a typical in-gel digestion procedure. Briefly, gel bands were destained, reduced with 2.5mM tris (2-carboxyethyl) phosphine and alkylated with 3.75mM iodoacetamide, followed by in-gel digestion with 13ng/ $\mu$ l of trypsin (Promega) overnight at 37<sup>0</sup>C. Peptide digests were analyzed by nano Liquid Chromatography-tandem mass spectrometry (LC-MS/MS), on a Thermo Fisher LTQ OrbitrapVelos connected to a Waters Acquity UPLC system (Waters Corp., Milford, MA), using a 90 minute gradient. Protein identification was performed with Proteome Discoverer 1.3 using the Sequest search engine. Database searches used the Uniprot complete mouse database (downloaded in December 2012 merged with a contaminant database from ABSciex, 50838 sequences, 24435643 residues). Settings were for a full trypsin digest, with two missed cleavages, one static modification (cysteine carbamidomethylation), two dynamic modifications (oxidized methionines and hydroxyproline), mass tolerance of 10 ppm for precursor mass and 0.5 Da for fragment masses. Percolator, a post-processing software using a target/decoy database approach, was used to evaluate the accuracy of peptide identifications. Peptide identifications were filtered with a q-value cutoff of 0.01 (1% global False Discovery Rate, FDR). Proteins were grouped using the maximum parsimony principle and this list was imported to ProteinCenter (Thermo) and

compared with the IPI mouse database for statistical analysis to identify over-represented Gene Ontology terms and functional classification.

#### **2.2.10 DNA Quantification**

The decellularized pancreata (n=3) were digested with papain solution at 60°C for 6 h. The native pancreata (n=3) were digested in papain solution as controls. Papain (Sigma Aldrich) was dissolved at 400 mg/ml in 0.1 M phosphate buffer (pH 6.0), with 5 mM cysteine hydrochloride (Sigma Aldrich), and 5 mM EDTA (Sigma Aldrich). The lysates were used for detection of the DNA and sulfated glycosaminoglycan (sGAG) content. A DNA quantification kit - Quant-iT™ PicoGreen® dsDNA Assay kit (Invitrogen) was used to measure DNA content according to manufacturer's instruction. The fluorescence reading (excitation: 485 nm and emission: 528 nm) was taken on a plate reader (Synergy 2, Biotek), and the absolute amount of DNA (ng/mL) was quantified against a lambda DNA standard curve (0 ng/mL- 1000 ng/mL).

#### **2.2.11 sGAG content characterization**

For qualitative determination of presence of GAG, Alcian Blue staining was done according to manufacturer's instruction (Newcomer Supply). Briefly, slides were deparaffinized and hydrated through graded ethyl alcohols to distilled water. Next, slides were placed in 3% acetic acid for 3 min and then directly into 1% Alcian Blue solution pH 2.5 and stained for 30 min in room temperature. The slides were washed in running tap water for 10 min followed by a distilled water rinse. The counterstaining was done in Nuclear Fast Red stain for 5 min before rinsing, dehydrated through graded ethyl alcohol and cleared in xylene. The slides were mounted with

xylene mounting medium. For qualitative measure of sGAG, the method to produce lysate for DNA quantification was used here as well. A sGAG quantification kit –Blyscan Sulfated Glycoaminoglycan Assay kit (Biocolor) was used to measure sGAG according to manufacturer’s instruction. Briefly, the specimen lysate was mixed with Blyscan dye to bind the GAG. The GAG-dye complex was then collected by centrifugation. After the supernatant was removed and the tube drained, the dissociation reagent was added. 100  $\mu$ l solutions were transferred into a 96-well plate. Absorbance against the background control was obtained at a wavelength of 656 nm on a microplate spectrophotometer and the GAG amount was calculated based on a standard curve obtained with the standard GAG supplied with the kit.

#### **2.2.12 Scanning Electron Microscopy (SEM) and Transmission Electron Microscopy (TEM)**

Native and decellularized pancreata were fixed in 2.5% glutaraldehyde in 0.1 M PBS (pH 7.4) for 60 minutes. The samples were washed thoroughly in 3 changes 0.1 M PBS for 15 minutes each. Next, the samples were fixed in 1% OsO<sub>4</sub> in 0.1 M PBS for 60 minutes. This was followed by another 3 changes of PBS washing steps for 15 minutes each. The samples were then dehydrated in gradient series of alcohol for 15 min each. Additionally, samples were critical point dried and coated with Au/Pd using a Cressington Coater 108A sputter coater. Electron microscope images were taken using a Jeol JSM-6335F field emission SEM. For TEM, the tissue sample was fixed in 2.5% glutaraldehyde in PBS. The tissue sample was then post-fixed in 1% osmium tetroxide in PBS, dehydrated through a graded series of alcohols and embedded in Epon (Energy Beam Sciences, Agawam, MA). Thin (60-nm) sections were cut using a Reichert Ultracut S (Leica, Deerborn, MI), mounted on 200 mesh copper grids and counterstained with

2% aqueous uranyl acetate for 7 min and 1% aqueous lead citrate for 2 min. Observation was with a JEOL 1011 transmission electron microscope (Peabody, MA)

### **2.2.13 Preparation of Pancreatic Tissue for Atomic Force Microscopy (AFM)**

#### **Measurement**

Both native and decellularized unfixed samples from murine pancreas were cryoprotected by soaking in 30% sucrose solution in PBS for 24 hours. The entire murine pancreas was then set in a mold and covered in OCT cold embedding media and frozen by exposure to dry ice overnight. The OCT block containing the pancreas was cryosectioned to a thickness of 20 microns and mounted on SuperFrostPlus glass slides. All samples were thawed in PBS for 30 minutes prior to testing.

### **2.2.14 AFM Measurement of Pancreatic Tissue Stiffness**

AFM force indentation measurements were performed using the MFP-3D Atomic Force Microscope (Asylum Research, CA, USA), mounted on top of an Olympus IX-71 fluorescence microscope (Olympus, Tokyo, Japan). All force measurements and analysis was done using the MFP3D software (Asylum Research) built on IgorPro 6 (Wavemetrics) as previously described [146]. For all measurements a glass silica sphere (radius 3.5 micron) was attached to the tip of a 100 micron silicon nitride cantilever (Veeco Systems) with a spring constant of  $\sim 0.6$  N/m. The stiffness of each tissue sample was measured at  $n=16$  random locations on each sample. The Sneddon model was used to determine the tissue stiffness from the force indentation plots.

### 2.2.15 Quantitative RT-PCR

RNA was extracted using NucleoSpin kit according to the manufacturer's protocol. The sample absorbance at 280 nm and 260 nm was measured using a BioRad Smart Spec spectrophotometer to obtain RNA concentration and quality. Reverse transcription was performed using ImProm II Promega reverse transcription kit following the manufacturer's recommendation. qRT-PCR analysis was performed for insulin markers, *ins1* and *ins2*.

The cycle number at the threshold level of log-based fluorescence is defined as Ct number, which is the observed value in most real-time PCR experiments, and therefore the primary statistical metric of interest.  $\Delta Ct$  is equal to the difference in threshold cycle for target and reference or control ( $\Delta Ct = Ct_{\text{target}} - Ct_{\text{reference}}$ ).  $\Delta\Delta Ct$  is equal to the difference between  $\Delta Ct_{\text{sample}}$  and  $\Delta Ct_{\text{control}}$  ( $\Delta\Delta Ct = \Delta Ct_{\text{sample}} - \Delta Ct_{\text{control}}$ ). The fold change of a target gene is defined by, fold change =  $2^{-\Delta\Delta Ct}$ . qRT-PCR analysis was repeated in triplicate.

### 2.2.16 Statistical Analysis

Quantification data were expressed as mean  $\pm$  SD. Significant differences among groups were determined by Wilcoxon rank-sum test for two-group comparisons or ANOVA followed by post-hoc analysis for multiple group comparisons. Probability values at  $P < 0.05$  (\*) indicated statistical significance.

## 2.3 RESULTS

### 2.3.1 Perfusion-decellularization of whole organ pancreas

Isolated mouse pancreata were cannulated and retrograde perfused via hepatic portal vein with anionic based detergent, 0.5% SDS to remove cellular content. Alternately, retrograde perfusion via pancreatic duct was also attempted for pancreas decellularization, however the process took longer and was also less effective in cell removal (data not shown). Macroscopically, a gradual change of color was observed during the perfusion decellularization process (Figure 2.1 (A-D)). Perfusion was continued until whole pancreas turned completely translucent (about 325 min) as depicted in Figure 2.1(D). This generated an acellular pancreas scaffold while retaining the gross anatomical structure of the pancreas. Histological examination by H&E staining showed no remnant cells after the completion of decellularization (Figure 2.1(E)). Immunostaining of two major constituents in native pancreas – acinar cells (Amylase) and islet  $\beta$ -cells (C-peptide) confirmed no residual presence of major pancreatic markers in the decellularized pancreas (Fig. 1F). To further assess the efficacy of decellularization, DNA quantification was performed using Picogreen assay. Picogreen analysis showed that DNA content decreased from  $7442.3 \pm 2450.2$  ng/mg dry weight in normal pancreas to  $41.3 \pm 11.9$  ng/mg dry weight in decellularized pancreas ( $P < 0.01$ ) (Figure 2.1(G)). These results suggest that perfusion mediated decellularization of pancreas efficiently removes pancreatic cellular components. Feasibility of this perfusion decellularization technique in human-sized organ was also demonstrated by decellularization of bovine pancreas (Figure A.1).

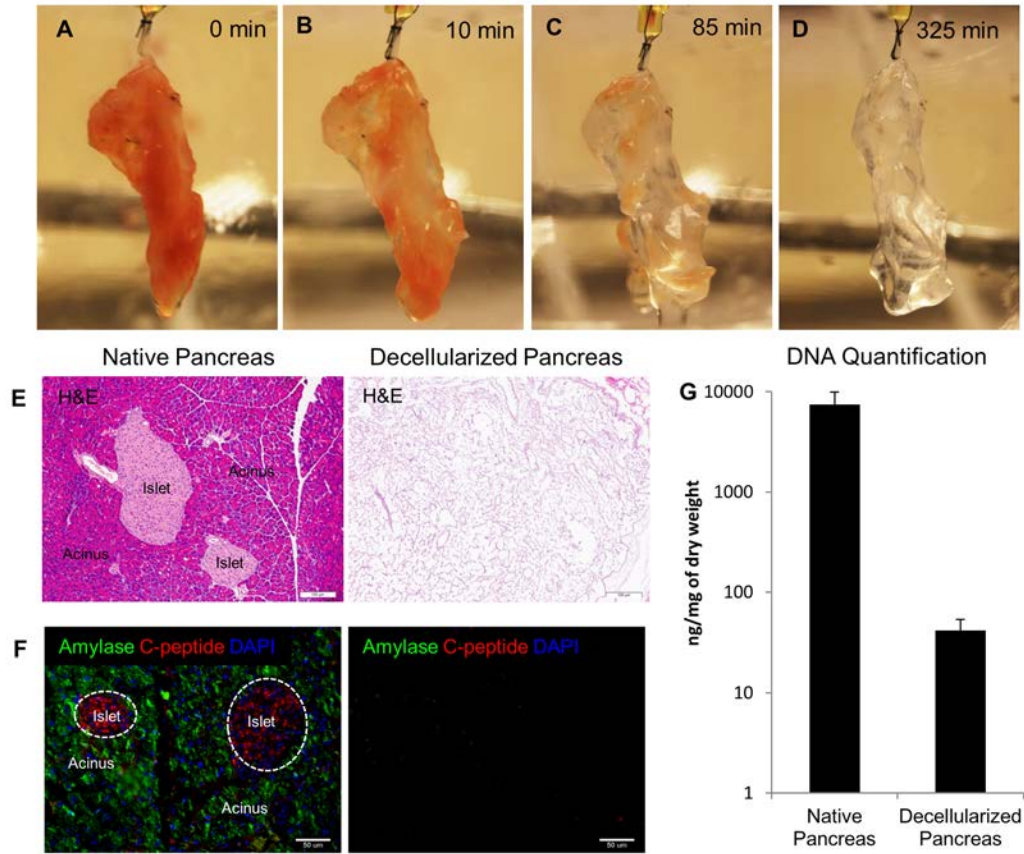


**Figure 2.1** Perfusion-decellularization of murine pancreas

(A-D) Panel images depict gradual change of color from perfusion-decellularization of mouse pancreas with 0.5% SDS. Resulting decellularized pancreas after 325 min (D) appeared translucent. (E) Histological comparison of native and decellularized pancreas by H&E staining showed removal of cells. (F) IHC evaluation of native and decellularized pancreas depict presence of major pancreatic constituents (C-peptide – red, and Amylase – green) in native pancreas (left) but absence in decellularized pancreas (right). (G) DNA quantification via picogreen analysis demonstrated less than 50ng/mg dry weight of DNA material present in the decellularized pancreas.

### **2.3.2 ECM characterization: Immunohistochemistry and Mass spectrometry-based proteomics analysis**

To first characterize the decellularized pancreas, immunohistochemical (IHC) staining was performed for the evaluation of major ECM components' spatial presence relative to that of native pancreas. In native pancreas, the ECM is composed primarily of networks of collagens and other structural proteins filled with a hydrogel of proteoglycans [9, 25]. IHC staining showed that collagen I, IV, fibronectin and laminin were detected in the native pancreas (Figure 2.2(A)). After decellularization, all four major ECM components were preserved, without any detectable DAPI or actin staining (Figure 2.2(B)). This finding suggests complete removal of cellular and cytoskeletal elements while maintaining the ECM composition. In addition, the resulting ECM structure and fibril orientation looked identical to that of the native organ (Figure 2.2(B)). The preservation of sulfated glycosaminoglycan (sGAG) proteins was evaluated qualitatively by alcian blue staining (Figure 2.2(C)), which demonstrated that sGAG proteins were retained after decellularization process. In addition, sGAG content was also assessed quantitatively using a blyscan assay which demonstrated considerable retention of sGAG content in the decellularized pancreas, amounting to 52% of that in native pancreas ( $P < 0.01$ ) (Figure 2.2(D)).

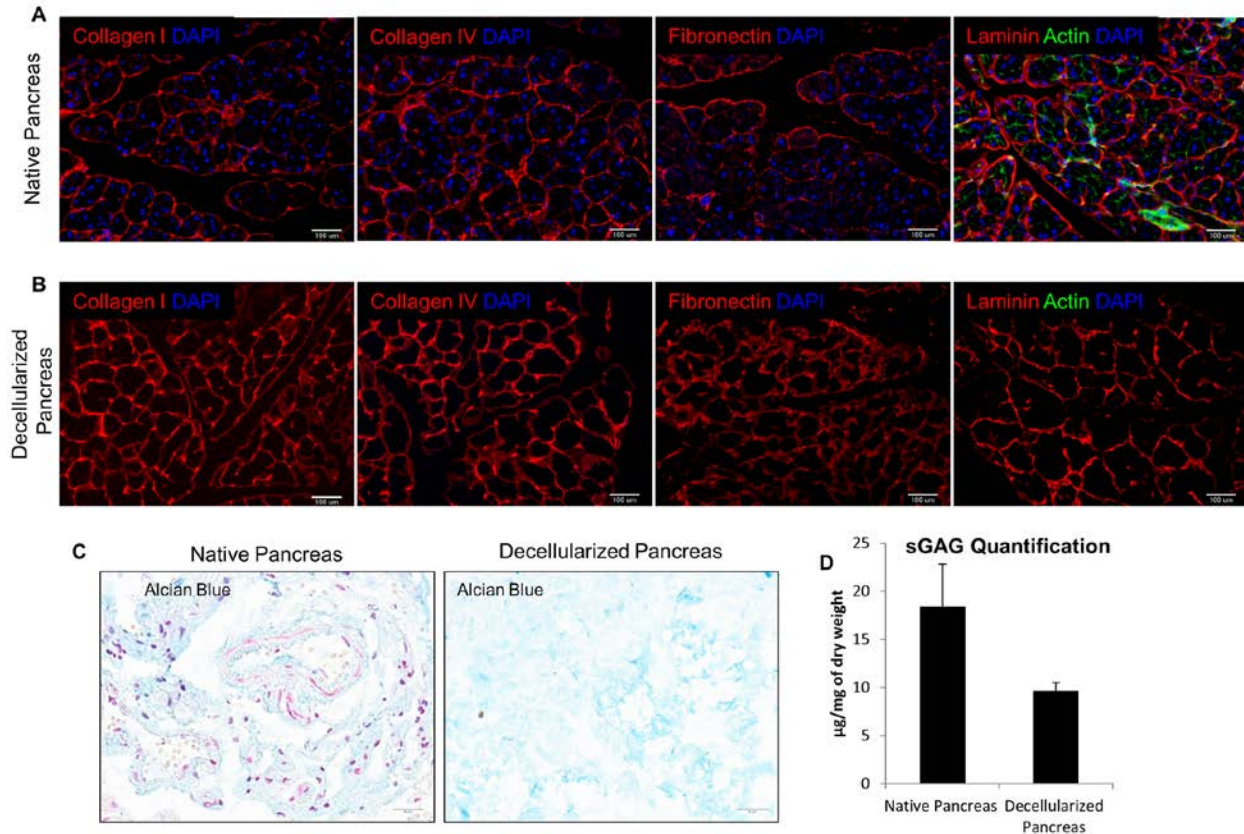


**Figure 2.2 ECM characterization of decellularized pancreas**

(A) IHC staining showed the presence of major ECM composition – Col I, Col IV, Fibronectin, laminin and phalloidin actin staining (green) in native pancreas. (B) Comparison with decellularized pancreas, IHC staining demonstrated the corresponding ECM markers found in native pancreas also preserved in decellularized markers but DAPI and actin cytoskeletal element were absent. This indicates complete removal of cellular materials but preservation of important ECM proteins. (C) Alcian blue staining qualitatively determined the retention of sGAG protein after decellularization. (D) Blyscan assays quantitatively determined the sGAG retention in decellularized pancreas was on average 52% of that in native pancreas ( $P < 0.05$ ).

Insolubility of the ECM is a challenge to characterizing the pancreatic ECM proteome by mass spectrometry-based proteomics. In order to improve solubility, pancreatic ECM was deglycosylated to remove GAG side chains of proteoglycans followed by solubilization in high molar urea. A GeLC-MS/MS proteomics approach was used whereby the high molecular weight

ECM proteins were separated by low percentage 1D gels, in-gel trypsin digested followed by LC-MS/MS analysis. Database searching used stringent 1% false discovery rate to report protein identifications. After protein grouping, a total of 114 unique proteins were identified in the pancreatic ECM (Supplemental table 1), the majority of which belonged to the ECM family based on Gene Ontology (GO) Cellular localization. The entire list of identified proteins was compared with the reference IPI mouse database to identify overrepresented GO cellular localization terms. The topmost GO terms included ECM and basement membrane (data not shown), suggesting that the decellularization process successfully removes cellular proteins yet preserves the ECM components. Table 2.1 is a categorized list of collagens, laminins, proteoglycans and ECM associated proteins.

**Table 2.1 Mass Spectrometry Composition Analysis**

<b>Protein Family</b>	<b>Gene</b>	<b>Description</b>
Collagens	Col6a3	Collagen alpha-3(VI) chain
	Col1a2	Collagen alpha-2(I) chain
	Col4a2	Collagen alpha-2(IV) chain
	Col4a1	Collagen alpha-1(IV) chain
	Col1a1	Collagen alpha-1(I) chain
	Col5a2	Collagen alpha-2(V)
	Col6a2	Collagen alpha-2(VI)
	Col6a1	Collagen alpha-1(VI)
	Col5a1	Collagen alpha-1(V) chain
	Col3a1	Collagen alpha-1(III)
	Col14a1	Collagen alpha-1(XIV) chain
	Col6a6	Collagen alpha-6(VI) chain
	Col5a3	Procollagen, type V, alpha 3
	Col7a1	Col7a1 Collagen alpha-1(VII) chain
	Gm7455	Collagen alpha-5(VI) chain
	Col4a3	Collagen alpha-3(IV) chain
	Col18a1	Collagen alpha-1(XVIII) chain
	Laminin	Lamb2
Lamc1		Laminin subunit gamma-1
Lama2		Laminin subunit alpha-2

**Table 2.1 (continued)**

	Lama5	Laminin subunit alpha-5
	Lamb1	Laminin subunit beta-1
	Lama1	Laminin subunit alpha-1
	Lama4	Laminin subunit alpha-4
Proteoglycans	Hspg2	Basement membrane-specific heparan sulfate proteoglycan core protein
	Aggrn	Aggrin
Nidogens	Nid1	Nidogen-1
	Nid2	Nidogen-2
Elastin associated	Fbn1	Fibrillin-1
Matricellular	Tnxb	Tenascin-X

### **2.3.3 Biophysical Characterization: structural and mechanical properties of decellularized pancreas**

Integrity of the vasculature within the decellularized pancreas was analyzed by trypan blue dye retrograde injection through hepatic portal vein to visualize the continuity of the circulatory branching (Figure 2.3(A)). Rapid diffusion through the vascular tree was also observed (Figure 2.3(A)). Transmission electron microscopy (TEM) and scanning electron microscopy (SEM) were performed to evaluate the effect of the decellularization procedure on the 3D architecture and ECM micro-structures of the decellularized pancreas. TEM analysis revealed intact basement membrane and organized fibers of collagen preserved upon decellularization (Figure 2.3(B-C)). SEM analysis of the cross-sectional images of the decellularized pancreatic constructs revealed that large ductal structures were retained whereas the microvilli cells lining the ducts were removed (Figure 2.3(D-E)). Nanofibrous structures of the ECM were well retained within the parenchyma (Figure 2.3(F-G)). Hollow and void spaces observed within the decellularized pancreas are likely attributes of the “footprints” left from pancreatic cells removed during the

decellularization process (Figure 2.3(H)). The recognizable scalloping pattern of arteries also indicates the preservation of vascular structure likely branched from the greater pancreatic artery (Figure 2.3(I)). These results suggest that perfusion decellularization of the pancreas adequately retained the ultrastructure and architecture of the native pancreas.

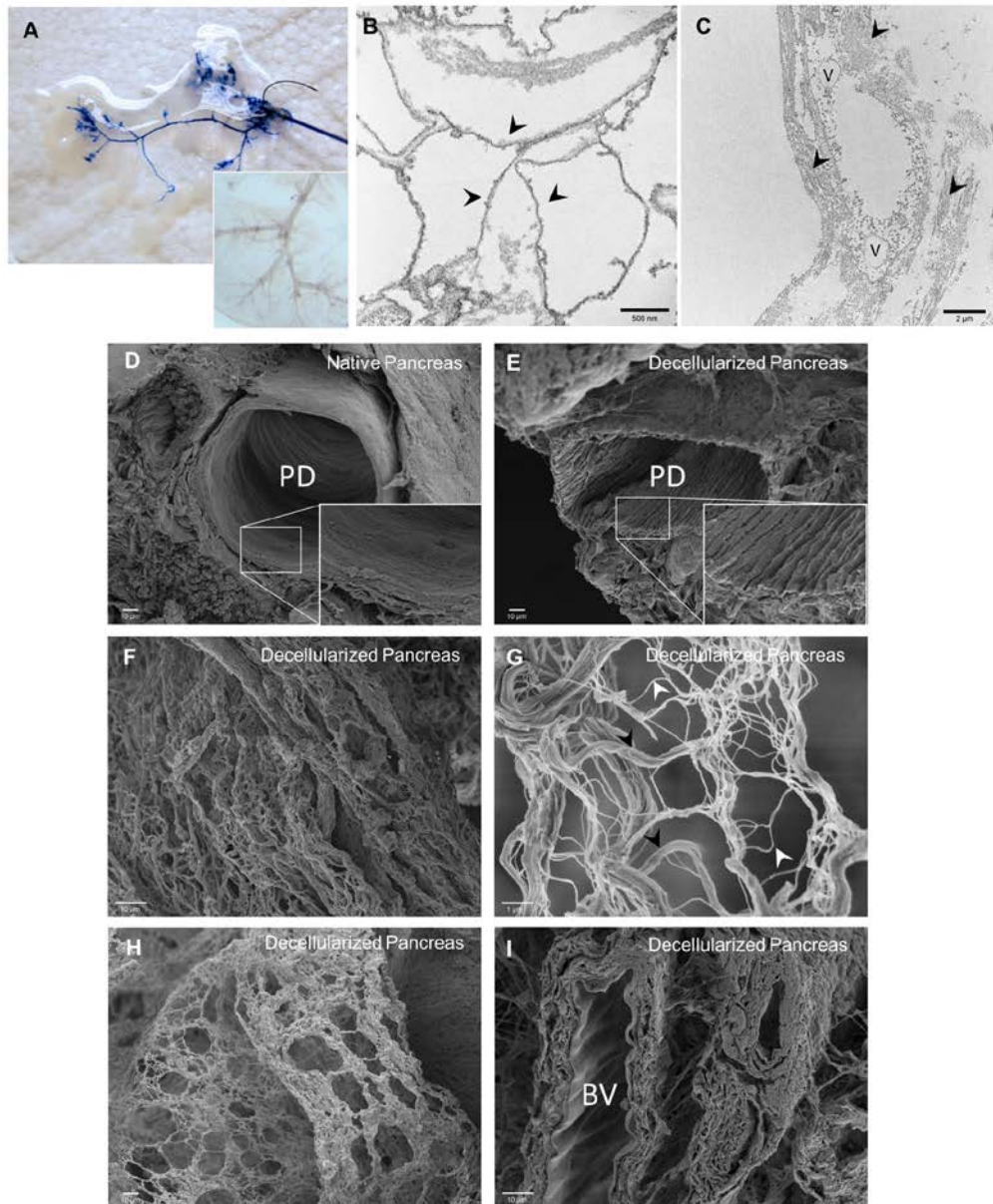


**Figure 2.3 Ultrastructural characterization of decellularized pancreas**

(A) Trypan blue dye infusion visualized the progressive flow from large vessels to the fine blood vessel branches along the channels without leakage. Inset shows light microscopy image of vasculature branches remained

intact after decellularization. (B) TEM of decellularized pancreas depicted the intact basement membrane (arrowhead points to the underlying basement membrane). (C) TEM image of decellularized pancreas showed the interstitial space with organized fibers of collagen (arrowhead). (D-E) SEM comparison of native and decellularized pancreas demonstrated preservation of 3D micro-structure of pancreatic duct after decellularization. Inset shows the absence of lining ciliated microvilli cells from the luminal surface of the duct after decellularization process. (F) SEM image of decellularized pancreas showed ECM fibers within the parenchymal space. (G) Higher magnification of 3D meshwork showed a variety of fibers - large bundle of Type I collagen (black arrowhead) associated with a variety of smaller fibers (white arrowhead). (H) SEM image of decellularized pancreas demonstrated large/small fibers interlinked in a plane that forms a boundary such as to previously occupied pancreatic parenchymal cells. (I) SEM image of decellularized pancreas demonstrated scalloping appearance of the internal elastic lamina of an artery, indicating intact blood vessel (BV).

Biomechanical characteristics of the decellularized pancreas were analyzed using AFM. Representative cantilever displacement/sample deflection curves (Figure 2.4(A)) shows that there was a discernible difference between the native and decellularized pancreas, with the stiffer decellularized sample having a much steeper slope. Young's modulus as determined from the AFM curves was found to be  $1210 \pm 77$  Pa for native mouse pancreas, while the Young's modulus of decellularized pancreas is on average 3 times greater ( $3736 \pm 1893$  Pa) (Figure 2.4(B)).

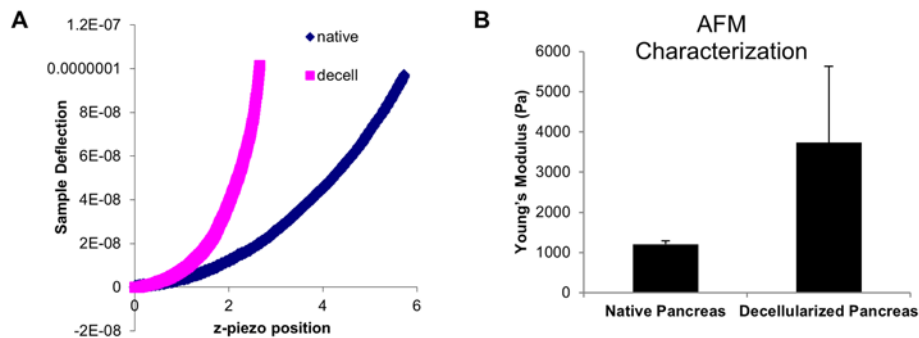


**Figure 2.4 Biomechanical properties of decellularization pancreas**

(A) Representative deflection plot from AFM evaluation of native and decellularized pancreas shows a steeper slope than force curve of decellularized pancreas from native pancreas, indicating higher Young's modulus. (B) Bar graph representatives of AFM force curve shows on average 3 times higher stiffness in the decellularized pancreas than native pancreas.

### 2.3.4 *In vivo* response to decellularized pancreas

Pancreas ECM was implanted subcutaneously in order to preliminarily evaluate *in vivo* biocompatibility in a mouse model. At 14 days post-surgery, histological analysis of the subcutaneous implantation site showed the presence of mononuclear cells surrounding the partially degraded ECM (Figure 2.5(A)). The pancreas ECM was non-cytotoxic after 14 days and like other efficiently decellularized ECM scaffolds [147, 148], was not associated with presence of multinucleate foreign body giant cells or other pathological signs of the foreign body response (Figure 2.5(B)). Furthermore, active angiogenesis was a feature of the decellularized pancreas implantation site (Figure 2.5(B), arrows). These preliminary results suggest that the perfusion-decellularized pancreas ECM described herein represents a cytocompatible scaffold capable of integrating within host tissue.

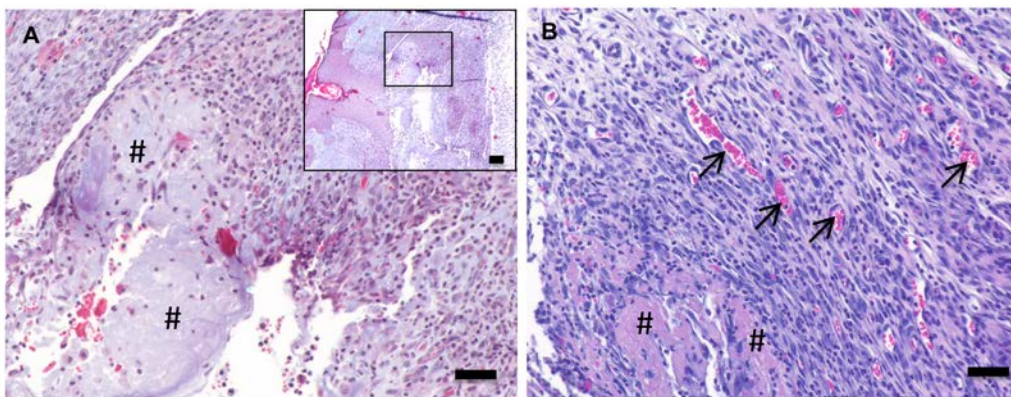


**Figure 2.5 Biocompatibility of perfusion-decellularized pancreas ECM**

A perfusion-decellularized pancreas ECM construct was surgically implanted within a subcutaneous pocket in a C57Bl/6 mouse model. After 14 days Mason's trichrome staining of the implant site (A) showed the ECM scaffold (#) infiltrated with host mononuclear cells. H&E staining (B) showed no signs of multinucleate giant cells and the presence of blood vessel (arrows). (Scale bars = 50um, inset = low power magnification, inset scale bar = 200um)

### **2.3.5 Recellularization of Decellularized Pancreatic Scaffold**

To evaluate the potential of decellularized pancreas as a scaffold for pancreatic tissue engineering, it was recellularized using relevant pancreatic cell lines. We first explored the effect of two dimensional (2D) slices of decellularized pancreatic matrix as a substrate for cell culture (Figure 2.6(A)). Decellularized pancreatic matrix was cut into slices of about 10-20  $\mu\text{m}$  thickness, as evaluated by multi-photon microscopy (Figure 2.6(B)). MIN-6 cells (25,000 cells/ $\text{cm}^2$ ) were seeded on the 2D slice and cultured for 5 days. After 5 days, MIN-6 cells were found attached and spread on the surface of 2D slice (Figure 2.6(C)).

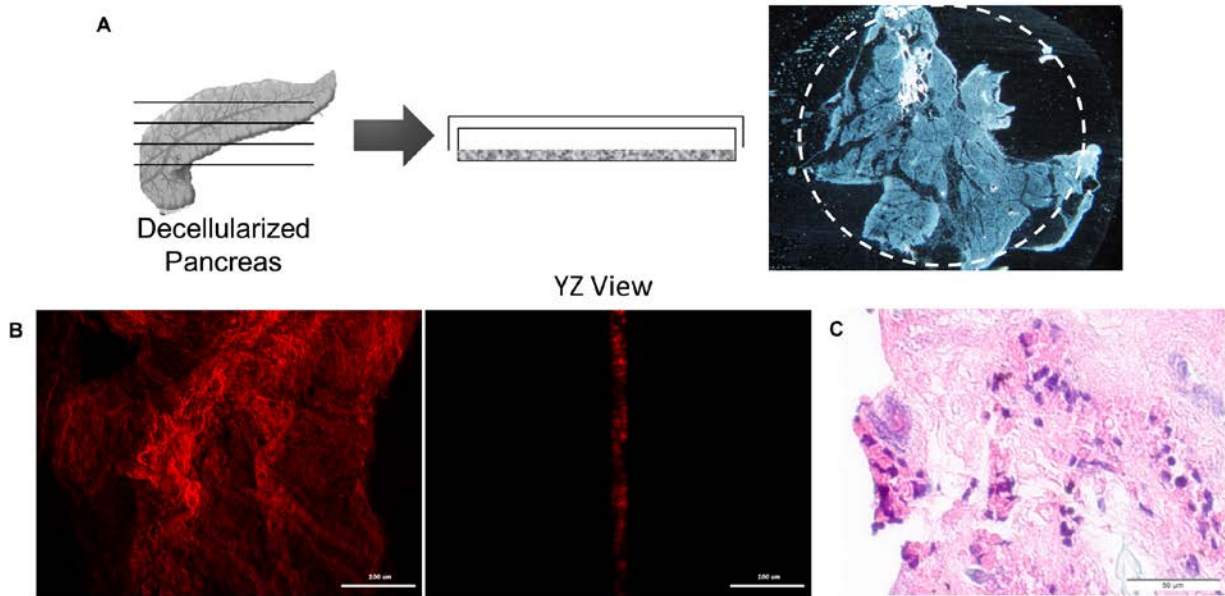


**Figure 2.6 MIN-6 culture on 2D slice pancreatic matrix**

(A) Diagram illustrates the generation of 2D pancreatic slice. White dashed circle depict the cloning cylinder applied to pancreatic slice to consolidate seeded cells to pancreatic substrate. (B) Multi-photon imaging on second harmonic generation (SHG) signal to visualize the collagen fibers demonstrated that thickness of the 2D slice pancreatic matrix is about 10-20  $\mu\text{m}$ . (C) H&E staining demonstrated the attachment of MIN-6 cells on 2D pancreatic slice after 5 days of culture, and insulin expression (C-peptide: green) was maintained.

To evaluate whole organ recellularization potential, endocrine  $\beta$  cell line, MIN-6 cells ( $30 \times 10^6$ ) were first seeded into the decellularized pancreas via hepatic portal vein by multistep infusion technique following the seeding strategy described for liver recellularization [117, 136]. Approximately  $10 \times 10^6$  cells were introduced at each step, for a total of 3 steps, with 20-min intervals between each step. Upon cell seeding, a uniform color change was observed throughout the whole decellularized pancreas, indicating a homogenous cell delivery (Figure 2.7(A-B)). The repopulated pancreas was then maintained in static culture for 5 days with culture media changed by perfusion through the pancreas every day. After 5 days, the reconstructed pancreas was

analyzed for engraftment, survival and functionality by IHC. From the histology, MIN-6 cells appeared to be engrafted both surrounding the parenchymal region and around the larger vessels (Figure 2.7(C)). TUNEL staining detected only minimal apoptosis (<18%), suggesting that the 3D decellularized pancreas scaffold is cytocompatible and supportive of cell growth (Figure 2.7(D)). Furthermore, these engrafted cells maintained their insulin expression over 5 days as evidenced by positive C-peptide staining (Figure 2.7(F)).

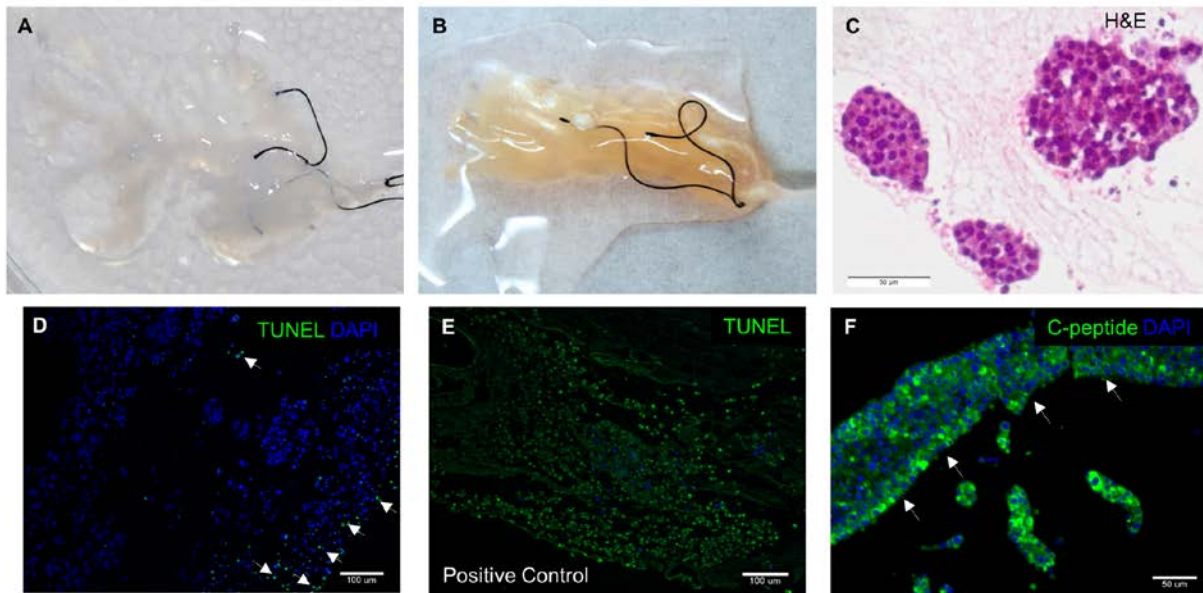


**Figure 2.7 Recellularization of decellularized pancreas**

(A) Decellularized whole pancreas before cell seeding. (B) Recellularization of the same pancreas via multi-step infusion of about 30 million cells via portal vein infusion. (C) H&E staining of the recellularized pancreas after 5 days showed the engraftment of the seeded cells at surrounding parenchymal region. (D) TUNEL staining of the recellularized construct showed less than 18% of apoptotic cells (arrowhead), demonstrating the cytocompatibility of the scaffold. (E) Positive control of TUNEL staining by adding DNase to the consecutive sections of recellularized pancreas's histological slide. (F) IHC of recellularized pancreas with MIN-6 only showed C-peptide+ cells engraftment around the larger vessel (arrowhead).

The native pancreas is a dual-functioning glandular organ comprised and capable of both endocrine and exocrine tissue and function, to this end, next the decellularized pancreas was reconstructed with both the endocrine  $\beta$  cell line (MIN-6) and exocrine acinar cell line (AR42J) by simultaneous seeding. The  $\beta$  cells were perfused through the hepatic portal vein as before, while the acinar cells were perfused through the pancreatic duct (Figure 2.8(A)). The two cell types were seeded in sequence, with the hepatic duct perfusion of the MIN6 cells preceding the pancreatic duct perfusion of acinar AR42J cells. This seeding strategy attempts to retain the cellular composition of native pancreas and the anatomical proximity of the cells to different secretory locations: (i.e.; endocrine  $\beta$  cells – vasculature; exocrine acinar cells – ductal system). As before, the dual cell-seeded pancreas constructs was maintained for up to 5 days in static culture. At day 5, IHC analysis showed that both cell types attached and localized to their specific topographical locations as a result of their different cell seeding route (Figure 2.8(B)). Immunofluorescence staining confirmed the expression of C-peptide, as an analogue of insulin marker identifying endocrine  $\beta$ -cells and amylase as a digestive enzyme identifying exocrine acinar-cells (Figure 2.8(B-C)). Most C-peptide+ cells were localized to the luminal spaces of large vessels and parenchymal regions similar to that observed in single cell reconstructed pancreas. Distinct from the localization of C-peptide+ cells, tubular ductal spaces lined with acinar cells expressing amylase were observed (Figure 2.8(C)). No inter-dispersed population of the two cell types were observed within the engraftment region, suggesting the preservation of the distinct architecture of vasculature and ductal structure (Figure 2.8(C)). These results indicate that the decellularized pancreas is capable of supporting multiple pancreatic cell types and this co-seeding strategy allows the reconstitution of major cellular constituents as in the native pancreas.

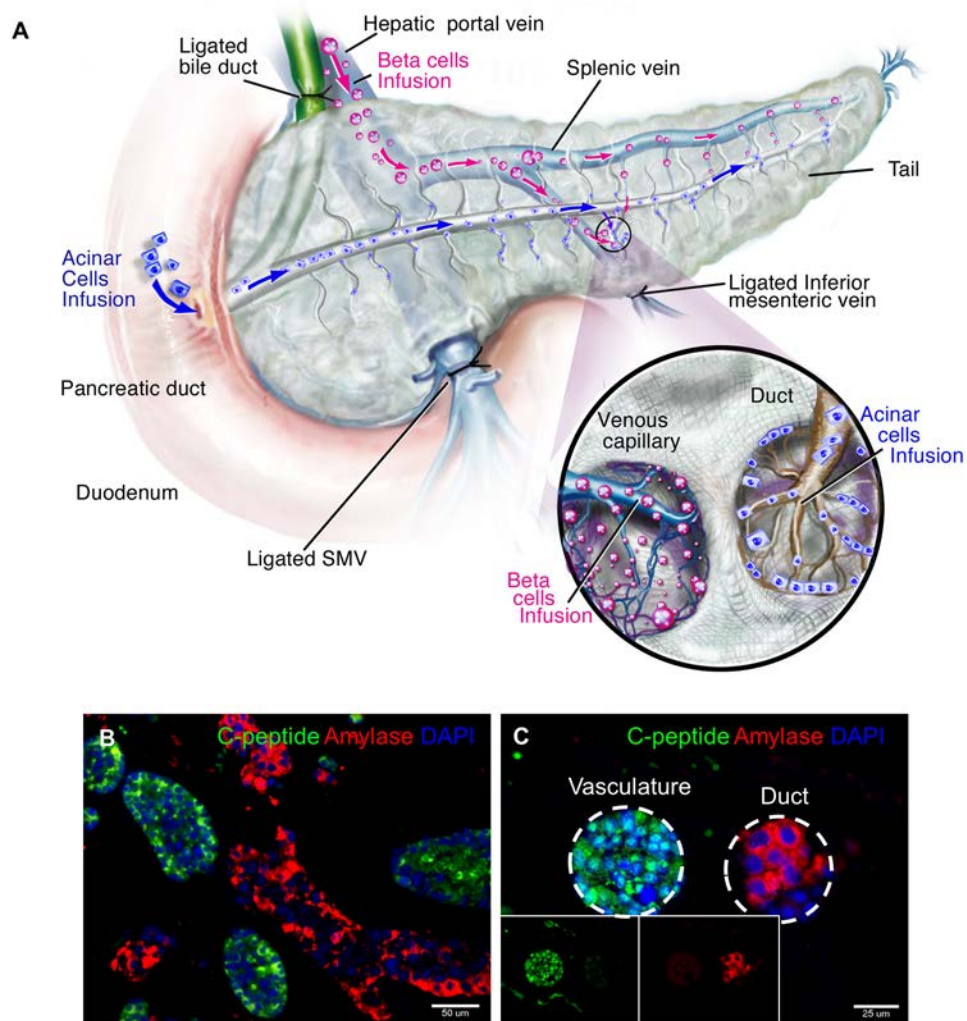


**Figure 2.8 Dual recellularization strategy with  $\beta$ - and acinar cell types**

(A) Two different cell types (MIN-6 and AR42J) were inoculated into the decellularized pancreas 3D scaffold utilizing two different seeding routes. (B) IHC of recellularization with both MIN-6 and AR42J cell lines showed engraftment of both cell types. Both cell types maintained their respective functional markers – MIN-6 (C-peptide – green) and AR42J (Amylase – red). (C) Vasculature and pancreatic duct situated next to each other with their respective seeded different population of cells (vasculature-MIN6 and duct-AR42J). Inset shows single channel images. This indicates that preservation of architecture of vasculature and ductal structure, hence different cell population were not inter-dispersed after seeding.

### 2.3.6 Modulation of $\beta$ -cell Insulin Gene Expression by Native Pancreatic ECM

Both primary pancreatic islets and individual isolated pancreatic  $\beta$ -cells have been demonstrated to have better *in vitro* function when cultured on ECM-derived substrates [102, 104-106, 149] and purified ECM proteins [27, 49, 150, 151]. Having confirmed engraftment and survival of the relevant pancreatic cell types in the native pancreatic scaffold, the contribution of this pancreas-derived ECM scaffold on cell function was next evaluated by the insulin gene expression level. For comparative evaluation, control cultures of MIN-6 cells (25,000 cells/cm<sup>2</sup>) were plated on surfaces with the following ECM proteins: collagen I, collagen type IV, fibronectin, and growth factor-reduced (GFR) Matrigel. In addition, the MIN-6 cells were also cultured on 2D slice configurations of pancreatic ECM for comparison between the effects of 2D versus 3D culture configurations. Upon plating, the MIN-6 cells readily attached to all tested substrates and remained viable over the culture period (data not shown). The cells were cultured for 5 days, after which the cell lysate was analyzed for insulin gene expression (*ins1* and *ins2* expression) by qRT-PCR (Figure 2.9). Quantitative RT-PCR of MIN-6 demonstrated significantly higher *ins1* and *ins2* gene expression when cultured on these ECM proteins and pancreatic ECM scaffold (P<0.05) compared to control (untreated plate) with the exception of collagen I gel. Among the ECM proteins tested, collagen IV and fibronectin substrates induced similar insulin gene expression levels. Matrigel promoted the highest insulin gene expression (6.9-fold *ins1* and 4.1-fold *ins2*). MIN-6 seeded on 3D pancreatic ECM exhibited higher insulin gene expression than 2D pancreatic ECM. Furthermore, 3D pancreatic ECM also demonstrated higher insulin gene expression when compared to single ECM proteins such as collagen IV and fibronectin but displayed similar level of insulin gene expression with the Matrigel coated surface (no significant difference). These results clearly demonstrate that  $\beta$ -cells interact closely with the

ECM substrates, and that interaction with specific substrates can significantly affect insulin gene expression. The native organ derived of decellularized pancreas was found to have a strong positive attribute to *ins1* and *ins2* gene expression, comparable to Matrigel coating and significantly higher than other tested single purified molecules.

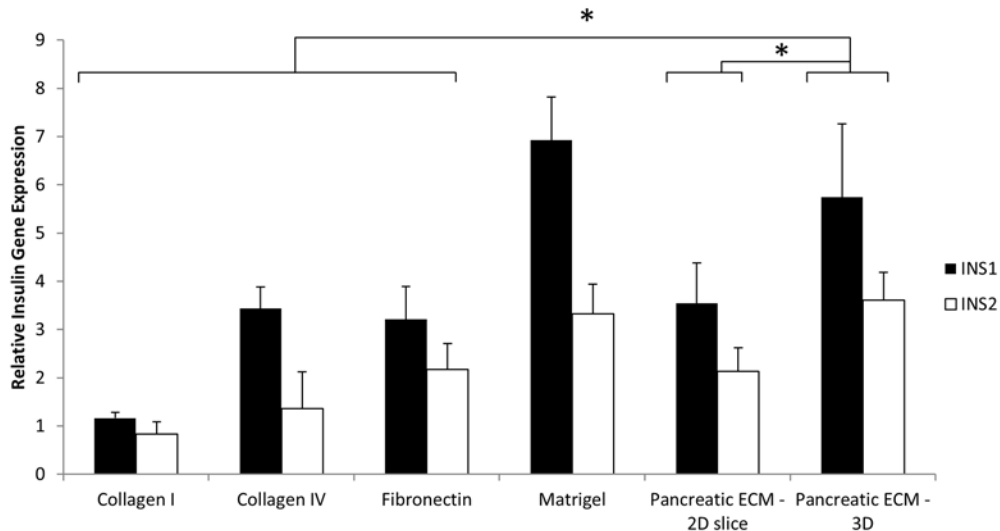


**Figure 2.9 Comparison of ECM mediated insulin gene expression of MIN-6 cells**

qPCR data demonstrated modulation of MIN-6 cell insulin gene expression by different types of ECM protein. 3D Pancreatic ECM demonstrated higher *ins1* and *ins2* genes expression than Collagen I, Collagen IV, Fibronectin and 2D pancreatic slice ECM but only comparable to Matrigel. Normalization was performed to MIN-6 cells seeded on control non-tissue culture treated plastic. \* indicates  $P < 0.05$

## 2.4 DISCUSSION

The objectives for successful decellularization are 1) complete or near complete removal of cellular material, and 2) preservation of ECM composition [152]. Commonly reported decellularization protocols require mechanical agitation or freezing and thawing which may take

up to days or weeks to remove all cellular materials [153-155]. Such protocols do not guarantee preservation of the ECM microstructure, which has been shown to be instrumental for the generation of functional tissue engineered constructs [156]. In contrast, our approach of whole organ perfusion decellularization reduces the diffusion distance required for decellularization agents to reach the cells and facilitates removal of the cellular material from the tissue by convective transport [60, 152, 157]. This technique allowed the efficient generation of acellular scaffold with preserved ECM, 3D architecture and perfusable network resembling a native organ (approximately 325 min as shown in our data Figure 2.1(D)). The resulting decellularized pancreas met the stringent requirement to define a successful decellularization [147] - absence of nuclear material with DAPI and H&E staining, and retained only less than 50ng dsDNA per mg ECM dry weight as shown by quantitative DNA measurement (Figure 2.1(E-G)). This requirement is crucial because residual DNA fragments in decellularized ECM have shown to lead to cytocompatibility issues *in vitro* and adverse immunological response upon implantation [148, 158, 159]. We and other groups have tried decellularization using similar strategies on other circulatory networks to reduce diffusion distance (e.g., bile duct in liver, pancreatic duct in pancreas) but it was much less effective likely due to incomplete distribution of a conduit network to reach all the cells throughout the target organ.

Another important consideration for organ decellularization is minimizing the undesirable alteration and loss of biologically active ECM components. Decellularized pancreas scaffolds demonstrated maintenance of key ECM proteins in adult pancreas [9, 25], including collagen I, collagen IV, laminin, and fibronectin, as well as sulfated GAG. Most of the ECM proteins retained their physiological organization after decellularization as noted by IHC (Figure 2.2(A)). This finding was further substantiated by mass spectrometry analysis to

comprehensively characterize the proteome of the decellularized pancreatic ECM. Retention of ECM protein/glycan compositions is typically characterized by IHC; this approach is however limited by its robustness and only confined to a small number of ECM candidates studied. Proteomic analysis by mass spectrometry is unbiased and does not require specific probes. Though our analysis was qualitative, notably all the top scoring proteins belonged to the ECM family (supplemental table 1). These identifications have a high number of peptide spectral counts providing rough measures of protein abundance.

Biomechanical evaluation of engineered scaffolds and decellularized constructs is an important assessment for the rate of preservation of functional integrity. Numerous studies have shown that biomechanical properties change after decellularization of tissues [138, 160, 161]. By using AFM, we measured the stiffness of the decellularized pancreas ECM. Our results demonstrated that Young's modulus of decellularized pancreas is on average 3 times greater than the native pancreas ( $P < 0.01$ , Figure 2.4(A-B)). This is partially attributed to the loss of GAG content from the decellularization protocol (Figure 2.2(D)). GAG proteins have a myriad of biological functions and some of them are associated with structural and biomechanical properties. GAGs possess a fixed negative charge that renders them hydrophilic and attracts water into the tissue causing an osmotic swelling, which in turn could contribute to tissue physical properties. Removal of GAG side chains by heparitinase/chondroitinase treatment has been shown to increase stiffness of basement membrane of tissue [131]. Although our result showed a higher Young's modulus in decellularized pancreas than native pancreas, it is still well within the mechanical property range of "soft tissue." [162, 163]. While the magnitude of increase depends on the specific organ under study, some studies have shown that a slight alteration of tissue biomechanical properties was not associated with any detrimental effect on

cellular functionality. For instance, successful repopulation of a cardiac matrix was demonstrated despite a higher tangential modulus was detected within the decellularized heart when compared to native rat ventricles [108], which is consistent with our findings.

Recent studies have suggested that the ECM composition and expression pattern are specific to a given anatomical location to direct or support site-appropriate cell attachment and function [111, 164]. In the native pancreas, the primary functional units of the pancreas divide easily into endocrine cells and exocrine cells. The endocrine cells are arranged mainly in groups as islets of Langerhans and secrete different polypeptides delivered to other parts of the body via the vasculature. In contrast, the secretions of acinar exocrine cells are carried away through the ductal system. To reconstitute the major functional processes in pancreas, we utilized these unique differential secretory channels to deliver two major pancreatic cell types – endocrine ( $\beta$ -cells) and exocrine (acinar cells) – in close proximity to their respective native niches. Our result showed that both cells types retained their functionality and distinct location upon recellularization (Figure 2.8(B-C)).

Reestablishment of a critical ECM- $\beta$ -cells interaction has been shown to improve  $\beta$ -cells survival and functions [27, 49, 105, 149-151]. In this study, we evaluated the effect of substrate on  $\beta$ -cell function. Insulin gene expression of MIN-6 cultured on Matrigel was found to be significantly higher than coated single purified proteins. This finding indicates that  $\beta$ -cells are responsive to ECM substrate differences. Hence it was expected that native pancreatic ECM scaffold with preserved native ECM milieu will also likely enhance insulin gene expression. Consistent to our hypothesis, *ins1* and *ins2* expression of MIN-6 cultured on decellularized pancreas 3D scaffold was higher than single purified molecules ( $P < 0.05$ , Figure 2.9) and comparable to Matrigel (no statistical difference). However, 2D substrates of pancreatic ECM

only showed similar level of insulin gene expression with single purified molecules. This is likely due to the reason that pancreatic cell niche *in vivo* is a 3D environment and previous studies have shown that cell-matrix interaction in 3D matrices are more favorable from those on 2D substrates [165, 166]. Our result was supportive of this previous finding with the 3D pancreatic scaffold demonstrating better support of  $\beta$ -cell function. The high insulin gene expression observed when  $\beta$ -cells are cultured on Matrigel suggests the benefits of synergistic effects from multi-faceted ECM proteins. Similarly, decellularized pancreas scaffold also possesses multiplex ECM composition and the effects are proving to be similar when compared to Matrigel. Even though Matrigel is widely used in various tissue engineering studies, it is limited in its translational potential due to its tumor cell origin. In contrast, decellularized xenogenic sources of ECM scaffolds are typically regulated by the FDA as medical device and currently in wide clinical use [167]. Hence, the development of a bioscaffold using decellularized pancreatic ECM will provide a better clinical translation opportunity for pancreatic tissue engineering and regenerative medicine applications.

## 2.5 CONCLUSION

This chapter presents the first step toward successful decellularization and 3D reconstruction of whole pancreas. Thorough characterization revealed that the decellularized pancreas retained its native 3D architecture, vasculature and ductal channels along with important ECM compositions. The preserved pancreatic ECM scaffold was non-cytotoxic, supportive of representative pancreatic cell types, and enhanced insulin function when seeded with  $\beta$ -cells. Such native organ derived scaffold is likely to have a great impact in pancreatic tissue engineering, by providing a

niche microenvironment for pancreatic cell types and even stem/progenitor cells. In conclusion, perfusion-decellularized pancreas offers a promising platform for pancreatic tissue engineering and regenerative medicine based strategy for whole-organ replacement.

### **3.0 DEVELOPMENT OF A PERFUSION BIOREACTOR FOR WHOLE ORGAN PANCREAS BIOENGINEERING**

#### **3.1 INTRODUCTION**

The preceding chapter focused on the development and assembly of a perfusion bioreactor to enable regenerative reconstruction of pancreas. Advancement of this perfusion-decellularization technology relies heavily on the efficiency of the perfusion system to adequately deliver the decellularization agents throughout the harvested organ. More importantly, the reconstruction of decellularized organs and maintenance within a tissue culture environment will necessitate an adequate perfusion system for mass nutrient transport. Hence there has been a strong focus on developing perfusion system to support whole-organ decellularization and recellularization [125, 168-173].

Early studies of perfusion-decellularization technology have employed gravity-based perfusion for whole-organ decellularization and recellularization. For instance, mouse kidneys were successfully decellularized by Ross et al. group with gravity-based perfusion at a constant physiologic fluid pressure of approximately 100 mmHg [140, 174]. Using similar gravity-driven approach, Scarritt et al. demonstrated complete decellularization of rat lungs using a column of liquid that was suspended 22 cm above the lung to drive the perfusion [175]. For recellularization, some groups including ours have adopted the same gravity perfusion method to

periodically supply nutrients to the repopulated organs [50, 110, 176]. These repopulated organs are usually cultured statically by submersion in media without continuous media perfusion and have shown to support functional organ reconstruction in heart [110, 176] and pancreas [50]. However, gravity-based perfusion is a concern because it may not force perfusion especially during cellular debris clogging, which will lead to incomplete perfusion and reduced decellularization and nutrient transport efficiency. Furthermore, gravity-based perfusion usually involve manual changing of solution or culture media, which will lead to higher likelihood of contamination. Some other groups employed pump-based perfusion to exert the necessary pressure and drive the solutions (e.g. detergent or culture media) through the organ [119, 125, 168-173]. While this approach has been successfully demonstrated in both small animal organs as well as large and human-scale organs, there is a dearth of information on the construction of the perfusion bioreactor which will allow convenient assembly of such a system in a research lab. Recently, a commercially available bioreactor named Organ Regenerative Control Acquisition (ORCA) bioreactor (Harvard Apparatus Regenerative Technologies, HART) was reported. This commercial bioreactor system is amenable to gas (e.g. O<sub>2</sub> and CO<sub>2</sub>) sensors integration and automation, which has been used for whole lung decellularization and recellularization [123, 169]. However, the expensive commercial equipment has often limited the dissemination of this perfusion decellularization technology [177] to the organ engineering community. Hence, there is an unmet need of developing a simple, cost-effective and easily assembled perfusion bioreactor in research lab settings to catalyze the development of organ bioengineering.

The objective of this chapter is to introduce a simple yet versatile bioreactor design which can be easily assembled with accessible resources in research laboratories. We described the

design, construction, and testing of a novel laboratory-scale bioreactor that is capable of decellularization of multiple intact whole organs (e.g. pancreas, liver and heart). With simple modification, the decellularization set-up was amenable to serve as a bioreactor to allow dynamic perfusion culture of reconstructed organs. We first demonstrated the bioreactor efficiency by maintaining the viable reconstruction of pancreas from a robust pancreatic  $\beta$  cell line for 7 days. Comparison with parallel static culture clearly indicated the superior performance of the perfusion bioreactor culture in promoting cellular engraftment, survival and function of the reconstructed pancreas. We further demonstrated the ability of this bioreactor to culture decellularized pancreas repopulated with hESC-derived definitive endoderm (DE) cells, as a first proof of concept towards regenerative reconstruction of pancreas.

## **3.2 METHODS**

### **3.2.1 Organ isolation and preparation**

All animal work performed was in accordance with animal welfare act, institutional guidelines and approved by Institutional Animal Care and Use Committee of the University of Pittsburgh. Female ICR mice (Taconic), between the ages of 6-12 weeks were induced anesthesia by ketamine/xylazine injection, and placed in the supine position. A laparotomy was performed and a single dose of heparin (2.0 units of heparin per gram of body weight) was injected into the inferior vena cava (IVC). After 5 min wait time for systemic circulation of the heparin, organs of interest (e.g. pancreas, liver and heart) were isolated using aseptic techniques. Heparin pre-filled 24G catheters were inserted into the arterial (heart) or venous vasculature (pancreas and liver)

and tightly secured with suture. The minor arterial and venous bifurcations were carefully ligated or cauterized to prevent leakage before placement into the decellularization chamber.

### **3.2.2 Decellularization chamber design and components**

The decellularization chamber, shown in Figure 3.1 and Figure A.2, has three main components: the organ chamber, detergent reservoir and peristaltic pump. All the parts were autoclaved or sterilized with ethylene oxide (EtO) gas before use. All assembly and manipulations of decellularized organs, cannula attachments, and subsequent recellularization were done using aseptic techniques in laminar flow hoods to prevent contamination.

#### **3.2.2.1 Organ chamber**

The organ chamber houses the biologic sample. It is made of customized glass media bottle secured onto a ring stand in the working space. The glassware is sealed by a silicone rubber stopper (Cole Parmer, size 12) at the top. The bottom has a drainage outlet that leads to the detergent reservoir with a stopcock and connecting tube in between. Two holes are bored into the silicone rubber stopper to fit two stainless steel 304 cannulae (Small parts, hypodermic round tubing, gauge 8) with female luer fitting (Small part, stainless steel 303) soldered on one end. The first cannula holds the decellularized organ at the end of the cannula; the other end with soldered luer fitting connects to a three-way stopcock that leads to the inlet tubing and a syringe. The second cannula leads to a syringe filter that prevents pressure build up and facilitates drainage into the detergent reservoir.

### **3.2.2.2 Detergent reservoir**

The detergent reservoir contains the detergent solution (0.5% SDS and 1% Triton-X 100 as described in previous study [50]) for the peristaltic pump to draw from and perfuse the target organs. It also collects the outlet perfusate from the organ chamber. When cloudiness is observed, fresh detergent will be replenished into the detergent reservoir. It is sealed by a silicone rubber stopper (Cole Parmer, size 12) at the top. Three holes are bored into the stopper to fit three stainless steel 304 tubes (Small parts, hypodermic round tubing, gauge 8) with female luer fitting (Small part, stainless steel 303) soldered on one end. The first cannula connects to the upper organ chamber via a tubing line to collect effluent detergent and drain into the detergent reservoir. The second cannula connects to the peristaltic pump via an outlet tubing to draw and recirculate the detergent from the detergent reservoir back to the organ chamber. The third cannula leads to a syringe filter snugly fit into the soldered female luer fitting to permit air exchange and equilibrate pressure in the reservoir. The first two cannulae are connected with their corresponding parts with 1/8-inch hose barb to luer connectors (Cole parmer).

### **3.2.2.3 Peristaltic pump**

With the tubing size used in this system (Masterflex BioPharm tubing, L/S16) the peristaltic pump (Masterflex L/S Digital Drive, 600 RPM) is capable of accurately and consistently pumping flow rates from 0.8 to 480mL/min through the flow chamber. We used a flow rate setting of 2mL/min (pancreas and liver) and 4mL/min (heart) for decellularization. Each pump is capable of driving 2 pump heads. For a high throughput set-up, a 12-channel peristaltic pump (Cole Parmer) can be utilized with perfusate flow divided equally between all cultured reconstructed organs in one organ chamber as demonstrated by Sullivan et al. [139]

### **3.2.3 Corrosion casting of vascular and ductal conduits**

To determine the integrity of vascular and ductal network in the decellularized pancreas scaffolds, we performed the corrosion casting. Catheterization of the anterior hepatic portal vein and pancreatic duct was performed followed by injection of 0.5-2mL polymer mixture depending on the pancreas size using Batson's 17 anatomic corrosion kit (Polysciences, Inc) as recommended by the manufacturer. Red pigment was added to perfuse the vasculature via the hepatic portal vein whereas blue pigment was added to perfuse the ductal network via the pancreatic duct. Polymerization took 4 h at 4°C and was followed by maceration in 1N KOH solution 8–24 h. The morphology and distribution of vascular and ductal network was observed under dissecting scope (Nikon SMZ800) and images were recorded with Olympus DP25 camera.

### **3.2.4 Cell culture**

#### **3.2.4.1 MIN-6 $\beta$ cell culture**

MIN-6  $\beta$  cell culture was performed as previously described [50] in chapter 2.2.3.

#### **3.2.4.2 Human Embryonic Stem Cells (hESC) culture**

The *H1* embryonic stem cell lines used in these experiments were obtained from the University of Pittsburgh Stem Cell Core, and are part of the NIH hESC registry eligible for NIH funding. Undifferentiated H1 hESCs were maintained in feeder-free culture in mTeSR medium (StemCell Technologies) on hESC-qualified Matrigel (BD Biosciences)–coated tissue culture plates. Cultures were fed every day with mTeSR medium and passaged with Accutase (StemCell Technologies) at 70% confluency. Experiments were performed with p55–p70 hESCs in 37°C incubator, 5% CO<sub>2</sub>, and 100% humidity.

### **3.2.4.3 Human ESC-Derived Definitive Endoderm (hESC-DE)**

A basal media of DMEM/F12 plus 0.2% BSA and B27 serum supplement was used for the induction of DE. Once hESCs reached an average colony size of 1 mm in diameter, DE was induced using 100 ng/mL ActivinA (R&D Systems) with 25 ng/mL Wnt3A (R&D Systems) for 4 days as previously described [69-71, 178, 179] .

### **3.2.5 Recellularization of decellularized pancreas with MIN-6 and hESC-DE cells**

Recellularization of pancreas was performed according to the method previously described [50] in chapter 2.2.5. For recellularization with DE cells, the cells were treated with 10  $\mu$ M Y-27632 (Millipore) for 2 h prior to passaging. Cells were incubated with Accutase (Life Technologies) for 5 min at 37°C to detach cells, and pipetted to obtain single cell. With the same step-wise inoculation method described with MIN6 recell, DE cells ( $9 \times 10^6$ ) were introduced into the decellularized pancreas. For both recellularizations, cells were allowed to attach overnight. A gentle rinse through the hepatic portal vein was followed in order to wash out any unattached cells after which either static or perfusion culture was resumed.

### **3.2.6 Cell labelling and LI-COR Whole Organ Imaging**

The cells were labeled with Vybrant DiD near infra-red (NIR) dye (Life Technologies) according to manufacturer's instruction to visualize cell distribution upon recellularization. The recellularized pancreas with labelled cells was detected with LI-COR Odyssey (21  $\mu$ m resolution, 1 mm offset with highest quality). The low auto-fluorescence from tissues and cells in the NIR results in excellent depth of tissue penetration (>2 cm) and provides a semi-quantitative estimate of signal, and shows cellular distribution.

### **3.2.7 Perfusion bioreactor design and components**

The perfusion bioreactor design, shown in Figure 3.4, utilized and recycled similar parts from decellularization chamber. It is composed of four main components: the organ culture chamber, air bubble trapper, coiled silicone oxygenator and peristaltic pump. All the parts were autoclaved or sterilized with EtO gas before use. After mounting the reconstructed organ into bioreactor, the whole set-up was placed in the incubator (37°C and 5% CO<sub>2</sub>) for whole organ culture.

#### **3.2.7.1 Organ culture chamber**

The reconstructed organ is contained within an autoclavable, glass media bottle (Fisherbrand) (Fig 3.4(B)). The organ culture chamber is sealed by a silicone rubber stopper (Cole Parmer, size 6.5). Three holes are bored into the stopper to fit three stainless steel 304 tubes (Small parts, hypodermic round tubing, gauge 8) with female luer fitting (Small part, stainless steel 303) soldered on one end. The first cannula holds the reconstructed organ at the end of the cannula; the other end with soldered luer fitting connects to a three-way stopcock that leads to the inlet tubing and an air bubble trapper. Second cannula draws medium out and connects to outlet tubing to the peristaltic pump. The third cannula leads to a syringe filter snugged fit into the soldered female luer fitting to permit gas exchange. The first two cannulae are connected with their corresponding tubing with 1/8-inch hose barb to luer connectors (Cole Parmer).

#### **3.2.7.2 Air bubble trapper**

The bubble trapper (Figure 3.4(C)) consists of a silicone rubber stopper attached to a 50 mL Falcon tube cut at the 20mL marking. Two holes are bored into the silicone rubber stopper to fit two stainless steel 304 cannulae (Small parts, hypodermic round tubing, gauge 8) – one inlet and one outlet – with female luer fitting (Small part, stainless steel 303) soldered on one end. Bubble

trap was prefilled with 5 mL of culture medium. To validate that the flow through the bubble trap was not significantly affected, the flow from the pump and flow out of the bubble trap was measured over the course of 10 minutes. Total volume pumped out of the bubble trap and pump was measured to be 10.7 mL and 10.9 mL respectively, signifying that 98.2% of the flow rate is conserved through the bubble trap.

### **3.2.7.3 Coiled silicone oxygenator**

Silicone tube oxygenator (Figure 3.4(D)) is composed of coiled silicone tubing to permit rapid equilibration of culture medium with most gas mixtures before reaching organ culture chamber. The inlet, outlet and oxygenator tubing are made of platinum-cured silicone (Masterflex BioPharm tubing, L/S16). The platinum-cured silicone tubing is gas permeable to oxygen and carbon dioxide. Furthermore, platinum-cured tubing is used to reduce the amount of leachable chemicals and is relatively low-protein binding.

### **3.2.7.4 Peristaltic Pump**

The peristaltic pump (Figure 3.4(E)) for perfusion bioreactor consists of the same set-up as the perfusion decellularization chamber described above. The only difference is that the flow rate used is 1mL/min for continuous perfusion culture of whole pancreas.

## **3.2.8 Static and perfusion culture conditions for recellularized pancreas**

A static culture condition was set up according to previously described method [50] in chapter 2.2.5. For the perfusion culture condition, a perfusion bioreactor was set up to circulate the medium from the main organ chamber into the vasculature of recellularized pancreatic construct

at a constant flow of 1mL/min. Culture medium for the MIN-6 recellularized pancreas was the same as the MIN-6 cell culture medium as described above (DMEM, 15% FBS and 1% Pen/Strep). For the DE-recellularized pancreas, it was cultured in basal medium consisting of DMEM/F12 plus 0.2% BSA and B27 serum without additional growth factor supplement. Both conditions were cultured in an incubator at 37°C with a 95% air / 5% CO<sub>2</sub> atmosphere for 7 days with a complete media change in day 4.

### **3.2.9 Immunofluorescence and histology**

Native, decellularized and recellularized organs were fixed, sectioned and stained following protocol previously described [50] in chapter 2.2.8. The following primary antibodies and dilutions were used: goat anti-Cxcr4 (1:100, abcam), goat anti-Sox17, goat anti-PDX1 (1:200, R&D Systems Inc.), rabbit anti-KI67 (1:200, Santa Cruz) rabbit anti-FOXA2 and rabbit anti-Cpeptide (1:100, Cell signaling). Secondary antibodies used were: donkey anti-rabbit Alexafluor 488/555 (1:500, Invitrogen) and donkey anti-goat Alexafluor 488/555 (1:500, Invitrogen). Quantification of positive staining per mm<sup>2</sup> was accomplished by converting all images to grayscale followed by analysis with Metamorph Image software.

#### **3.2.9.1 TUNEL staining**

For apoptotic cell detection, deoxynucleotidyl TUNEL assay (APO-BrdU TUNEL Assay Kit, Molecular Probes) was used, following the manufacturer's instructions. Similarly with immunofluorescence staining, TUNEL quantification was performed by counting positive cell staining per mm<sup>2</sup> and analyzed with Metamorph Image software.

### **3.2.10 Quantitative RT-PCR**

qRT-PCR was performed as previously described [50] in chapter 2.2.15.

### **3.2.11 Statistical Analysis**

Statistical analysis was performed as previously described [50] in chapter 2.2.16.

## **3.3 RESULTS**

### **3.3.1 Design of a perfusion bioreactor system for whole organ decellularization**

We have developed a perfusion bioreactor system which can be directly used to decellularize multiple intact organs without any design modification. The design of the bioreactor system for decellularization has an inlet connected to the organ mounted inside the organ chamber for detergent distribution throughout the organ via vasculature network perfusion. The effluent detergent fluid exits the organ's venous system and drains into the detergent reservoir via the organ chamber's outlet line (Figure 3.1(A), A.2, flow direction shown by arrow). The perfusion flow rate is maintained at 2mL/min for pancreas. This whole process is a closed-loop system where the detergent was recirculated back by a peristaltic pump from the detergent reservoir to organ chamber until complete decellularization was achieved (2-4 hours).

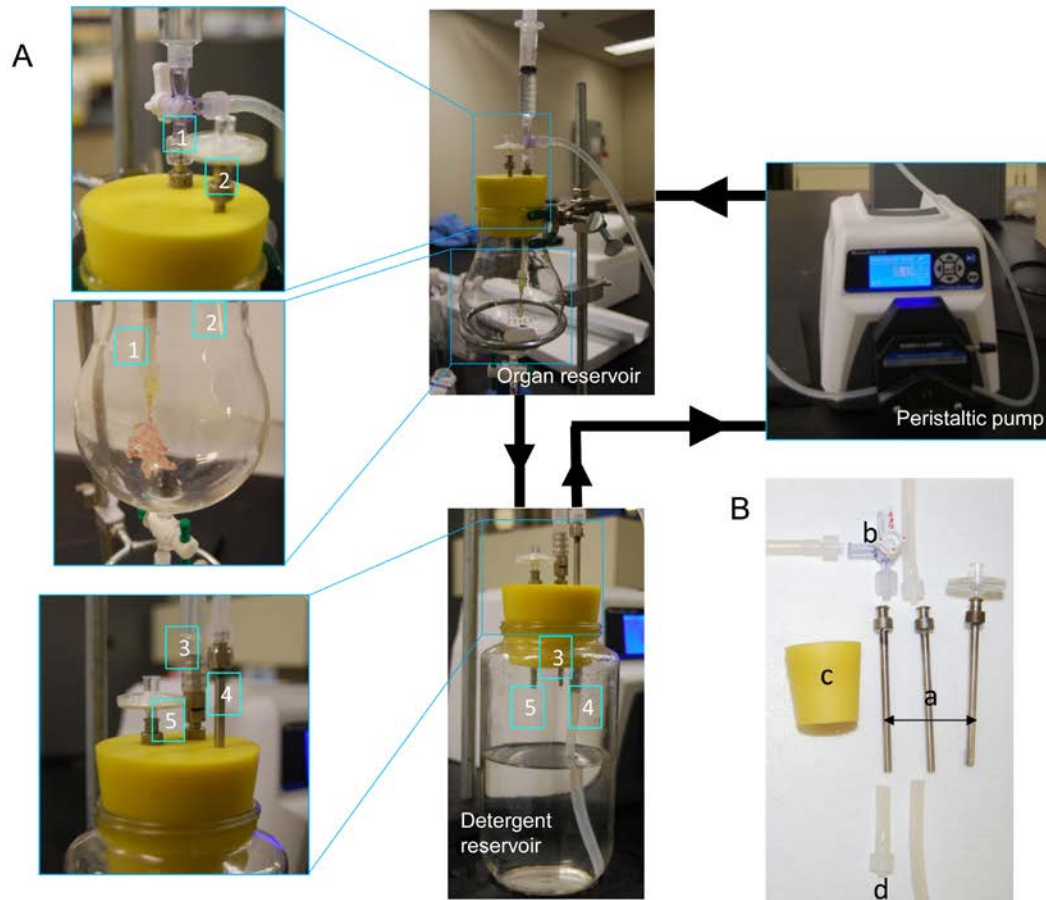


**Figure 3.1 Perfusion bioreactor design for whole organ decellularization**

(A) Detergent (black arrow) flows from the detergent reservoir via a three-way stopcock to the organ chamber and into the organ by means of a peristaltic pump. The first cannula, #1 is connected to the three-way stopcock on one end and luer connection to the target organ on the other end. The second cannula, #2 is connected to a syringe filter to allow venting and prevent pressure build up. Perfused detergent is drained from the bottom of the organ chamber by gravity into the detergent reservoir via the third cannula, #3. The fourth cannula, #4 allows the drawing of detergent from detergent reservoir via peristaltic pump to the organ chamber. The fifth cannula #5 is attached to a syringe filter to permit air exchange in sterile fashion and equilibrate pressure in the detergent reservoir. (B) Bioreactor components: a) Stainless steel cannulae, b) three-way stopcock, c) silicone stopper and d) luer lock connectors (1/8-inch hose barb) that were used for assembling the perfusion-decellularization system.

Throughout the decellularization process, murine pancreas displayed progressive whitening culminating in a translucent appearance at the end of the process (about 325 min) (Figure 3.2(A)). At macroscopic level, decellularized pancreas maintained their overall shape and gross structure. At the microscopic level, no intact cellular material was observed histologically in the exocrine and endocrine components or pancreatic ducts of the pancreas (Figure 3.2(B)). In our previous study [50], we demonstrated that major ECM components (e.g. Col I, Col IV, Laminin, Fibronectin) and ultrastructure of the pancreas were preserved using this method of decellularization. In the current study we further performed corrosion casting of a decellularized pancreas to show preservation of vascular (red) and ductal (blue) system similar to a normal pancreas (Figure 3.2(G)). These results suggest that decellularized pancreas is devoid of any cellular material but still preserves architecture and microstructure resembling a native pancreas.

The developed perfusion system was designed and built as a versatile and scalable apparatus targeting decellularization of other intact organs and multiple organs. First, the versatility of the perfusion bioreactor system in decellularizing other intact organs was verified by decellularization of liver and heart. Liver was perfused at the same flow rate as pancreas (2mL/min) while heart was perfused at a higher rate of 4mL/min given the high density of heart tissues [108]. Similar to pancreas, the decellularization of liver and heart generated translucent acellular liver and heart ECM scaffolds (within 320 min, Figure 3.2(C, E)). H&E staining showed no cell remnants with preservation of major ECM structure (Figure 3.2(D, F)). Secondly, the scalability of the developed system was demonstrated by adding a second pump head onto the peristaltic pump to connect an extra independent line and cannulae for mounting of additional organs to allow processing multiple organs in parallel (Figure A.3). These results demonstrate

that our simple perfusion bioreactor assembly is versatile enough to successfully decellularize various organs and easily scalable with only minor changes in operating parameter and design modification.

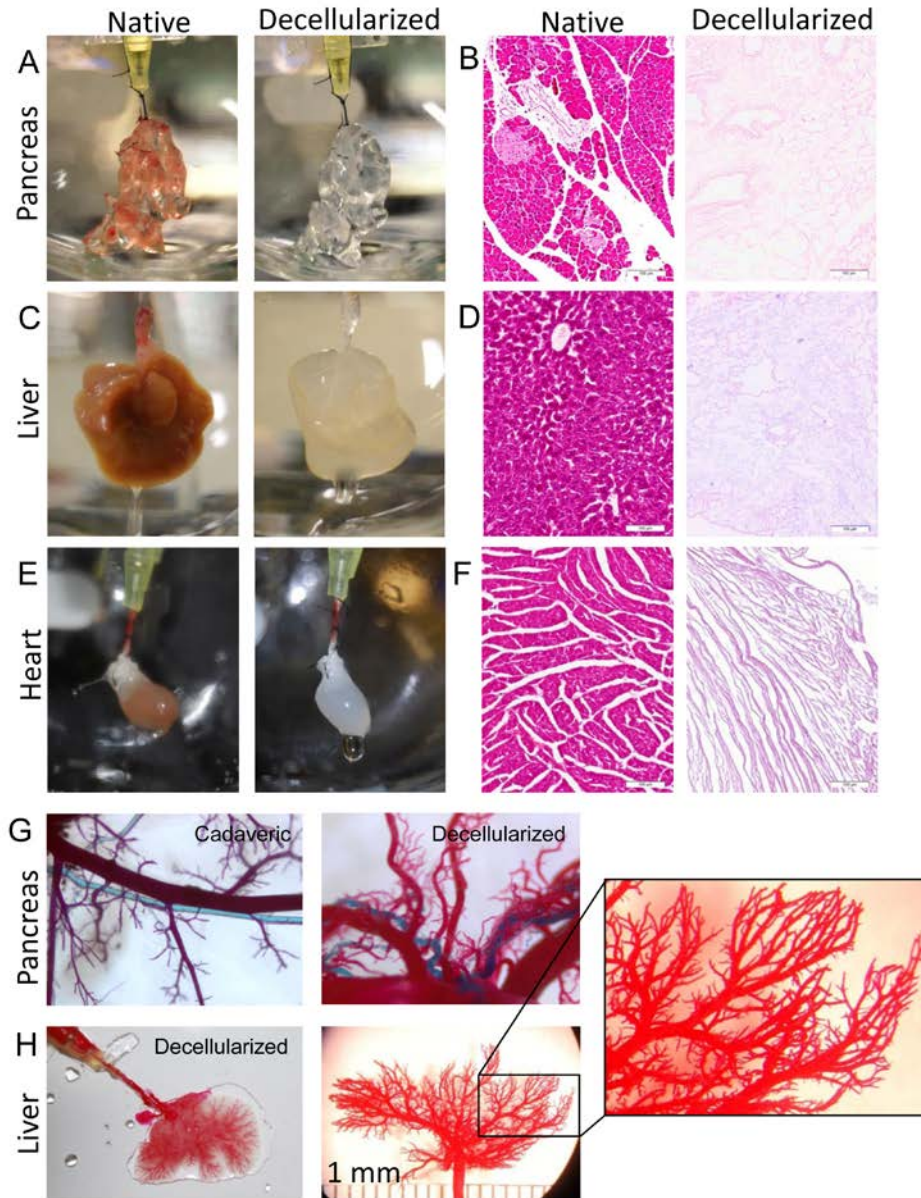


**Figure 3.2 Perfusion-decellularization of murine pancreas, liver and heart**

(A, C, E) Macroscopic images of cadaveric mouse pancreas, liver and heart (left) and the same pancreas, liver, heart after decellularization (right). (B, D, F) Representative H&E staining of sections from the cadaveric

mouse pancreas, liver, heart (left) and decellularized pancreas, liver, heart (right) showed removal of cells. (G) Representative photographs of intact microvascular (red) and ductal network (blue) from corrosion cast model of native pancreas (left) and the decellularized pancreas (right). (H) Representative macroscopic (scale bar 1mm) and microscopic (inset) photographs of intact microvascular (red) network from corrosion cast model of decellularized liver.

### **3.3.2 Recellularization and perfusion bioreactor development for organ culture**

In order to demonstrate feasibility of viable and functional organ reconstruction, the decellularized pancreas was first reconstructed with MIN6, a well-established pancreatic  $\beta$  cell line. A concentrated suspension of MIN6 cells (30 million cells in 1mL) were instilled through the hepatic portal vein using multi-step cellular infusion steps as described previously by Soto-Gutierrez et al. [117] and our group [50] (Figure 3.3A, B). The cells were labeled with Vybrant DiD near infra-red dye which allowed whole-organ imaging using Odyssey® CLx Infrared Imaging System. As illustrated in Figure 3.3C, pseudocolor fluorescence images showed the cells' distribution throughout the head and the tail of the pancreas. This confirms the cell delivery and retention in the decellularized pancreas after multi-step cellular infusion steps (Figure 3.3(B, C)). After seeding and cells were allowed to attach for another 2 hours before the pancreatic construct was connected to the designed bioreactor set-up to provide a perfusion culture condition. In parallel, a static culture condition was also set up to compare the difference between these two culture conditions (as shown in schematic Figure 3.3(A)).

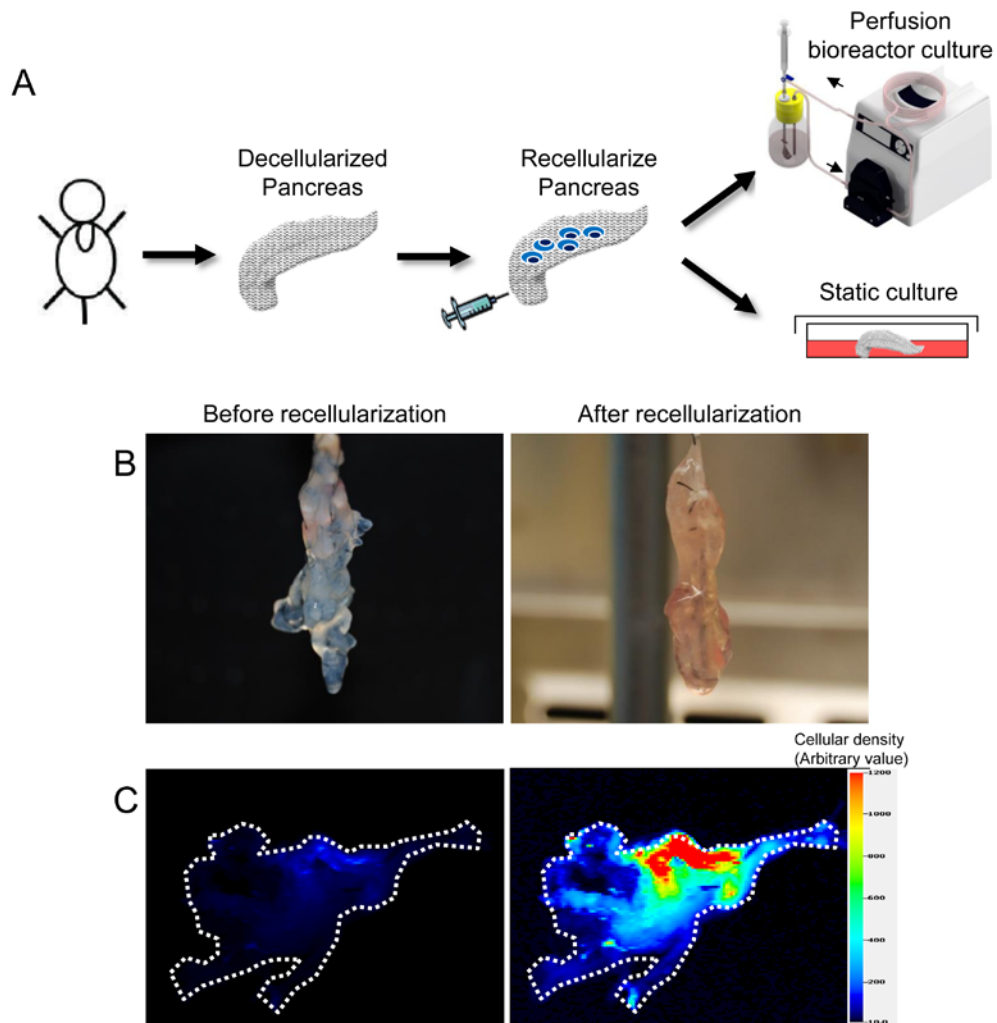


**Figure 3.3 Recellularization of decellularized pancreas**

(A) Schematic summarizing the decellularization-recellularization of pancreas and *in-vitro* culture experiment comparing static and dynamic bioreactor culture for 7 days. (B) Decellularized whole pancreas before cell seeding (left) and recellularization of the same pancreas via multi-step infusion of about 30 million cells via portal vein infusion (right). (C) Pseudocolored fluorescence image illustrates the rapid dispersion of cells. The average signal intensity in the head region of the pancreas was higher than the average signal intensity of the distal pancreas indicating more cells concentrated in the head of the pancreas.

The culture of whole organs needs to be maintained under sterile *in vitro* conditions. Hence we designed our perfusion bioreactor to be small and self-contained to be able to fit inside a standard tissue culture incubator as shown in Figure 3.4(A). It contains an organ culture reservoir (Figure 3.4(B)) filled with culture media where the recellularized pancreas is mounted for perfusion. The bioreactor is a closed-loop system and the total volume of culture medium used is about 60mL. The perfusion to vascular network of recellularized pancreas is provided via a peristaltic pump (Figure 3.4(E)) that circulates the culture media from the organ culture reservoir (Figure 3.4(B)) to the silicone oxygenator (Figure 3.4(D)) at 1mL/min to equilibrate with 5% CO<sub>2</sub> and 95% room air followed by a bubble trapper (Figure 3.4(C)) before re-entering the organ culture reservoir and reaching the cannulated pancreas. The bioreactor design being completely enclosed may not facilitate adequate oxygen and CO<sub>2</sub> exchange. Hence we adjusted the length of gas-permeable silicone tubing to allow equilibration with the incubator conditions. The tube length required to reach equilibration was mathematically modeled and determined to be 1 meter (Appendix A.1.1). With the designed set-up we verified the maintenance of phenol red color in the culture medium all through the 7 days of whole-organ perfusion culture, to ensure proper gas exchange and pH regulation inside the bioreactor. However, the high permeability of silicone tubing may result in formation of air bubbles, which is detrimental to organ cultures [119, 180]. Hence we included a bubble trap in between the silicone tubing and the inlet to the reconstructed organ to eliminate air bubbles before entering the recellularized pancreas (Bubble trapper in action, supplementary video 1). Inclusion of the bubble trap only slightly damped the flow rate from the pump (~ 1.8%), as determined by measuring the flow into and out of the bubble trap. Finally, the sterility of the designed bioreactor was verified by periodically checking the perfused culture medium for contamination by conventional streak

samples throughout the 7 day culture period. The microbiological evaluation showed no microbiological contamination (Figure A.4) even after continued culture of 14 days. These results demonstrate the successful assembly of a compact, closed-loop system to maintain sterile *in vitro* culture of reconstructed pancreas.

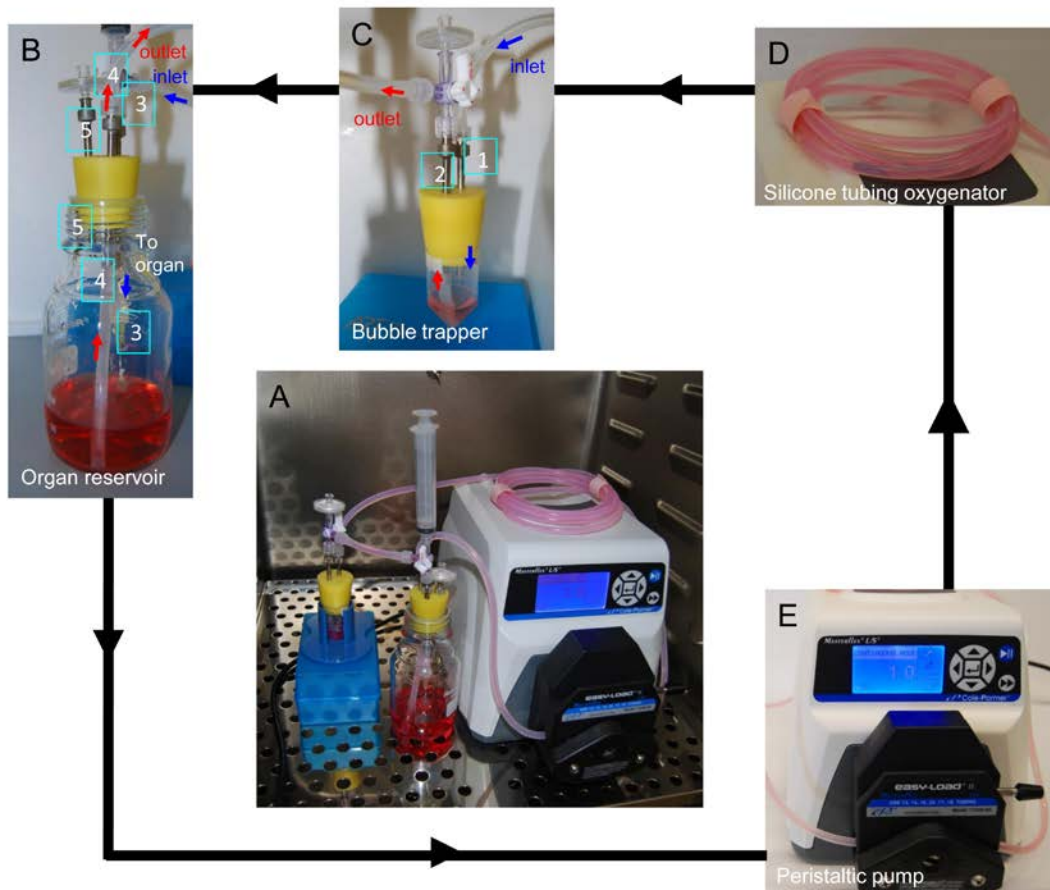


**Figure 3.4 Perfusion bioreactor setup for reconstructed pancreas culture**

(A) Photograph of the perfusion bioreactor inside a standard tissue culture incubator. (B) Photograph of organ reservoir that houses the cultured reconstructed pancreas. It is composed a 250ml media glass bottle, three stainless steel cannulae and a silicone stopper (size 6.5). Cannula #3 brings the debubbled culture media from the bubble trapper to the cultured organ. Cannula #4 draws the media from organ reservoir and recirculates to silicone oxygenator by means of peristaltic pump. Cannula #5 connects to a syringe filter to allow venting and prevent pressure build up. (C) Photograph of the bubble trapper showing the first cannula, #1 is connected to the inlet

coming from silicone oxygenator and the second cannula #2 is connected to a three-way stopcock that leads to the organ reservoir. (D) Photograph of silicone oxygenator composed of extended length of silicone tubing coiled together. (E) Photograph of the peristaltic pump to drive the culture medium (black arrow) flows from the (B) organ reservoir through the (D) silicone oxygenator and (C) bubble trapper and circulates back into the organ.

### **3.3.3 Perfusion bioreactor culture enhances $\beta$ -cell engraftment, viability and insulin expression over static culture**

One of the main goals in pancreas bio-engineering is the maintenance of  $\beta$ -cell phenotype and insulin function. To test the feasibility of this objective in a whole-organ set-up, decellularized pancreas reconstructed with MIN-6 cells were cultured under static or perfusion culture conditions for 7 days, and subsequently characterized for engraftment, survival and insulin expression. After cell seeding through multi-step infusion, it was observed that the MIN6  $\beta$ -cells lined the vascular channels and surrounding parenchymal region throughout the entire scaffold. Significant differences were subsequently observed between the static and perfusion cultures of the reconstructed pancreas after 7 days. As observed by H&E staining, reconstructed pancreas cultured in the bioreactor had significantly more cells per high-power field (HPF) than static cultured pancreas ( $202 \pm 38$  vs.  $89 \pm 21$ ,  $P < 0.05$ , Figure 3.5(A)). For cell survival assessment, TUNEL assay detected higher number of apoptotic cells under static condition ( $21.8 \pm 4.7\%$ , with  $P < 0.05$ , Figure 5(B, C)). Interestingly, most apoptotic cells in the static culture condition were located in the core region of the engraftment whereas cells located in the peripheral region with basement membrane contact were mostly negative for TUNEL staining (Figure 3.5(B)). This may be due to insufficiency of nutrient transport to the core region or lack of ECM contact to prevent  $\beta$ -cell apoptosis, often referred to as anoikis [49, 181]. In contrast, the perfusion culture

resulted in significant reduction in cell death with no preferential localization of TUNEL positive staining.

Insulin/C-peptide synthesis is the primary function of pancreatic  $\beta$  cells. To first evaluate this function, immunostaining of C-peptide (cleaved molecule of insulin) was performed after exposure to static and perfusion culture. Consistent with engraftment and survival, perfusion culture also resulted in increased number of C-peptide+ cells (Figure 3.5(D)). The static and perfusion cultures were further compared by quantitative RT-PCR of the recellularized pancreas. We used a combination of proteinase K and mechanical homogenization to remove fibrous ECM for isolation of RNA from recellularized pancreas. Analysis of insulin (*ins1* and *ins2*) gene expression by qRT-PCR demonstrated significantly higher *ins1* and *ins2* gene expression in perfusion bioreactor culture over corresponding static culture ( $1.82 \pm 0.35$  and  $1.43 \pm 0.18$ ,  $P < 0.05$ ) (Figure 3.5(E)). Worth noting that RNA concentration was also significantly higher under perfusion culture suggesting that there is higher number of cells retaining insulin expression with this culture condition. Collectively, these results demonstrate that perfusion bioreactor culture enhances  $\beta$  cell engraftment, survival and insulin expression in the whole-organ setup. While suitable for proof-of-concept studies,  $\beta$  cell lines lack significant application for clinical or *in-vitro* drug testing studies. The production of a regenerative reconstructed pancreas from renewable cell source such as human pluripotent stem cells, on the other hand, would be ideal due to its unlimited potential for self-renewal, expansion and differentiation. Hence, next we tested the feasibility of repopulating the decellularized pancreas with hESC-derived DE cells, as a first step towards regenerative reconstructed pancreas.

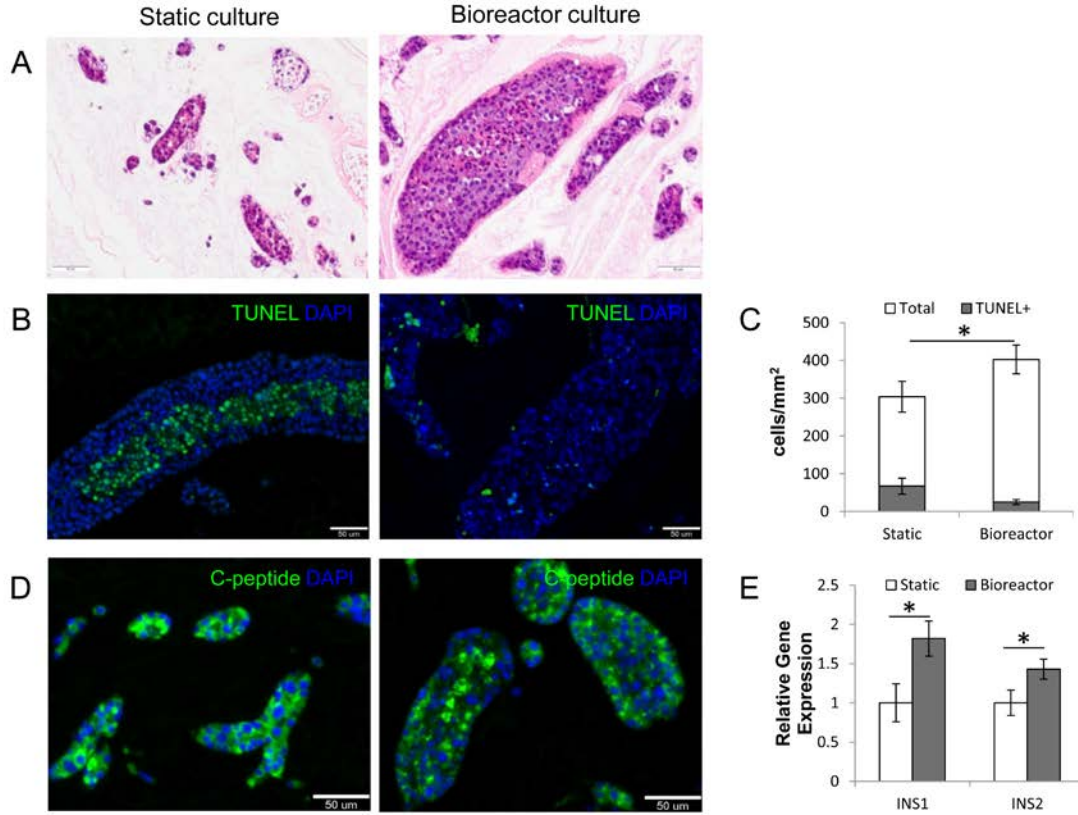


**Figure 3.5 Comparison between static and bioreactor culture for repopulated pancreas with pancreatic  $\beta$ -cell, MIN-6**

(A) H&E images of repopulated pancreas after 7 days of static (left) and bioreactor (right) culture showing higher cellular engraftment in bioreactor culture. (B) Representative TUNEL staining of the repopulated pancreas showed higher number of apoptotic cells detected in the static culture (left) compared to the bioreactor culture (right). Localization of TUNEL+ cells in static culture were found predominantly in the core region, away from basement membrane. (C) Image analysis of TUNEL staining showing higher percentage of TUNEL+ cells in the static culture. (D) IHC analysis showed higher number of C-peptide+ cells detected in the bioreactor culture (right) compared to static culture (left). (E) Quantitative RT-PCR analysis showed higher ins1 and ins2 gene expression in bioreactor culture than static culture. \* indicates  $P < 0.05$

### **3.3.4 Perfusion bioreactor culture enhances proliferation and differentiation of hESC-DE repopulated pancreas over static culture**

Towards regenerative reconstruction of whole pancreas, hESCs were first pre-differentiated *in vitro* towards a DE phenotype via a stage-wise directed differentiation protocol. We have previously reported a highly efficient protocol to direct hESCs towards endoderm lineage using Activin A and Wnt3A [69-71, 178, 179] (Figure 3.6(A)). At day 4, the specific DE marker genes, *SOX17* and *FOXA2* were highly upregulated as evidenced by qRT-PCR analysis (Fig. 6B). Next, we checked the co-expression of *CXCR4* and *SOX17* to confirm the DE commitment by immunostaining (Figure 3.6(C)). In addition, flow cytometry analysis demonstrated that the culture at day 4 comprised an average of 85% *SOX17* and 90% *CXCR4* positive cells (Figure 3.6(D)). These data confirm the successful derivation of DE cells from H1 hESCs using exogenous factors.

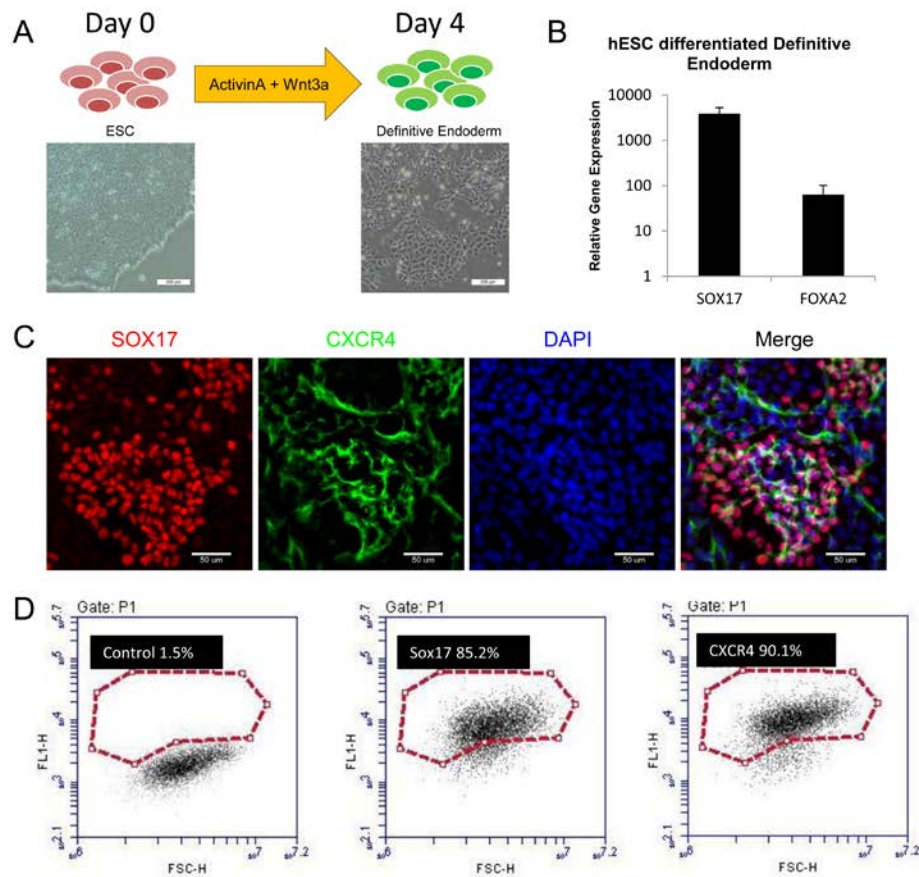


**Figure 3.6 Differentiation of human embryonic stem cells (H1) to definitive endoderm**

(A) Schematic showing the *in vitro* differentiation protocol. Lower panel is the corresponding bright field images of undifferentiated H1 and definitive endoderm cells after chemical induction. (B) Quantitative RT-PCR analysis on day 4 showing upregulation of definitive endoderm genes (sox17 and foxa2) relative to undifferentiated day 0 cells. (C) Immunostaining analysis detected positive definitive endoderm markers - nuclear staining of SOX17 (red) and cytoplasmic staining of CXCR4 (green). (D) Flow cytometry analysis of differentiated human ES cells revealed that after 4 days' induction with ActivinA and Wnt3A, more than 85% of cells were positive for definitive endoderm markers, SOX17 and CXCR4.

Next, DE committed hESC (hESC-DE,  $3 \times 10^6$  cells) were seeded into the decellularized pancreas following a similar seeding procedure as described above for MIN-6  $\beta$ -cell and cultured in the reconstructed pancreas in either static or perfusion bioreactor condition for 7 days. We seeded 10-fold less cells compared to MIN-6 cells and examined the feasibility of

subsequent *in situ* expansion of DE cells as a potential alternative to large-scale expansion of pluripotent stem cells *in vitro* for the repopulation of decellularized organs. After 7 days culture, the reconstructed pancreata were characterized for engraftment, proliferation and maintenance of DE phenotype. Consistent with our previous observation, perfusion bioreactor culture of the recellularized pancreas resulted almost two times higher engraftment of the hESC-DE cells as compared to static culture (Figure 3.7(A, C)). The static culture configuration resulted in a more sporadic and heterogeneous cell distribution, with some areas remaining relatively acellular and other displaying notable lower cell attachment and retention (Figure 3.7(A)). Cell proliferation within the whole pancreas cultured under 2 different culture conditions were assessed by the quantification of KI67+ cells from all DAPI+ cells (Figure 3.7(B)). Quantitative image analysis demonstrated markedly reduced proliferation of cells in the pancreatic constructs maintained under static culture for 7 days ( $45\pm 5\%$ , Figure 3.7(C)), whereas  $72\pm 7\%$  of the cells cultured in perfusion bioreactor were positive for Ki67 antibody. This suggests that under perfusion culture condition, the hESC-DE-cells can be maintained in a proliferative state, hence suggesting the feasibility of *in situ* expansion for whole organ reconstruction.

Having confirmed the viability and proliferation of the engrafted DE cells, the next step was to analyze its phenotype. DE phenotype of the engrafted cell population was confirmed by nuclear FOXA2 expression. While FOXA2+ cells were detectable for both static and perfusion bioreactor cultured pancreas, there were significant higher number of FOXA2+ cells detected under perfusion culture than static culture ( $29\pm 4\%$  vs.  $13\pm 5\%$ ,  $P < 0.05$ ) (Figure 3.7(D,E)). Also under static culture some engrafted cells acquired a flattened morphology and lost expression of FOXA2 transcription factor. We further quantified the gene expression of DE markers under 2 different culture configurations with qRT-PCR. Consistent with

immunostaining assessment, gene expression analysis showed a 2.2-fold ( $P < 0.05$ ) increase in *FOXA2* expression in perfusion culture over static culture (Figure 3.7(F)).

Since DE phenotype was adequately preserved in the perfusion cultured whole pancreas, we further analyzed if any of the early pancreatic markers were expressed in this endoderm population. While no pancreas specific chemical induction is being presented to the DE cells, they are interacting with pancreas-specific ECM. Although we are exposing human cells to ECM from mouse origin, studies have shown that components of ECM (e.g. collagens, glycoproteins, proteoglycans, mucins, elastic fibers, and growth factors) are generally highly conserved across species [182, 183]. We analyzed the cells for transcription factor pancreatic and duodenal homeobox1 (*PDX1*) expression, which is the master regulator giving rise to all pancreatic lineage cells [184]. As illustrated in Figure 3.7(G-H), a small fraction of the DE cells were indeed observed to express *PDX1* transcription factor in the perfusion bioreactor cultured pancreas. However no such detectable population was observed in the static culture condition (Figure 3.7(G, H)). qRT-PCR analysis corroborated with this finding with minimum to no *PDX1* gene expression detected in the static culture condition (7-fold increase over static culture, Figure 3.7(I)). These results clearly indicate the superior performance of perfusion bioreactor culture over static culture while reconstructing whole organ pancreas. Taken together, our results demonstrate for the first time the capacity of regenerative reconstruction of pancreas using hESC derived cell types. When cultured under perfusion, the hESC derived DE cells demonstrated excellent engraftment, proliferation and maintenance of phenotype. Furthermore, the engrafted cells retained the potential for further differentiation into the pancreatic lineage, as judged by the spontaneous *PDX1* expression.

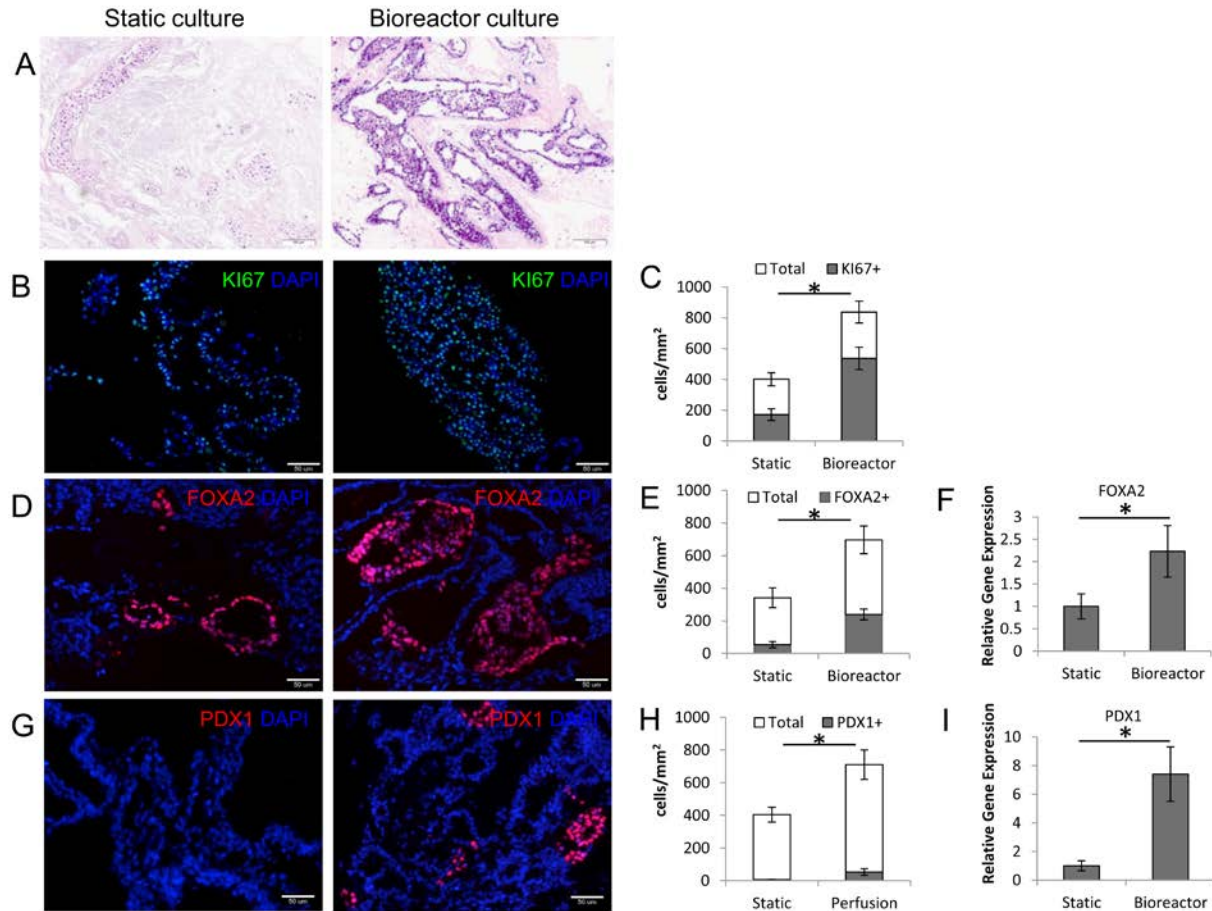


**Figure 3.7 Comparison between static and bioreactor culture for repopulated pancreas with hESC-derived DE**

(A) H&E images of repopulated pancreas after 7 days of static (left) and bioreactor (right) culture showing higher cellular engraftment in bioreactor culture consistent with observation in the MIN-6 repopulated pancreas culture. (B) Representative KI-67 staining of the repopulated pancreas showed higher number of proliferative cells detected in bioreactor culture (right) than the static culture (left). (C) The corresponding image analysis of KI-67 staining showing higher percentage of KI67+ cells detected in bioreactor culture and corroborated the qualitative immunostaining observation. (D) Representative images of definitive endoderm marker, FOXA2 (red) showed higher number of definitive endoderm committed cells in the bioreactor culture (right) than static culture (left), indicating better maintenance of definitive endoderm phenotype with bioreactor culture. (E) The corresponding image analysis of FOXA2 staining showing higher percentage of FOXA2+ cells detected in bioreactor culture and corroborated the qualitative immunostaining observation. (F) Quantitative RT-PCR analysis on day 7 of bioreactor

culture showing higher upregulation of FOXA2 genes relative to static culture. (G) Representative immuno-staining image showing minimal PDX-1+ cells detected only in bioreactor culture condition (right). (H) The corresponding image analysis of PDX-1 staining showing a low percentage of PDX1+ (~4%) cells detected in bioreactor culture and corroborated the qualitative immunostaining observation. (I) Quantitative RT-PCR analysis detected higher PDX-1 gene expression in bioreactor culture relative to static culture. \* indicates  $P < 0.05$

### 3.4 DISCUSSION

The design of perfusion systems and bioreactors to facilitate the development of organ engineering strategies is a nascent but rapidly growing field [108, 112, 171, 172, 177, 185]. Herein, we present the design and assembly of a simple and cost-efficient perfusion system comprised of parts that are routinely found in research laboratories for the decellularization and *in vitro* bioreactor culture of reconstructed pancreas seeded with MIN-6 beta cells and hESC differentiating cells. We show that bioreactor culture of reconstructed pancreas display improved cell engraftment, viability and phenotypic maintenance over static culture.

In spite of its simplicity, our bioreactor is versatile and scalable. We tested this perfusion decellularization set-up on multiple intact organs: pancreas, liver and heart. Our assembled perfusion system achieved complete decellularization of the three tested organs with minor adjustments of the flow rate based on the inherent characteristics of the tissues. For example, we used only 2mL/min of flow rate for pancreas and liver given the high vascular density and delicate capillary network. Conversely for the heart with higher density of tissue, we increased the flow rate to 4mL/min to achieve complete decellularization – consistent with reports by other groups [108, 186, 187]. Notably, it may be possible to use low or graduated flow rates to allow a more gradual adaptation to changes in vascular resistance and flow, while minimizing the

chances of ECM damage [168, 188]. Recently, several groups reported a decellularization technique to vary volume, flow or pressure with automation [168, 169, 189]. This enables better control of perfusion parameters in a reproducible matter and reduces the variability between investigators and experiments. While it is possible to implement such varying flow in our existing set-up, currently even with a fixed low flow rate we could consistently preserve the ECM structure and micro-architecture such as intact vasculature and ductal conduit of the decellularized pancreas and liver as demonstrated by corrosion casting assay (Figure 3.2G-H). We demonstrated the feasibility for scale-up in Figure A.3, a higher throughput can be achieved by using a larger reservoir and silicone stopper to house additional organs and incorporate more cannulae for additional lines respectively. Similar approach was successfully demonstrated by Sullivan et al. using a 12-channel peristaltic pump to accommodate additional pump heads to drive the perfusion of additional lines for decellularization of porcine kidneys [139].

Upon recellularization with relevant cell types, the whole organ construct needs to be cultured under media perfusion in order to allow adequate nutrient supply to ensure cell viability throughout the thickness of organ. This is particularly important for whole organs, where the thickness is too high for simple diffusive transport to meet the oxygen demand of engrafted cells cultured under high seeding density. Our bioreactor design allowed nutrient circulation via the preserved organ vasculature in a closed and compact system amenable to aseptic culture in a standard tissue culture incubator. However since the bioreactor is completely closed loop we took special measures to ensure gas exchange within the incubator, by including extra lengths of silicone tubing. Silicone tubing is highly permeable to oxygen and carbon dioxide, as well as most other common gasses [190]. We incorporated a mathematical model to determine the residence time within the silicone tubing required to allow perfusate gas concentration to

equilibrate with the surrounding of 5% CO<sub>2</sub> and 95% room air before reaching the recellularized pancreas (Appendix A.1.1). Extending the length of the silicone tubing to meet the calculated residence time based on the slowest flow rate ensured adequate gas exchange. With this slow flow rate (1mL/min), Petersen et al. has reported to be suitable in delivering nutrients for *in vitro* culture of engineered tissues/organs [185]. Conversely, high perfusion flow rate (>5mL/min) may lead to undesired shear stress to seeded cells [191, 192]. In case of an enhanced oxygen demand from a higher cell density of the reconstructed organ, or more mature cells with higher oxygen demand, it is possible to further supplement with oxygen carriers such as perfluorocarbons [126, 193]. While extended silicone tubing is a simple contraption to allow gas exchange, it can result in a build-up of air bubbles. Hence we designed a bubble trap to capture the air bubbles before they enter the vasculature of the recellularized pancreas. This is a critical step in the bioreactor setup since introduction of air bubbles within the organ vasculature can have the severely detrimental effect of completely halting fluid flow [180], and cause extensive tissue damage [119].

The lack of an abundant source of human pancreatic islets is a major limitation in cell therapy approaches to diabetes treatment, hence prompting investigation into alternative cell sources. Human pluripotent stem cells have emerged as a promising avenue, and recent breakthroughs in pluripotent stem cells differentiation established the feasibility of generating  $\beta$  cells *in vitro* [55, 56]; this offers the unique opportunity to reconstruct pancreatic tissues from an expandable and renewable cell source. When compared with mature cells, stem/progenitor cells may have higher proliferation capacity, innate hypoxic resistance, superior functional plasticity, and the ability to migrate and localize within a given site-appropriate 3D anatomical location [111, 153, 194, 195]. Toward this end, we examined the feasibility of reconstructing

decellularized pancreas with hESC-derived DE cells for *in situ* expansion and subsequent differentiation into pancreatic cell types within their native 3D environment. Our result showed that perfusion bioreactor culture significantly improved the cellular engraftment of hESC-DE seeded pancreatic construct. Static culture of the recellularized pancreas was found to be inadequate to maintain cellular proliferation and DE phenotype. With the perfusion bioreactor culture, on the other hand, we not only observed enhanced proliferation and phenotype maintenance, a small number of cells were also observed to demonstrate pancreatic commitment (as evidenced by PDX-1+ cells). Importantly, the DE-seeded pancreatic construct was cultured in basal culture medium without any growth factor induction. This reflects the potential role of decellularized ECM in directing stem cell fate as suggested by others [140, 153, 176, 186, 195, 196].

The system we have described in this report is expected to help the tissue and organ engineering community build their own bioreactors in-house. While the proposed design is sufficient to decellularize as well as maintain reconstructed organ culture, it can further benefit from continued design improvements to allow for successive advancements in perfusion bioreactor design. For instance, the importance of monitoring organ growth and development using noninvasive imaging detection is not to be overlooked. Current data metrics from whole organ culture typically involves end-point analysis to assess cell survival, proliferation and function on the growing organ. New, noninvasive methods to evaluate organ and cell growth such as near-infrared (IR) imaging allows for deep tissue imaging with limited tissue scattering and auto-fluorescence [197]. We have demonstrated the feasibility of this noninvasive method of monitoring in our recellularized pancreas (Figure 3.3C). Ren et al. recently reported a non-invasive resazurin reduction perfusion assay to assess cell viability and proliferation on bio-

engineered whole organ constructs [198]. Another group, Uzarski et al. reported the monitoring of recellularized kidney and liver by sampling of physical and biochemical markers such as hydrodynamic pressure and soluble biomarkers (e.g. albumin and kidney injury molecule-1) respectively [125]. Another area of improvement is the potential to fit the bioreactor with specific sensors to ensure a controlled environment. Biomimetic physical, electrical, or chemical stimuli could also be built-in to improve and promote its function. For example, mechanical stretching of heart tissue has been found to promote cell alignment [199] while electrical stimulation causes the coordinated beating of heart cells [200]. In addition, further studies are ongoing in our laboratory to define the optimal perfusion parameters and chemical growth factor complementation to promote differentiation and functional maturation of the reconstructed pancreas.

### 3.5 CONCLUSION

This chapter presents the development of a simple, cost-effective and scalable organ perfusion system that could be implemented to both decellularization and recellularization of vascularized intact organs. The reported design was successfully applied to pancreas, liver and heart to obtain whole organ bioscaffolds. Repopulation and culture of an engineered whole-organ pancreas could be performed in the adapted perfusion bioreactor with a  $\beta$ -cell line and hESC-derived DE cells toward the goal of producing an intact bio-engineered pancreas. After establishing the design and assembly of the bioreactor system, we next examine the feasibility to repopulate decellularized scaffolds with renewable hPSC in the chapter 4.

## **4.0 REPOPULATION OF DECELLULARIZED ORGAN SCAFFOLD WITH HUMAN EMBRYONIC STEM CELLS-DERIVED PANCREATIC PROGENITOR CELLS**

### **4.1 INTRODUCTION**

After developing a perfusion bioreactor that could be implemented to both decellularization and recellularization in Chapter 3, here in chapter 4 we focus on establishing the feasibility to repopulate whole organ scaffolds with renewable cell types such as human embryonic stem cells (hESC). Recent progress in repopulation of decellularized organ scaffolds with human pluripotent stem cells present a promising new avenue for the development of regenerative organs for the treatment of injured or diseased organs. Significant progress has been achieved using this approach in the whole organ engineering of heart [120, 135], lung [195, 196, 201, 202], and kidney [140, 203]. With the same approach, pancreas organ engineering will likely have tremendous impact in regenerating bio-engineered pancreas for diabetes therapy. The objective of this chapter to study the potential of hPSC derived pancreatic lineage cells to repopulate and differentiate in decellularized organ scaffolds.

Identifying a regenerative cell source is critical for tissue engineering and regenerative medicine therapy. Pancreatic tissue engineering studies to date have focused on the use of primary islets and immortalized endocrine  $\beta$  cell lines for restoring insulin function in diabetic

animal models [49-51, 62]. Primary human islets from donors, however, are scarce and also difficult to maintain in long term culture and cannot be expanded *in vitro*. Hence there is great interest in the use of human pluripotent stem cells (hPSC) (i.e. human embryonic (hESC) or induced pluripotent stem cells (hiPS)) to derive functional islets. The unlimited self-renewal potential of hPSCs make them particularly attractive for regenerative therapy. Hence hPSC derived pancreatic cell types will likely be attractive cell source for reconstruction of decellularized organ. By recapitulating the early pancreatic developmental stage, step-wise *in vitro* differentiation protocols have successfully generated pancreatic progenitors [61, 66-68] and insulin-producing cells from hPSC [78, 79]. Similarly, cardiac and lung lineage cells have been generated from hPSC and shown to successfully repopulate decellularized hearts [120, 135] and lungs [195, 196, 201, 202]. In addition, the complex ECM from these decellularized organs promoted further maturation into functional cell types (e.g. contractile cardiomyocytes for heart, and multi-ciliated airway cells for lungs). These prior studies clearly motivate the need and indicate the potential benefits that can be attained by repopulating whole organ scaffolds with hPSC differentiated cells. We hypothesize that similar enhancement may be expected in pancreas bioengineering. To this effect, we propose the repopulation of decellularized organ scaffolds with hPSC derived pancreatic cells.

In the present chapter, we will evaluate the possibility of repopulating decellularized organ scaffolds (e.g. pancreas and liver) with pancreatic progenitor cells derived from hPSC. We have previously reported efficient differentiation of pancreatic progenitor cells from hPSCs on adherent cultures [70, 71], which we used to repopulate our decellularized pancreas. More recently, we reported an efficient derivation of PP aggregates by alginate encapsulation of hPSCs and subsequent differentiation under encapsulation [69]. The differentiated hPSC-PP aggregates

not only express enhancement of pancreatic differentiation than the parallel adherent cultures, but also retain cell-cell contact which makes them more amenable to organ repopulation. However, engraftment of these hPSC-PP aggregates required a more extensive vascular support, which was found to be superior in decellularized liver over the decellularized pancreas scaffold. Decellularized liver repopulated with hPSC-PP aggregates resulted in extensive and uniform cellular engraftment and viability throughout the thickness of the scaffold. More importantly, the seeded hPSC-PP aggregates matured into mono-hormonal C-peptide positive cells after 9 days of bioreactor culture. This chapter demonstrated the feasibility of using decellularized organ scaffolds for regenerative bioengineering of pancreas with potential applications in diabetes therapy, drug discovery and regenerative medicine.

## **4.2 METHODS**

### **4.2.1 Human pluripotent stem cells (hPSC) culture and two-dimensional (2D) pancreatic differentiation**

The H1 embryonic stem cell lines were maintained in feeder free conditions as previously described in chapter 3.2.4.2. The first step of pancreatic differentiation is definitive endoderm (DE) induction. Once hESCs reached an average colony size of 1 mm in diameter, DE was induced as previously described [71] in chapter 3.2.4.3. Pancreatic progenitor was induced with 0.2  $\mu$ M KAAD-cyclopamine for 2 days and 0.2  $\mu$ M KAAD-cyclopamine with 2  $\mu$ M retinoic acid (Sigma-Aldrich) for 2 days. Finally, maturation was induced by 10  $\mu$ M nicotinamide (Sigma-Aldrich) for 2 days and 10  $\mu$ M nicotinamide with 30  $\mu$ M DAPT (Santa Cruz Biotechnology) for 7 days. A basal media of DMEM/F12 plus 0.2% BSA and B27 serum supplement was used for

the differentiation. Cultures were performed with p55–p70 hESCs in 37°C incubator, 5% CO<sub>2</sub>, and 100% humidity. All cytokines and small molecules were from R&D Systems unless otherwise specified.

#### **4.2.2 Decellularization of pancreas and liver**

All animal work performed was in accordance with animal welfare act, institutional guidelines and approved by Institutional Animal Care and Use Committee of the University of Pittsburgh. Mouse pancreas and liver were perfusion-decellularized using SDS and TritonX-100 protocol as previously described [50] in chapter 2.2.2 and chapter 3.2.2.

#### **4.2.3 Characterization of decellularized pancreas and liver**

Removal of cellular material from decellularized pancreata and livers was confirmed using hematoxylin & eosin (H&E) staining and scanning electron microscopy (SEM). Preservation of matrix protein was confirmed with immunostaining of matrix proteins (e.g. collagen IV). To characterize the preserved vascular network in the decellularized pancreas and liver scaffolds, we performed the corrosion casting using Batson's 17 anatomic corrosion kit (Polysciences, Inc) and quantify vasculature network and organization using ImageJ angiogenesis analyzer [204, 205].

#### **4.2.4 Differentiation of hPSC in alginate capsules**

Single-cell suspension of undifferentiated hESCs was encapsulated according to previous study [69]. Briefly, hESCs were pretreated with 10  $\mu$ M Y-27632 (Millipore) before harvested into single cells with Accutase (Life Technologies). Single-cell solution of hESC ( $1 \times 10^6$  cells/mL) were suspended in filtered 1.1% (w/v) low-viscosity alginate (Sigma-Aldrich) with 0.2% (v/v) gelatin (Sigma-Aldrich) and added drop-wise to a solution of 100 mM CaCl<sub>2</sub> (Sigma-Aldrich)

with 10 mM HEPES (Sigma-Aldrich) using a 22-gauge needle. Alginate capsules were incubated for 6–8 min in the CaCl<sub>2</sub> solution. Capsules were washed three times with phosphate-buffered saline (PBS) and suspended in appropriate medium with 10 μM Y-27632 for 4 days prior to differentiation. To initiate differentiation, similar step-wise induction cocktails were utilized as described in the 2D protocol above. First, DE was induced using 100 ng/mL ActivinA and 25 ng/mL Wnt3A for 4 days. Afterward, PP was induced with 0.2 μM KAAD-cyclopamine for 2 days and 0.2 μM KAAD-cyclopamine with 2 μM retinoic acid (Sigma-Aldrich) for 2 days. All cytokines and small molecules were from R&D Systems unless otherwise specified. All differentiation media were made using DMEM/F12 (Life Technologies), supplemented with 0.2% bovine serum albumin (BSA; Sigma-Aldrich) and 1xB27 (Life Technologies).

#### **4.2.5 Seeding of hPSC derived PP cells and 3D PP aggregates in decellularized scaffolds**

Cell seeding was performed according to the method previously described [50] in chapter 2.2.5 and 3.2.5. For seeding with 3D PP aggregates, cells were first decapsulated with 100 mM EDTA (Sigma) and washed twice with PBS followed by same seeding steps as hESC-PP. For both cell types, cells were allowed to attach overnight. A gentle rinse through the hepatic portal vein was followed in order to wash out any unattached cells after which bioreactor culture was resumed.

#### **4.2.6 Bioreactor culture of repopulated pancreas and liver**

For *in vitro* culture of repopulated pancreata (n=2) and livers (n=3) with hESC-derived PP cells, a perfusion bioreactor was set up as previously described in chapter 3.2.8. The repopulated organs were cultured in maturation media consists of DMEM/F12 plus 0.2% BSA and B27 serum with nicotinamide (10 μM, Sigma Aldrich) and notch inhibition (30 uM DAPT, Santa

Cruz) for 9 days. The bioreactor was placed in an incubator at 37°C with a 95% air / 5% CO<sub>2</sub> atmosphere with one complete media change in day 4.

#### **4.2.7 Cell labelling and LI-COR Whole Organ Imaging**

Cell labeling and LI-COR whole organ imaging was performed as previously described in Chapter 3.2.6.

#### **4.2.8 Flow cytometry analysis**

hPSC-PP and 3D PP aggregates were characterized by flow cytometry using primary antibodies including goat anti-PDX1 and goat anti-NKX6.1 (1:200, R&D Systems). First the cells were treated with Accutase and passed through cell strainer (40µm, Fisherbrand) to obtain uniform single-cell suspension. Next, the cells were fixed with 4% formaldehyde (Thermo Scientific) in PBS for 30 min followed by permeabilization with 0.1% Saponin (Sigma-Aldrich) with 0.5% BSA in PBS for 30 min. Blocking for nonspecific binding was performed by incubating cells with 3% BSA with 0.25% dimethyl sulfoxide and 0.1% Saponin in PBS for 30 min. After primary antibodies incubation for 30 min at room temperature, samples were washed 3 times (5 min each) before incubating with secondary antibodies Alexafluor 555 (Life Technologies) for 30 min at room temperature. Secondary antibodies stained only samples were used as the negative control. In the final step, samples were washed and suspended in PBS before transferring to flow cytometry tubes. Accuri C6 © Flow Cytometer was used to quantify the protein expression. The gate was set beyond cells positive for secondary antibody only to eliminate false positives.

#### **4.2.9 Histology and immunofluorescence staining**

Decellularized and recellularized organs were fixed, sectioned and stained following protocol previously described [23] in chapter 2.2.8. The following primary antibodies and dilutions were used: (1:100, abcam), goat anti-Sox17, goat anti-PDX1, goat anti-ISL1, goat anti-NKX6.1 (1:200, R&D Systems Inc.), rabbit anti-KI67 (1:200, Santa Cruz) rabbit anti-FOXA2 and rabbit anti-Cpeptide (1:100, Cell signaling). Secondary antibodies used were: donkey anti-rabbit Alexafluor 488 and 555 (1:500, Invitrogen) and donkey anti-goat Alexafluor 488 and 555 (1:500, Invitrogen). For apoptotic cell detection, deoxynucleotidyl TUNEL assay (APO-BrdU TUNEL Assay Kit, Molecular Probes) was used, following the manufacturer's instructions.

#### **4.2.10 Quantitative RT-PCR**

qRT-PCR was performed as previously described [50] in chapter 2.2.15.

#### **4.2.11 Statistical analysis**

Statistical analysis was performed as previously described [50] in chapter 2.2.16.

### **4.3 RESULTS**

#### **4.3.1 hPSC-derived pancreatic progenitors (hPSC-PP) engraft in decellularized whole-organ scaffolds and maintain pancreatic phenotype**

Figure 4.1A-D illustrates the overall workflow used to repopulate decellularized mouse pancreas with hPSC. To examine the potential of hPSC to repopulate decellularized whole-organ scaffolds

and generate pancreatic tissue *in vitro*, the first step was to obtain decellularized pancreatic scaffolds from adult mice. Using a perfusion-decellularization protocol with SDS, TritonX-100 detergent solution as previously described [50] (Figure 4.1D), we achieved rapid and complete decellularization of the mouse pancreas. Histologic staining and electron microscopy (EM) analyses of decellularized scaffolds confirmed removal of all host cells (Supplementary Figure A.7).

Next, we differentiated hPSCs to the pancreatic progenitor stage (hPSC-PP) and used it to repopulate the decellularized pancreas. This stage seems most suitable because of their commitment to express the transcription factor pancreatic and duodenal homeobox1 (Pdx1), which is the master regulator giving rise to all pancreatic lineage cells [184]. We used our previously published directed differentiation protocol [70, 71] to induce the differentiation of pancreatic progenitors (PP) from human H1 ES cells (Figure 4.1A-C). During embryonic development, pancreatic-specific progenitors originate from definitive anterior endoderm found in the developing foregut [58, 206, 207]. Therefore, we first generate definitive endoderm from hPSC using Activin A (100 ng/ml) and Wnt3a (25 ng/ml) for 4 days (day 0-4). At day 4, uniform expression of endoderm transcription factor Sox17 was observed by immunostaining, quantified to be  $82 \pm 8\%$  by image analysis (Figure 4.1B), indicating DE fate commitment of hPSC. This is consistent with previously reported flow cytometry analysis of DE differentiation [71]. We then induce pancreatic progenitor cell fate by sonic hedgehog inhibition (KAAD Cyclopamine, 0.2 $\mu$ M) for 4 days (day 4-8) and retinoic acid from days 6-8. We detected an average of  $29\% \pm 5\%$  of cells expressing the transcription factor pancreatic and duodenal homeobox1 (Pdx1) (Figure 4.1C, 2E). These results indicate the success in inducing pancreatic lineage by exogenous

growth factors as has also been previously described by other groups with hPSCs [57, 58, 69, 70, 78, 79, 206].

After the derivation of PP cells from hPSC, we then seeded the hPSC-PP cells (10 million cells in 3 steps) into the decellularized pancreas scaffold via the portal vein and cultured the repopulated pancreas in an in-house designed bioreactor (manuscript in preparation). The bioreactor allows media perfusion through the preserved vasculature and maintain viability of the repopulated organ. The repopulated pancreas was maintained under perfusion culture in the bioreactor with circulating maturation media for 9 days. The media was supplemented with Notch inhibitor (10  $\mu$ M nicotinamide with 30  $\mu$ M DAPT), a known inducer of beta cell maturation [57, 76, 208, 209]. In parallel, we also seeded hPSC-PP cells on matrigel – a commonly used substrate, as control. After culturing for 9 days, the recellularized pancreata were characterized for engraftment, proliferation and pancreatic fate of the seeded cell population. Histologic assessment revealed notable cell engraftment within the scaffold (Figure 4.1E). Human nuclei staining confirmed the engrafted cells were from human origin (i.e. hPSC-derived PP; Figure 4.1F). Cell proliferation within whole-pancreas cultures was confirmed by Ki-67 staining (Figure 4.1G). Immunostaining for endoderm transcription factor, Foxa2, revealed a small population of cells still expressing Foxa2 (Figure 4.1H). However prior studies have shown that Foxa2 expression persists to adulthood, where it is expressed throughout the islet and in acinar cells [210, 211]. Pdx1 expression could be detected in the nucleus of the engrafted cells, confirming the retention of pancreatic progenitor phenotype (Figure 4.1I). In contrast, the matrigel control showed strong Pdx1 expression only in the small portion of cells which formed mini-clusters with strong cell-cell contact (Figure 4.1L), and not in majority of the cells spread on the matrix.

The Notch signaling pathway promotes the maintenance of pancreatic progenitor properties and their expansion [212, 213]. Small molecule DAPT, a gamma-secretase inhibitor that blocks Notch signaling has been reported to be effective for differentiating human ES cells and iPS cells into insulin-producing cells [57, 76, 209]. However in our experiment with recellularized pancreas with hPSC-PP cells, treatment with DAPT did not result in further specification toward insulin positive phenotypes. A small number of Nkx6.1+ cells were detected (Figure 4.1J) but no insulin (C-peptide) expression was found by immunostaining (Figure 4.1K).

Taken together, these data indicate that the decellularized pancreas is suitable for reconstruction with hPSC derived cell types. However pancreatic differentiation also seems to be favored by the strong cell-cell contact, which is lost in the current setting where the hPSC derived cells are harvested from adherent cultures into single cell suspension by enzyme digestion. Instead, maintaining the hPSCs in aggregates, with retained cell-cell contact, can be expected to be advantageous. Several groups have developed techniques for deriving hPSC-PP in aggregate cultures [72, 75, 78, 214]. We [69] have recently demonstrated the advantage of aggregate cultures over adherent culture in enhancing pancreatic phenotype. Hence, in the next step we tested the feasibility of repopulating the decellularized scaffolds with hPSC-PP aggregates.

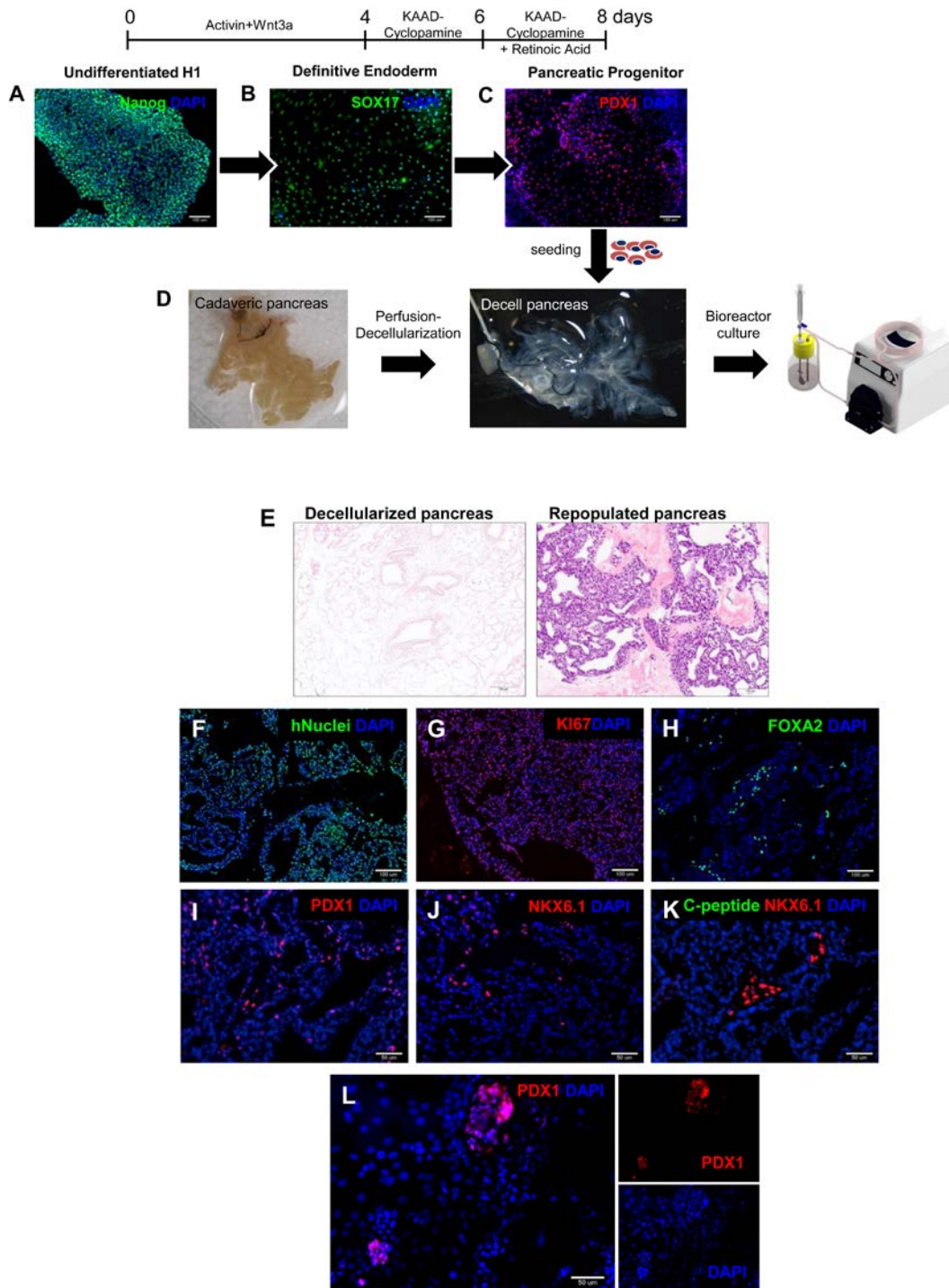


**Figure 4.1 Schematic summarizing the hPSC differentiation and decellularization-recellularization of pancreas.**

(A-C) Two-dimensional (2D) directed differentiation protocol of hPSC to pancreatic progenitor (PP) cells in vitro. (B) Immunostaining staining of definitive endoderm (DE - green) intermediates, Sox17+ cells. (C)

Immunostaining of PP, Pdx1+ cells (red). Cytokines were added at different steps indicated on top of panel. (D) Perfusion-decellularization of cadaveric pancreas and the seeding with hPSC-PP for 9 days bioreactor culture. (E) H&E staining of decellularized pancreas (left) and repopulated pancreas after 9 days bioreactor culture (right). (F) Positive human nuclei staining (hnuclei - green) demonstrates the engrafted cells are from human origin (hPSC-PP) but not from residual mouse pancreatic cells (G) Immunostaining of proliferation marker, Ki67 - green (H) endoderm transcription factor, Foxa2 endoderm marker (green), and (I) pancreatic progenitor marker, Pdx1 - red. (J) Immunostaining detection of endocrine progenitor transcription factor, Nkx6.1 (red) but (K) no detection of insulin expression, C-peptide (green). (L) Immunostaining of Pdx1 (red) was only found positive in clustering cells of matrigel control sample.

### **4.3.2 hPSC-PP aggregates as an alternate candidate to repopulate decellularized scaffolds**

We have previously developed a platform to enable efficient differentiation of hPSCs to PP, enclosed within alginate capsules [69]. Figure 4.2A outlines the procedure, where self-renewing hPSCs are encapsulated in alginate capsules and propagated for 6 days, at which time the cells form small colonies. The encapsulated colonies are further differentiated following the procedure detailed earlier (Figure 4.1A), inducing DE differentiation at Day 10 and pancreatic progenitor phenotype at Day 14. At the end of the PP stage differentiation (day 14), the size of the spherical clusters were within the range of 100–300  $\mu\text{m}$  in diameter (Figure 4.2B). The hPSC-PP aggregates could be conveniently decapsulated by 100 mM EDTA treatment. Immunostaining of the decapsulated hPSC-PP aggregates showed highly co-localized Pdx1+ and Nkx6.1+ staining (~75%, Figure 4.2C), hence indicating strong pancreatic commitment. qRT-PCR analysis revealed strong upregulation of pancreatic progenitor transcription factors Pdx1 and Nkx6.1 and downregulation of pluripotency marker Oct4; these were significantly higher than parallel differentiation under adherent cultures ( $P < 0.01$ , Figure 4.2D). Flow cytometry analysis also

confirmed higher population of differentiated cells in 3D aggregates as compared to adherent cultures, as judged by fraction of cells expressing Pdx1 ( $55.9\% \pm 7.1\%$  versus  $24.2\% \pm 4.5\%$ ,  $P < 0.01$ ; Figure 4.2E) and Nkx6.1 ( $37.8\% \pm 5.6\%$  versus  $15.0 \pm 2.4\%$ ,  $P < 0.01$ ; Figure 4.2E). Recent evidence suggests that Nkx6.1 strongly correlate with endocrine specific differentiation and  $\beta$  cell function [66, 68]. Accordingly, the reduced number of Nkx6.1+ cells obtained from our adherent cultures (Figure 4.1I-J) could be the reason behind lack of maturation of the engrafted cells in the decellularized scaffold.

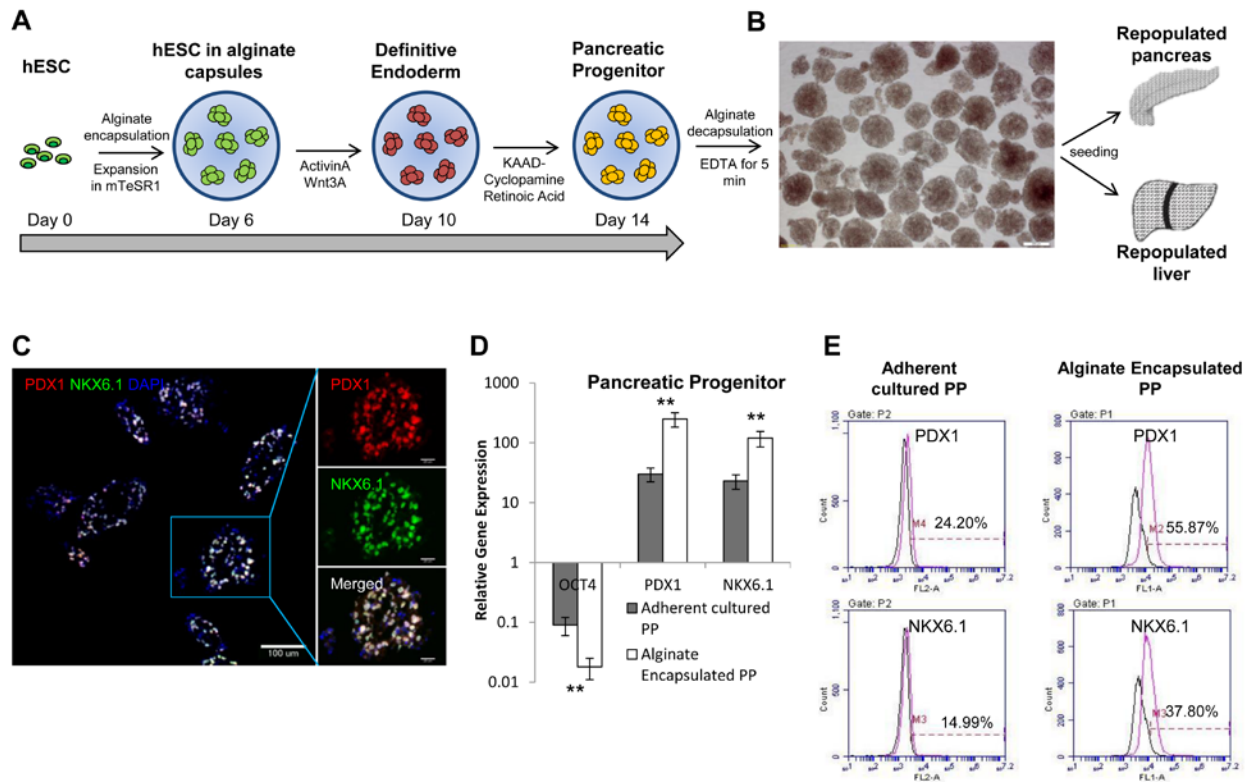


**Figure 4.2 Schematic summarizing the large scale differentiation of hESC in alginate capsules and repopulation into decellularized pancreas and liver.**

(A) Step-wise differentiation protocol in alginate capsules to derive 3-dimensional (3D) PP aggregates. (B) Bright-field image of decapsulated 3D PP aggregates after differentiation for 14 days. (C) Immunostaining of 3D PP aggregates demonstrates high co-localized staining of Pdx1 – red and Nkx6.1 – green, in the nucleus. (D) qRT-PCR analysis of 2D differentiated PP and 3D PP aggregates (data normalized to GAPDH and average fold change of gene

expression over hESC). (E) Flow cytometry analysis for the percentage of pancreatic progenitor cells, Pdx1 and Nkx6.1 between 2D differentiated PP and 3D PP aggregates. (F) Growth curve of hESC-3D PP aggregates using alginate capsules technology. Error bars indicate  $\pm$  SEM and n=3 independent experiments for qRT-PCR and flow cytometry. \*\* P<0.01.

### **4.3.3 An alternate, highly vascularized platform to allow reconstruction with cell aggregates: Decellularized liver scaffold**

Our previous analysis clearly demonstrates the enhanced efficiency of pancreatic differentiation when hPSCs are cultured and maintained as aggregates. Even from islet functionality standpoint there is evidence that both primary  $\beta$ -cells [215, 216] and pluripotent stem cells (PSC) derived  $\beta$ -cells [69, 75] secrete more insulin when maintained in 3D aggregates than in adherent monolayers. However, while 3D aggregates improve cell function it also restricts nutrient availability into aggregate core. Diffusive transport can at best support the nutrient demand for cell clusters up to 200  $\mu$ m [217], beyond which active convective transport or intra-cluster vasculature will be required for nutrient delivery. Furthermore, the inclusion of aggregates in whole organ scaffolds will introduce an additional mass transfer resistance, where the transport efficiency will be largely dependent on the vascular network of the decellularized organ. To determine a suitable scaffold for hPSC-PP aggregates, but from the vascular standpoint, we attempted to decellularize liver because of its unique liver sinusoids blood vessels, giving them a larger cross-sectional area (about 30  $\mu$ m in diameter) than capillaries [218], hence permitting efficient media perfusion and enhancing nutrient delivery. In addition, liver originates from endodermal germ layer with close anatomical proximity and association with pancreas. To this

end, we hypothesized that decellularized liver could yield an alternate compatible organ scaffold to support the repopulation of hPSC PP-aggregates.

Similar to pancreas, the decellularization of liver generated translucent acellular liver ECM scaffolds (Figure 4.3A-B). Histology and immunostaining showed no cell remnants with preservation of major ECM structure (Figure 4.3C-D). In order to quantitatively compare the preserved vascular network in pancreas and liver, we first performed corrosion casting on both the decellularized organs. The preserved vascular network and organization was quantified using ImageJ angiogenesis analyzer [204, 205] (Figure 4.3E-F). Comparing between liver and pancreas vasculature, we found that decellularized liver has a significant higher number of branching points per field ( $285 \pm 39$  versus  $101 \pm 19$ ,  $P < 0.01$ ; Figure 4.3H) and higher vessel density ( $36.5\% \pm 9.8\%$  versus  $15.4\% \pm 5.2\%$ ,  $P < 0.01$ ; Figure 4.3H) than decellularized pancreas. Hence decellularized liver has a more extensive preserved vasculature which is expected to enhance nutrient perfusion and hence more suitable for repopulation with hPSC-PP aggregates.

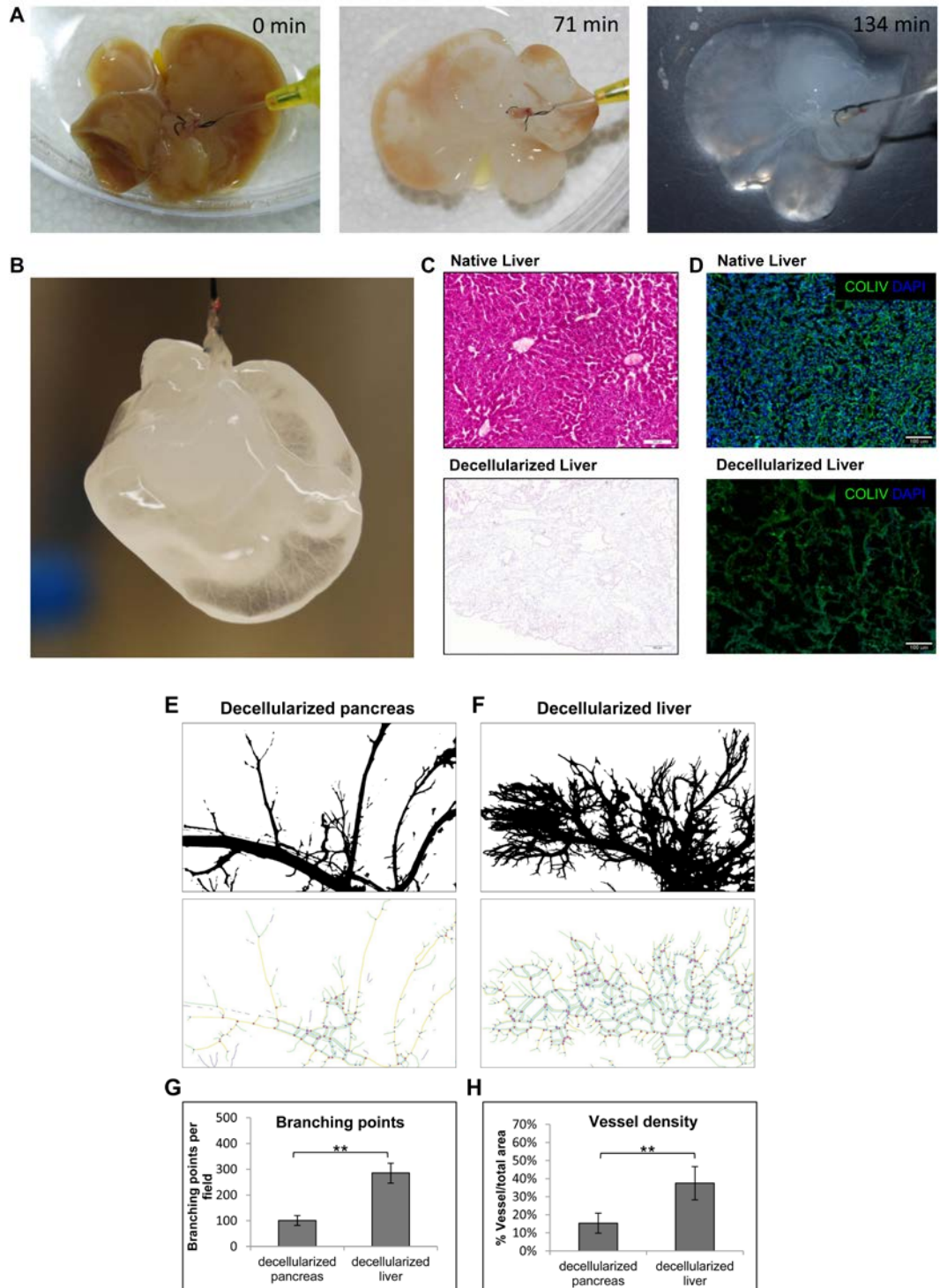


**Figure 4.3 Decellularization and characterization of mouse liver.**

(A) Panel images depict gradual change of color from perfusion-decellularization of mouse liver. (B) Resulting decellularized liver after 134 min appeared clear and translucent. (C) Histological comparison of native

and decellularized liver by H&E staining showed removal of cells. (D) Immunohistochemistry demonstrated the presence of major ECM protein (Collagen IV – green) in native liver also preserved in decellularized liver but cellular stain (DAPI) were absent. (E-F) Top panel shows threshold images from decellularized pancreas and liver used for ImageJ angiogenesis analysis, bottom panel shows the marked skeleton detected by the angiogenesis analyzer. The resulting calculation output of (G) branch points and (H) vessel density between decellularized pancreas and liver. Error bars indicate  $\pm$  SEM and n=3 independent experiments for vessel image analysis. \*\* P<0.01.

To test this hypothesis, we delivered the decapsulated hPSC-PP aggregates (using the same multi-step seeding approach) into both the portal vein of a decellularized liver and into decellularized pancreas. Both the reconstructed organs were cultured in perfusion bioreactor for 9 days with maturation medium described above. In order to track the cells within the organ scaffold, the hPSC-PP aggregates were pre-labelled with Vybrant DiD near infra-red (NIR) dye before seeding into decellularized scaffolds. The pseudocolor fluorescence images from LI-COR presented in Figure 4.4A (pancreas) and Figure 4.4B (liver) illustrates the cells' distribution throughout the repopulated liver and pancreas scaffolds. This confirms the cell delivery and retention in the decellularized liver and pancreas after the multi-step cellular infusion steps. The repopulated pancreas scaffold displayed a few saturated fluorescence spots, suggesting cellular occlusion. This will likely lead to pressure drop and subsequent under perfusion of media to the repopulated pancreas. In contrast, the cellular distribution in the repopulated liver scaffold were homogenously distributed as evidenced by uniform pseudocolor fluorescence detected throughout the liver scaffold. Quantitative comparison of the mean fluorescence intensity (MFI) of the reconstructed scaffold between the two organs revealed a significantly higher MFI in liver than in pancreas at all three seeding steps (P<0.05; Figure 4.4C), confirming higher cellular engraftment in liver. In parallel, we also directly quantified the post-seeding cellular retention within the organ by collecting the perfusate and counting the total cell loss after each seeding. As

illustrated in Figure 4.4D, the repopulated liver retained significantly more cells than the repopulated pancreas ( $78\% \pm 5\%$  versus  $59\% \pm 6\%$ ,  $P < 0.05$ ), which is consistent with the results from LI-COR imaging. In particular, after the 3<sup>rd</sup> seeding, a very high number of cells (2 - 4 million) were observed in the perfusate, perhaps due to the near saturation of the scaffold with the seeded cells. Both the reconstructed scaffolds were connected to bioreactor and cultured for 9 days. As illustrated in Figure 4.5, reconstructed liver retained a near complete cellular coverage (Figure 4.5D), and was significantly higher than repopulated pancreas (Figure 4.5A).

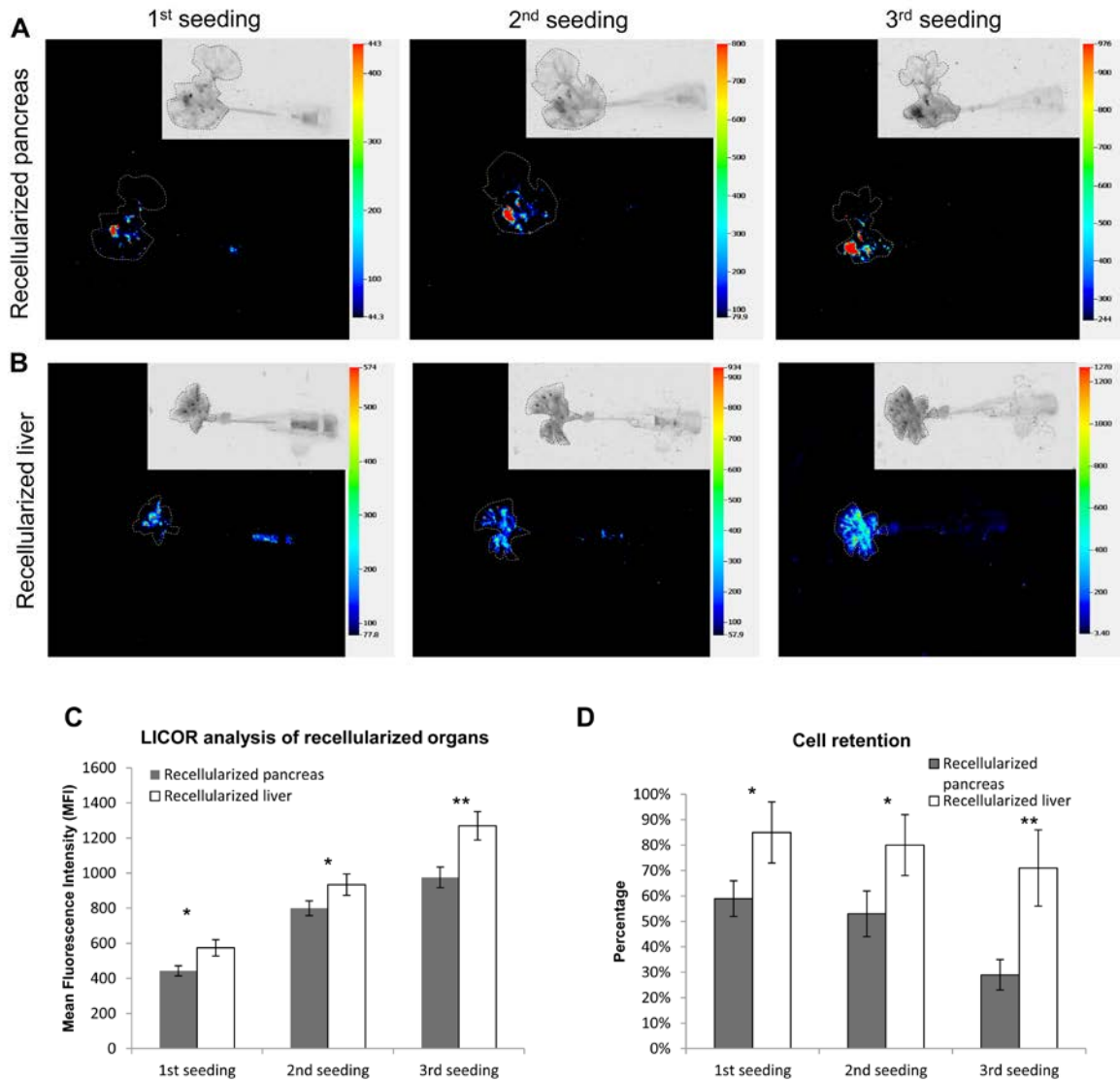


**Figure 4.4** Cell seeding and distribution comparison between repopulated pancreas and liver.

(A-B) LICOR images of repopulated pancreas and liver with labeled DiD dye demonstrate the cell engraftment and distribution within the scaffolds. (C) Relative mean fluorescence intensity (MFI) of the both repopulated organs at three seeding steps (signal was normalized to pre-seeded decellularized scaffolds). (D) Cell count of percentage cell loss after each seeding step. Error bars indicate  $\pm$  SEM and n=3 independent experiments for cell seeding analysis. \* P<0.05; \*\* P<0.01.

Histological analysis of the reconstructed pancreas revealed majority of the hPSC-PP aggregates were concentrated along the vascular channel (Figure 4.5B) and less so in the parenchyme. Also significant cell debris and apoptotic cells were apparent in the reconstructed pancreas, as confirmed by TUNEL staining (Figure 4.5C). In contrast, we obtained large cellular engraftment of approximate 1000  $\mu$ m in the repopulated liver (Figure 4.5D, E, 6B). Further, TUNEL staining was minimal in the repopulated liver (<5%, Figure 4.5F). Taken together, these data suggests that the vascular structure of the liver allows large engraftment of the hPSC-PP cell aggregates, but in repopulated pancreas hPSC-PP primarily gets localized in the vessels. Furthermore, the liver vasculature allows adequate nutrient perfusion to retain viability of the engrafted cells. Hence overall, decellularized liver was deemed to be more suitable for reconstruction with 3D hPSC-PP aggregates.

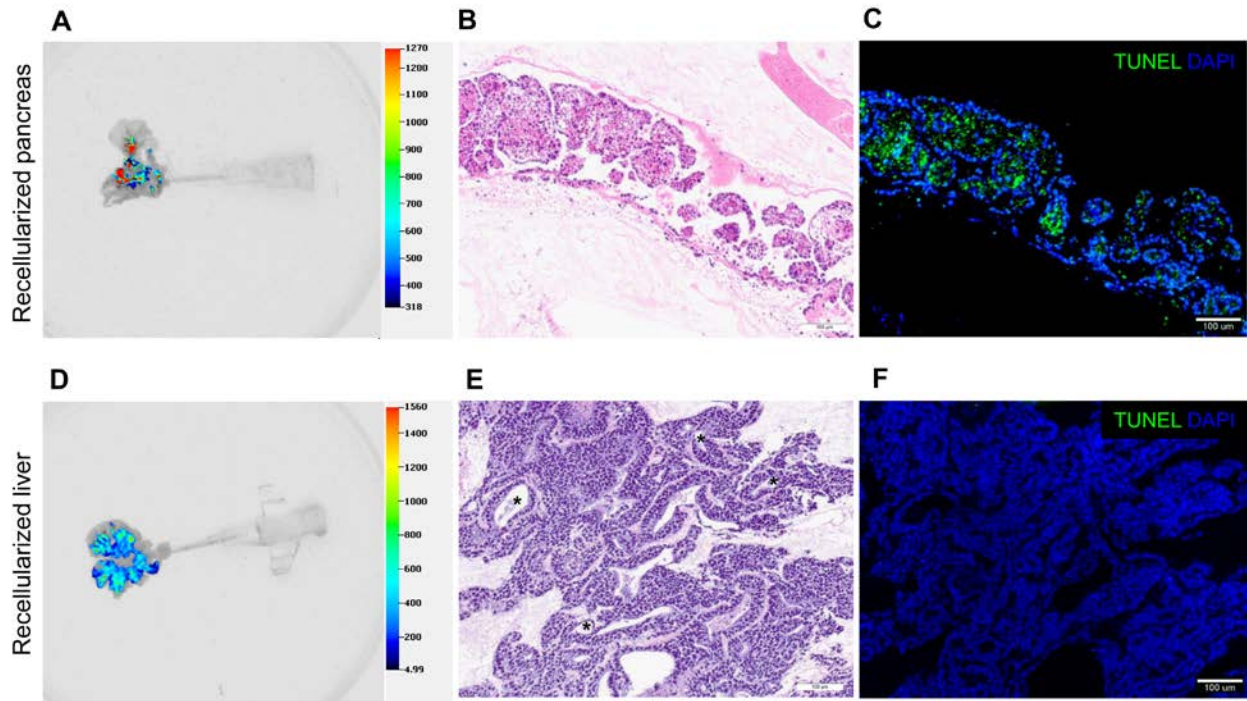


**Figure 4.5 Engraftment and viability of repopulated pancreas and liver after 9 days bioreactor culture.**

(A) LICOR image of repopulated pancreas shows cellular distribution localized only at certain regions of the scaffold. (B) H&E staining of repopulated pancreas shows cellular engraftment concentrated on the larger vessel of pancreas with high number of cellular debris (C) Corresponding section stained with TUNEL (green) detected high number of apoptotic cells. (D) LICOR image of repopulated liver shows homogenous cellular distributed throughout the scaffold. (E) H&E staining of repopulated liver shows high cellular engraftment within the scaffold, asterisk denotes presence of vessel lumen. (F) Corresponding section of TUNEL staining (green) shows engraftment cells were viable with minimal TUNEL+ cells (<5%) detected.

#### **4.3.4 Pancreas regeneration in liver scaffold**

While liver is not the native environment for endocrine pancreas, the significant engineering advantages of the liver scaffold prompted us to investigate feasibility of maintaining pancreatic phenotype and maturation of the hPSCs in a liver scaffold. This will allow us to harness these

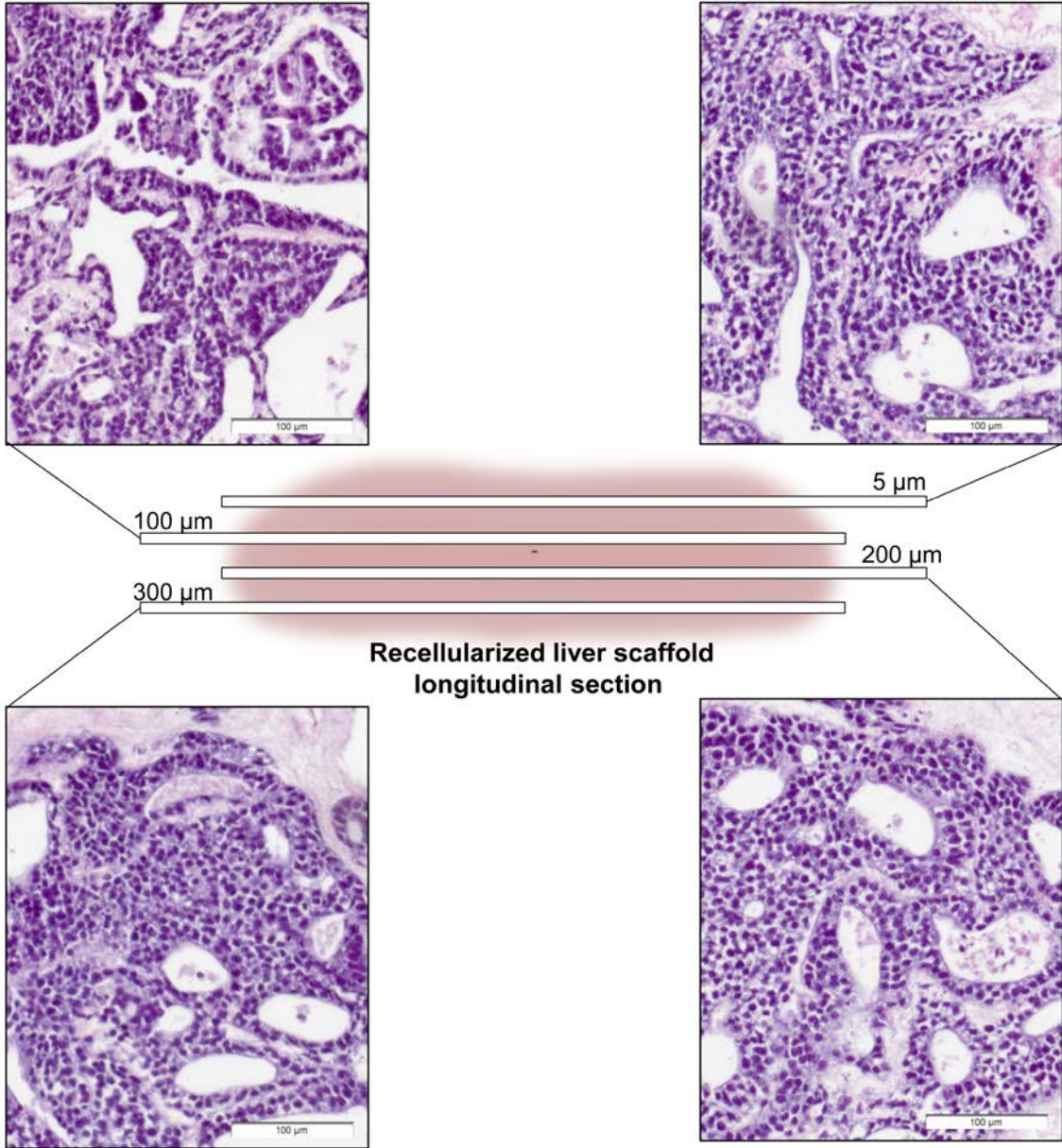
scaffolds' extensive vasculature to repopulate and grow engineered organs. With the promising success in engraftment and viability, we next evaluated the consistency of engraftment across the tissue depth. We analyzed this through H&E staining at different depths of repopulated liver after 9 days of bioreactor culture. As illustrated in Figure 4.6A, we observed significant cell engraftment in all the tested tissue depths, demonstrating that decellularized livers were thoroughly and homogeneously repopulated after seeding.

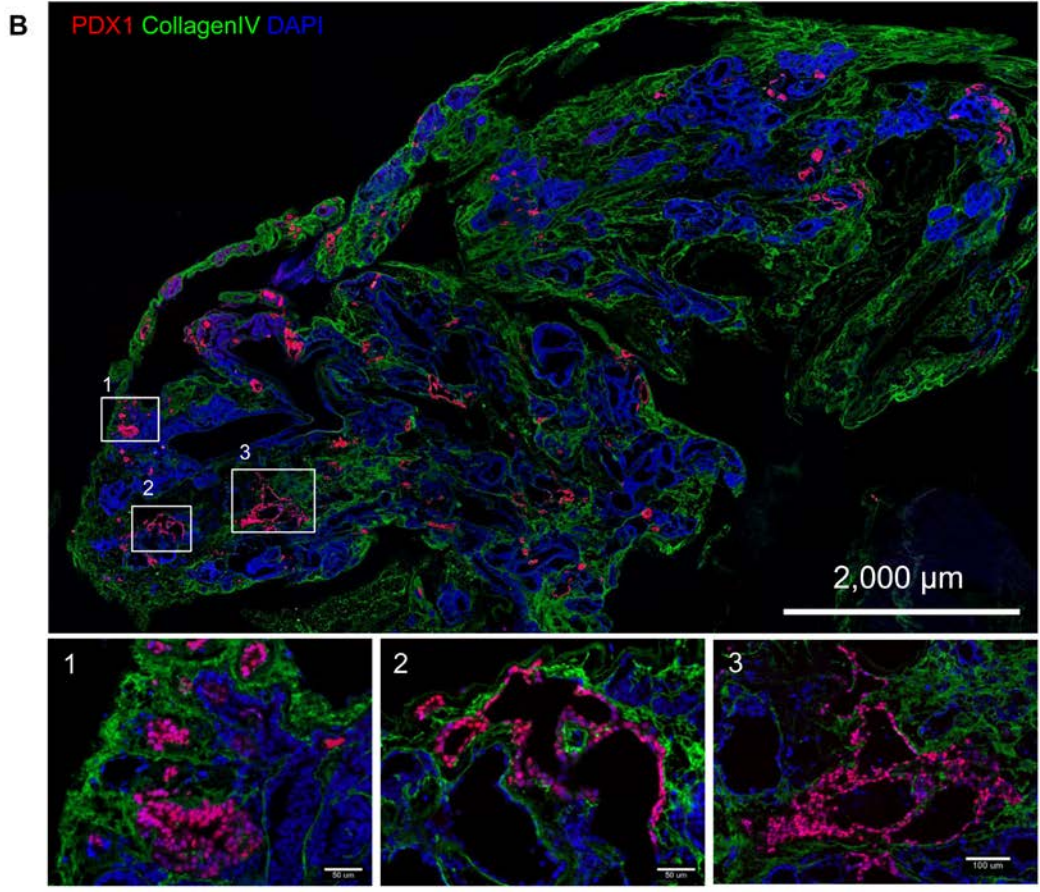
Having confirmed thorough engraftment of the hPSC-PP cells, we cultured the repopulated liver in the bioreactor, with maturation media, and analyzed for pancreatic specific markers. Quite encouragingly, a high number of Pdx1<sup>+</sup> cells were detected throughout the repopulated liver, lined by basement membrane proteins collagen IV, as illustrated in Figure 4.6B. We further confirmed that the engrafted cells were from hPSC origin by staining for human specific nuclei marker (Figure 4.6C). The repopulated liver also stained positive for proliferation marker, Ki67 (Figure 4.6D), although at a much reduced level as compared to the repopulated pancreas with hPSC-PP cells from adherent cultures (Figure 4.1G). Immunostaining for islet-cell specific markers such as Isl-1 and Nkx6.1 confirmed a larger pool of endocrine progenitor population (Fig. 4.6G-J) in the repopulated liver. In contrast, Isl-1<sup>+</sup> cells were undetectable and Nkx6.1<sup>+</sup> cells were only found in minimal numbers in repopulated pancreas with hPSC-PP cells from adherent cultures (Figure 4.1J-K). These results suggest that the decellularized liver scaffold repopulated with hPSC-PP aggregates gives rise to a more mature phenotype, with an increase in the number of endocrine lineage differentiated cells and a concurrent reduction in cell proliferation.

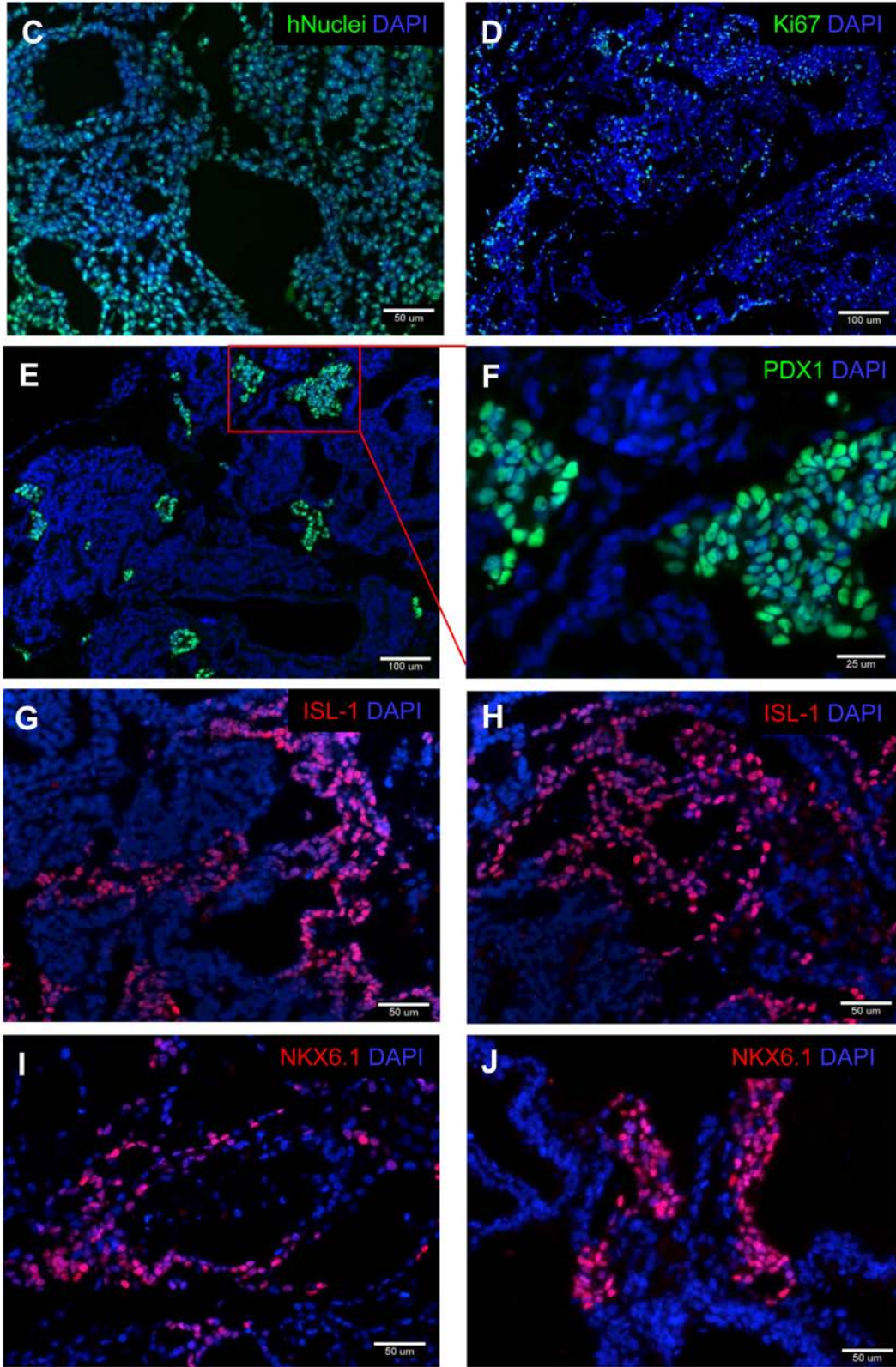
Several studies over the past decade have demonstrated that it is possible to generate pancreatic cells from hPSC; including both monohormonal insulin-expressing cells as well as

polyhormonal cells expressing insulin and glucagon [78, 79, 219]. Normally, polyhormonal cells do not express Nkx6.1 and are non-glucose responsive [6, 220]. In contrast, monohormonal insulin+ cells typically express Nkx6.1, and are glucose responsive. In our reconstructed organ scaffold, we detected a small number of C-peptide+ cells with almost all of them co-expressing Nkx6.1+ (arrowhead, Figure 4.6M). Furthermore, among the C-peptide+ cells, none were co-expressed with glucagon, indicating that they represent monohormonal endocrine cells (Figure 4.6L). In contrast, cultures on matrigel control revealed significant double positive staining of C-peptide and glucagon (Figure 4.6K) and only low numbers of Nkx6.1+ cells were detected (Supplementary Figure A.8), suggesting a predominantly polyhormonal population. qRT-PCR analysis also corroborated this finding and revealed significantly higher Nkx6.1 gene expression in the repopulated liver than matrigel (937-fold versus 1.3-fold,  $P < 0.01$ ; Figure 4.6N). Although the insulin gene expression was about the same between repopulated liver and the matrigel control, the glucagon expression was significantly higher in matrigel than the repopulated liver (7.48-fold versus 2.23-fold,  $P < 0.05$ ; Figure 4.6N). This is consistent with the immunostaining result and could be attributed to the polyhormonality observed in matrigel. Altogether, these results indicate that decellularized liver reconstructed with hPSC-PP aggregates exhibit excellent engraftment throughout the organ. The engrafted cells show high pancreatic islet specific markers (Pdx1, Isl1 and Nkx6.1) and could be further matured into monohormonal C-peptide-positive cells.

**A**







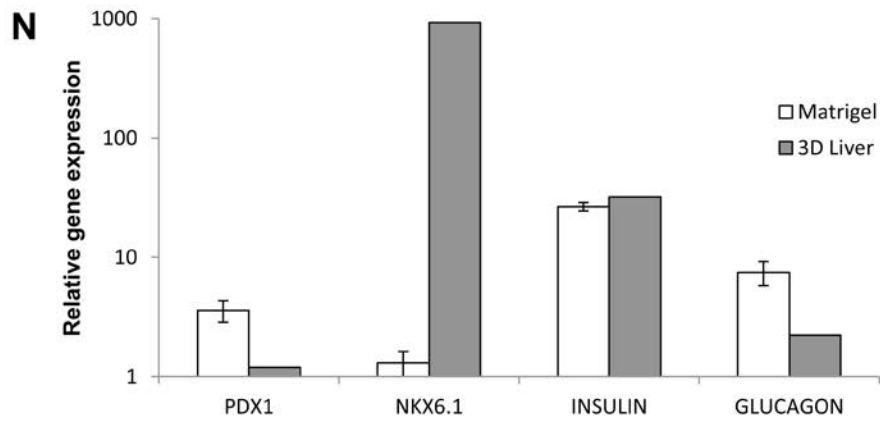
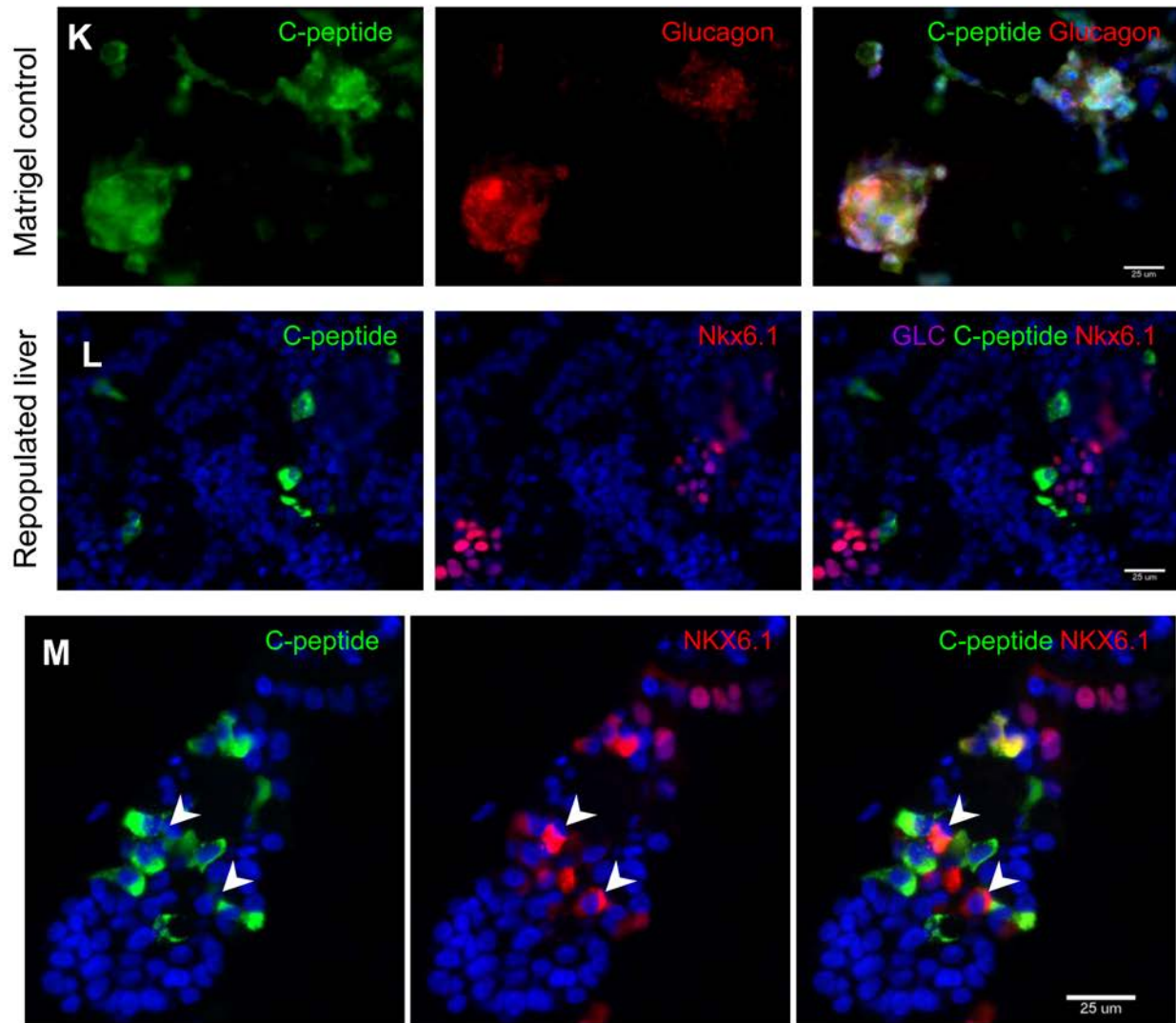


**Figure 4.6** Characterization of 3D PP aggregates repopulated liver after 9 days bioreactor culture.

(A) H&E staining of day 9 tissue sections generated from various depths shows repopulation of entire decellularized liver. (B) Immunostaining of repopulated liver section shows lined cells (DAPI-blue) throughout the thickness (500 – 1000  $\mu\text{m}$ ) of the liver matrix protein (Collagen IV – green). Inset shows high magnification of pancreatic committed, Pdx1+ (red) cells detected within the repopulated liver. (C) Positive human nuclei (hnuclei – green) confirmed engrafted cells were from human origin (i.e. 3D PP aggregates) but not from residual mouse liver cells. (D) Lower number of proliferative cells, Ki67+ (green) was detected compared to when repopulated with 2D differentiated PP cells. (E) Immunostaining of repopulated liver detected positive cells with Pdx1 transcription factor. (F) Higher magnification inset shows the nuclear localization of Pdx1. (G-H) Immunostaining of the few engrafted cells acquired more pancreatic endocrine progenitor fate showing Isl-1+ cells (red). (I-J) Immunostaining at day 9 also detected Nkx6.1+ cells. (K) Immunostaining of matrigel control shows positive for polyhormonal cells (Glucagon – red, Cpeptide – green). (L) Repopulated liver shows maturation into mono-hormonal insulin+ (Cpeptide – green) cells (without glucagon – purple) and co-expressed Nkx6.1 (red), endocrine marker. (M) Co-expression staining of C-peptide and Nkx6.1 (white arrowhead). (N) qRT-PCR analysis of 3D PP aggregates seeded into mouse liver scaffold in bioreactor and compared to matrigel culture. (data normalized to GAPDH and average fold change of gene expression over pre-seeded 3D PP aggregates). Error bars indicate  $\pm$  SEM and n=3 for matrigel experiment, n=1 for repopulated liver qRT-PCR analysis.

#### 4.4 DISCUSSION

Recent progress in repopulation of decellularized organ scaffolds with human pluripotent stem cells present a promising new avenue for the development of regenerative organs for the treatment of injured or diseased organs. Significant progress has been achieved using this approach in the organ engineering of heart [120, 135], lung [195, 196, 201, 202], liver [116, 117, 136] and kidney [140, 203]. With a similar approach, organ engineering of pancreas is likely to have tremendous impact in regenerating bio-engineered pancreas for diabetes therapy. However, this has not been achieved to date. In this chapter, we report, for the first time, the repopulation

of decellularized organs with hPSC-derived pancreatic progenitor cells. We demonstrated the feasibility of repopulating decellularized pancreas with hPSC-PP cells from adherent culture. However, given the enhanced differentiation potential and the retention of cell-cell contact of hPSC-PP in aggregates, we explored repopulation with the hPSC-PP aggregates instead. But, the additional mass transfer resistance of aggregates requires an extensive vasculature network for efficient nutrient transport, which was found to be superior in liver over pancreas scaffold. Hence, we demonstrated the feasibility of repopulating decellularized liver with hPSC-PP aggregates, which showed significantly higher cellular engraftment and viability than repopulated decellularized pancreas with hPSC-PP aggregates. Finally, with chemical complementation and bioreactor culture, these seeded PP aggregates grown within the whole liver scaffold with homogeneity and matured *in situ* into monohormonal insulin-expressing cells.

Early organ engineering studies primarily focused on repopulating decellularized organ scaffolds with primary cells or immortalized cell lines [108, 111, 136]. While these studies present a promising new avenue for organ regeneration, the lack of abundant functionally mature cells is a major limitation to the clinical application of engineered organs. Human pluripotent stem cells (i.e. ES and iPS cells) represent an attractive cell source owing to its virtually unlimited replicative capacity and the potential to differentiate into a variety of cell types. By recapitulating embryonic and fetal developmental stages using external growth factors or small molecule inhibitors, recent PSC differentiation protocol has enabled the generation of pancreatic  $\beta$  cells *in vitro* with high efficiency [78, 79]. In our previous study and current work, we demonstrated that alginate encapsulated hPSCs exhibited significantly matured pancreatic phenotypes (higher Pdx1 and Nkx6.1 expressions) than parallel adherent cultures on matrigel coated TCP. Furthermore, these differentiated hPSC-PP aggregates allow convenient harvesting

for reseeding into the scaffold, without greatly disrupting the cell environment within the aggregates. In contrast, harvesting of differentiated cells from adherent cultures results in single-cell suspension from the enzymatic digestion. This will lead to loss of critical cell-to-cell contact, which is known to activate apoptotic pathway in hPSCs. While Rho-associated protein kinase (ROCK) inhibitor (i.e. Y-27632) has been illustrated to boost cell survival in this process, it only improves the viability by ~20% [221, 222]. Because of the preserved cell-cell and cell-ECM contact within the aggregates it was hypothesized to be a superior candidate for organ reconstruction. While the large aggregate dimension (diameter varies between 100 to 350  $\mu\text{m}$ ) may present other challenges such as vessel occlusion which will lead to under perfusion and necrotic core from nutrient deprivation, our histological analysis in repopulated liver revealed that lumen of liver capillary segments remained patent surrounded by large viable engraftment of PP aggregates (Figure 4.5E).

Previous reports of successful reconstruction of decellularized organ scaffolds with PSC-derived cell types [120, 135, 195, 196, 201] have reinforced the importance of a 3D ECM setting for supporting cell adherence, organization, and maturation. Organ-specific differences in ECM composition, morphology, and structural properties may also potentiate lineage specification after recellularization and maturation within native organ's environment [164, 196, 223]. Accordingly, decellularized pancreas will be deemed best suited for pancreatic maturation of hPSCs. However pancreas is a complex organ supporting two different functions by two distinct cell population: 1) the endocrine cells, arranged mainly in groups as islets of Langerhans composed of different cells ( $\alpha$ ,  $\beta$ ,  $\delta$  and PP), and 2) the exocrine (acinar) cells. It is noteworthy that only 2% of the pancreas is made up of endocrine cells, with the rest of it predominantly exocrine cells. Hence, in pancreas scaffold it is likely that the repopulated cells will be majorly

exposed to the exocrine microenvironment of the pancreas. While there is reported evidence of feasibility to reprogram exocrine cells into endocrine lineage [81, 82], it is not obvious if the exocrine ECM will be specifically supportive of endocrine differentiation. Although extracting endocrine ECM from isolated islets will be the most relevant, however there are still technical challenges in retaining islet-specific ECM due to its low availability in pancreas. In addition, the complex inter-dispersed ECM components of islets makes it difficult for detergent extraction without compromising the native islet ECM structure [127].

In this chapter, we propose to use the decellularized liver as an alternate organ scaffold to reconstruct pancreas. Despite the organ-specific differences between liver and pancreas, both of these organs have the same development origin of endoderm germ layer. There is also some reported evidence of feasibility of trans-differentiation of mature hepatocytes into functional endocrine pancreas [84, 85]. However, the most significant advantage using liver over pancreas as a supporting scaffold stems from a bioengineering perspective. The liver possesses significantly higher vascular density which allows for thorough media perfusion, enhancing nutrient delivery to and waste removal from the 3D reconstructed organ. As a result, we observed more homogenous repopulation of the hPSC-PP aggregates with higher viability within the liver scaffold as compared to pancreas. Furthermore, the complex native liver ECM has been reported to maintain a higher open fenestrations upon cellular seeding than individual ECM components and matrigel [224]. Thus, this unique feature is likely to facilitate free movement of plasma into the parenchymal space and further enhance the nutrient transport for the seeded cell population. From a clinical perspective, liver has been used as a supportive transplantation site for pancreatic islets via portal vein infusion [225] (same delivery route as our seeding method). The relatively simpler architecture of liver with distinct inlet and outlet vasculature facilitate the

process of vessel anastomosis when connecting the reconstructed organ to host vessels during transplantation. Some other groups have also shown that alternate organ scaffolds can be supportive of cellular function from a different tissue origin. For example, Willenberg et al. seeded immortalized beta cell lines into kidney scaffold and demonstrated the feasibility of repurposing of kidney scaffolds for growth of insulin producing beta cells [226]. More recently, Sionov et al. reported long term maintenance of human islets insulin secretion (three months) when seeded on lung acellular microscaffolds [227].

Our decellularized liver reconstructed with hPSC-PP cells under perfusion bioreactor culture with appropriate chemical complementation, demonstrated further maturation into monohormonal insulin-expressing cells. In contrast, the parallel cultures on matrigel control under identical chemical induction differentiated into immature polyhormonal cells (co-expression of C-peptide<sup>+</sup> and Glucagon<sup>+</sup>). This is consistent with other studies that have reported  $\beta$ -cell colonies or organoids grown in Matrigel expressed  $\beta$ -cell markers at low or undetectable levels and were not responsive to glucose [186, 228]. Matrigel is a solubilized ECM preparation extracted from the Engelbreth-Holm-Swarm (EHS) mouse sarcoma, despite the abundance of ECM protein, however it lacks the proper ECM configuration of a native organ, which likely limits the maturation of hPSC-PP cells. Another possible explanation could be attributed to the synergistic effect of appropriate combination of complex ECM proteins in decellularized organs and chemical complementation. Decellularized organs preserve a plethora of ECM proteins and matrix associated proteoglycans that are important modulators of growth factor binding and signaling [101, 229]. When supplemented with appropriate growth factors, ECM and its associated proteins function to stabilize the ligand receptor complexes, increase the local gradients and promote ligand internalization and processing [230-232].

Despite the importance of native ECM, the decellularized organ ECM alone is likely to be limited in its ability to provide all of the necessary signals required for differentiation of ESCs without the additional chemical complementation or use of appropriate growth factors [135, 223]. In our previous study of pancreas reconstruction with hPSC derived DE cells (manuscript in preparation), we only saw minimal differentiation of DE cells toward PP cells when cultured in basal medium without any growth factor/small molecule induction. This limitation was also reported by Nakayama *et al.* where they did not observe an organ-specific effect of kidney versus lung scaffolds on ESC differentiation without chemical complementation [223].

For whole organ reconstruction, there is a need for integrating other stromal cell population to reconstitute the overall supporting microenvironment for organ regeneration. Seeding of supporting cell types such as fibroblast, endothelial and mesenchymal stem cells has shown to enhance the attachment, viability and matrix remodeling of the repopulated organs [233-235]. In the context of pancreas, our previous work has shown the importance of co-culture and the critical role of endothelial cell populations in supporting islet differentiation [70, 236, 237]. In this study, we primarily studied pancreas reconstruction with hPSC-PP aggregates, but we also attempted to co-seed PP cells with endothelial cells to examine the feasibility of multiple cell type repopulation (supplemental Figure A.9).

As discussed earlier, our choice of liver as a viable scaffold is purely from a bioengineering standpoint. With decellularized pancreas we did not observe significant viable engraftment when seeded with hPSC-PP aggregates; hence the organ specific effect of pancreas scaffold on islet maturation remains to be investigated. The multitude of complex biochemical and biophysical properties (e.g. stiffness, topology, ECM, growth factors, etc.) within a whole organ scaffold makes it challenging to identify the specific contributing factor that leads to a

certain desirable cell fate. One way to make a more level comparison between organ-specific scaffolds is to dissolve the decellularized ECM into hydrogel bioink solutions as recently reported by Skardal et al. [238]. These bioink solutions can then be integrated with a 3D bioprinting platform to provide the important biochemical cues of different tissue types and evaluate the cellular response. Similarly, organ ECM extract can be spotted onto protein microarray to examine matrix specificity effect on stem cell behavior which will be investigated in the next chapter.

#### **4.5 CONCLUSION**

Although our results represent only an initial step toward the ultimate goal of generating fully functional bio-engineered pancreas *in vitro*, these studies are the first demonstration of feasibility to regenerate endocrine pancreas with renewable source of human pancreatic progenitors in decellularized organ scaffolds, paving way for diabetes therapy, organ engineering and drug discovery applications.

## **5.0 FABRICATION OF 2D AND 3D ORGAN-SPECIFIC ECM ARRAY FOR INVESTIGATING CELL-ECM INTERACTION DURING STEM CELL DIFFERENTIATION**

### **5.1 INTRODUCTION**

Organ specific ECMs have been used for regenerative medicine and tissue engineering in humans [239-241], typically to match ‘like with like’ [154, 196] – for instance, stem cells cultured on liver ECM to create new liver tissue [136]. However, in the previous chapter, we observed the compatibility of liver ECM scaffold in supporting pancreatic differentiation of hPSC. A broader screening of organ ECM properties may elucidate variability in ECM composition and mechanism of how organ specific ECM influences cell behavior *in vitro*. Here in Chapter 5, we describe the development of miniaturized 2D and 3D ECM arrays composed of organ-specific ECM. With this tool, it permits rapid evaluation of the matrix-specificity of organ-derived ECM and its cell-ECM interaction during stem cell differentiation.

The ECM is a complex tissue-specific structure composed of collagens, proteoglycans, and glycoproteins. Multiple studies using variety of techniques (summarized in review by Rozario et al. [231]) have confirmed the effect of ECM on stem cell fate commitment. *In vitro* studies with isolated ECM proteins have shown the effects of laminin and fibronectin on definitive endoderm differentiation of mouse embryonic stem cells [242]. Furthermore, varying

combinatorial ECM proteins such as fibronectin, laminin, and collagen type IV interspersed within collagen I hydrogel have demonstrated to influence the osteogenic and endothelial differentiation of human embryonic stem cells [243]. Recognizing the need for a multi-matrix system in reconstructing the ECM microenvironment, there has been a focused effort in developing high throughput multicomponent ECM array platforms. Most of these platforms are ECM protein microarrays to facilitate the screening of stem cell fate after exposure to various ECM molecules in an adherent two-dimensional (2D) configuration [100, 244-247]. Further recognizing the benefits of reproducing the three-dimensional (3D) culture microenvironment has initiated the development of 3D hydrogels on a chip by depositing cell-laden alginate solution using microarray spotting techniques [248, 249]. More recently, multiplexed 3D cellular microarray was developed for combinatorial screening of stem cell differentiation in response to multiple ECM and growth factors [100, 248-252]. Majority of these approaches use purified ECM proteins and its combinations in an attempt to reconstruct the cell environment. While promising, there is still inadequate information on engineering the complexity of the native, tissue-specific ECM in an *in-vitro* setting. To date, attempts to generate tissue-mimetic ECM that recapitulate the function of the ECM *in vivo* have had limited success using combinatorial single purified ECM [253, 254]. On the other hand, tissue/organ-specific ECM has been shown to expose the cells to a more physiologically relevant milieu with higher fidelity to *in vivo* condition and promote tissue-specific cellular development and maturation [196, 238, 255].

Advancement in organ decellularization techniques have made it possible to extract organ/tissue specific ECM while closely preserving their native composition and microstructure [101, 254-256]. The resulting decellularized tissue/organ ECM have been shown to be promising in regulating stem cell differentiation *in-vitro* and to study the comprehensive roles of ECM in

mesenchymal stem cell phenotype commitment [254, 256, 257]. More recently in the context of pluripotent stem cell (PSC), it was observed that exposure to organ-specific decellularized ECM scaffolds can enhance organ-specific maturation of PSC in lung [196, 201, 258], heart [120, 135, 259], and kidney [140, 203]. These studies exposed the cells to a multitude of biochemical and biophysical properties contained within the decellularized tissue/organ scaffolds. In addition to the effect from ECM compositional differences, for instance when comparing hPSC seeded in decellularized lung versus kidney scaffolds [223], the cells also experience different tissue stiffness and topological structure, which both influence stem cell fate [162, 260, 261]. There is currently lack of systematic quantitative studies to unravel the contribution of each factors related to organ-specific properties. Hence, it remains a challenge to study the effects of organ-specific ECM composition that leads to a desirable cell fate.

In this chapter, we report the fabrication of an array platform to expose the organ-derived ECM to cells cultured in either adherent 2D configuration or non-adherent 3D aggregates. We demonstrated that these miniaturized arrays could function as a tool to investigate cell-ECM interaction during hPSC differentiation, while being compatible with rapid quantitative imaging using LI-COR scanner. We first derived organ-specific matrix by extracting ECM from decellularized pancreas, liver and heart using chaotropic agents. Characterization of resulting ECM extracts revealed the retention of complex and diverse ECM compositional profiles in all three organs. To elucidate the role of organ-specific ECM in influencing stem cell function, organ-specific ECM extracts were immobilized onto the array surface in 2D and 3D configurations. We demonstrated the utility of the ECM array in 2D configuration by examining the cell-ECM adherence of human PSC derived pancreatic progenitor (PP) cells. Our result showed differential adherence profiles when hPSC-PP cells were plated onto the 2D ECM array,

suggesting hPSC-PP cells were sensitive to organ-specific differences in the decellularized matrices. In the 3D ECM array with non-adherent PP aggregate culture, our platform showed excellent compatibility with enhanced maturation into insulin expressing cells in organ-derived ECMs compared to matrigel. Collectively, this platform demonstrated the use of complex native-derived ECM in an array platform to rapidly interrogate stem cell fate and function. The developed platform will pave way for rational design of engineered tissue-specific stem cell niches and support the developing field of stem cell biology, tissue engineering and regenerative medicine.

## **5.2 METHODS**

### **5.2.1 Organ decellularization and ECM extraction**

We used a perfusion decellularization protocol reported previously [50], to obtain organ-specific decellularized pancreas, liver and heart scaffolds. The decellularized organs were lyophilized in Virtis Benchtop K freeze dryer, operating at 60 mTorr for 3 days. 30-50 mg of the lyophilized tissues was pulverized (Figure 5.1Aii). This was followed by treatment with 50 µg/ml DNase (Roche) for 10 min and washing 3 times with PBS. Each decellularized tissues were incubated in 4M guanidine HCl, 8M Urea in PBS overnight with gentle shaking at 4°C. Samples were centrifuged at 13,000 g for 10 min at 4°C to remove insoluble material and the supernatants were dialyzed on floating V-series membranes (Millipore) against PBS for one hour. The final ECM extracts were filter-sterilized through PVDF syringe filter units (0.22 µm, Millipore), and then stored at 4°C until further use.

### **5.2.2 ECM characterization and SDS-PAGE**

Organ's ECMs were assessed for protein and ECM content as follows: bicinchoninic acid (BCA) assay (ThermoFisher) was used for protein quantification (n=3 for each organ) according to manufacturer's instruction. For ECM quantification, the ECM extracts (n=3 for each organ) were analyzed with the Sircol Collagen and Blyscan GAG assay kits (Biocolor Life Sciences Assays, Carrickfergus, UK) according to the manufacturer's instructions. The ECM content was normalized to the starting dry weight of each lyophilized decellularized organ.

For SDS-PAGE, ECM samples were loaded at 4ug per well. 20ul of sample was mixed with 20ul of 2X NuPAGE LDS sample buffer + 5%  $\beta$ -mercaptoethanol and heated at 98°C for 5 minutes. This resulting mixture was loaded onto a NuPAGE 3-8% Tris-Acetate Gel in 1X Tris-Acetate Running Buffer for 5 hours at 60V constant. Gel was stained using Bio-Rad Bio-Safe Coomassie stain for 4 hours, and destained overnight in distilled water. The resulting gel was imaged using The Bio-Rad ChemiDoc XRS+ system.

### **5.2.3 Nitrocellulose coating of slides and dishes**

Patterning substrates were prepared by first coating Superfrost™ Plus Microscope glass slides (Fisher) or 6-well tissue culture plates (Fisher) with nitrocellulose [262]. Static water contact angle measurements were performed to assess the hydrophobicity of the coated surface. Matrigel was used as a control ECM to pattern the surface and test protein immobilization efficiency. Matrigel was applied to nitrocellulose-coated surface in droplets of 1 $\mu$ l-3 $\mu$ l containing 100  $\mu$ g/ml concentration. After about 1 min, droplets were removed by aspiration, and the substrate surface was blocked by washing twice with 1% bovine serum albumin (BSA)/PBS (Sigma Aldrich).

Lectin peanut agglutinin (PNA) –Alexa 647 (Invitrogen, Molecular Probes) was used to detect the immobilized ECM protein and to verify the efficiency of the spotted ECM. PNA lectin stain was used at a concentration of 200  $\mu\text{g/ml}$  in PBS and followed by three PBS washes. Microspot diameters were measured using slide scanning images recorded with Metamorph 7.5.6.0 (Molecular Device) software on an Olympus IX81 inverted microscope. The fluorescence intensities (RFU) of the PNA lectin stain was quantified with LI-COR odyssey scanner using the 700nm wavelength channel.

#### **5.2.4 2D organ-specific ECM array fabrication**

Each of the organ-derived ECM extracts was diluted to 100  $\mu\text{g/ml}$ , and 1  $\mu\text{l}$  of ECM solution were spotted with a repeater pipette (Eppendorf) onto the nitrocellulose-coated glass slides or tissue culture plates. After about 1 min, droplets of ECM solutions were aspirated and blocked by washing twice with 1% BSA/PBS. Five by five microspots were generated in square arrays per well in a 6 well plate, and six by four microspots were generated in rectangular arrays on glass slides. The arrays can be stored in blocking buffer at 4°C until further use. All arrays were used within 3 months after fabrication.

#### **5.2.5 Atomic Force Microscopy (AFM) surface roughness and stiffness measurement**

Roughness measurements and AFM (MFP3D, Asylum Research) imaging of the 2-D immobilized ECM was performed in PBS at room temperature at a scan speed of 1 Hz with a resolution of  $256 \times 256$  pixels. The scan size was 10 x 10 microns. Surfaces were scanned with a

silicon nitride conical tip of  $k = 0.8 \text{ N m}^{-1}$  (Veeco, Ltd), and root mean square (RMS) surface roughness analysis was performed on 4 regions per sample [263].

For stiffness measurement of 3D ECM arrays containing organ-derived alginate microspots, silicon nitride cantilevers ( $k = 0.2 \text{ N m}^{-1}$ ) attached to silica microspheres ( $r = 3400 \text{ nm}$ ) were used. Force measurements were taken at 16 locations over a 4 x 4 grid and two microspot samples were measured per condition. The resulting force curves were analyzed within the AFM-MFP3D software using Hertzian-fit for indentation depth of <10 microns [146].

### **5.2.6 Human embryonic stem cell culture and differentiation into pancreatic progenitor cells**

The H1 hESC lines culture and differentiation into pancreatic progenitor cells were performed as previously described [71] in chapter 4.2.1.

For 3-D PP aggregates, alginate-encapsulated cells [69] were grown into small aggregates as previously described in Chapter 4.2.4 and treated using the same induction protocol to as described above. DMEM/F12 plus 0.2% BSA and B27 supplement was used for the differentiation. Cultures were performed with p55–p70 hESCs in 37°C incubator, 5% CO<sub>2</sub>, and 100% humidity.

### **5.2.7 Cell adhesion on 2D ECM arrays**

Cell adhesion assays were carried out on 2D ECM array in chamber glass slides (Nunc™ Lab-Tek™). hPSC-derived PP cells were treated with 10μm of the rock inhibitor (RI) Y-27632 for 4 hours before dissociation into single cells using TrypLE Express (Fisher). Single-cell

suspensions of hPSC derived-PP cells in serum free media (DMEM/F12 with B27) were plated into the patterned ECM microspots. For short-term attachment assays, cell suspensions were incubated for 2 hours in serum free medium and shaking the plates every 15 minutes. The arrays were then gently aspirated to remove unattached cells and fixed for cell staining and counting. For long term attachment, after first 2 hours of cell attachment and removal of unattached cells, fresh culture medium with serum was added and the cells were allowed to attach overnight.

### **5.2.8 Differentiation of PP aggregates in 3D ECM array**

For PP aggregate differentiation in 3D ECM arrays, PP aggregates were generated using the alginate differentiation platform described above. Alginate differentiated PP aggregates were treated with 10 $\mu$ m of the rock inhibitor (RI) Y-27632 for 4 hours before decapsulation with 100mM EDTA. This was followed by passing the PP aggregates through 100  $\mu$ m mesh-sized cell strainer to avoid inclusion of larger aggregates in the microspots. Approximately 8,000-12,000 PP aggregates were mixed in 1ml of alginate and ECM extract solutions to micro-spot on top of the BaCl<sub>2</sub>/PLL bottom layer using the repeater pipette. Subsequently, the cell-laden 3D ECM array was cultured in maturation medium consisting of DMEM/F12 plus 0.2% BSA and B27 supplement with nicotinamide (10  $\mu$ M, Sigma Aldrich) and 10 $\mu$ m of the rock inhibitor (RI) Y-27632 for 2 days. Fresh maturation media with notch inhibition (30  $\mu$ M DAPT, Santa Cruz) was added and cultured for another 7 days. The medium was changed daily for a total for 9-day culture period.

### **5.2.9 Cell viability assay: live/dead staining and quantification**

Cell viability on the 2D and 3D ECM array was assessed via a Live/Dead assay (Invitrogen). Briefly, calcein AM (1  $\mu$ M) and EthD-1 (2  $\mu$ M) were added together with culture medium to the cell seeded arrays and incubated for 15 minutes under light protection at room temperature. Samples were washed twice with PBS. Live cells (green) and dead cells (red) were identified by epifluorescence microscopy. Quantification of live/dead cells was accomplished by converting all individual (red and green) channels to grayscale and followed by analysis with Metamorph Image software.

### **5.2.10 On-chip immunofluorescence assay and LI-COR Odyssey scanner analysis**

2D cells or encapsulated cells in 3D ECM arrays were fixed for 15 min with 4% formaldehyde (Thermo Scientific). ImmEdge Hydrophobic Barrier Pen (Vector Laboratories) was used to confine the antibody solutions to microspot of interest. For 3D ECM array staining, we used dH<sub>2</sub>O supplemented with 10mM BaCl<sub>2</sub> to replace PBS for all the washing steps. The blocking buffer was also supplemented with 10mM BaCl<sub>2</sub> when staining on 3D ECM arrays. Following fixation, samples were permeabilized with 0.1% TritonX100 for 15 min and blocked with Odyssey Blocking buffer (LI-COR Biosciences) for 1 hour. We used the following primary antibodies: goat anti-PDX1 (1:400, R&D Systems), goat anti-NKX6.1, rabbit anti-Cpeptide (1:200, Cell signaling). Incubation time for primary antibodies was overnight in 4°C. Slides were washed three times (5–10 min) with PBS. Infrared anti-goat and anti-rabbit IRDye800CW secondary antibody (1: 800, LI-COR Biosciences) and DRAQ5 (1: 10,000, Invitrogen) in blocking were then added to the arrays and incubated for 1 hour at room temperature. This was

followed by washing with PBS for three times. The plates were imaged on an Odyssey infrared scanner using slide or plate settings with sensitivity of 5 in both the 700 and 800 nm wavelength channels. Data were acquired by using Odyssey image studio software, exported and analyzed in Excel (Microsoft). The background was assessed by staining with only secondary antibody only, and the control values were then subtracted from the specific staining. The imaging data were normalized to cell numbers by dividing by the DNA (DraQ5) fluorescence signal.

### **5.2.11 3D ECM array fabrication**

Following the protocol by Fernandes et al. [248], poly-*L*-lysine (PLL) (0.01% w/v) (Sigma Aldrich) and BaCl<sub>2</sub> (0.1M) were mixed in 1:2 volume ratio and spotted on the nitrocellulose coated surface using a repeater pipette (Eppendorf). A mixture of 1.1% (w/v) low-viscosity alginate (Sigma-Aldrich), ECM extracts and hPSC-PP cell suspension (2.5x10<sup>6</sup> cells/ml) in DMEM/F12 media was prepared and micro-spotted on top of the BaCl<sub>2</sub>/PLL bottom layer using a repeater pipette.

### **5.2.12 Immunofluorescence staining and confocal imaging of 3D cultures**

The immunofluorescence staining protocol is identical to the on-chip immunofluorescence protocol described above except for the following. For blocking buffer, 10% donkey serum (Jackson Immuno) was used. Anti-rabbit 488 and 555 Alexafluor secondary antibodies (1:500, Invitrogen) were used. The only primary antibody used here is Cpeptide (1:100, Cell signaling). Z-stacks images were acquired using a Nikon A1 laser confocal system (5 μm steps).

### **5.2.13 Array microscopy imaging and quantification**

Microscope images of each array were acquired at 4x using an Olympus IX81 microscope. Images were recorded using Metamorph 7.5.6.0 (Molecular Device) software. The arrays were imaged using phase-contrast, DAPI, GFP, Cy3 and Cy5 optics. Scan slide module from Metamorph software were utilized, and array images were montaged. For quantification purposes except for live/dead staining, the slides were acquired using Odyssey image studio software, exported and analyzed in Excel (Microsoft). Each array (on glass or tissue culture wells) was imaged using a focus height that gave the maximum signal for each wavelength channel (700nm and 800nm) at the center of the array.

### **5.2.14 Statistical analysis**

Statistical analysis was performed as previously described [50] in chapter 2.2.16.

## **5.3 RESULTS**

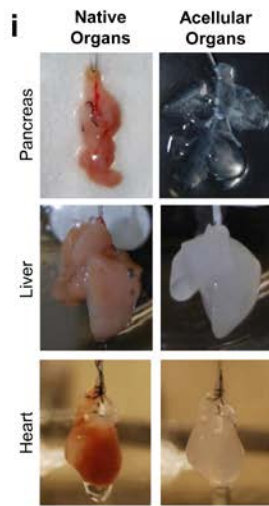
### **5.3.1 Preparation and characterization of decellularized organ ECM extracts**

Figure 5.1A illustrates the overall workflow used to create an ECM array using decellularized organ ECM extracts. The first step consists of perfusion-decellularization of whole organs to obtain organ-derived ECM scaffolds. We have previously demonstrated perfusion-decellularization of whole-organs [50] using an in-house bioreactor. With the same

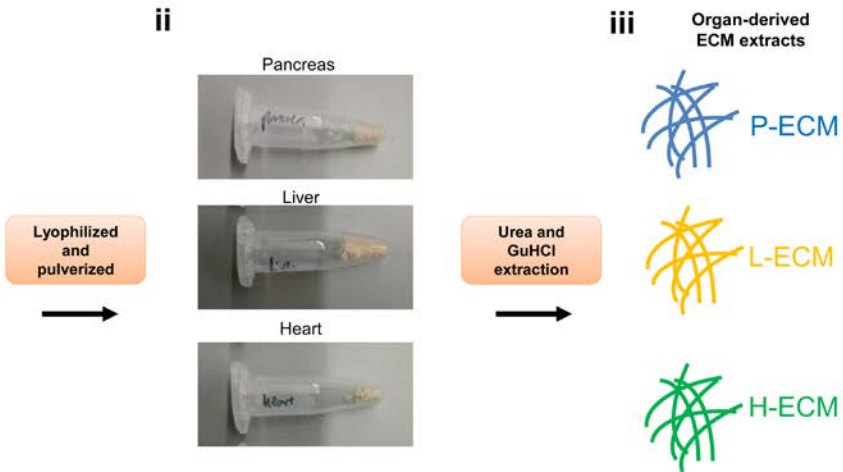
decellularization protocol, we successfully decellularized whole organ pancreas, liver and heart. Figure 5.1A(i) depicts the translucent acellular organ scaffolds generated after the complete removal of the cellular materials from the native organ. This is followed by lyophilization and pulverization steps to obtain organ-specific ECM powder (Figure 1A(ii)). We then extracted the ECM using high molar of chaotropic agents (8M Urea and GuHCl), a commonly used protocol for ECM preparation [264-266]. The resulting extracts were dialyzed against PBS to yield pancreas-, liver- and heart-organ-specific ECM extracts (denoted as P-ECM, L-ECM and H-ECM respectively). We first characterized the organ-derived ECM extracts through sodium dodecyl sulphate (SDS)-PAGE for the presence of ECM proteins or other peptides (Figure 5.1B). We loaded the same concentration of organ-derived ECM extracts (4 $\mu$ g/well) and controls (collagen I and matrigel) on each well of the gel. SDS page analysis revealed that all three organ-derived ECM extracts contained a number of high molecular weight ECM proteins (~250 KD) and low molecular weight (<100 KD) protein components that were absent in commercial bovine collagen type I and matrigel (Figure 5.1B). There were also considerable differences in terms of the bands detected among the three organ-derived ECM extracts. Next, the organ-specific ECM extracts were analyzed for protein (BCA assay) and ECM content such as collagen and glycosaminoglycans (GAGs). BCA assay revealed highest protein content in H-ECM ( $8.07 \pm 4.7$   $\mu$ g/mg dry weight), followed by L-ECM ( $6.90 \pm 3.1$   $\mu$ g/mg dry weight) and P-ECM ( $3.98 \pm 1.5$   $\mu$ g/mg dry weight) but without statistical significance among the three extracts (n=3, P>0.05; Figure 5.1C). For the ECM content, sircol collagen assay demonstrated significant higher collagen content in H-ECM ( $0.78 \pm 0.2$   $\mu$ g/mg dry weight, n=3) than L-ECM ( $0.48 \pm 0.05$   $\mu$ g/mg dry weight, P<0.05; Figure 5.1D) but not significantly higher than P-ECM ( $0.53 \pm 0.07$   $\mu$ g/mg dry weight, P>0.05). There was also no significant difference between L-ECM and P-ECM in

terms of the collagen content ( $P>0.05$ ). While L-ECM was low on collagen content, it was high for sGAG content, as quantified by Blyscan assay to be  $0.14 \pm 0.02 \mu\text{g}/\text{mg}$  dry weight,) significantly higher than H-ECM and P-ECM ( $0.08 \pm 0.01$  and  $0.03 \pm 0.001 \mu\text{g}/\text{mg}$  dry weight respectively,  $P<0.01$ ; Figure 5.1E). This observation indicated that P-, L-, and H-ECM preserved complex multi-faceted ECM proteins, suggesting better mimicry of the native organs' intricate ECM composition.

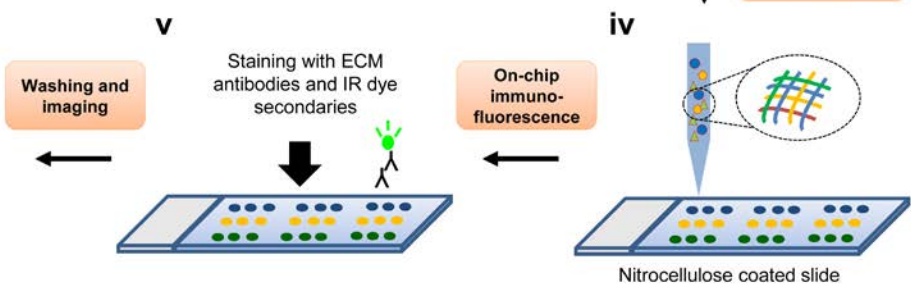
**A**



**Step 1: Fabricating organ-specific ECM**



**Step 2: Patterning and characterizing ECM array**



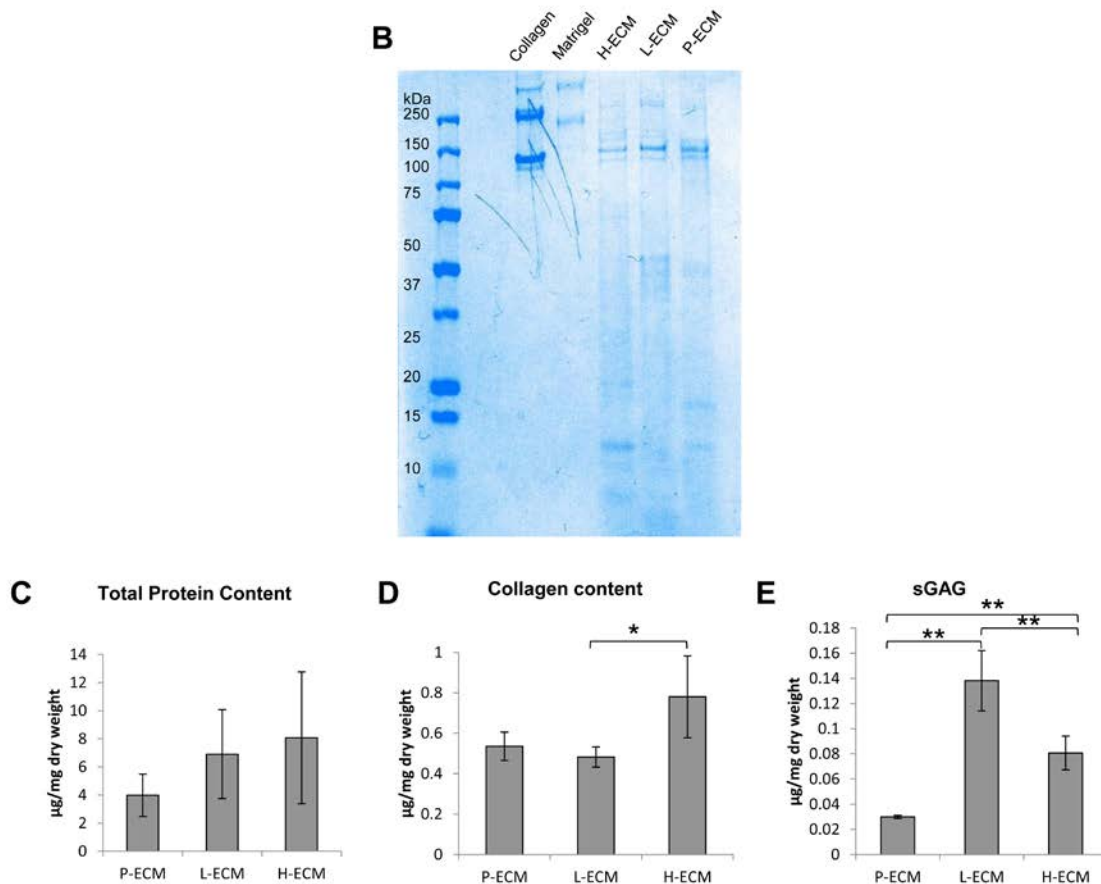


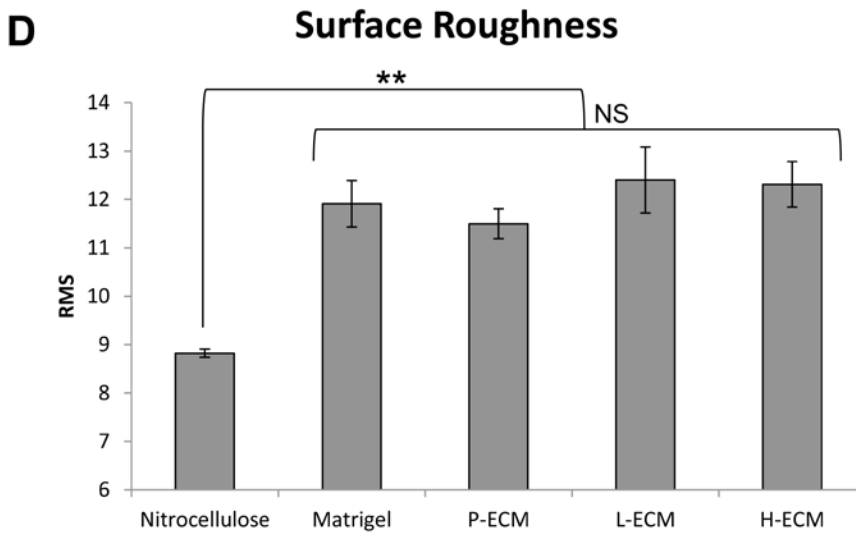
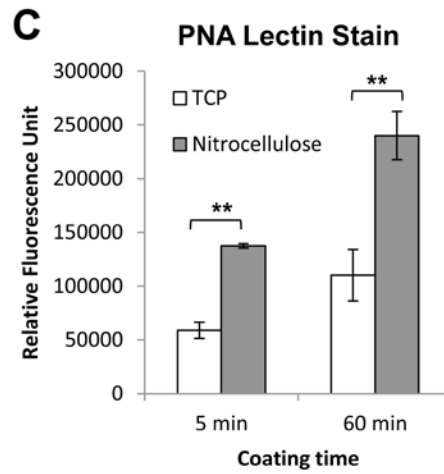
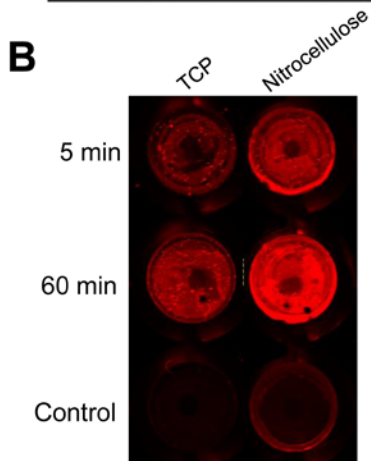
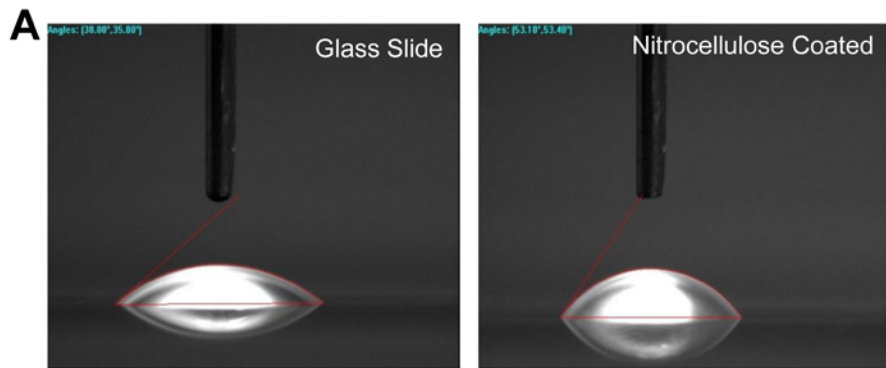
**Figure 5.1 Fabrication and characterization of ECM extracts from decellularized pancreas, liver and heart.**

(A) Schematic illustrating the experimental workflow to generate organ-specific 2D ECM array. Step 1: Whole organ-decellularization of pancreas, liver and heart and schematic illustration of the ECM extraction process to yield organ-specific ECM. Step 2: Organ-specific ECM were patterned on the nitrocellulose slide using a repeater pipette. On-chip immunofluorescence characterization of ECM proteins was performed followed by slide scanning with LI-COR imager. (B) Representative SDS-PAGE gel of P-ECM, L-ECM and H-ECM protein extracts contain abundant low molecular weight proteins (<100 KD) that are absent in collagen I and Matrigel. (C) Total protein content quantification for P-ECM, L-ECM and H-ECM by BCA assay. (D) Sircol collagen assay showed collagen content from P-ECM, L-ECM and H-ECM extracts. (E) sGAG content quantification for P-ECM, L-ECM and H-ECM by Blyscan assay. (Error bars indicate  $\pm$  SEM and  $n=3$  independent experiments, \*\*  $P<0.01$ ).

### 5.3.2 Fabrication of organ-derived ECM array

Having extracted the ECM from individual native organs, we next fabricated the patterning substrates, presenting the organ-derived ECM as individual microspots. We first coated glass slides with a thin nitrocellulose layer to immobilize the ECM proteins. Nitrocellulose coating rendered the surfaces more hydrophobic and resulted in water contact angles of  $53.3^\circ \pm 0.2^\circ$ , significantly higher than uncoated glass surface ( $36.9^\circ \pm 1.1^\circ$ ,  $n=3$ ,  $P<0.01$ ; Figure 5.2A). This method allows adequate protein adsorption while providing sufficient optical clarity for microscopy and scanning applications [245]. To verify the efficiency of protein deposition, we coated matrigel on tissue culture plastic (TCP) pre-treated with nitrocellulose and compared with non-treated TCP for 5 min and 60 min. Immunostaining by Lectin peanut agglutinin (PNA) detected significantly higher fluorescence intensity on surfaces pre-coated with nitrocellulose ( $137500 \pm 2210$  versus  $58900 \pm 3370$  for 5 min coating;  $240000 \pm 20405$  versus  $110050 \pm 28520$  for 60 min coating,  $P<0.01$ ,  $n=3$ ; Figure 5.2B-C), indicating efficient deposition of ECM-associated carbohydrate structures on nitrocellulose surface. After confirming the efficient adsorption of matrigel, we then evaluated our organ-derived ECM by microspotting them onto nitrocellulose-coated glass slide. All organ-derived ECMs (P-, L- and H-ECM) and control ECM (matrigel) were spotted at the same concentration of 100  $\mu\text{g/ml}$ . Atomic force microscopy (AFM) evaluation of microspotted organ-derived ECM extracts showed significant higher surface roughness - root mean square (RMS) than nitrocellulose only surface ( $P<0.01$ ,  $n=5$ ; Figure 5.2D, Supplemental Figure A.10), confirming their immobilization onto the nitrocellulose coated surface. Furthermore, the RMS value were about the same for all the organ-derived ECM extracts and matrigel control, indicating similar amount of proteins were immobilized. In order to reproducibly pattern protein microspots of similar amount of protein,

we used a repeater pipette that dispenses constant volumes of ECM protein solution. We used matrigel as our testing ECM solution here. Matrigel measured in 1 - 3 $\mu$ l volume were spotted with a diameter ranging from 1500  $\mu$ m – 2300  $\mu$ m to yield spatially separated ECM microspots (Figure 5.2E). Each array contains up to 24 microspots for a glass slide (Figure 5.3A) or 25 microspots for a well in 6 well plate (Figure 5.6A). To render the glass surface in between the patterns resistant to unspecific protein and cell attachment, the remaining nitrocellulose layer can be easily blocked with BSA. Slide scanning images of PNA lectin staining showed that each volume of microspot had similar diameter (<5% difference) and the diameter correlated linearly ( $R^2 = 0.95$ ) with increasing volume (Figure 2F). The same trend was observed with LI-COR quantification of near-infrared (680 nm) PNA stain – it correlated linearly with increasing volume and there was narrow variability of RFU for each volume (Figure 5.2G), confirming the reproducible spotting quality that can be achieved by the repeater pipette dispersion. Taken together, these data suggest that this spotting technique is reproducible, and the platform is efficiently pattern-able with organ-derived ECM proteins to generate an organ-specific ECM array.



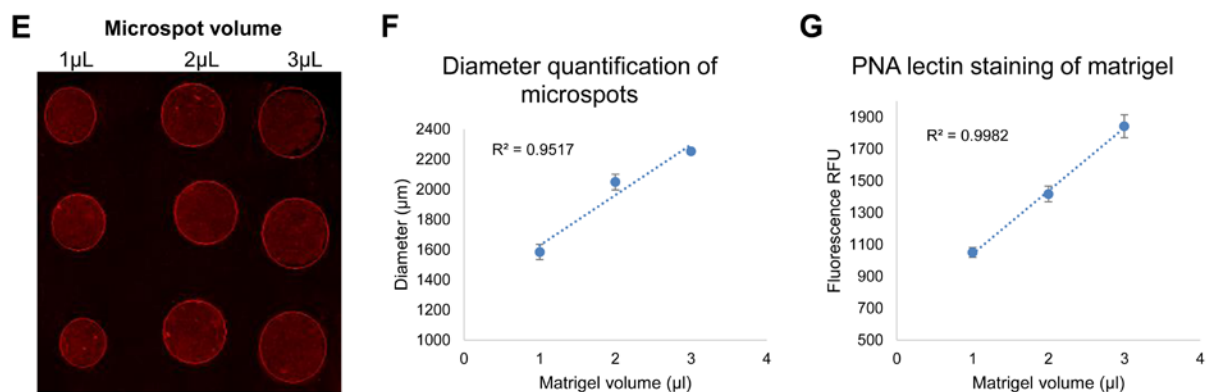


**Figure 5.2 Surface coating and immobilization of ECM proteins to generate 2D ECM array.**

(A) Water contact angles measurement showed increased hydrophobicity in nitrocellulose coated surface. (B) PNA lectin staining of adsorbed matrigel protein on tissue culture plastic (TCP) surface versus TCP surface coated with nitrocellulose after 5 and 60 min of matrigel coating time. (C) Corresponding quantification of PNA lectin fluorescence intensity showed higher amount of ECM proteins were immobilized on nitrocellulose coated surface. (D) AFM measurement of local root mean square (RMS) for surface roughness evaluation. Significant higher RMS value in microspotted organ-derived ECM than nitrocellulose only surface indicate organ-specific ECMs were immobilized onto the nitrocellulose coated surface. No significant difference was detected among different organs, indicating similar amount of proteins were immobilized. (E) PNA lectin stain visualized microspotted 2D ECM array with 1  $\mu$ l, 2  $\mu$ l and 3  $\mu$ l of matrigel (triplicates). (F) Correlation plot shows the varying size of microspot can be achieved by varying the volume of matrigel droplets. (G) Quantification of PNA lectin stain shows the fluorescence intensity as a function of increasing volume of matrigel droplets. (Error bars indicate  $\pm$  SEM and n=3 independent experiments, \*\* P<0.01).

### 5.3.3 ECM array combined with quantitative imaging permits analysis of ECM composition of organ-derived ECMs

Next, we characterized the individual matrix protein components of the organ-derived ECM spotted on the array by on-chip, immunofluorescence staining with IR-dye, and fluorescence

quantification by LI-COR Odyssey imager (Figure 5.3A). As a validation for this assay, we micro-spotted matrigel to study the sensitivity and the detection range for Laminin and Collagen IV proteins. LI-COR image analysis detected increasing fluorescence intensity for both Laminin and Collagen IV staining with increasing concentration of spotted matrigel. The protein fluorescence intensity correlated linearly ( $R^2 > 0.97$ ; Supplemental Figure A.11) with matrigel concentration for both proteins over a range of dilution factors (1:4 to 1:16). Having validated our array platform, we next used it to characterize the ECM composition in P-, L-, and H-ECM, testing for a range of ECM proteins including Collagen I, Collagen IV, Fibronectin and Laminin. These ECM molecules were chosen because they are known to be critical in determining stem cell fate [232] and are primary components in various organs, including the pancreas [15, 267]. We quantitatively determined the levels of individual ECM proteins and compared to matrigel, rat tail collagen I (positive controls) and gelatin (negative control) (Figure 5.3B-E). As expected, the on-chip immunofluorescence assay was able to detect the ECM protein profiles on both the positive ECM controls (high laminin and collagen IV for matrigel; high collagen I for rat tail collagen; Figure 5.3B-C). Negative ECM control - gelatin is a denatured form of collagen and resulted in lower collagen I fluorescence intensity (Figure 5.3B). Interestingly, despite the identical ECM preparation protocols and amount of protein being microspotted, the composition of the organ-derived ECM varied dramatically, illustrating the complex and different ECM compositional profiles among the three organs. There was no significant difference detected for Collagen I and Collagen IV ECM protein levels among the three organs ( $P > 0.05$ ,  $n=3$ ; Figure 3B-C), consistent with the previous assessment by Sircol collagen assay (Figure 5.1D). However, laminin level was detected at much higher level in H-ECM ( $363.2 \pm 15.8$ ) than P- and L-ECM ( $84.9 \pm 7.9$ ;  $153.5 \pm 22.1$  respectively,  $P < 0.05$ ,  $n=3$ ; Figure 5.3D). In addition, fibronectin level

was also detected to be significantly higher in L-ECM ( $16.9 \pm 3.4$ ) than P- and H-ECM ( $2.9 \pm 1.2$ ,  $4.2 \pm 1.2$  respectively;  $P < 0.01$ ,  $n = 3$ ; Figure 5.3E). These data indicate that the ECM array combined with immunostaining and LI-COR analysis allows sensitive quantitative evaluation of different organ-derived ECM.

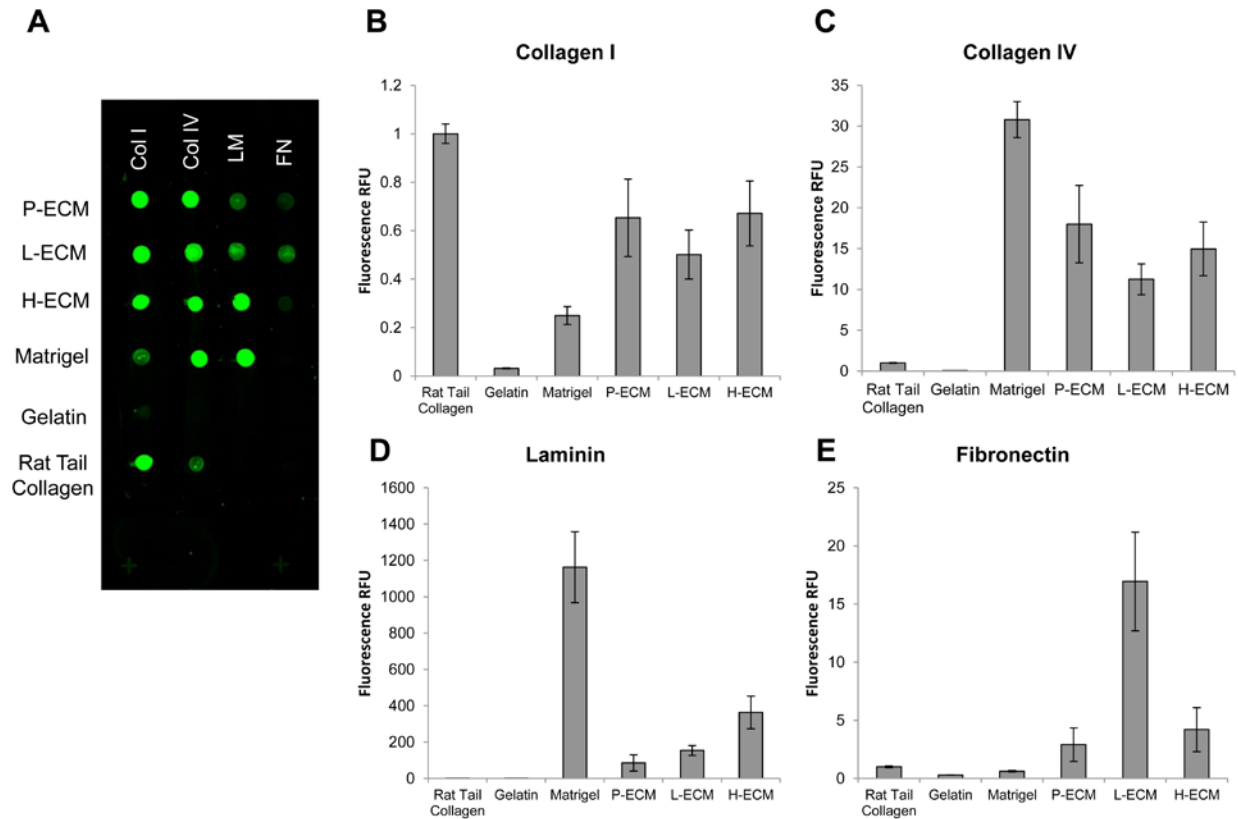


**Figure 5.3 On-chip, near IR Dye, immunofluorescence staining and LI-COR quantification.**

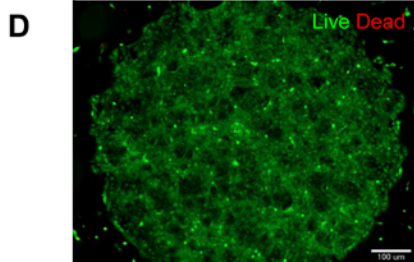
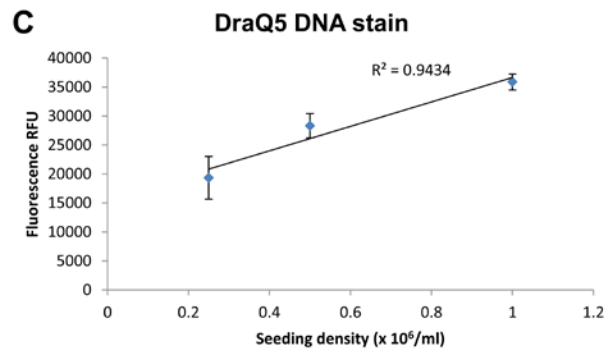
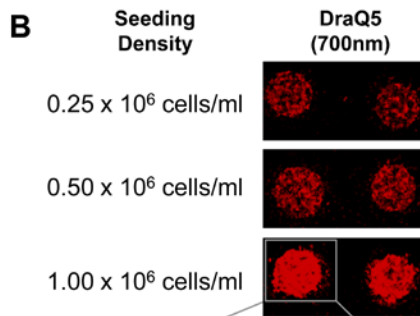
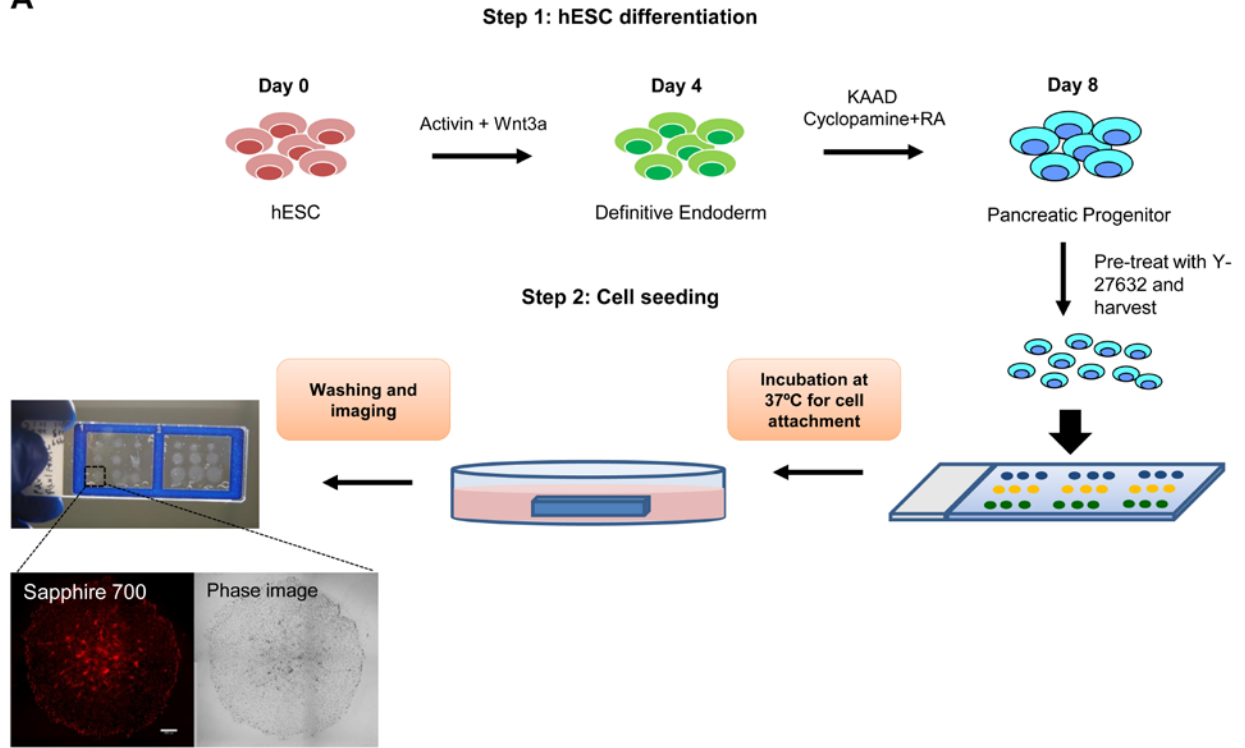
(A) Representative LI-COR image of stained 2D organ-specific ECM array. Matrigel, Gelatin and Rat tail collagen I were microspotted as controls. (B-E) Quantification of ECM proteins, Collagen I (B), Collagen IV (C), Laminin (D) and Fibronectin (E) and normalized to rat tail collagen I. Specific composition of matrigel, rat tail collagen I and gelatin (denatured collagen I) were detected consistent with reported literature composition, suggests the sensitivity and validation of the assay to semi-quantify the ECM composition of organ-derived ECMs.

### 5.3.4 Organ-derived ECM array to probe cell–ECM adhesion

Cell adhesion to the ECM is essential for a coordinated morphogenesis and growth of functional tissue [268, 269]. To measure the adhesive properties of the organ derived ECM, we used pancreatic progenitor (PP) cells derived from hPSC as described in our previous published studies [70, 71], and seeded them onto the organ-derived ECM array. As depicted in step 1 of schematic in Figure 5.4A, we first generated definitive endoderm from human embryonic stem cells (hESCs) using activin A (100 ng/ml) and wnt3a (25 ng/ml) for 4 days (day 0-4). We then induced pancreatic progenitor cell fate by sonic hedgehog inhibition (KAAD Cyclopamine, 0.2 $\mu$ M) for 4 days (day 4-8) and retinoic acid from day 6-8. With this reported protocol, we were able to efficiently generate up to 60% of PP cells [69, 71, 236] expressing the transcription factor pancreatic and duodenal homeobox1 (Pdx1), which is the master regulator giving rise to all pancreatic lineage cells [184]. The pre-differentiated PP cells were then seeded onto the arrays in serum-free media and allowed to adhere for 2 h at 37 °C (step 2 of schematic Figure 5.4A). To ensure uniform seeding, the slides were agitated every 15 min. We first tested this approach with matrigel spotted arrays. The PP cells adhered preferentially to matrigel spotted regions and did not attach to the nitrocellulose coated regions lacking ECM proteins. The cell patterning was robust over the array surface (3 x 3 ECM microspots), yielding near confluent cellular microspots as shown in Figure 5.4B. To quantify cells bound to each spot, cell nuclei were stained with DraQ5 DNA stain, a DNA-binding dye that fluoresce in the infrared spectrum and the slides were scanned and quantified with LI-COR to detect the fluorescent intensity of DraQ5. As shown in Figure 5.4C, the cell density correlated strongly with the cell seeding density of the hPSC-PP cells, which confirms both the quantification technique and compatibility of the array

with hPSC derived cell types. Live/dead images of the adhered cells demonstrated good viability 24 hours after cell seeding, indicating cytocompatibility of the ECM array (Figure 5.4D).

Using the same methodology, we next seeded the hPSC-PP cells on organ-derived ECM (P-, L- and H-ECM) spotted arrays and evaluated their adhesion (Figure 5.4E). Live/dead images after 24 hours showed most adhered cells were viable but there were considerable differences in cell adhesion between the three organ ECMs (Figure 5.4F). This was further confirmed by quantification using LI-COR analysis of DRAQ5 DNA stain. Adhesion of the hPSC-PP cells to L-ECM was the highest among the three organ-derived ECMs, while H-ECM exhibited the lowest hPSC-PP cell adhesion ( $P < 0.01$ ). Interestingly, in spite of having pancreatic tissue origin, P-ECM exhibited significantly lower adhesion of hPSC-PP cells as compared to L-ECM ( $P < 0.05$ ; Figure 5.4G). These results clearly suggest that adhesion of hPSC-PP cells was responsive to the composition differences between organ-derived ECMs.

**A**

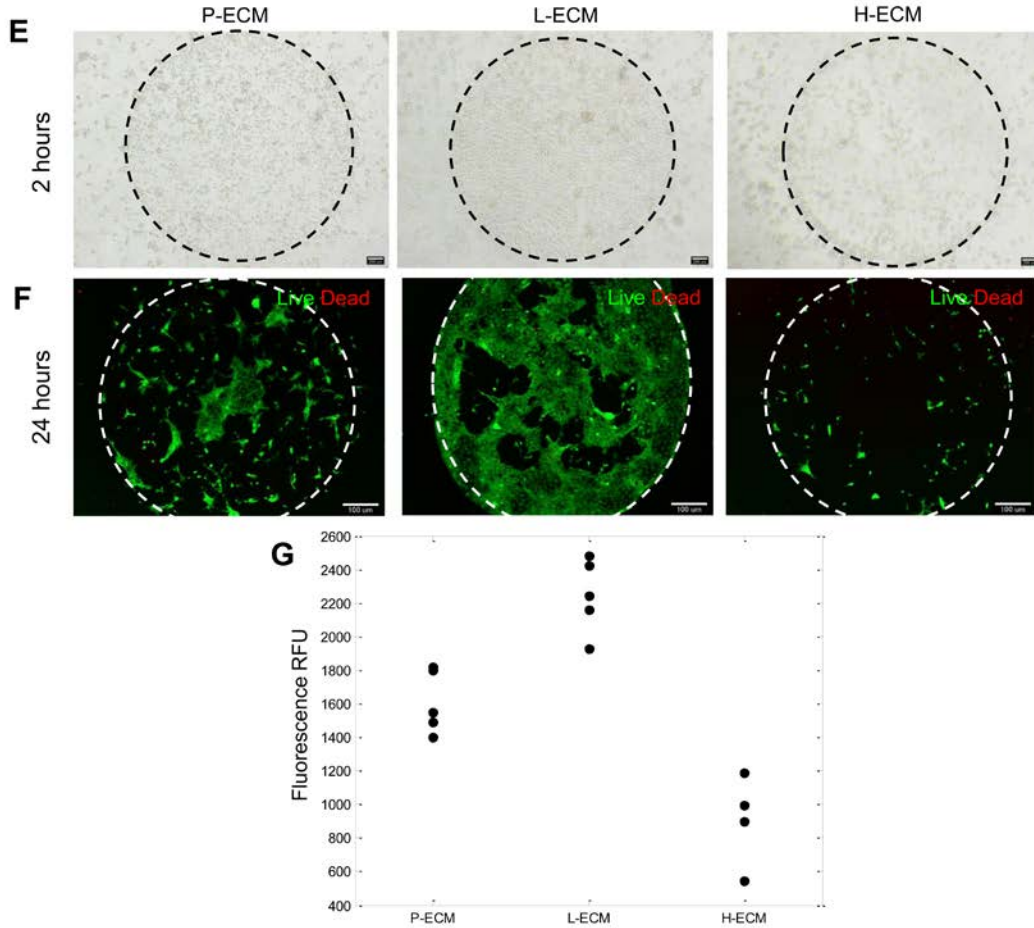


**Figure 5.4 hPSC-derived PP cells on 2D ECM array to investigate Cell-ECM adherence.**

(A) Schematic representation of cell-ECM adherence assay on fabricated organ-specific ECM array. Step 1: differentiation protocol of hPSC to pancreatic progenitor cells. Step 2: Cell seeding of harvest hPSC-PP onto ECM array. (B) Different cell seeding densities were tested to seed PP cells on matrigel microspotted surface. (C) Corresponding DNA DraqQ5 quantification showed detection of fluorescence intensity increase linearly with increased cell seeding density. We determined  $1 \times 10^6$  million cells/ml to be the optimal density as it gave rise to a uniform confluent cellular microspot under matrigel condition (positive control). (D) Live/dead staining of one of the confluent cellular microspot showed high viable cells indicating the cytocompatibility of the platform. (E) Phase-contrast images of short term cell seeding (5 min) on different organ-derived ECM on the 2D ECM array. Each organ ECM showed different cell adherence profiles. (F) Live/dead staining of washed 2D ECM array after long term cell seeding (24 hours). Similar adherence profile was observed with the short term cell seeding. (G)

Quantification of DraQ5 stained 2D ECM array after cell seeding. L-ECM showed the highest PP cells adherence, followed by P-ECM and H-ECM. (n = 4-5, \* P<0.05)

### **5.3.5 Fabrication and characterization of 3D organ-derived ECM array**

While the ECM array is a useful tool to interrogate cell-ECM interaction under adherent culture, the increasing appreciation of the importance of three-dimensional (3D) spatial organization of cells has prompted the development of 3D cellular arrays [248, 249, 251, 252, 270] which better mimics the complexity of the native microenvironment. In addition, many ECM proteins don't have an adhesive role but are still critical for stem cell growth, survival, differentiation and morphogenesis [231, 232, 271]. Hence, it is important to develop a 3D system to globally present the ECM proteins while supporting 3D culture of hPSCs. Alginate is a suitable hydrogel matrix which adequately supports hPSC growth and differentiation while being inert to cell adhesion [69, 272]. Further, alginate hydrogels have been previously developed into a 3D cell on-a-chip array for mouse embryonic stem cell [248] and human neural stem cell [249] differentiation. Here, we modified the technique to incorporate our organ-derived ECM into alginate, while encapsulating pre-differentiated hPSC cells. Instead of using poly (styrene-*co*-maleic anhydride) (PS-MA)-treated surface, we used nitrocellulose coated surface, which has been shown to have a higher protein binding capacity than PSMA-treated surface (80-100  $\mu\text{g}/\text{cm}^2$  [273] versus 68.2  $\mu\text{g}/\text{cm}^2$  [274, 275]). After pretreating the glass slides with nitrocellulose, mixture of poly-L-lysine (PLL) and  $\text{BaCl}_2$  were microspotted onto predetermined positions using the same repeater pipette microspotting technique as described above. Alginate was pre-mixed with specific organ-derived ECM. hPSC-PP cells were harvested and suspended within the alginate-ECM matrix material before micro-spotting onto the predetermined positions on nitrocellulose-coated glass

slides. 3D cell-laden gel were formed by the deposition of the pre-mixed alginate and ECM solution containing hPSC-PP cells on top of the PLL/BaCl<sub>2</sub> bottom layer as shown in schematic Figure 5.5A. Under these conditions, the positively charged PLL serves as a substrate to bind Ba<sup>2+</sup> ions and assist the attachment of the negatively charged alginate. The divalent Ba<sup>2+</sup> ions bind preferentially to the G-blocks in the alginate and cause instantaneous gelation of the alginate chains to give rise to 3D cell-laden microspots (1µl) with a height and diameter of 250 µm and 1600 µm respectively (Figure 5.6B).

With the platform now being 3D, we wanted to test the sensitivity of LI-COR imaging platform in detecting the protein expression throughout the thickness of the 3D gel microspots with the same on-chip, immunofluorescence staining method. Previous studies have shown that LI-COR was able to detect near infrared and infrared fluorescence signals of up to 2 mm thickness [276, 277], which is within the thickness range of our 3D gel microspots (250 µm). In addition, we wanted to ensure that the ECM proteins were stably incorporated into the 3D gel microspots throughout the culture period (up to 10 days). To validate this, we microspotted premixed matrigel and alginate (cell free) at various concentration (0 µg/ml – 200 µg/ml) onto the PLL/BaCl<sub>2</sub> pre-spotted array and maintained it in maturation media for 10 days at 37 °C culture incubator. The range of matrigel concentration on the 3D gel array were stained with PNA lectin and quantified by LI-COR Odyssey imager at day 0 and day 10 (Figure 5.5B). We observed good linearity among the range of matrigel evaluated (Day 0, R<sup>2</sup> = 0.94; Day 10, R<sup>2</sup> = 0.98; Figure 5.5C), indicating sensitivity of the immunostaining and LI-COR imaging under 3D configuration. Furthermore, majority of the matrigel was retained within the alginate throughout the 10 day culture period with less than 20% loss of ECM protein at higher matrigel concentration (i.e. 100 µg/ml and 200 µg/ml; Figure 5.5D). Specific ECM antibody staining also

detected similar protein levels (Supplemental Figure A.12) compared to the quantitative evaluation by 2D ECM array as described above (Figure 5.3), indicating retained ECM after inclusion into alginate gel array, as would be expected.

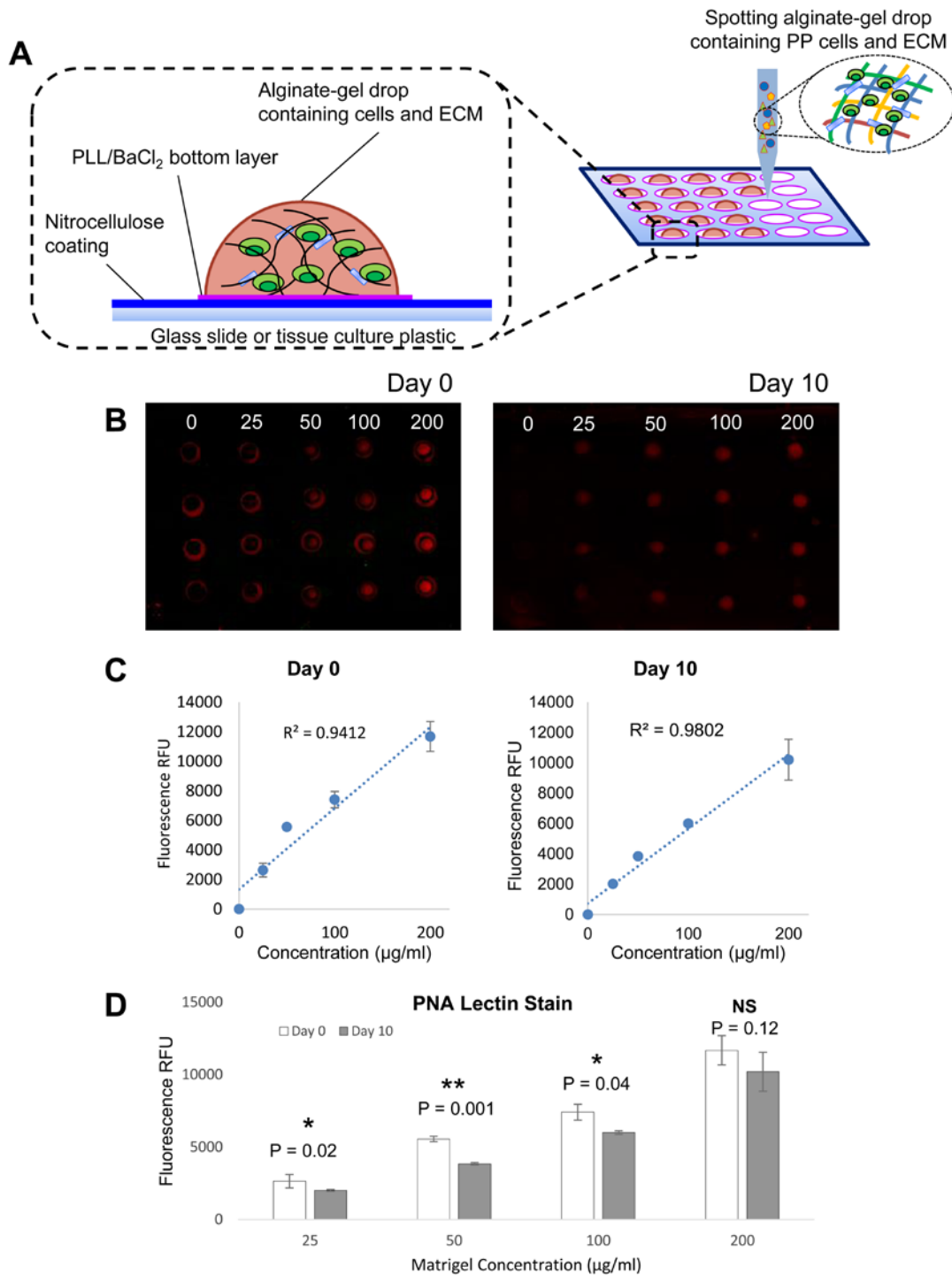


**Figure 5.5 Fabrication and characterization of 3D organ-specific ECM array.**

(A) Schematic representation of alginate microspots with cells and ECM extracts on nitrocellulose glass slide pre-spotted with PLL/BaCl<sub>2</sub>. (B) PNA lectin staining on matrigel alginate microspots (without cells) on 3D ECM array on day 0 and day 10 on a range of matrigel quantification (0-200 µg/ml) (C) Corresponding correlation

plot of PNA lectin fluorescence signals at day 0 and day 10 showed good correlation of fluorescence intensity (RFU) over the range of matrigel concentration evaluated, indicating the good linearity and sensitivity of the assay. (D) Comparison of PNA lectin stain fluorescence signal at day 0 and day 10 over a range of different incorporated matrigel concentration. The incorporated matrigel after 10 days in culture showed less than 20% decrease in fluorescence signals, indicating released or degraded ECM components was nominal. At higher concentration of matrigel (100-200  $\mu\text{g/ml}$ ), the difference between day 0 and day 10 was smaller and insignificant ( $P>0.05$ ). (Error bars indicate  $\pm$  SEM and  $n=3$  independent experiments, \*  $P<0.05$ ).

### **5.3.6 Differentiation of hPSC-PP is responsive to organ-specific ECM, as detected in the 3D array**

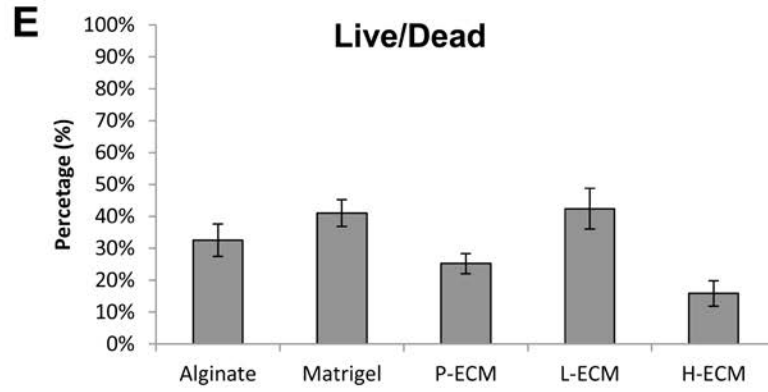
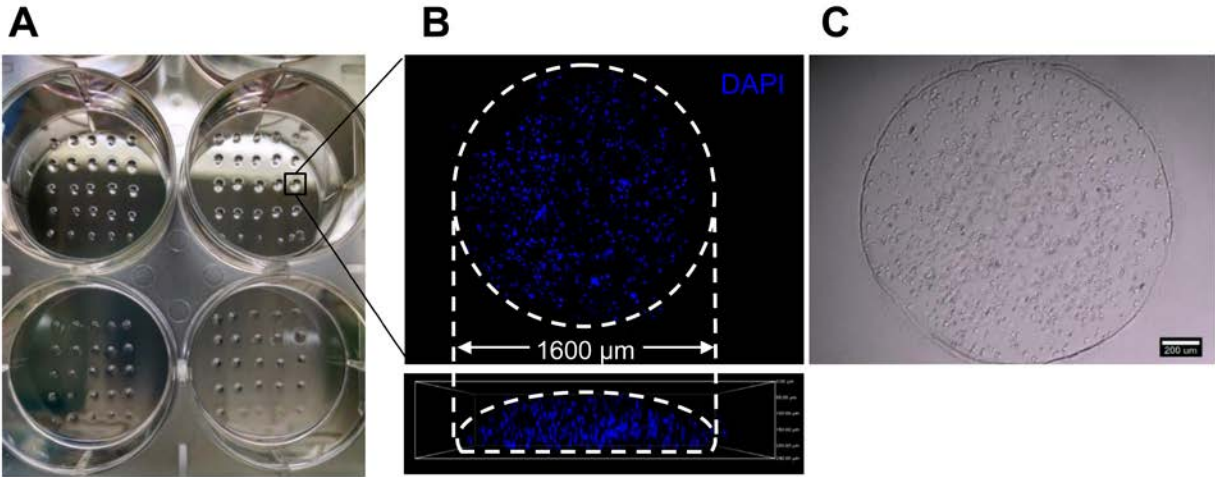
Next, we used this miniaturized 3D alginate-ECM array to study the differentiation of encapsulated hPSC-PP cells. The pre-differentiated hPSC-PP cells were harvested with enzymatic digestion to yield single cell suspension (cell density of  $2.5 \times 10^6$  cells/ml) and mix with specific organ ECM-alginate solutions. Arrays of 25 alginate microspots (Figure 5.6A) ( $n=5$  for each ECM condition) were prepared and cultured in maturation media with notch inhibition, a known inducer of beta cell phenotype [57, 69, 71] for 9 days. During this period, the cells remained confined within the microspots, with no spot breakage (Figure 5.6C) and no visible gel detachment from the slide, indicating the microspots were structurally stable. Confocal microscopy images also indicated that the encapsulated cells were evenly distributed inside the alginate-ECM microspots (Figure 5.6B). However, live/dead staining showed significant cell death (up to 80%) in the 3D cell-laden alginate-ECM microspots (Figure 5.6D-E). This is most likely due to cell-cell contact inhibition while harvesting the hPSCs, which is known to activate the apoptotic pathway in hPSCs [222]. While we added Rho-associated protein kinase (ROCK)

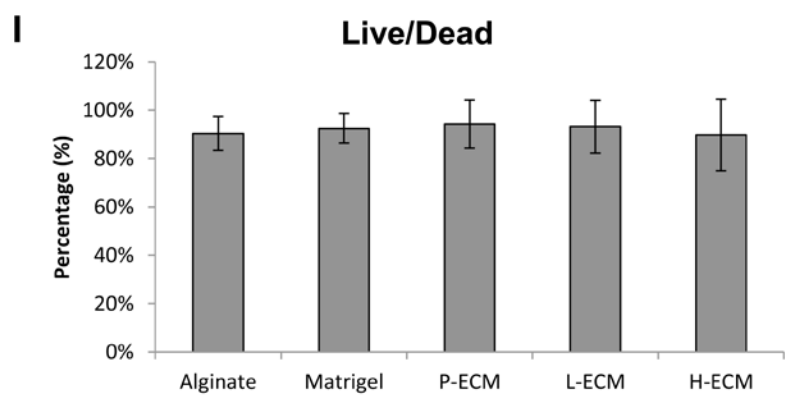
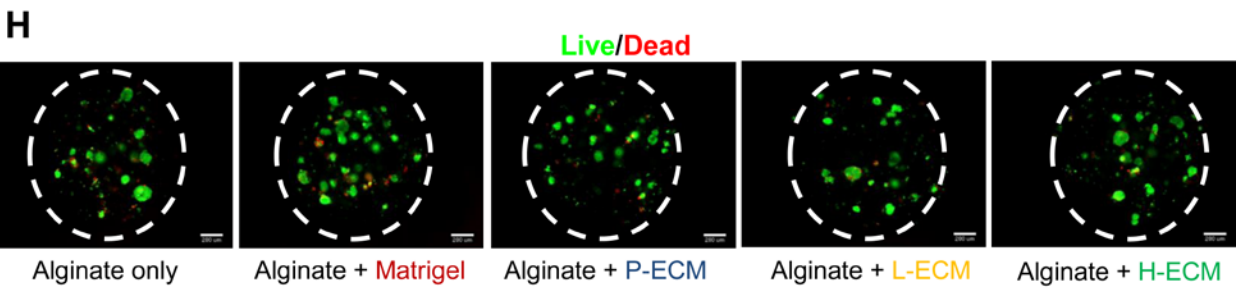
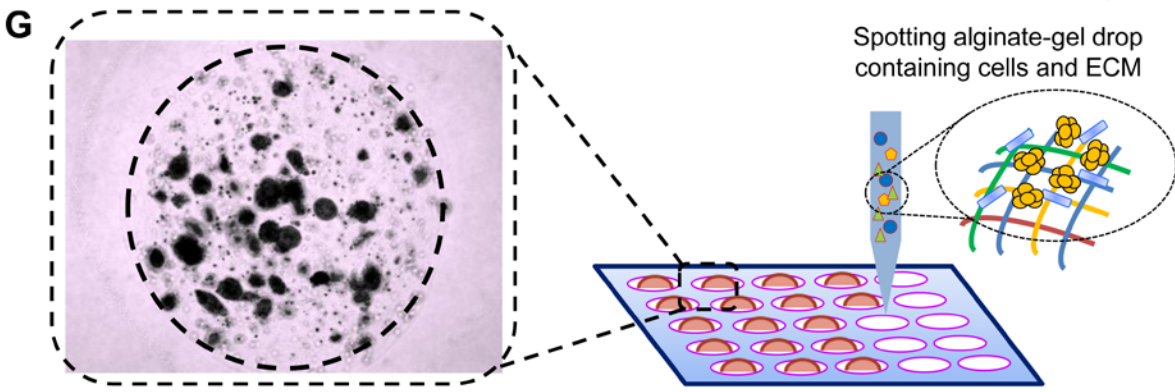
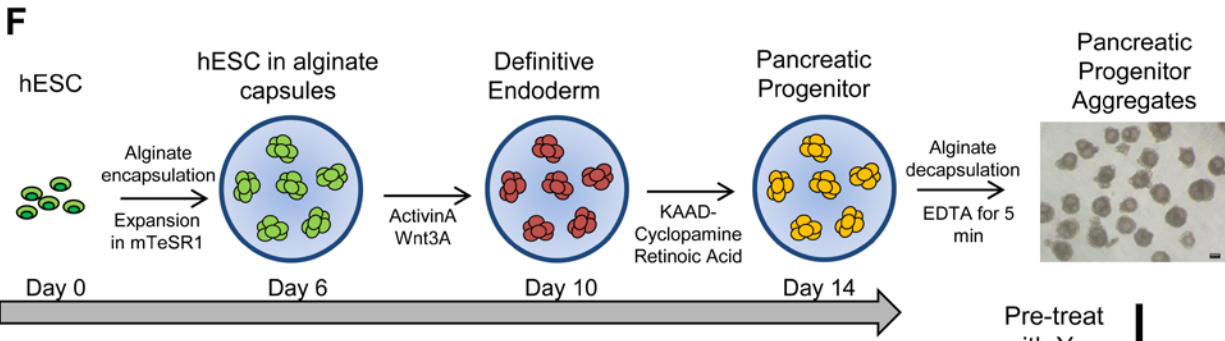
inhibitor (i.e. Y-27632), which has been illustrated to boost cell survival in this process [221, 222], we still observed significant cell death.

In order to retain high viability of hPSC-PP cells in our 3D ECM array platform, we chose to encapsulate cell clusters instead of single cell hPSC-PPs. We hypothesize that the preserved cell-cell contact in the clusters will not activate apoptotic pathway and hence will retain high viability. In our previous study we have reported the excellent potential of alginate capsules as a platform for pancreatic differentiation of stem cells[69]. The encapsulated single cells form small colonies within the alginate capsule that subsequently differentiate into pancreatic progenitor cells upon induction. These hPSC-PP aggregates can be easily harvested by mild treatment of EDTA to dissolve away the alginate capsules. Schematic in Figure 5.6F illustrates the differentiation protocol to generate 3D hPSC-PP aggregates and encapsulate into the 3D ECM gel array (Figure 5.6G). To ensure relatively homogenous-sized aggregates were encapsulated, we passed the hPSC-PP aggregates through a cell strainer (100  $\mu\text{m}$  mesh size) to avoid inclusion of cell clusters larger than the microspot gel size. This will avoid cellular overgrowth and protrusion out of the alginate microspots as shown in our Supplemental Figure A.13. After culturing for 9 days in different organ ECM gel array, live/dead staining of encapsulated hPSC-PP aggregates showed excellent viability ( $>90\%$ , Figure 5.6H-I) much higher than what was experienced with the encapsulated single cell hPSC-PPs. In comparing across different organ-derived ECM, no significant difference was observed in the viability of PP aggregates ( $P>0.05$ , Figure 5.6I).

Having achieved high viability, we next investigated the differentiation outcome of hPSC-PP aggregates exposed to different organ-derived ECM in the 3D alginate microspots. We cultured the encapsulated hPSC-PP aggregates in different organ-derived ECM alginate

microspots (n=5 for each organ) for 9 days in the presence of notch inhibition (DAPT). Parallel cultures on alginate with and without matrigel were used as controls. Immunostaining and LICOR imaging was performed to assess pancreatic maturation using pancreatic and islet-specific transcription factors such as Pdx1, Nkx6.1, and insulin protein marker, C-peptide. The result showed that higher PDX1 expression was detected in all the alginate-ECM microspots compared to alginate only controls (Figure 5.6J-K). NKX6.1 did not show any differences between P-ECM, H-ECM, matrigel and the alginate only control. However, L-ECM elicited a substantial increase of all PP markers, including C-peptide protein expression (Figure 5.6K). Interestingly, P-ECM only showed a modest increase in C-peptide level but did not show significant increase of PP markers or C-peptide when compared to H-ECM or controls ( $P > 0.05$ , Figure 5.6K). Confocal sectioning also corroborated this finding and detected higher expression of C-peptide staining in L-ECM alginate microspots (Figure 5.6L). To ensure that this observation was attributed to the ECM-specific differences and not any physical parameters of the gel, like stiffness, we performed AFM stiffness measurement of the alginate microspots after incorporation of ECM proteins. Our result revealed no stiffness differences between the alginate microspots alone and alginate microspots incorporated with ECM proteins (Supplemental Figure A.14). Collectively, these data suggest that the hPSC-PP aggregates were responsive to organ-derived ECM differences and further matured into insulin-expressing cells, with highest differentiation phenotype observed in L-ECM matrix. Furthermore, such stem cell differentiation phenomena can be studied in a miniaturized 3D alginate-ECM array.





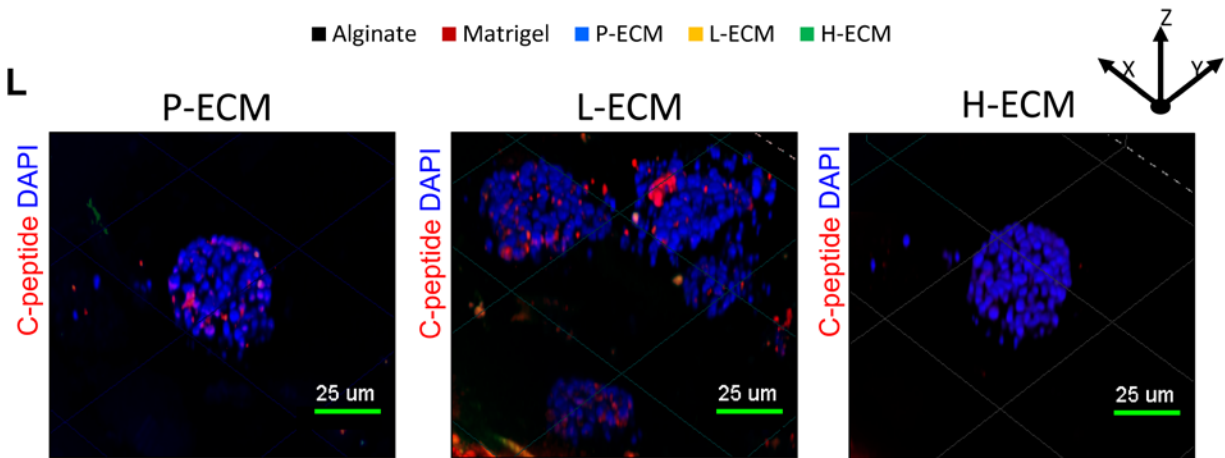
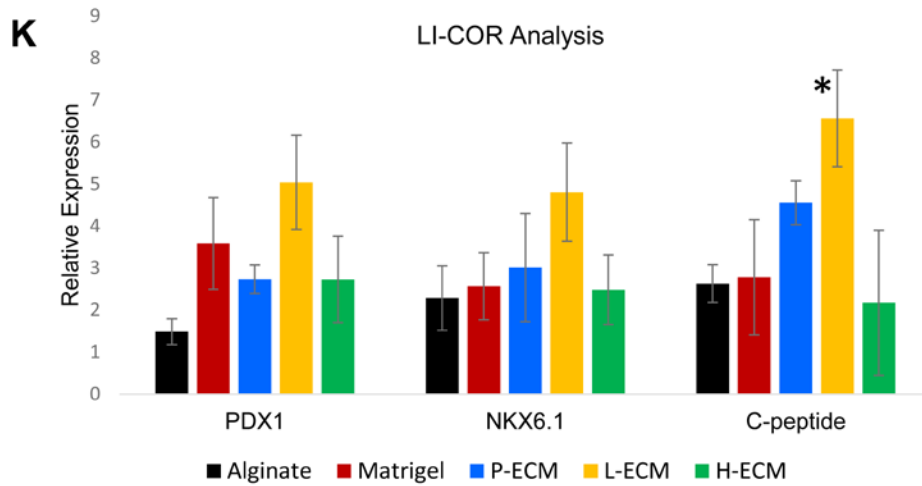
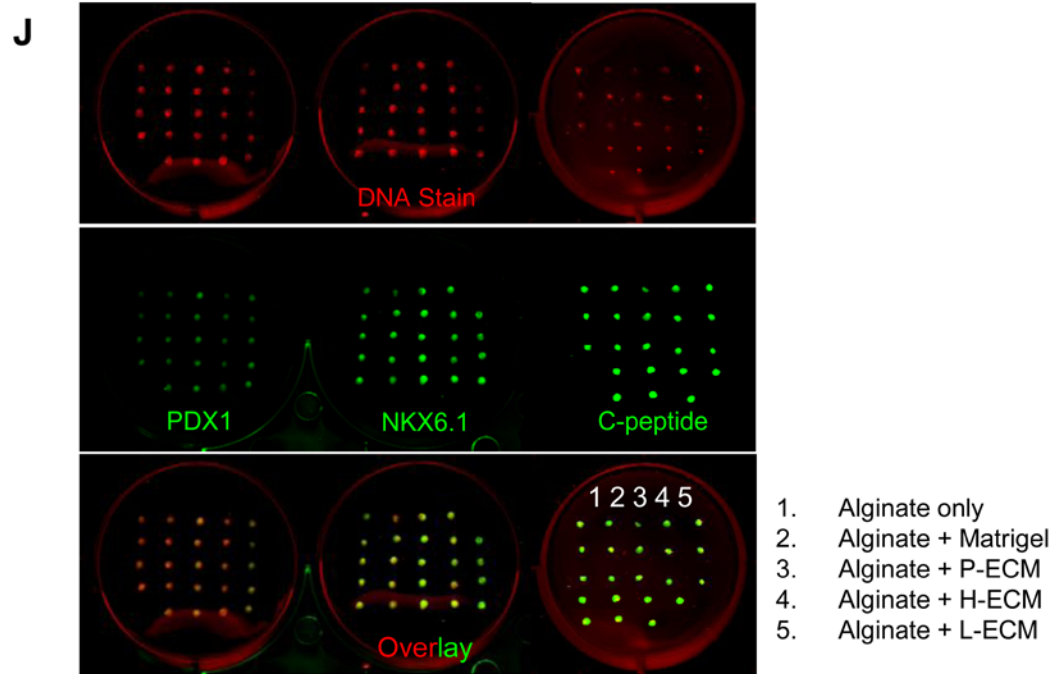


Figure 5.6 hESC-derived PP cells on 3D ECM array to investigate differentiation.

(A) Photograph of the organ-specific 3D ECM array, 25 microspots were generated in each well (6 well plate) (n=5 for each ECM). (B) Confocal images showing the three-dimensional distribution of hESC-PP cells after encapsulated onto the 3D ECM array. Shown in each panel is the top view and side view of the microspot, from a z-stack of 5  $\mu\text{m}$  sections. Each spot is 1  $\mu\text{l}$  resulting in a diameter of 1600  $\mu\text{m}$  and a height of 250  $\mu\text{m}$ . (C) Corresponding phase-contrast image showing one of the 3D microspot encapsulated with PP cells. (D) Representative live/dead images of hESC-derived PP cells encapsulated in organ-ECM microspots on the 3D array. High number of dead cells were detected. (E) Live/dead quantification confirmed high percentage of dead cells across all the ECM conditions. However, there was no significant difference observed between each ECM condition. (F) Step-wise differentiation protocol in alginate capsules to generate PP aggregates. After decapsulation with treatment of 100 mM EDTA, PP aggregates were filtered through 100  $\mu\text{m}$  mesh-sized cell strainer to avoid larger clumps inclusion in the 3D ECM array. Right panel showed the phase contrast image of relatively smaller and more homogenous sized PP aggregates used in the 3D ECM array. (G) Representative phase contrast image of PP aggregates inside the 3D alginate-ECM microspot. (H) After cultured inside 3D ECM array for 9 days, live/dead images showed good viability in all the organ ECM conditions. (I) Quantification of live/dead images confirmed the viability >90% in all ECM conditions including the controls (matrigel and alginate only). (J) LI-COR image showed the immunostaining characterization of the differentiation of PP cells in 3D ECM array. PP aggregates were encapsulated in organ-specific 3D ECM array and cultured in maturation medium with notch inhibition for 9 days, fixed and stained for analysis on the LI-COR Odyssey instrument. DraQ5 (red) was used as a counter stain for cell number and the Pdx1, Nkx6.1 and C-peptide (green) antibodies followed by an IRDye-800CW secondary antibody for quantitation of pancreatic maturation. (K) The PP aggregates were responsive to different organ ECM and gave rise to different levels of Pdx1, Nkx6.1 (pancreatic progenitors) and C-peptide (insulin) markers. (L) Representative stacked confocal images showed the specific C-peptide staining on the PP aggregates and consistent with the expression level found with LI-COR. L-ECM microspots demonstrated the highest number of insulin-expressing cells. (Error bars indicate  $\pm$  SEM, 5 microspots for ECM condition, n=3 independent experiments, \* P<0.05).

## 5.4 DISCUSSION

Extracellular matrix (ECM) components are important physiological regulators of stem cell function and fate [232, 244, 278]. In order to facilitate the high throughput analysis of cell-ECM interaction to dictate stem cell fate and function, several groups have developed combinatorial ECM array platform using single purified proteins in 2D adherent [100, 244] and 3D hydrogel [250-252] configurations. However, recapitulating the native ECM microenvironment niche with single purified proteins has proved to be inadequate [100, 254], hence more complex ECM has also been investigated using cell-derived matrix *in-vitro* [144, 255] or decellularized tissue or organ [50, 101]. Herein, we have developed an ECM array using native-mimicry ECM from decellularized organs (namely pancreas, liver and heart). The system is compatible with quantitative imaging, and permits rapid evaluation of the matrix protein profiles of different organ-derived ECM, along with the sensitive measurement of the cell-ECM interaction both in 2D adherent cultures as well as 3D non-adherent culture. In this report, we evaluated the effect of ECM specifically on pancreatic differentiation of hPSCs, but the developed platform is versatile to be applied to characterize any lineage specific differentiation.

To generate organ-specific ECM components, we employed a protocol combining decellularization, lyophilization, pulverization, and protein extraction to create organ ECM-derived solutions from pancreas, liver and heart. It is important to note that chaotropic agent extraction process does not completely solubilize the ECM. The residual ECM pellet is likely to contain mostly collagen as reported by Lin et al. [266]. When compared to the ECM extracted by urea (a chaotropic agent), they found that the SDS-PAGE profile of the collagenous ECM pellet was similar to that of purified collagen, and it did not exhibit high potency to support mesenchymal stem cell (MSC) function. In contrast, ECM extracted by urea contained multiple

bioactive ECM components that accelerated MSC proliferation, attachment, spreading, migration and multi-lineage differentiation. Hence it was likely to contain majority of the bioactive ECM component. In addition, Matrigel is also extracted with urea from Engelbreth-Holm-Swarm (EHS) tumors. It contains multiple ECM components such as laminin, collagen IV and entactins, and is commonly used as a bioactive culture substrate to promote cell differentiation and function [279]. Hence we expect that by using chaotropic agent extraction method, we were able to extract the bioactive portion of organ-specific ECMs. Consistent with Lin et al.'s finding [266], our result from immunostaining, SDS-PAGE and biochemical characterization of the organ-derived ECM extracts revealed retention of multi-components ECM, distinctly different than purified rat tail collagen I (Figure 5.1F and Figure 5.3A-E). Even though we are preserving multi-component ECM, it is likely that we are not capturing the full spectrum of ECM proteins from native organs, and losing some fraction from the harsh treatments of decellularization and ECM extraction. Nevertheless, we have previously demonstrated the effectiveness of this ECM processing approach, and the resulting ECM has been shown to recapitulate essential components of native ECM from different tissues including retina [265, 280], embryoid bodies [144] and pancreas [50].

Quantitative comparisons of cell-ECM interaction require reproducible substrate preparation and sensitive detection assay. Using a nitrocellulose-coated surface in combination with repeater pipette microspotting, we were able to generate arrays of microspots with highly reproducible protein content. There are several advantages of using nitrocellulose-coated surface for patterning ECM proteins. First, nitrocellulose coating is clear and permits excellent optical observation of the cells. Secondly, it is inert and doesn't appear toxic to cells. When blocked only with BSA, nitrocellulose is a very poor substrate for cell attachment [262]. Lastly,

nitrocellulose coating is well suited to bind a broad range of different ECM proteins via a combination of intermolecular forces, dominated by hydrophobic and van der Waals [281], without compromising the protein structure of the immobilized ECM extracts. The protein binding capacity of the nitrocellulose coating is instantaneous, nearly irreversible, and quantitative to 80–100  $\mu\text{g}/\text{cm}^2$  [273], much higher than poly(styrene-co-maleic anhydride) (PS-MA) coating (another common surface coating for protein immobilization), which shows only 68.2  $\mu\text{g}/\text{cm}^2$  of protein binding capacity [274, 275]. Several alternate substrate preparation have been developed for patterning protein microarrays [244, 251, 282], but the optimal substrate for patterning ECM proteins remains to be investigated. To develop an array platform for quantitative characterization, we utilized an on-chip, near IR-dye, immunofluorescence staining method with LI-COR Odyssey scanner. This method provides a robust high-throughput method for the quantitation of immunofluorescent staining and has advantages over microscopy-based screening approaches with regard to throughput and sensitivity. Acquisition and quantification of our generated arrays with 25 microspots can be accomplished in less than 10 min on the LI-COR odyssey scanner. This is in contrast to other reported studies involving hours-long acquisition time on a high-throughput microscope in the visible spectrum [244, 248, 249, 283]. In addition, the high sensitivity of the LI-COR scanner and the near-IR dyes provided robust signals at lower antibody dilutions than were possible using a microscopy-based system and dyes in the visible spectrum. With the increased sensitivity, however, there is an enhanced probability of artifact from unspecific antibody background staining. Hence, appropriate controls need to be included in the experimental plan to adequately remove the effect of background from acquired data.

The fabricated ECM array was first applied to characterize the cell-ECM interaction for cell attachment, and its specificity to organ-derived ECM. Analysis of the decellularized extracts

for individual ECM proteins revealed that pancreas, liver and heart each has differing levels of ECM proteins such as collagen I, collagen IV, laminin and fibronectin (Figure 5.3). When seeded with hPSC-PP cells, we observed differential adhesion profile responding to different organ-specific ECM with the L-ECM resulted in highest PP cells adhesion. Pancreatic progenitor (PP) cells display  $\alpha\text{v}\beta\text{3}$  and  $\alpha\text{v}\beta\text{5}$  integrins to mediate adhesion and migration both *in vitro* and *in vivo* model of pancreatic islet development [284]. These integrins are among the receptors that have been shown poised to receive signals from ECM components including fibronectin, collagen IV and vitronectin [285, 286]. Hence it can be postulated that the favorable adhesion of hPSC-PP cells to L-ECM can be attributed to the significantly higher fibronectin content found in L-ECM over P- and H-ECM.

While the 2D ECM array was efficient in analyzing the composition and adhesive properties of the ECM, it restricts us to analyze cell-ECM interactions for adherent cells only. However, ECM proteins are known to contribute beyond just adhesive function to dictate cell fate commitment [231, 232]. Hence to explore the cell-ECM interactions under non-adhesive cultures, we devised an encapsulation system in an inert hydrogel, which allows cell growth without adhering to the hydrogel. In our earlier work we have reported culture and differentiation of hESCs into islet-like cells in alginate capsules [69]. In addition to providing means for adhesion-free culture, it also provides a 3D environment to the cells, which is gaining increasing appreciation as a vital component of cell microenvironment, more so for human pluripotent stem cells [287]. While our previous report was in free suspension culture of encapsulated hPSCs, Fernandes et al. [248] have reported an alginate-based matrix array immobilized on glass slide to facilitate toxicity and drug screening applications [249]. With this immobilization technique, it is now possible to distribute nanoliter volumes of different samples in a spatially addressable

footprint for high throughput applications. They applied this platform for screening of human neural stem cells toxicity [249] and mouse embryonic stem cells differentiation [248]. In this study, we adopted the alginate immobilization platform and modified it to introduce the organ-derived ECM to the encapsulated hPSCs. The incorporation of ECM was stable with near-complete retention of the ECM throughout the culture period (Figure 5.5D). The negligible ECM loss from the array spots further rules out the concern of possible influence from adjacent array spots. Inclusion of ECM also did not modify the alginate stiffness thus confirming the observed effect is not from likely physical hydrogel parameters (Supplemental figure A.14).

Our alginate-ECM array is a versatile platform. It allows the feasibility of simultaneous multi-parametric modulation. In our study we modified the ECM composition of the array spot while keeping the physical gel parameters unchanged. It is possible to simultaneously change gel physical parameters, for example the array stiffness, by micro-spotting different divalent cation (e.g.  $\text{Ca}^{2+}$  or  $\text{Sr}^{2+}$ ) or different concentration of  $\text{BaCl}_2$  cationic solutions onto the nitrocellulose surface, which will give rise to different stiffness upon alginate gelation. In our study, we microspotted only one concentration of  $\text{BaCl}_2$  solution (10mM), which led to identical low stiffness (1kPA) across the different ECM conditions tested. This low stiffness was chosen mainly to be within the “soft” tissue range of native pancreatic tissue, which has been identified to be another critical parameter to modulate cell fate [162, 288]. In addition, the platform is also versatile enough to allow the encapsulation of single cells or cell aggregates. Encapsulation of single cells and its propagation into colonies under encapsulation is the most common practice for most of the cell lines. Hence we demonstrated the feasibility of microspotting single cells of MIN6 beta cells and maintaining viable culture in the 3D alginate gel array for 10 days (supplemental figure A.15). However such single cell encapsulation tends to be restrictive for

hPSCs because hPSCs are prone to cell death after being made single cell. While there was significant survival of the single-cell encapsulated hPSC-PP in our array platform, the dissociation process still led to significant cell death, as expected. These dead cells remained entrapped in the alginate matrix which is an undesirable culture condition. While we observed good viability of hPSC-PP cells in the 2D cell-ECM adhesion assay, likely only viable cells were capable of integrin-ECM mediated adhesion. Loosely attached dead cells were expected to be washed away during the staining process. In contrast, the 3D cell-laden ECM array involved the encapsulation of all dissociated cells, which likely include the entrapment of significant dead cells. Hence we developed a methodology to generate hPSC-PP aggregates and encapsulate these aggregates without dissociation. The preserved cell-cell contact in the aggregates protect the cells from apoptosis, and furthermore, it results in stronger differentiated phenotype, as demonstrated by our previous study [69] and reports from other groups [72, 75, 78, 214].

Recent studies have shown the manifestation of enhanced stem cell functions and intricate tissue formation when organ-specific ECM scaffolds were employed [196, 289]. The ECM scaffolds were shown to have the capacity to direct tissue-specific stem cell lineage commitment and maintain the phenotype of mature cell populations. However, the organ specific effect observed from these studies cannot be solely attributed to the ECM composition difference as these studies employed decellularized whole-organ scaffolds that are complex and vastly different beyond biochemical ECM properties (e.g. difference in growth factors, biophysical properties such as stiffness and topology etc.). In our studies, we implemented a more level comparison between different organs by extracting only the bioactive ECM components devoid of any confounding biophysical factors. Despite the identical extraction protocol, organ-specific differences were detected in all three organs in terms of their ECM compositional profiles. These

differences in turn led to different maturation outcome in the hPSC-PP cells, when complemented with chemical induction. Surprisingly, P-ECM, in spite of its pancreas origin, was not the most suitable in promoting the differentiation of hPSC-PP cells into insulin-expressing cells. In contrast, the liver derived ECM had the best performance among the organs compared in this study. It is noteworthy that majority of the pancreas is composed of exocrine tissue with only 2% made up of islet cells. While the differences in the ECM composition between endocrine and exocrine pancreas is not obvious, it is still non-specific to the pancreatic endocrine cell population, which is of interest in this study. On the other hand, liver is developmentally close to pancreas (i.e. both from endoderm germ layer) with previous successful reports of hepatocytes trans-differentiation into insulin-producing cells [290]. Liver has also been successfully used as a favorable transplant site to support islet insulin function during islet transplantation. In addition, liver has a very high density of vasculature and there is a substantial amount of interaction between islets and the ECM associated with vasculature. It has also been proposed that the vasculature basement membrane could be a favorable niche for promoting insulin gene expression and  $\beta$  cell proliferation [291]. It should also be noted that there is likely a beneficial effect that can be attributed to the variety of matrix-bound growth factors and cytokines retained in the ECM extracts, which have been demonstrated effective for inducing differentiation and maintaining cellular phenotypes [238, 289, 292]. Collectively, our results strongly suggest that hPSC-PP cell maturation was responsive to the different organ-derived ECM, as judged by the analysis in our 3D cell-laden alginate-ECM array. Our developed array is conducive for hPSC studies, in particular pre-differentiated hPSCs. While our focus here was on pancreatic differentiation, it can be directly applied to any other lineage-specific differentiation of hPSC.

## 5.5 CONCLUSION

In conclusion, we developed an ECM array platform that allows culture of cells under both adherent 2D configuration and non-adherent 3D aggregate configuration. Our array system enables rapid and sensitive measurement of the differential effect of organ-specific ECM towards stem cell differentiation, in a miniaturized and parallel fashion. While studies have demonstrated the conception that tissue differentiation using decellularized ECM requires matching on a 'like-for-like' basis [154, 196], interestingly, our ECM array analysis showed the positive effect of liver ECM to induce pancreatic differentiation of hPSC over pancreas ECM and heart ECM. Our platform is easily applicable to other lineage-specific differentiation of hPSC, and versatile to create organ-specific matrices from any organ of interest. The developed platform will allow rational design of engineered stem cell niches and support the rapidly developing field of stem cell biology, tissue engineering and regenerative medicine.

## **6.0 OVERALL CONCLUSIONS AND FUTURE WORK**

The studies presented in this dissertation merges together advancements in stem cell and tissue engineering towards engineering a regenerative pancreas. We accomplished this by (1) engineering a 3D scaffold derived from native organ by perfusion-decellularization technique, (2) repopulating the scaffold with differentiating hPSCs and (3) cultured with an in-house designed bioreactor. Exposure to the native ECM microenvironment is expected to provide inductive cues to the population of differentiating hPSCs. Lastly, we investigated the matrix-specificity by developing miniaturized arrays to investigate cell-ECM interaction during hPSC differentiation.

### **6.1 TO DECELLULARIZE AN INTACT WHOLE PANCREAS AND CHARACTERIZE THE POTENTIAL OF THE NATURAL 3D SCAFFOLD TO SUPPORT PANCREATIC TISSUE AND WHOLE ORGAN ENGINEERING**

The production of an intact acellular organ such as the pancreas by perfusion-decellularization offers a promising alternate approach for pancreatic tissue engineering and functional organ replacement. In chapter 2, we demonstrated that perfusion-decellularization of whole pancreas results in the generation of a natural pancreas ECM scaffold with a perfusable vascular tree, ductal network and intact 3D architecture, which acts as a suitable template for pancreatic tissue

engineering and whole organ regeneration. Comprehensive characterization of the decellularized pancreatic matrix showed the preservation of complex multi-faceted ECM proteins, 3D spatial orientation and microstructure, and relative stiffness of native pancreas. Decellularized pancreatic matrix was non-cytotoxic and promoted angiogenesis when subcutaneously implanted in a mouse model. Repopulation of decellularized pancreas with pancreatic cells showed the cytocompatibility of the scaffold. The recellularized constructs maintained their respective phenotypic expression ( $\beta$ -cells: C-peptide; acinar cells: Amylase) after 5 days of culture. Finally, we demonstrated that the decellularized pancreas matrix is supportive of  $\beta$ -cell function, as evidenced by the strong up-regulation of insulin gene expression. Such native organ derived scaffold is likely to have a great impact in pancreatic tissue engineering, by providing a niche microenvironment for pancreatic cell types and even stem/progenitor cells.

For future work related to this aim, it will be critical to examine the efficiency of decellularization protocols to remove cells. In this study, we used ionic detergent SDS, which has shown to be very effective to solubilize cells and cleave proteins but also potentially harmful if not properly removed from the resulting 3D scaffolds. It is noteworthy that any decellularization protocol will cause changes in the retained ECM; the objective of decellularization is to remove cells and cell remnants with minimum disruption of the important ECM proteins. If the detergent used is too disruptive, important biochemical properties from the native organs may be lost and hinder the functionality of the engrafted cells. Other milder detergent such CHAPS (Zwitterionic detergent) or non-ionic detergent Triton-X 100 have been successfully used in other organs such as lungs [111], liver [117] and heart [133], but yet to be demonstrated its efficiency in pancreas. There is a delicate balance between complete decellularization and preservation of biological activities. In addition, it remains to be

investigated whether islet-specific ECM can be preserved with this decellularization technique. A minimal 2% of the entire pancreas consists of endocrine islets, while the rest is exocrine, making it challenging to isolate and preserve islet-specific ECM particularly challenging.

## **6.2 TO REPOPULATE THE DECELLULARIZED PANCREAS WITH HESCS AND MATURE INTO INSULIN-EXPRESSING CELL IN WHOLE ORGAN BIOREACTOR CULTURE**

Whole organ engineering has emerged as a promising alternative avenue to fill the gap of donor organ shortage in organ transplantation. Recent breakthroughs in the decellularization of solid organs and repopulation with desired cell populations have generated neo-organ constructs with promising functional outcomes. The realization of this goal requires engineering advancement in the perfusion-based bioreactors to (i) efficiently deliver decellularization agents, followed by (ii) its reconstruction with relevant cell types and (iii) maintenance of viability and function of the reconstructed organ. In Chapter 3, we presented the development and assembly of a perfusion bioreactor to enable regenerative reconstruction of pancreas. The assembled bioreactor is versatile to efficiently decellularize multiple organs, as demonstrated by complete decellularization of pancreas, liver and heart in the same set-up. Further, the same system is amenable to support organ reconstruction with diverse cell types. Using our in-house bioreactor system, we demonstrated pancreas reconstruction with both immortalized MIN-6 beta cells and differentiating human pluripotent stem cells. Importantly, we show the significant advantage of perfusion culture over static culture in enhancing cell engraftment, viability and phenotypic maintenance of the reconstructed pancreas. In addition, this study is a significant step forward for

whole organ engineering as it allows cost-effective and easy assembly of perfusion bioreactors to enable rapid advancement in regenerative organ reconstruction.

After establishing the bioreactor system to support organ reconstruction, we next sought a cell source suitable for repopulating the decellularized pancreas scaffold and regenerate a bioengineered pancreas in Chapter 4. Early organ engineering studies seeded decellularized organ scaffolds with primary cells and immortalized cell lines [108, 111, 136]. While these studies present a promising new avenue for organ regeneration, the lack of abundant functionally mature cells is a major limitation to the clinical application of engineered organs. Human pluripotent stem cells (i.e. ES and iPS cells) represent an attractive source of cells owing to its virtually unlimited replicative capacity and the potential to differentiate into a variety of cell types. By recapitulating embryonic and fetal developmental stages using external growth factors or small molecule inhibitors, recent PSC differentiation protocol has enabled the generation of pancreatic  $\beta$  cells *in vitro* with high efficiency [78, 79]. In this chapter, we evaluated the possibility of repopulating decellularized organ scaffolds (e.g. pancreas and liver) with pancreatic progenitor cells derived from hPSC. We have previously reported efficient differentiation of pancreatic progenitor cells from hPSCs on adherent cultures [70, 71], which we used to repopulate our decellularized pancreas. More recently, we reported an efficient derivation of PP aggregates by alginate encapsulation of hPSCs and subsequent differentiation under encapsulation [69]. The differentiated hPSC-PP aggregates not only express enhancement of pancreatic differentiation than the parallel adherent cultures, but also retain cell-cell contact which makes them more amenable to organ repopulation. However, engraftment of these hPSC-PP aggregates required a more extensive vascular support, which was found to be superior in decellularized liver over the decellularized pancreas scaffold. Decellularized liver repopulated

with hPSC-PP aggregates resulted in extensive and uniform cellular engraftment and viability throughout the thickness of the scaffold. More importantly, the seeded hPSC-PP aggregates matured into mono-hormonal C-peptide positive cells after 9 days of bioreactor culture. This is the first demonstration, to the best of our knowledge, of the feasibility of repopulating decellularized organ scaffolds with hPSC derived pancreatic progenitor cells, paving the way for diabetes therapy, organ engineering and drug discovery applications.

For future work, the bioreactor design can further benefit from a few continued design improvements. For instance, the importance of monitoring organ growth and development using noninvasive imaging detection is not to be overlooked. Current data metrics from whole organ culture typically involves end-point analysis to assess cell survival, proliferation and function of the engineered organ. New, noninvasive methods to evaluate organ and cell growth such as near-infrared (IR) imaging allows for deep tissue imaging with limited tissue scattering and auto-fluorescence [197]. Another area of improvement is to fit the bioreactor with specific sensors to ensure a controlled environment. Biomimetic physical, electrical, or chemical stimuli could also be built-in to improve and promote organ function. For example, mechanical stretching of heart tissue has been found to promote cell alignment [199] while electrical stimulation causes the coordinated beating of heart cells [200].

For whole organ reconstruction, there is a need for integrating other stromal cell population to reconstitute the overall supporting microenvironment for organ regeneration. Seeding of supporting cell types such as fibroblast, endothelial and mesenchymal stem cells has shown to enhance the attachment, viability and matrix remodeling of the recellularized organs such as recellularized lung [121], kidney [118] and liver [233-235]. The derivation of these cells from patient-specific iPS cells opens door for personalized medicine and build customized organ

avoiding the need of immune suppression. In addition, extended bioreactor culture (e.g., 14 or 21 days) would likely allow the seeded cells to further expand within the matrix and adopt more mature phenotypes. Implantation into the host animal for an extended “*in vivo* culture” period may also be advantageous for further regeneration. Complete recapitulation of cellular components and functional beta cells would likely be aided by the recipient’s endogenous environment and repair program [67].

### **6.3 TO EVALUATE THE MATRIX-SPECIFICITY OF ORGAN-DERIVED ECM IN HUMAN EMBRYONIC STEM CELL DIFFERENTIATION**

The process of stem cell differentiation is regulated by multi-parametric cues from the surrounding microenvironment including extracellular matrix (ECM), soluble factors, matrix stiffness, substrate topography and adjacent cell-cell interactions [293]. Stem cells interact with the ECM, which is a complex tissue-specific structure via several different cell surface receptors, of which the largest family is integrins [294]. The cell-ECM interaction allows cells to sense mechanical and biochemical cues and respond directly by inducing downstream cellular signaling, modulating the response of other integrins and influencing organ-specific lineage commitment [278, 292, 295, 296]. Hence it is of interest to quantify the contribution of organ-specific ECM, alone and in synergy with the other microenvironmental factors, in modulating stem cell fate.

In this final chapter, we developed an ECM array system that enables rapid and sensitive measurement of the differential effect of organ-specific ECM toward stem cell differentiation under both adherent 2D and non-adherent 3D culture configuration. We generated organ-specific

ECM by decellularizing whole organs (e.g. pancreas, liver and heart) and extracting ECM using chaotropic agents (e.g. Urea and GuHCl). Other ECM digestion methods such as enzymatic pepsin digestion could also be implemented yet the optimal ECM digestion protocol remains to be investigated. Despite the identical extraction protocol, biochemical and SDS-PAGE characterization revealed considerable differences in ECM compositional profiles between the three organs. By micro-spotting organ-derived ECM onto nitrocellulose-coated surface, we were able to pattern them into ECM islands and generated organ-specific ECM arrays. The effect of cell-ECM adhesion of stem cell fate was evaluated by seeding pre-differentiated hPSC-PP cells on the array. Interestingly, the hPSC-PP cells were responsive to different organ-derived ECM and expressed different adherence profiles, further confirming the matrix-specificity of each organ. In the 3D ECM array with non-adherent PP aggregate culture, our platform showed excellent compatibility with enhanced maturation into insulin expressing cells in organ-derived ECMs compared to matrigel. Interestingly, P-ECM being the origin of the tissue did not show higher insulin expression than L-ECM. Overall, this method allows the investigation of cell-ECM interaction during stem cell differentiation in a miniaturized and parallel fashion. Furthermore, our method of ECM array fabrication is easily applicable to other organ types, allowing versatile characterization of organ-specific matrices and characterize any lineage specific differentiation of stem cells. The developed platform will allow rational design of engineered stem cell niches and support the rapidly developing field of stem cell biology, tissue engineering and regenerative medicine.

For future work, it is critical to evaluate the potential retention of matrix-bound growth factors and cytokines retained in the ECM extracts, which have been demonstrated effective for inducing differentiation and maintaining cellular phenotypes [238, 289, 292]. In our study, we

evaluated four major ECM proteins (i.e. Collagen I, Collagen IV, Laminin and Fibronectin) preserved in the organ-ECM extracts; however there is likely other ECM proteins that have an effect on pancreatic differentiation of stem cells, but was not investigated in this study. More comprehensive characterization such as mass spec or growth factor analysis is required to truly understand the precise contribution of each of these factors. Another area for future investigation is the parallel investigation of stiffness' effect with ECM incorporated in the array. Since our array is versatile to allow simultaneous multi-parametric modulation, it will be interesting to investigate the combinatorial effect of stiffness and ECM in this miniaturized platform. The stiffness within a tissue environment is another critical parameter to modulate cell fate [162, 288]. Studies have shown that stiffer matrix will promote the differentiation of MSC to bone lineage whereas softer matrix to adipose lineage [162]. When organs ECMs are coupled with their corresponding tissue stiffness, it is likely to give rise to a synergistic promotion of organ-specific differentiation. For example, it is intuitive to think that the combination of H-ECM with a stiffer gel could result in the promotion of cardiac differentiation whereas the P-ECM with a softer gel may result in promotion of pancreatic differentiation. In contrast, the mismatch of stiffness and ECM would likely result in less favorable lineage specific differentiation. This remains an interesting hypothesis to be tested, whether organ-specific ECM effect will act in synergy or be overridden by the stiffness modulation.

Overall, the findings described in this dissertation present an alternative therapeutic solution to diabetes by generating a bioengineered pancreas from native organ scaffolds and renewable hPSCs. Specifically, we demonstrated that MIN-6  $\beta$ -cell and hPSC-derived PP cells cultured in 3D organ scaffolds exhibit improved insulin expression over other commercially available ECM proteins (e.g. matrigel and other individual ECM proteins). These findings

strongly point toward the importance of 3D native complex ECM in supporting  $\beta$ -cell differentiation and function. However, preclinical testing will be required to determine whether the significant improvement in functionality observed *in vitro* can extend to *in vivo* settings and for how long. While not a focus of this dissertation, the protection of insulin-producing cells from immune attack will also need to be addressed to limit the need for immunosuppressive drugs.

## APPENDIX A

### SUPPLEMENTARY TABLES AND FIGURES

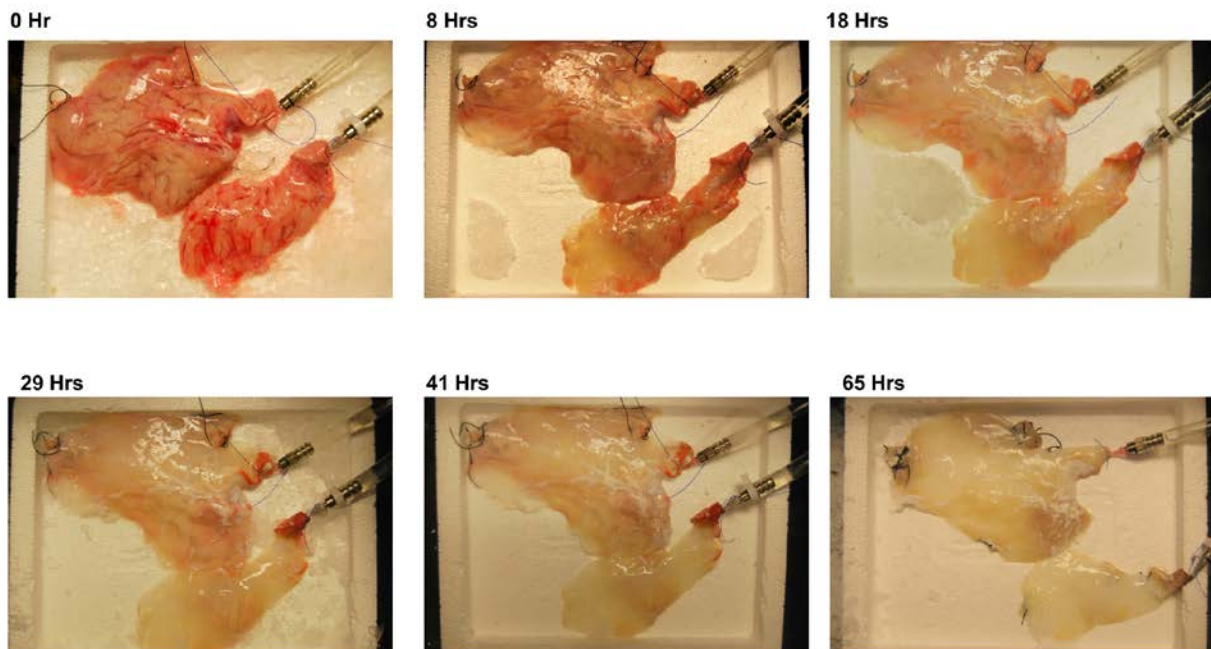


**Figure A.1 Decellularization of bovine pancreas.**

Panel images show progressive decellularization of bovine pancreas over the course of 65 hours.

**Table 6.1 Supplemental table for ECM proteins detected with mass spec analysis**

Accession	Description	$\Sigma$ Coverage	$\Sigma$ # Proteins	$\Sigma$ # Unique Peptides	$\Sigma$ # Peptides	$\Sigma$ # PSMs	MW [kDa]
P11087	Collagen alpha-1(I) chain OS=Musmusculus GN=Col1a1 PE=1 SV=4 - [CO1A1_MOUSE]	18.58	2	17	19	3240	137.9
Q01149	Collagen alpha-2(I) chain OS=Musmusculus GN=Col1a2 PE=2 SV=2 - [CO1A2_MOUSE]	32.22	2	28	28	2972	129.5
P08122	Collagen alpha-2(IV) chain OS=Musmusculus GN=Col4a2 PE=2 SV=4 - [CO4A2_MOUSE]	15.70	2	18	18	2632	167.2
P08121	Collagen alpha-1(III) chain OS=Musmusculus GN=Col3a1 PE=2 SV=4 - [CO3A1_MOUSE]	16.80	1	17	17	1121	138.9
Q3U962	Collagen alpha-2(V) chain OS=Musmusculus GN=Col5a2 PE=1 SV=1 - [CO5A2_MOUSE]	12.69	1	10	13	851	144.9
Q9JL12	Collagen type V alpha 3 chain OS=Musmusculus GN=Col5a3 PE=2 SV=1 - [Q9JL12_MOUSE]	7.53	1	8	8	533	171.9
P02463	Collagen alpha-1(IV) chain OS=Musmusculus GN=Col4a1 PE=2 SV=4 - [CO4A1_MOUSE]	4.31	2	3	5	479	160.6
P02535-3	Isoform 3 of Keratin, type I cytoskeletal 10 OS=Musmusculus GN=Krt10 - [K1C10_MOUSE]	18.61	6	1	11	346	49.5
J3QQ16	Protein Col6a3 OS=Musmusculus GN=Col6a3 PE=4 SV=1 - [J3QQ16_MOUSE]	13.30	3	29	29	328	288.5
E9PZ16	Endorepellin OS=Musmusculus GN=Hspg2 PE=4 SV=1 - [E9PZ16_MOUSE]	10.95	3	37	37	289	469.5
P11679	Keratin, type II cytoskeletal 8 OS=Musmusculus GN=Krt8 PE=1 SV=4 - [K2C8_MOUSE]	9.59	3	1	8	240	54.5
O88207	Collagen alpha-1(V) chain OS=Musmusculus GN=Col5a1 PE=2 SV=2 - [CO5A1_MOUSE]	4.73	9	8	8	217	183.6
Q04857	Collagen alpha-1(VI) chain OS=Musmusculus GN=Col6a1 PE=2 SV=1 - [CO6A1_MOUSE]	15.22	1	12	12	211	108.4
Q61292	Laminin subunit beta-2 OS=Musmusculus GN=Lamb2 PE=2 SV=2 - [LAMB2_MOUSE]	15.51	1	22	22	206	196.5
F8VQJ3	Laminin subunit gamma-1 OS=Musmusculus GN=Lamc1 PE=4 SV=1 - [F8VQJ3_MOUSE]	8.71	3	13	13	200	177.1
Q02788	Collagen alpha-2(VI) chain OS=Musmusculus GN=Col6a2 PE=2 SV=3 - [CO6A2_MOUSE]	13.83	2	14	14	191	110.3
Q61001	Laminin subunit alpha-5 OS=Musmusculus GN=Lama5 PE=1 SV=4 - [LAMA5_MOUSE]	7.15	1	20	20	166	403.8
E9Q1Z0	Protein 4732456N10Rik OS=Musmusculus GN=4732456N10Rik PE=3 SV=1 - [E9Q1Z0_MOUSE]	15.61	6	1	11	116	58.2
A2AQ53	Fibrillin 1 OS=Musmusculus GN=Fbn1 PE=4 SV=1 - [A2AQ53_MOUSE]	6.51	2	15	17	115	312.1
F8VQ43	Laminin subunit alpha-2 OS=Musmusculus GN=Lama2 PE=4 SV=1 - [F8VQ43_MOUSE]	5.36	2	14	14	91	343.6
E9Q557	Desmoplakin OS=Musmusculus GN=Dsp PE=3 SV=1 - [DESP_MOUSE]	9.57	2	24	24	87	332.7
E9Q6A6	Collagen alpha-6(VI) chain OS=Musmusculus GN=Col6a6 PE=4 SV=2 - [E9Q6A6_MOUSE]	5.34	3	11	11	73	246.3

**Table 6.1 (continued)**

P11276	Fibronectin OS=Musmusculus GN=Fn1 PE=1 SV=4 - [FINC_MOUSE]	5.33	1	11	11	57	272.4
E9Q3W4	Plectin OS=Musmusculus GN=Plec PE=4 SV=1 - [E9Q3W4_MOUSE]	3.83	28	18	18	57	498.8
E9QPE7	Myosin-11 OS=Musmusculus GN=Myh11 PE=4 SV=1 - [E9QPE7_MOUSE]	5.16	2	2	8	48	223.2
E9Q2T3	Protein Tnxb OS=Musmusculus GN=Tnxb PE=4 SV=1 - [E9Q2T3_MOUSE]	4.45	2	12	12	48	339.7
O08638	Myosin-11 OS=Musmusculus GN=Myh11 PE=1 SV=1 - [MYH11_MOUSE]	4.26	2	1	7	47	226.9
Q792Z1	MCG140784 OS=Musmusculus GN=Try10 PE=2 SV=1 - [Q792Z1_MOUSE]	8.13	1	2	2	45	26.2
Q02257	Junction plakoglobin OS=Musmusculus GN=Jup PE=1 SV=3 - [PLAK_MOUSE]	16.24	3	11	11	43	81.7
Q63ZW6	Col4a5 protein OS=Musmusculus GN=Col4a5 PE=2 SV=1 - [Q63ZW6_MOUSE]	3.67	2	2	4	41	161.7
Q80X19-2	Isoform 2 of Collagen alpha-1(XIV) chain OS=Musmusculus GN=Col14a1 - [COEA1_MOUSE]	7.30	5	9	9	41	191.2
P02469	Laminin subunit beta-1 OS=Musmusculus GN=Lamb1 PE=1 SV=3 - [LAMB1_MOUSE]	3.64	3	6	6	40	197.0
Q9CPN9	Protein 2210010C04Rik OS=Musmusculus GN=2210010C04Rik PE=2 SV=1 - [Q9CPN9_MOUSE]	8.10	1	2	2	39	26.4
B1AVK5	Procollagen type IV alpha 6 OS=Musmusculus GN=Col4a6 PE=4 SV=1 - [B1AVK5_MOUSE]	2.25	1	3	3	38	163.9
P07356	Annexin A2 OS=Musmusculus GN=Anxa2 PE=1 SV=2 - [ANXA2_MOUSE]	26.25	4	7	7	32	38.7
Q61FZ8	MCG1050941 OS=Musmusculus GN=Gm5414 PE=2 SV=1 - [Q61FZ8_MOUSE]	8.88	2	1	5	31	60.2
A6H584	Collagen alpha-5(VI) chain OS=Musmusculus GN=Col6a5 PE=1 SV=2 - [CO6A5_MOUSE]	1.63	2	3	3	30	289.4
P10493	Nidogen-1 OS=Musmusculus GN=Nid1 PE=1 SV=2 - [NID1_MOUSE]	2.65	1	3	3	26	136.5
Q63870	Collagen alpha-1(VII) chain OS=Musmusculus GN=Col7a1 PE=2 SV=3 - [CO7A1_MOUSE]	1.53	1	3	4	25	295.1
Q78PY7	Staphylococcal nuclease domain-containing protein 1 OS=Musmusculus GN=Snd1 PE=1 SV=1 - [SND1_MOUSE]	7.58	2	5	5	25	102.0
P16546-2	Isoform 2 of Spectrin alpha chain, non-erythrocytic 1 OS=Musmusculus GN=Sptan1 - [SPTN1_MOUSE]	4.12	8	10	10	25	282.2
E9Q1F2	Actin, cytoplasmic 1, N-terminally processed OS=Musmusculus GN=Actb PE=3 SV=1 - [E9Q1F2_MOUSE]	17.97	16	1	5	22	32.5
Q8VDD5	Myosin-9 OS=Musmusculus GN=Myh9 PE=1 SV=4 - [MYH9_MOUSE]	4.13	1	6	7	22	226.2
Q9QZR9	Collagen alpha-4(IV) chain OS=Musmusculus GN=Col4a4 PE=2 SV=1 - [CO4A4_MOUSE]	4.93	1	6	6	21	164.0
P21981	Protein-glutamine gamma-glutamyltransferase 2 OS=Musmusculus GN=Tgm2 PE=1 SV=4 - [TGM2_MOUSE]	4.66	2	3	3	21	77.0

**Table 6.1 (continued)**

Q61495	Desmoglein-1-alpha OS=Musmusculus GN=Dsg1a PE=2 SV=2 - [DSG1A_MOUSE]	4.73	4	5	5	21	114.5
A1BN54	Alpha actinin 1a OS=Musmusculus GN=Actn1 PE=2 SV=1 - [A1BN54_MOUSE]	4.85	4	4	4	20	102.7
P63268	Actin, gamma-enteric smooth muscle OS=Musmusculus GN=Actg2 PE=2 SV=1 - [ACTH_MOUSE]	14.10	16	1	5	18	41.8
O88322	Nidogen-2 OS=Musmusculus GN=Nid2 PE=1 SV=2 - [NID2_MOUSE]	2.21	1	3	3	18	153.8
P62806	Histone H4 OS=Musmusculus GN=Hist1h4a PE=1 SV=2 - [H4_MOUSE]	29.13	1	3	3	17	11.4
P68373	Tubulin alpha-1C chain OS=Musmusculus GN=Tuba1c PE=1 SV=1 - [TBA1C_MOUSE]	5.35	3	2	2	17	49.9
A2AJY2	Collagen alpha-1(XV) chain OS=Musmusculus GN=Col15a1 PE=4 SV=1 - [A2AJY2_MOUSE]	2.30	4	3	3	17	138.2
P00688	Pancreatic alpha-amylase OS=Musmusculus GN=Amy2 PE=1 SV=2 - [AMYP_MOUSE]	10.04	5	5	5	15	57.3
E9Q5F6	Ubiquitin-related 2 (Fragment) OS=Musmusculus GN=Ubc PE=4 SV=1 - [E9Q5F6_MOUSE]	32.84	12	2	2	15	22.6
P07901	Heat shock protein HSP 90-alpha OS=Musmusculus GN=Hsp90aa1 PE=1 SV=4 - [HS90A_MOUSE]	4.09	2	2	3	15	84.7
P97927	Laminin subunit alpha-4 OS=Musmusculus GN=Lama4 PE=1 SV=2 - [LAMA4_MOUSE]	1.54	10	3	3	14	201.7
Q9Z1Z0-3	Isoform 3 of General vesicular transport factor p115 OS=Musmusculus GN=Uso1 - [USO1_MOUSE]	6.25	3	3	3	14	54.7
Q61879	Myosin-10 OS=Musmusculus GN=Myh10 PE=1 SV=2 - [MYH10_MOUSE]	1.92	3	2	4	13	228.9
Q9JIF7	Coatamer subunit beta OS=Musmusculus GN=Copb1 PE=1 SV=1 - [COPB_MOUSE]	3.36	1	3	3	13	107.0
P14148	60S ribosomal protein L7 OS=Musmusculus GN=Rpl7 PE=2 SV=2 - [RL7_MOUSE]	6.30	2	1	2	12	31.4
Q61753	D-3-phosphoglycerate dehydrogenase OS=Musmusculus GN=Phgdh PE=1 SV=3 - [SERA_MOUSE]	3.56	1	2	2	12	56.5
Q8BU30	Isoleucine--tRNA ligase, cytoplasmic OS=Musmusculus GN=Iars PE=2 SV=2 - [SYIC_MOUSE]	2.14	1	3	3	12	144.2
P17897	Lysozyme C-1 OS=Musmusculus GN=Lyz1 PE=1 SV=1 - [LYZ1_MOUSE]	12.16	2	2	2	11	16.8
Q9WT17-4	Isoform 4 of Unconventional myosin-Ic OS=Musmusculus GN=Myo1c - [MYO1C_MOUSE]	1.87	4	2	2	11	111.2
P46978	Dolichyl-diphosphooligosaccharide--protein glycosyltransferase subunit STT3A OS=Musmusculus GN=Stt3a PE=1 SV=1 - [STT3A_MOUSE]	1.84	4	2	2	11	80.5
E9PVA8	Protein Gcn111 OS=Musmusculus GN=Gcn111 PE=4 SV=1 - [E9PVA8_MOUSE]	1.57	2	4	4	11	292.8
B7FAV1	Filamin, alpha (Fragment) OS=Musmusculus GN=Flna PE=4 SV=1 - [B7FAV1_MOUSE]	1.16	5	3	3	11	274.5
F8VQ40	Laminin subunit alpha-1 OS=Musmusculus GN=Lama1 PE=4 SV=1 - [F8VQ40_MOUSE]	1.27	2	4	4	11	337.9

**Table 6.1 (continued)**

Q9EST1	Gasdermin-A OS=Musmusculus GN=Gsdma PE=2 SV=1 - [GSDMA_MOUSE]	6.73	4	3	3	11	49.6
E9Q3D6	Heat shock protein HSP 90-beta (Fragment) OS=Musmusculus GN=Hsp90ab1 PE=4 SV=1 - [E9Q3D6_MOUSE]	11.11	3	1	2	11	22.5
P10126	Elongation factor 1-alpha 1 OS=Musmusculus GN=Eef1a1 PE=1 SV=3 - [EF1A1_MOUSE]	4.11	2	2	2	11	50.1
P17809	Solute carrier family 2, facilitated glucose transporter member 1 OS=Musmusculus GN=Slc2a1 PE=1 SV=4 - [GTR1_MOUSE]	2.85	1	2	2	10	53.9
Q8VDN2	Sodium/potassium-transporting ATPase subunit alpha-1 OS=Musmusculus GN=Atp1a1 PE=1 SV=1 - [AT1A1_MOUSE]	1.96	1	2	2	10	112.9
P99024	Tubulin beta-5 chain OS=Musmusculus GN=Tubb5 PE=1 SV=1 - [TBB5_MOUSE]	7.66	7	1	3	10	49.6
B7ZN27	Cad protein OS=Musmusculus GN=Cad PE=2 SV=1 - [B7ZN27_MOUSE]	2.00	5	4	4	9	235.7
P22892	AP-1 complex subunit gamma-1 OS=Musmusculus GN=Ap1g1 PE=1 SV=3 - [AP1G1_MOUSE]	2.31	2	2	2	9	91.3
P10852	4F2 cell-surface antigen heavy chain OS=Musmusculus GN=Slc3a2 PE=1 SV=1 - [4F2_MOUSE]	3.42	2	2	2	8	58.3
Q61555	Fibrillin-2 OS=Musmusculus GN=Fbn2 PE=1 SV=2 - [FBN2_MOUSE]	0.86	1	1	3	8	313.6
P58252	Elongation factor 2 OS=Musmusculus GN=Eef2 PE=1 SV=2 - [EF2_MOUSE]	2.21	5	2	2	8	95.3
Q9D6F9	Tubulin beta-4A chain OS=Musmusculus GN=Tubb4a PE=1 SV=3 - [TBB4A_MOUSE]	7.66	5	1	3	8	49.6
Q76MZ3	Serine/threonine-protein phosphatase 2A 65 kDa regulatory subunit A alpha isoform OS=Musmusculus GN=Ppp2r1a PE=1 SV=3 - [2AAA_MOUSE]	3.40	1	2	2	8	65.3
Q9QZS0	Collagen alpha-3(IV) chain OS=Musmusculus GN=Col4a3 PE=1 SV=2 - [CO4A3_MOUSE]	5.51	2	5	5	7	161.6
P70168	Importin subunit beta-1 OS=Musmusculus GN=Kpnb1 PE=1 SV=2 - [IMB1_MOUSE]	3.08	1	2	2	7	97.1
Q922D8	C-1-tetrahydrofolate synthase, cytoplasmic OS=Musmusculus GN=Mthfd1 PE=1 SV=4 - [C1TC_MOUSE]	8.88	1	6	6	6	101.1
Q68FD5	Clathrin heavy chain 1 OS=Musmusculus GN=Cltc PE=1 SV=3 - [CLH_MOUSE]	1.43	2	2	2	6	191.4
Q02053	Ubiquitin-like modifier-activating enzyme 1 OS=Musmusculus GN=Uba1 PE=1 SV=1 - [UBA1_MOUSE]	4.16	1	3	3	6	117.7
Q8BMJ2	Leucine--tRNA ligase, cytoplasmic OS=Musmusculus GN=Lars PE=2 SV=2 - [SYLC_MOUSE]	2.72	1	3	3	5	134.1
P32037	Solute carrier family 2, facilitated glucose transporter member 3 OS=Musmusculus GN=Slc2a3 PE=1 SV=1 - [GTR3_MOUSE]	3.25	1	2	2	5	53.4
Q9D0R2	Threonine--tRNA ligase, cytoplasmic OS=Musmusculus GN=Tars PE=1 SV=2 - [SYTC_MOUSE]	3.60	1	2	2	5	83.3
D3YXT0	NADH dehydrogenase [ubiquinone] iron-sulfur protein 2, mitochondrial OS=Musmusculus GN=Ndufs2 PE=3 SV=1 - [D3YXT0_MOUSE]	6.41	3	3	3	5	49.5

**Table 6.1 (continued)**

P28481-2	Isoform 3 of Collagen alpha-1(II) chain OS=Musmusculus GN=Col2a1 - [CO2A1_MOUSE]	4.17	7	1	3	4	131.8
Q3UQ28	Peroxidasin homolog OS=Musmusculus GN=Pxdn PE=2 SV=2 - [PXDN_MOUSE]	1.56	1	2	2	4	165.0
F8WIT2	Annexin OS=Musmusculus GN=Anxa6 PE=3 SV=1 - [F8WIT2_MOUSE]	2.85	2	2	2	4	75.2
Q504P4	Heat shock cognate 71 kDa protein OS=Musmusculus GN=Hspa8 PE=2 SV=1 - [Q504P4_MOUSE]	3.35	9	2	2	4	68.7
B9EJ54	MCG21756, isoform CRA_b OS=Musmusculus GN=Nup205 PE=2 SV=1 - [B9EJ54_MOUSE]	0.85	1	2	2	4	227.3
O70133	ATP-dependent RNA helicase A OS=Musmusculus GN=Dhx9 PE=1 SV=2 - [DHX9_MOUSE]	2.17	4	3	3	4	149.4
Q3V3R1	Monofunctional C1-tetrahydrofolate synthase, mitochondrial OS=Musmusculus GN=Mthfd1l PE=1 SV=2 - [C1TM_MOUSE]	3.89	1	3	3	4	105.7
P52480-2	Isoform M1 of Pyruvate kinase isozymes M1/M2 OS=Musmusculus GN=Pkm - [KPYM_MOUSE]	3.20	2	2	2	4	57.9
P52431	DNA polymerase delta catalytic subunit OS=Musmusculus GN=Pold1 PE=1 SV=2 - [DPOD1_MOUSE]	1.99	2	2	2	4	123.7
Q3TXS7	26S proteasome non-ATPase regulatory subunit 1 OS=Musmusculus GN=Psm1 PE=1 SV=1 - [PSMD1_MOUSE]	3.46	1	3	3	4	105.7
D3YWT0	Signal peptidase complex catalytic subunit SEC11A OS=Musmusculus GN=Sec11a PE=4 SV=1 - [D3YWT0_MOUSE]	10.00	4	2	2	4	19.6
Q8BP47	Asparagine--tRNA ligase, cytoplasmic OS=Musmusculus GN=Nars PE=1 SV=2 - [SYNC_MOUSE]	3.40	1	2	2	4	64.2
P39061-2	Isoform 3 of Collagen alpha-1(XVIII) chain OS=Musmusculus GN=Col18a1 - [COIA1_MOUSE]	1.75	4	2	2	3	134.1
Q9JHU4	Cytoplasmic dynein 1 heavy chain 1 OS=Musmusculus GN=Dync1h1 PE=1 SV=2 - [DYHC1_MOUSE]	0.34	1	2	2	3	531.7
F8WJL5	Glyceraldehyde-3-phosphate dehydrogenase OS=Musmusculus GN=Gapdh PE=3 SV=1 - [F8WJL5_MOUSE]	6.95	7	2	2	3	32.5
Q6URW6-2	Isoform 2 of Myosin-14 OS=Musmusculus GN=Myh14 - [MYH14_MOUSE]	0.80	3	1	2	3	227.6
O54734	Dolichyl-diphosphooligosaccharide--protein glycosyltransferase 48 kDa subunit OS=Musmusculus GN=Ddost PE=1 SV=2 - [OST48_MOUSE]	4.99	1	2	2	3	49.0
P09405	Nucleolin OS=Musmusculus GN=Ncl PE=1 SV=2 - [NUCL_MOUSE]	3.82	1	3	3	3	76.7
A2AVJ7	Ribosome binding protein 1 OS=Musmusculus GN=Rrbp1 PE=4 SV=1 - [A2AVJ7_MOUSE]	1.23	2	2	2	2	158.3
Q9JL18-2	Isoform 2 of Squamous cell carcinoma antigen recognized by T-cells 3 OS=Musmusculus GN=Sart3 - [SART3_MOUSE]	4.49	2	2	2	2	45.3
Q7TMB8-2	Isoform 2 of Cytoplasmic FMR1-interacting protein 1 OS=Musmusculus GN=Cyfp1 - [CYFP1_MOUSE]	1.68	4	2	2	2	144.9
Q9EPL8	Importin-7 OS=Musmusculus GN=Ipo7 PE=1 SV=2 - [IPO7_MOUSE]	2.02	1	2	2	2	119.4
P10107	Annexin A1 OS=Musmusculus GN=Anxa1 PE=1 SV=2 - [ANXA1_MOUSE]	6.94	1	2	2	2	38.7

**Table 6.1 (continued)**

E9QKZ2	Importin-9 OS=Musmusculus GN=Ipo9 PE=4 SV=1 - [E9QKZ2_MOUSE]	2.12	2	2	2	2	115.9
--------	--------------------------------------------------------------	------	---	---	---	---	-------

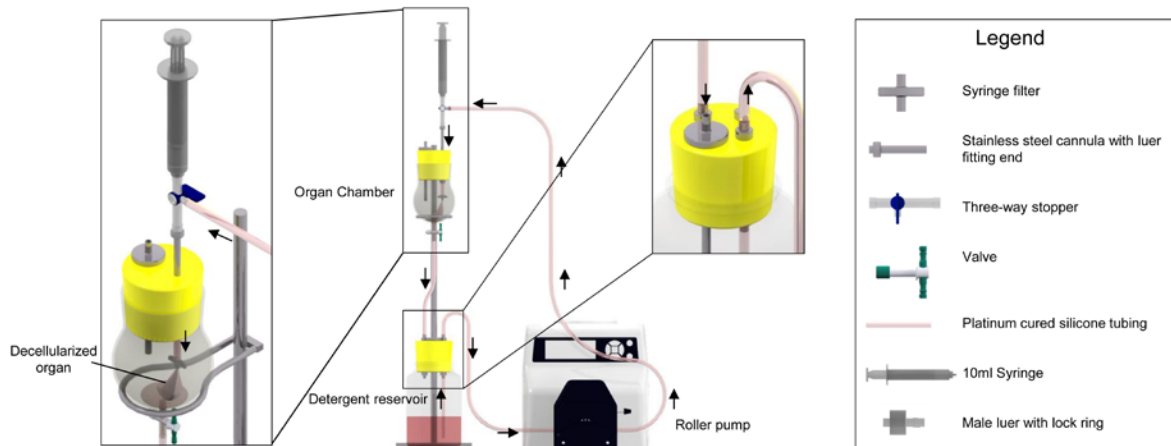


**Figure A.2 ProE schematic drawing of perfusion-decellularization set-up**

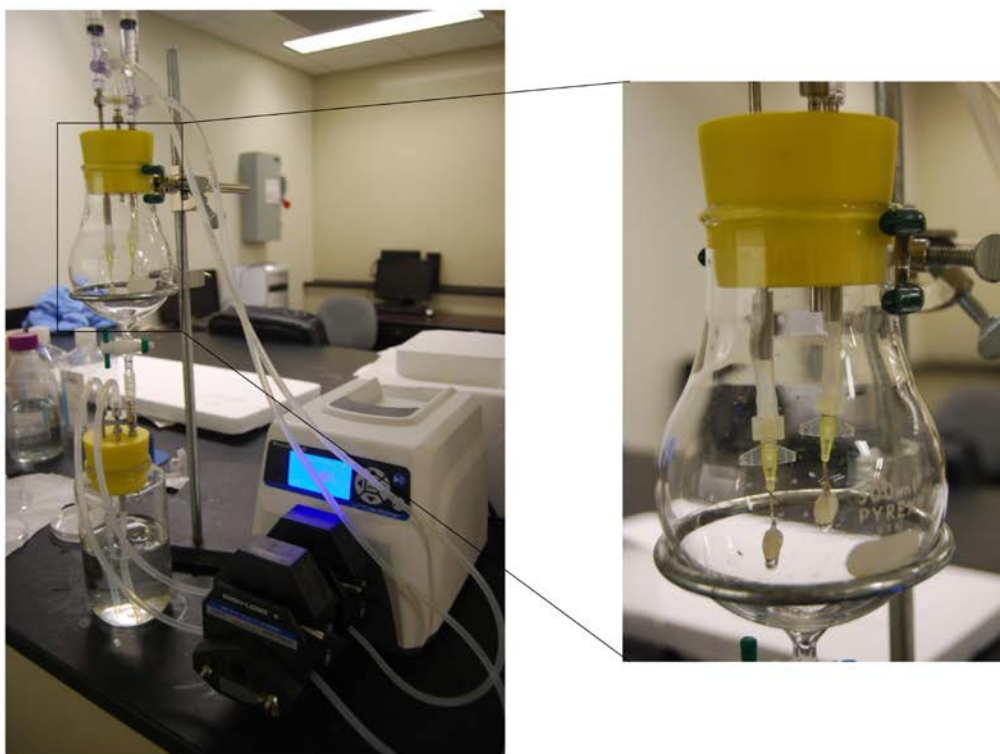


**Figure A.3 Perfusion system is compatible for scaling up**

The photograph shows the capability of peristaltic pump to accommodate two pump head and drive the perfusion of additional lines for decellularization for a proof-of-concept for scale up. Inset with higher magnification of two hearts being decellularized.



**Figure A.4 Microbiological testing for bioreactor culture**

The microbiological evaluation showed no microbiological contamination. Negative control (left): Culture medium before exposure to bioreactor culture, positive control (right): culture medium added with E-Coli bacteria.

### **A.1.1 Mathematical modeling of oxygen diffusion across oxygenator in in-house bioreactor**

Silicone tubing used in the bioreactor acts as a medium for exchange of gases between the aqueous media and the environment. This tubing has a high oxygen permeability ( $\kappa$ ) of  $5.97 \times 10^{-17} \frac{m^3 \cdot m}{m^3 \cdot s \cdot Pa}$  [Cole-Parmer tubing reference]. While travelling the length of the tube, the media will get oxygenated continuously until oxygen concentration reaches equilibrium with the surrounding ambient air in contact with the tubing. The minimum theoretical length of the tubing required for maximum oxygenation of the media can be calculated using a steady state mass balance equation. In the following paragraphs, salient features of a mathematical model used to determine this length are given.

The fundamental balance equation across a cylindrical control volume (Figure A.5) can be written as:

Oxygen in – Oxygen out + Oxygen transferred across tube thickness = 0

$$F_i(z)A - F_i(z+dz)A + F_r Adz = 0 \quad \dots(1)$$

where,

$F_i(z)$ : molar flux of oxygen at  $z$  (Unit :  $\text{mol} / \text{m}^2 - \text{s}$ )

$F_i(z+dz)$ : molar flux of oxygen at  $z+dz$

$A$ : cross-sectional area of flow channel

$F_r$ : molar flux across the tube surface

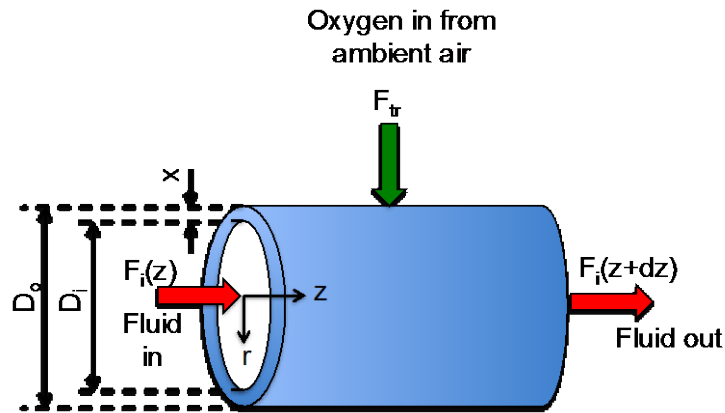


Figure A.5 Cylindrical control volume used for the mass balance equation

Here, the aqueous media is assumed to be an incompressible fluid flowing at constant temperature. The oxygen concentration of the media entering the silicone tubing is very low and therefore, assumed to be zero. Any presence of oxygen at the tube inlet will only slightly overestimate the minimum length. It is assumed that each type of gas from the ambient or the media is diffusing through the thickness of the tube independently of each other and the ambient air inside the incubator is assumed to be an ideal gas. Hence, a balance equation for oxygen can

be written independently of other gases like N<sub>2</sub>, CO<sub>2</sub> etc. The flux of oxygen transfer is related to the oxygen partial pressure drop across the tubing by Darcy's law as follows:

$$F_{tr} = \frac{\kappa}{V_m} \frac{\Delta P}{x} \quad \dots(2)$$

where,

$\kappa$ : permeability of oxygen through the pipe tubing

$V_m$  : molar volume of oxygen (2.45 x 10<sup>-7</sup> m<sup>3</sup>/mol, calculated using Ideal Gas approximation at 37 °C and 1 atm pressure)

$x$ : thickness of the tube

$\Delta P$  : Drop in oxygen partial pressure across the thickness of the tube =  $y_{ambient}P_{ambient} - y(z)P(z)$

Here,  $P$  denotes the absolute pressure and  $y$  denotes mole fraction of oxygen

Once oxygen has entered the inner surface of the tube, it is immediately dissolved into the aqueous medium. Once dissolved, the diffusion of oxygen in the radial direction is instantaneous and therefore, an average oxygen concentration in the aqueous medium can be tracked along the axial 'z' direction with no change in the radial direction. The solubility of oxygen transferred through the tube wall into the aqueous flow is governed by Henry's law for dilute solutions at STP, given by:

$$y(z)P(z) = k_H C_{O_2}(z) \quad \dots(3)$$

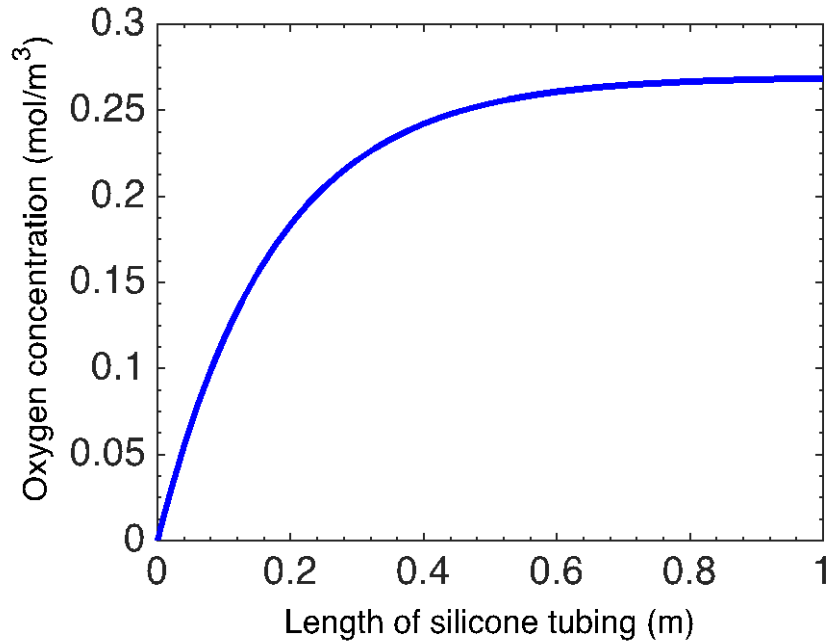
The Henry's law can be used to relate the partial pressure of oxygen at the inner surface of the tubing to the average concentration in the aqueous media. The solubility constant ( $k_H$ ) for oxygen at STP is  $77942 \text{ Pa m}^3 / \text{mol}$ .

Volumetric flow rate ( $Q$ ) through the pipe can be related to the average flow velocity ( $v$ ) through the relation,  $Q = v \cdot A$  ... (4)

Using Equations (1-4), the rate of change of oxygen concentration across the length of the tubing is given by:

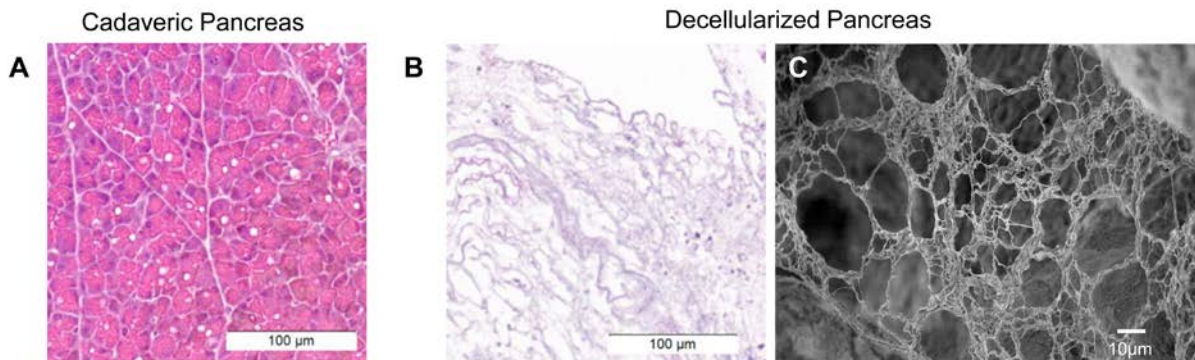
$$v \frac{dC_{O_2}(z)}{dz} = \frac{\kappa}{V_m} \frac{(y_{ambien} P_{ambien} - k_H C_{O_2}(z))}{x} \quad \dots(5)$$

Figure A.6 shows the model predicted concentration of oxygen along the length of the tube. The oxygen concentration rises gradually and reaches a steady value from 0.8 to 1 m. A final length of 1 m is chosen in the final design.



**Figure A.6 Average axial oxygen concentration.**

The curve shows the mean concentration as predicted by Equation 5. Geometric constants for the tubing are: Inner Diameter = 3.1 mm, Outer Diameter = 6.1 mm. Flow rate is kept constant at 1 ml/min.



**Figure A.7 Decellularization of adult mouse pancreas.**

(A) H&E staining of cadaveric pancreas. (B) H&E staining image shows complete removal of cells (left) and SEM image shows the intact matrix of architecture of decellularized pancreas.

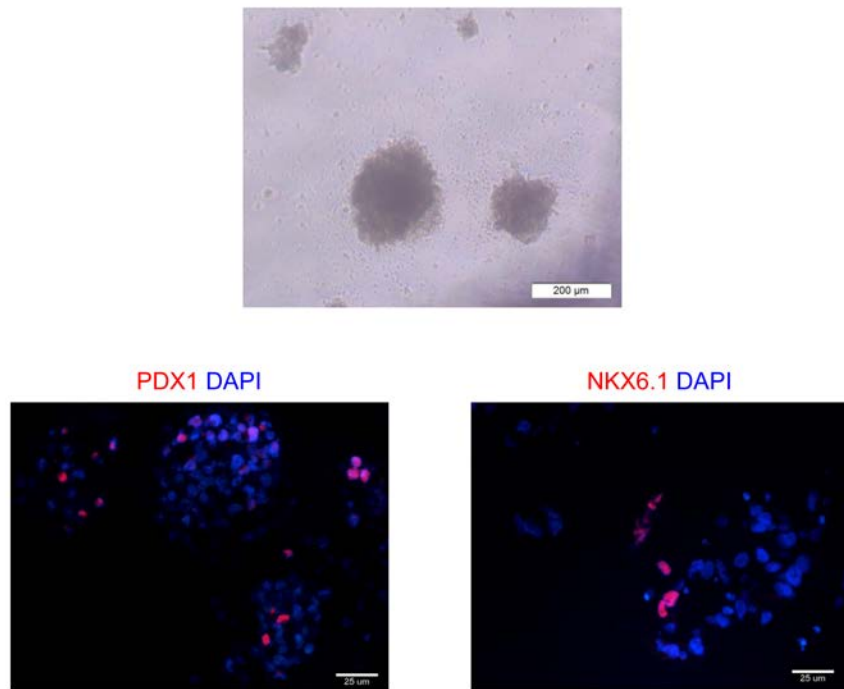


**Figure A.8 Matrigel culture of 3D PP aggregates as control.**

(A) Phase image of 3D PP aggregates cultured on matrigel. (B) Immunostaining shows low expression of Pdx1 and Nkx6.1 indicating inability of matrigel to promote differentiation of 3D PP aggregates.

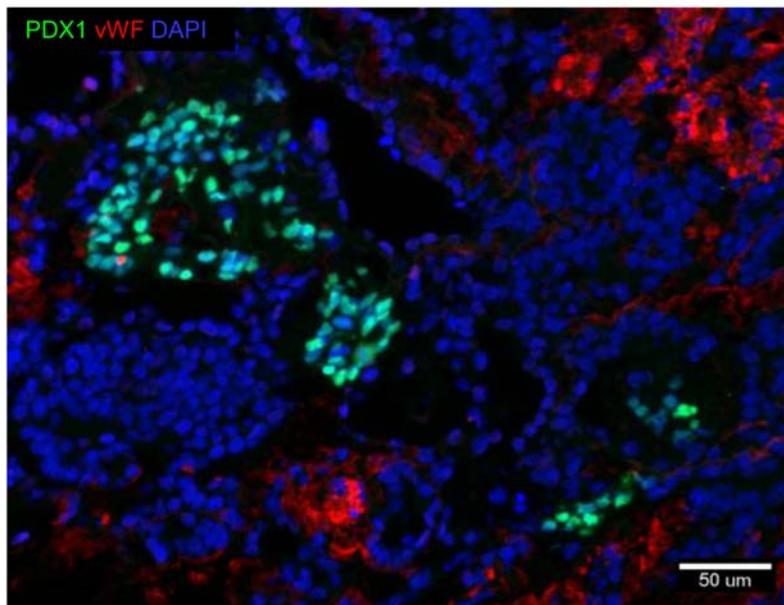


**Figure A.9 Co-seeding of endothelial and PP cells into decellularized liver.**

(A) Immunostaining shows the presence of pancreatic transcription factor, Pdx1 (green) and endothelial marker, vWF (red) on the engrafted cells.

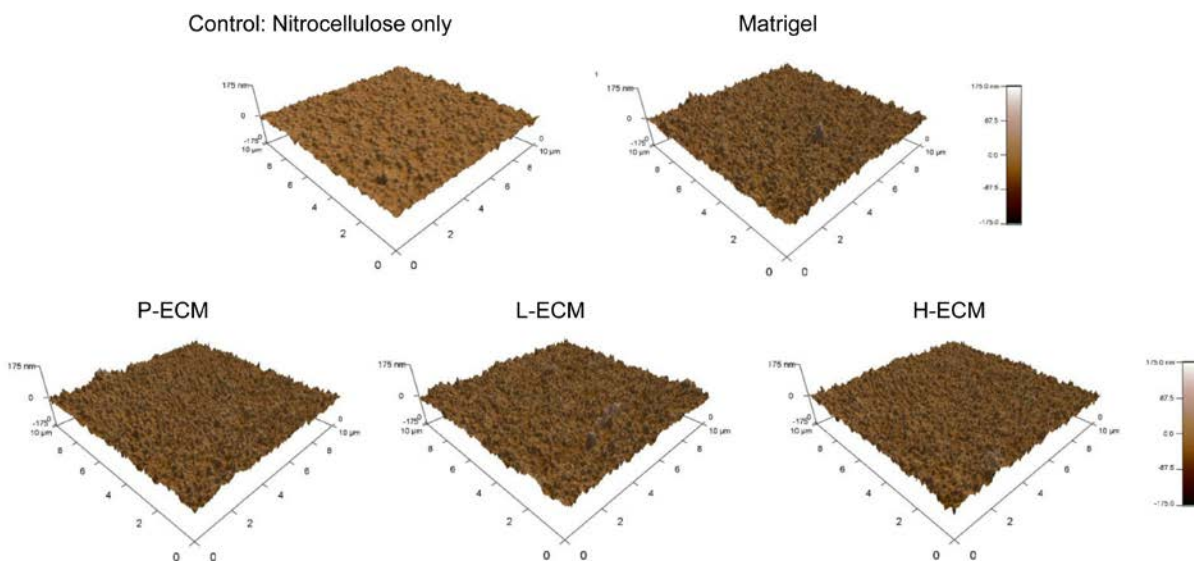


**Figure A.10 AFM images showing the surface roughness of 2D ECM array.**

Different organ-ECM were immobilized onto nitrocellulose coated glass and showed higher RMS value than nitrocellulose only surface.

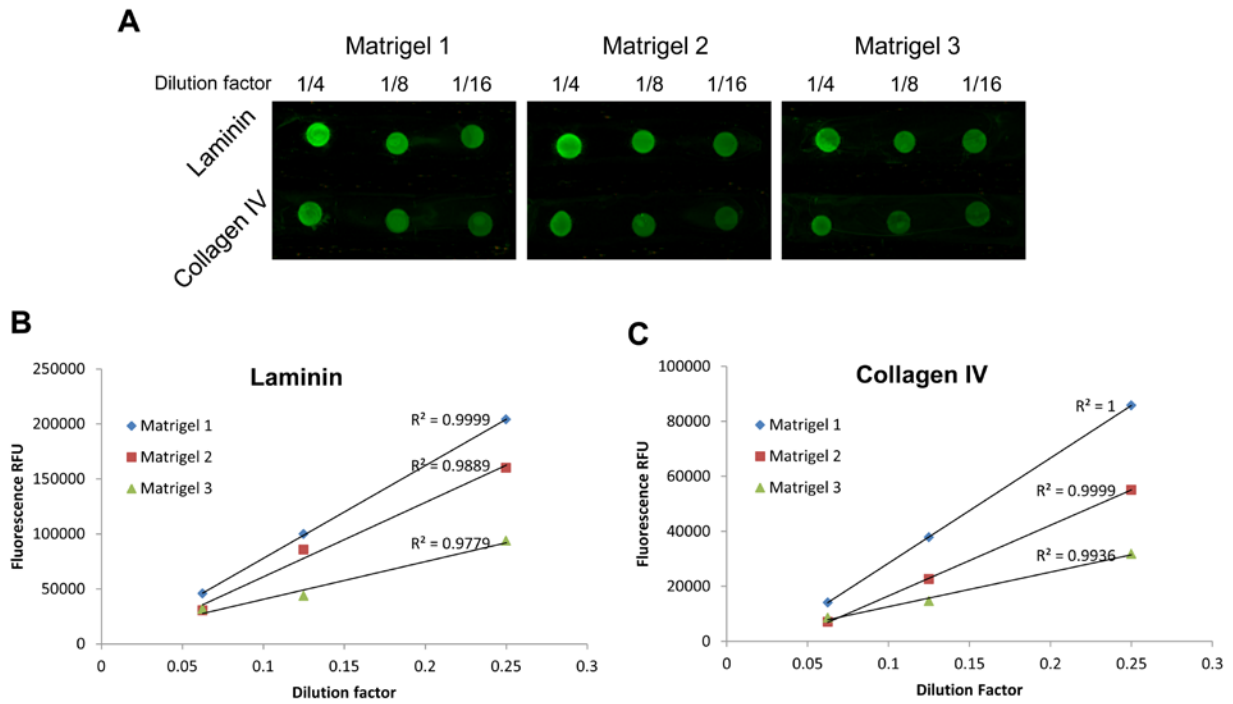


**Figure A.11 Sensitivity analysis of the on-chip IR Dye immunofluorescence staining with LI-COR scanner.**

(A) LI-COR images 2D ECM array showed stained matrigel microspots with laminin and collagen IV antibodies. Three different lots of matrigel were evaluated. (B) Correlation plot of fluorescence intensity from laminin staining showed good linearity across different dilutions of matrigel. (C) Correlation plot of fluorescence intensity from collagen IV staining showed good linearity across different dilutions of matrigel.

## LICOR sensitivity 2D vs 3D

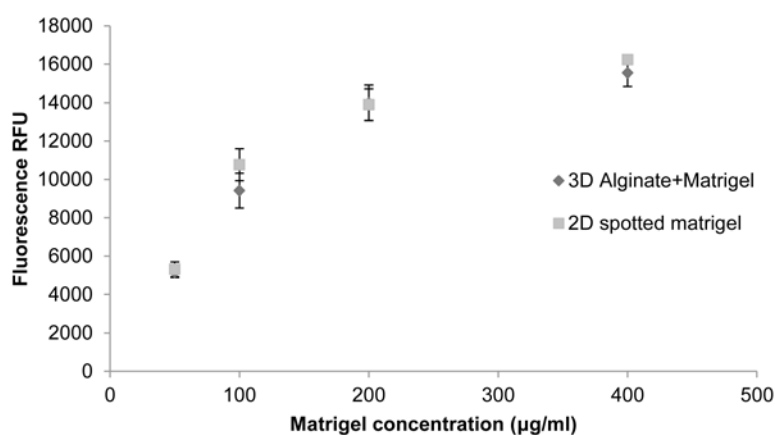


**Figure A.12 LICOR sensitivity for 2D and 3D analysis**

Collagen IV staining of matrigel on 2D spotted matrigel and 3D alginate-matrigel mixture. Analysis shows similar RFU intensity detected in both configurations indicating the sensitivity of the LICOR detection and scalable to 3D configuration.



**Figure A.13 Spot breakage was observed when larger PP aggregates were cultured inside the 3D alginate microspots.**

(A) Day 5 phase contrast image of the PP aggregates inside 3D alginate microspot. (B) Live/dead image of the PP aggregates inside 3D alginate microspot. (C) Merged phase contrast and live/dead image of the PP aggregates inside 3D alginate microspot.

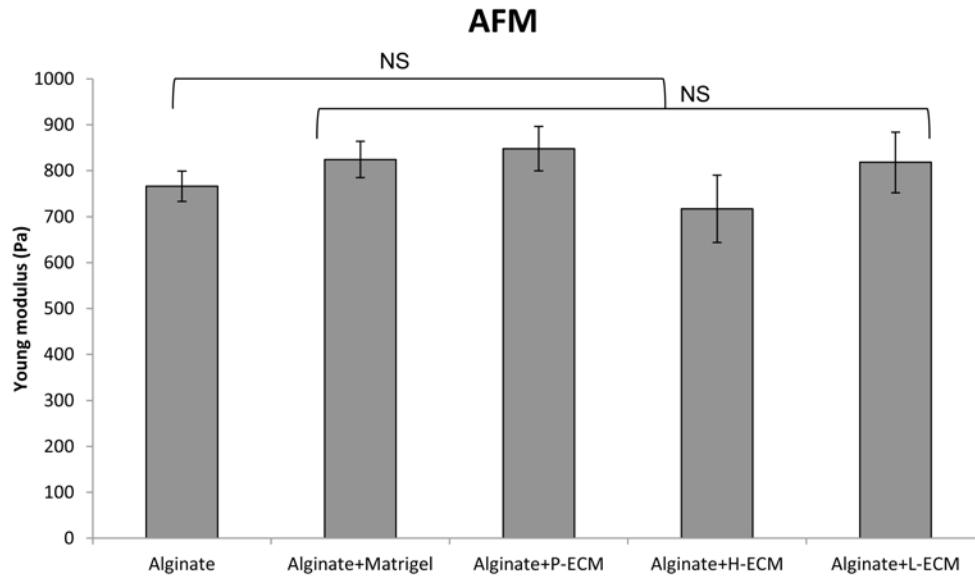


**Figure A.14 AFM stiffness measurement of the 3D ECM array.**

The AFM stiffness measurement showed no significant change in young modulus after incorporation of organ-derived ECM or matrigel. (n=5, P>0.05)

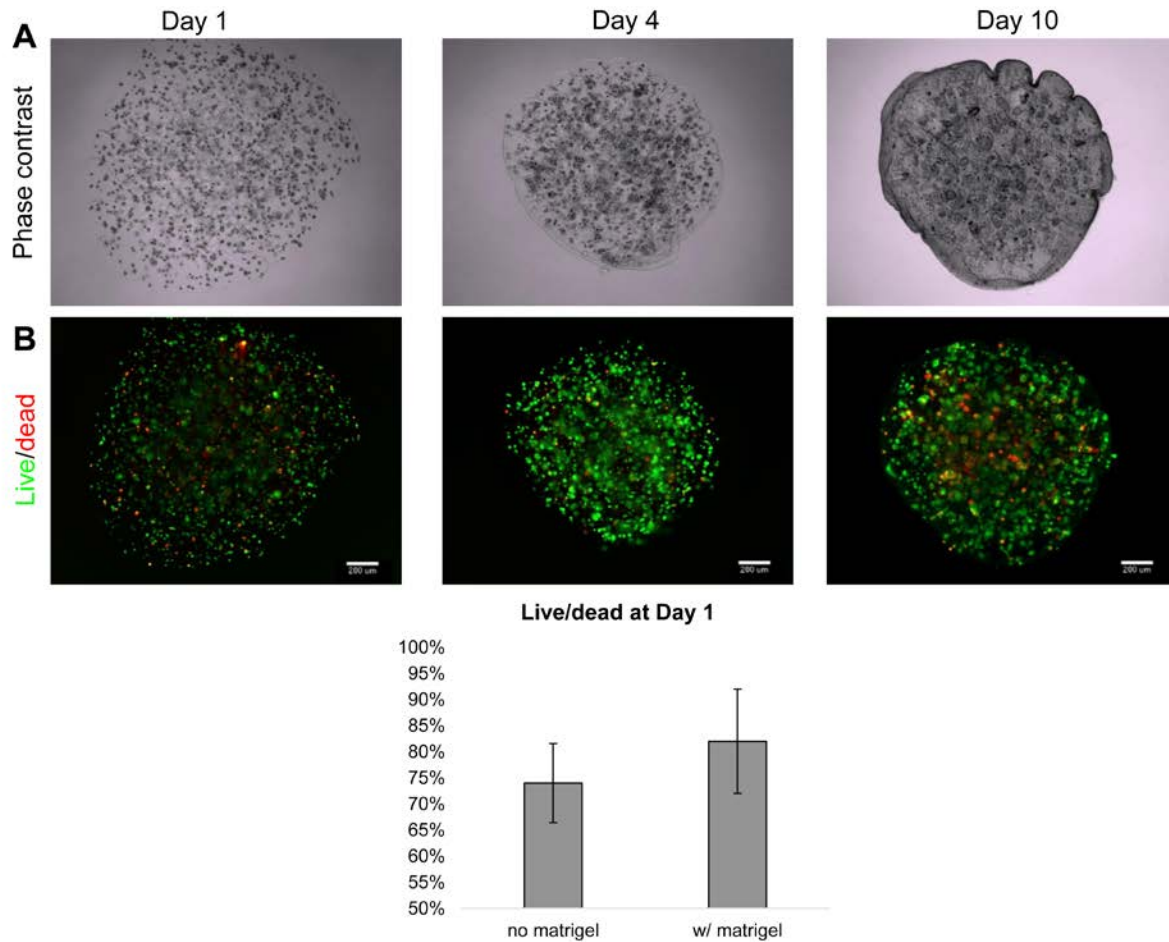


**Figure A.15 Single cells of MIN-6 beta cells exhibited good viability throughout 10 days culture inside 3D alginate microspots with and without matrigel.**

(A) Phase contrast images of the cell-laden 3D alginate microspots on day 1, day 4, and day 10. (B) Live/dead images of viable MIN-6 beta cells in 3D alginate microspots on day 1, day 4, and day 10. (C) Quantification of percentage live/dead of the MIN-6 beta cells in 3D alginate microspots on day 10. No significant difference were found between matrigel and without matrigel incorporated alginate microspots. (n=5, P>0.05)

## BIBLIOGRAPHY

- [1] MacFarlane W, Bone A, Harrison M. Pancreas Biology, Pathology, and Tissue Engineering. In: Santin M, editor. *Strategies in Regenerative Medicine*: Springer New York; 2009. p. 1-21.
- [2] Kim SK, Hebrok M, Melton DA. Notochord to endoderm signaling is required for pancreas development. *Development*. 1997;124:4243-52.
- [3] Hebrok M, Kim SK, Melton DA. Notochord repression of endodermal Sonic hedgehog permits pancreas development. *Genes Dev*. 1998;12:1705-13.
- [4] Hebrok M, Kim SK, St Jacques B, McMahon AP, Melton DA. Regulation of pancreas development by hedgehog signaling. *Development*. 2000;127:4905-13.
- [5] Kumar M, Jordan N, Melton D, Grapin-Botton A. Signals from lateral plate mesoderm instruct endoderm toward a pancreatic fate. *Dev Biol*. 2003;259:109-22.
- [6] Jorgensen MC, Ahnfelt-Ronne J, Hald J, Madsen OD, Serup P, Hecksher-Sorensen J. An illustrated review of early pancreas development in the mouse. *Endocr Rev*. 2007;28:685-705.
- [7] Hisaoka M, Haratake J, Hashimoto H. Pancreatic morphogenesis and extracellular matrix organization during rat development. *Differentiation*. 1993;53:163-72.
- [8] Jiang FX, Harrison LC. Extracellular signals and pancreatic beta-cell development: a brief review. *Mol Med*. 2002;8:763-70.
- [9] Meyer T, Chodnewska I, Czub S, Hamelmann W, Beutner U, Otto C, et al. Extracellular matrix proteins in the porcine pancreas: a structural analysis for directed pancreatic islet isolation. *Transplant Proc*. 1998;30:354.
- [10] Van Deijnen JH, Van Suylichem PT, Wolters GH, Van Schilfgaarde R. Distribution of collagens type I, type III and type V in the pancreas of rat, dog, pig and man. *Cell Tissue Res*. 1994;277:115-21.
- [11] Bulow HE, Hobert O. The molecular diversity of glycosaminoglycans shapes animal development. *Annu Rev Cell Dev Biol*. 2006;22:375-407.
- [12] Jiang FX, Cram DS, DeAizpurua HJ, Harrison LC. Laminin-1 promotes differentiation of fetal mouse pancreatic beta-cells. *Diabetes*. 1999;48:722-30.

- [13] Falk M, Ferletta M, Forsberg E, Ekblom P. Restricted distribution of laminin alpha1 chain in normal adult mouse tissues. *Matrix Biol.* 1999;18:557-68.
- [14] Virtanen I, Gullberg D, Rissanen J, Kivilaakso E, Kiviluoto T, Laitinen LA, et al. Laminin alpha1-chain shows a restricted distribution in epithelial basement membranes of fetal and adult human tissues. *Exp Cell Res.* 2000;257:298-309.
- [15] Crisera CA, Kadison AS, Breslow GD, Maldonado TS, Longaker MT, Gittes GK. Expression and role of laminin-1 in mouse pancreatic organogenesis. *Diabetes.* 2000;49:936-44.
- [16] Gittes GK, Galante PE, Hanahan D, Rutter WJ, Debase HT. Lineage-specific morphogenesis in the developing pancreas: role of mesenchymal factors. *Development.* 1996;122:439-47.
- [17] Li Z, Manna P, Kobayashi H, Spilde T, Bhatia A, Preuett B, et al. Multifaceted pancreatic mesenchymal control of epithelial lineage selection. *Developmental Biology.* 2004;269:252-63.
- [18] Jiang FX, Georges-Labouesse E, Harrison LC. Regulation of Laminin 1-Induced Pancreatic  $\beta$ -Cell Differentiation by  $\alpha$ 6 Integrin and  $\alpha$ -Dystroglycan. *Molecular Medicine.* 2001;7:107-14.
- [19] De Breuck S, Lardon J, Rooman I, Bouwens L. Netrin-1 expression in fetal and regenerating rat pancreas and its effect on the migration of human pancreatic duct and porcine islet precursor cells. *Diabetologia.* 2003;46:926-33.
- [20] Fitzgerald DP, Seaman C, Cooper HM. Localization of Neogenin protein during morphogenesis in the mouse embryo. *Dev Dyn.* 2006;235:1720-5.
- [21] Yebra M, Montgomery AMP, Diaferia GR, Kaido T, Silletti S, Perez B, et al. Recognition of the Neural Chemoattractant Netrin-1 by Integrins  $[\alpha]6[\beta]4$  and  $[\alpha]3[\beta]1$  Regulates Epithelial Cell Adhesion and Migration. *Developmental Cell.* 2003;5:695-707.
- [22] Cirulli V, Beattie GM, Klier G, Ellisman M, Ricordi C, Quaranta V, et al. Expression and Function of  $\alpha$ v $\beta$ 3 and  $\alpha$ v $\beta$ 5 Integrins in the Developing Pancreas. *The Journal of Cell Biology.* 2000;150:1445-60.
- [23] Kaido T, Yebra M, Cirulli V, Montgomery AM. Regulation of human beta-cell adhesion, motility, and insulin secretion by collagen IV and its receptor  $\alpha$ 1 $\beta$ 1. *J Biol Chem.* 2004;279:53762-9.
- [24] Otonkoski T, Banerjee M, Korsgren O, Thornell LE, Virtanen I. Unique basement membrane structure of human pancreatic islets: implications for  $\beta$ -cell growth and differentiation. *Diabetes, Obesity and Metabolism.* 2008;10:119-27.
- [25] Meyer T, Czub S, Chodnewska I, Beutner U, Hamelmann W, Klock G, et al. Expression pattern of extracellular matrix proteins in the pancreas of various domestic pig breeds, the Goettingen Minipig and the Wild Boar. *Ann Transplant.* 1997;2:17-26.

- [26] Jiang FX, Naselli G, Harrison LC. Distinct distribution of laminin and its integrin receptors in the pancreas. *J Histochem Cytochem.* 2002;50:1625-32.
- [27] Nikolova G, Jabs N, Konstantinova I, Domogatskaya A, Tryggvason K, Sorokin L, et al. The vascular basement membrane: a niche for insulin gene expression and Beta cell proliferation. *Dev Cell.* 2006;10:397-405.
- [28] van Deijnen JH, Hulstaert CE, Wolters GH, van Schilfgaarde R. Significance of the perinsular extracellular matrix for islet isolation from the pancreas of rat, dog, pig, and man. *Cell Tissue Res.* 1992;267:139-46.
- [29] Virtanen I, Banerjee M, Palgi J, Korsgren O, Lukinius A, Thornell LE, et al. Blood vessels of human islets of Langerhans are surrounded by a double basement membrane. *Diabetologia.* 2008;51:1181-91.
- [30] Armanet M, Wojtuszczyz A, Morel P, Parnaud G, Rousselle P, Sinigaglia C, et al. Regulated laminin-332 expression in human islets of Langerhans. *FASEB J.* 2009;23:4046-55.
- [31] Parnaud G, Hammar E, Rouiller DG, Armanet M, Halban PA, Bosco D. Blockade of beta1 integrin-laminin-5 interaction affects spreading and insulin secretion of rat beta-cells attached on extracellular matrix. *Diabetes.* 2006;55:1413-20.
- [32] Hughes SJ, Clark A, McShane P, Contractor HH, Gray DW, Johnson PR. Characterisation of collagen VI within the islet-exocrine interface of the human pancreas: implications for clinical islet isolation? *Transplantation.* 2006;81:423-6.
- [33] Whitcomb DC. Pancreatitis. In: Services UDoHaH, editor.: National Institute of Health; 2008.
- [34] Ansari D, Rosendahl A, Elebro J, Andersson R. Systematic review of immunohistochemical biomarkers to identify prognostic subgroups of patients with pancreatic cancer. *Br J Surg.* 98:1041-55.
- [35] Castellanos E, Berlin J, Cardin DB. Current treatment options for pancreatic carcinoma. *Curr Oncol Rep.* 13:195-205.
- [36] Shaw JE, Sicree RA, Zimmet PZ. Global estimates of the prevalence of diabetes for 2010 and 2030. *Diabetes Research and Clinical Practice.* 2010;87:4-14.
- [37] Maraschin Jde F. Classification of diabetes. *Adv Exp Med Biol.* 2012;771:12-9.
- [38] Liao YH, Verchere CB, Warnock GL. Adult stem or progenitor cells in treatment for type 1 diabetes: current progress. *Can J Surg.* 2007;50:137-42.
- [39] MacFarlane WM, Bone AJ, Harrison M. Pancreas Biology, Pathology, and Tissue Engineering. In: Santin M, editor. *Strategies in Regenerative Medicine: Springer Science*; 2009. p. 261-78.

- [40] Srinivasan P, Huang GC, Amiel SA, Heaton ND. Islet cell transplantation. *Postgrad Med J*. 2007;83:224-9.
- [41] Mercado-Pagan AE, Stahl AM, Shanjani Y, Yang Y. Vascularization in bone tissue engineering constructs. *Ann Biomed Eng*. 2015;43:718-29.
- [42] Welsh N. Prospects for gene therapy of diabetes mellitus. *Gene Ther*. 2000;7:181-2.
- [43] Shapiro A, Lakey J, Ryan E, Korbitt G, Toth E, Warnock G, et al. Islet Transplantation in Seven Patients with Type 1 Diabetes Mellitus Using a Glucocorticoid-Free Immunosuppressive Regimen. *New England Journal of Medicine*. 2000;343:230-8.
- [44] Langer RM. Islet transplantation: lessons learned since the Edmonton breakthrough. *Transplant Proc*. 42:1421-4.
- [45] Vardanyan M, Parkin E, Gruessner C, Rodriguez Rilo HL. Pancreas vs. islet transplantation: a call on the future. *Curr Opin Organ Transplant*. 2010;15:124-30.
- [46] Gruessner AC, Sutherland DER. Pancreas transplant outcomes for United States (US) and non-US cases as reported to the United Network for Organ Sharing (UNOS) and the International Pancreas Transplant Registry (IPTR) as of June 2004. *Clinical Transplantation*. 2005;19:433-55.
- [47] Badylak SF, Weiss DJ, Caplan A, Macchiarini P. Engineered whole organs and complex tissues. *Lancet*. 2012;379:943-52.
- [48] Weber LM, Anseth KS. Hydrogel encapsulation environments functionalized with extracellular matrix interactions increase islet insulin secretion. *Matrix Biol*. 2008;27:667-73.
- [49] Weber LM, Hayda KN, Anseth KS. Cell-matrix interactions improve beta-cell survival and insulin secretion in three-dimensional culture. *Tissue Eng Part A*. 2008;14:1959-68.
- [50] Goh SK, Bertera S, Olsen P, Candiello JE, Halfter W, Uechi G, et al. Perfusion-decellularized pancreas as a natural 3D scaffold for pancreatic tissue and whole organ engineering. *Biomaterials*. 2013;34:6760-72.
- [51] Mirmalek-Sani SH, Orlando G, McQuilling JP, Pareta R, Mack DL, Salvatori M, et al. Porcine pancreas extracellular matrix as a platform for endocrine pancreas bioengineering. *Biomaterials*. 2013;34:5488-95.
- [52] Conrad C, Schuetz C, Clippinger B, Vacanti JP, Markmann JF, Ott HC. Bio-engineered endocrine pancreas based on decellularized pancreatic matrix and mesenchymal stem cell/islet cell coculture. *Journal of the American College of Surgeons*. 2010;211:S62.
- [53] Calafiore R, Basta G, Luca G, Boselli C, Bufalari A, Giustozzi GM, et al. Transplantation of allogeneic/xenogeneic pancreatic islets containing coherent microcapsules in adult pigs. *Transplant Proc*. 1998;30:482-3.

- [54] Yang L, Li S, Hatch H, Ahrens K, Cornelius JG, Petersen BE, et al. In vitro trans-differentiation of adult hepatic stem cells into pancreatic endocrine hormone-producing cells. *Proceedings of the National Academy of Sciences of the United States of America*. 2002;99:8078-83.
- [55] Rezania A, Bruin JE, Arora P, Rubin A, Batushansky I, Asadi A, et al. Reversal of diabetes with insulin-producing cells derived in vitro from human pluripotent stem cells. *Nat Biotech*. 2014;32:1121-33.
- [56] Pagliuca Felicia W, Millman Jeffrey R, Gürtler M, Segel M, Van Dervort A, Ryu Jennifer H, et al. Generation of Functional Human Pancreatic  $\beta$  Cells In Vitro. *Cell*. 2014;159:428-39.
- [57] D'Amour KA, Bang AG, Eliazer S, Kelly OG, Agulnick AD, Smart NG, et al. Production of pancreatic hormone-expressing endocrine cells from human embryonic stem cells. *Nat Biotech*. 2006;24:1392-401.
- [58] Kroon E, Martinson LA, Kadoya K, Bang AG, Kelly OG, Eliazer S, et al. Pancreatic endoderm derived from human embryonic stem cells generates glucose-responsive insulin-secreting cells in vivo. *Nat Biotech*. 2008;26:443-52.
- [59] Baptista PM, Orlando G, Mirmalek-Sani SH, Siddiqui M, Atala A, Soker S. Whole organ decellularization - a tool for bioscaffold fabrication and organ bioengineering. *Conf Proc IEEE Eng Med Biol Soc*. 2009;2009:6526-9.
- [60] Song JJ, Ott HC. Organ engineering based on decellularized matrix scaffolds. *Trends in Molecular Medicine*. 2011;17:424-32.
- [61] Schulz TC, Young HY, Agulnick AD, Babin MJ, Baetge EE, Bang AG, et al. A scalable system for production of functional pancreatic progenitors from human embryonic stem cells. *PLoS ONE*. 2012;7:e37004.
- [62] Cheng JY, Raghunath M, Whitelock J, Poole-Warren L. Matrix components and scaffolds for sustained islet function. *Tissue Eng Part B Rev*. 2011;17:235-47.
- [63] Efrat S, Linde S, Kofod H, Spector D, Delannoy M, Grant S, et al. Beta-cell lines derived from transgenic mice expressing a hybrid insulin gene-oncogene. *Proc Natl Acad Sci U S A*. 1988;85:9037-41.
- [64] Thomson JA, Itskovitz-Eldor J, Shapiro SS, Waknitz MA, Swiergiel JJ, Marshall VS, et al. Embryonic stem cell lines derived from human blastocysts. *Science*. 1998;282:1145-7.
- [65] Lumelsky N, Blondel O, Laeng P, Velasco I, Ravin R, McKay R. Differentiation of embryonic stem cells to insulin-secreting structures similar to pancreatic islets. *Science*. 2001;292:1389-94.

- [66] Nostro MC, Sarangi F, Yang C, Holland A, Elefanty AG, Stanley EG, et al. Efficient generation of NKX6-1+ pancreatic progenitors from multiple human pluripotent stem cell lines. *Stem Cell Reports*. 2015;4:591-604.
- [67] Rezania A, Bruin JE, Riedel MJ, Mojibian M, Asadi A, Xu J, et al. Maturation of human embryonic stem cell-derived pancreatic progenitors into functional islets capable of treating pre-existing diabetes in mice. *Diabetes*. 2012;61:2016-29.
- [68] Rezania A, Bruin JE, Xu J, Narayan K, Fox JK, O'Neil JJ, et al. Enrichment of human embryonic stem cell-derived NKX6.1-expressing pancreatic progenitor cells accelerates the maturation of insulin-secreting cells in vivo. *Stem Cells*. 2013;31:2432-42.
- [69] Richardson T, Kumta PN, Banerjee I. Alginate Encapsulation of Human Embryonic Stem Cells to Enhance Directed Differentiation to Pancreatic Islet-Like Cells. *Tissue Eng Part A*. 2014.
- [70] Jaramillo M, Mathew S, Mamiya H, Goh SK, Banerjee I. Endothelial cells mediate islet-specific maturation of human embryonic stem cell-derived pancreatic progenitor cells. *Tissue Eng Part A*. 2015;21:14-25.
- [71] Jaramillo M, Mathew S, Task K, Barner S, Banerjee I. Potential for pancreatic maturation of differentiating human embryonic stem cells is sensitive to the specific pathway of definitive endoderm commitment. *PLoS One*. 2014;9:e94307.
- [72] Jiang J, Au M, Lu K, Eshpeter A, Korbitt G, Fisk G, et al. Generation of insulin-producing islet-like clusters from human embryonic stem cells. *Stem Cells*. 2007;25:1940-53.
- [73] Takahashi K, Yamanaka S. Induction of pluripotent stem cells from mouse embryonic and adult fibroblast cultures by defined factors. *Cell*. 2006;126:663-76.
- [74] Maehr R, Chen S, Snitow M, Ludwig T, Yagasaki L, Golland R, et al. Generation of pluripotent stem cells from patients with type 1 diabetes. *Proc Natl Acad Sci U S A*. 2009;106:15768-73.
- [75] Takeuchi H, Nakatsuji N, Suemori H. Endodermal differentiation of human pluripotent stem cells to insulin-producing cells in 3D culture. *Sci Rep*. 2014;4:4488.
- [76] Thatava T, Nelson TJ, Edukulla R, Sakuma T, Ohmine S, Tonne JM, et al. Indolactam V/GLP-1-mediated differentiation of human iPS cells into glucose-responsive insulin-secreting progeny. *Gene Ther*. 2011;18:283-93.
- [77] Thatava T, Kudva YC, Edukulla R, Squillace K, De Lamo JG, Khan YK, et al. Inpatient Variations in Type 1 Diabetes-specific iPS Cell Differentiation Into Insulin-producing Cells. *Mol Ther*. 2013;21:228-39.
- [78] Pagliuca FW, Millman JR, Gurtler M, Segel M, Van Dervort A, Ryu JH, et al. Generation of functional human pancreatic beta cells in vitro. *Cell*. 2014;159:428-39.

- [79] Rezania A, Bruin JE, Arora P, Rubin A, Batushansky I, Asadi A, et al. Reversal of diabetes with insulin-producing cells derived in vitro from human pluripotent stem cells. *Nat Biotechnol.* 2014;32:1121-33.
- [80] Criscimanna A, Speicher JA, Houshmand G, Shiota C, Prasad K, Ji B, et al. Duct cells contribute to regeneration of endocrine and acinar cells following pancreatic damage in adult mice. *Gastroenterology.* 2011;141:1451-62, 62 e1-6.
- [81] Lemper M, Leuckx G, Heremans Y, German MS, Heimberg H, Bouwens L, et al. Reprogramming of human pancreatic exocrine cells to [beta]-like cells. *Cell Death Differ.* 2015;22:1117-30.
- [82] Zhou Q, Brown J, Kanarek A, Rajagopal J, Melton DA. In vivo reprogramming of adult pancreatic exocrine cells to [bgr]-cells. *Nature.* 2008;455:627-32.
- [83] Baeyens L, De Breuck S, Lardon J, Mfopou JK, Rooman I, Bouwens L. In vitro generation of insulin-producing beta cells from adult exocrine pancreatic cells. *Diabetologia.* 2005;48:49-57.
- [84] Berneman-Zeitouni D, Molakandov K, Elgart M, Mor E, Fornoni A, Dominguez MR, et al. The temporal and hierarchical control of transcription factors-induced liver to pancreas transdifferentiation. *PLoS One.* 2014;9:e87812.
- [85] Meivar-Levy I, Ferber S. New organs from our own tissues: liver-to-pancreas transdifferentiation. *Trends Endocrinol Metab.* 2003;14:460-6.
- [86] Juhl K, Bonner-Weir S, Sharma A. Regenerating pancreatic beta-cells: plasticity of adult pancreatic cells and the feasibility of in-vivo neogenesis. *Curr Opin Organ Transplant.* 2010;15:79-85.
- [87] Dufrane D, Gianello P. Macro- or microencapsulation of pig islets to cure type 1 diabetes. *World J Gastroenterol.* 2012;18:6885-93.
- [88] van der Windt DJ, Bottino R, Kumar G, Wijkstrom M, Hara H, Ezzelarab M, et al. Clinical islet xenotransplantation: how close are we? *Diabetes.* 2012;61:3046-55.
- [89] Chun S, Huang Y, Xie WJ, Hou Y, Huang RP, Song YM, et al. Adhesive growth of pancreatic islet cells on a polyglycolic acid fibrous scaffold. *Transplant Proc.* 2008;40:1658-63.
- [90] Yuan Y, Cong C, Zhang J, Wei L, Li S, Chen Y, et al. Self-assembling peptide nanofiber as potential substrates in islet transplantation. *Transplant Proc.* 2008;40:2571-4.
- [91] Zhao M, Song C, Zhang W, Hou Y, Huang R, Song Y, et al. The three-dimensional nanofiber scaffold culture condition improves viability and function of islets. *J Biomed Mater Res A.*94:667-72.

- [92] Racanicchi L, Conti V, Basta G, Montanucci P, Calafiore R. Effects of Poly-L-Lysine and Collagen on FH-B-TPN Cell Differentiation Into Endocrine Cell Phenotype. *Transplantation Proceedings*. 2008;40:419-21.
- [93] Fujita-Yamaguchi Y, Sacks DB, McDonald JM, Sahal D, Kathuria S. Effect of basic polycations and proteins on purified insulin receptor. Insulin-independent activation of the receptor tyrosine-specific protein kinase by poly(L-lysine). *Biochem J*. 1989;263:10.
- [94] Mason MN, Mahoney MJ. Selective  $\beta$ -Cell Differentiation of Dissociated Embryonic Pancreatic Precursor Cells Cultured in Synthetic Polyethylene Glycol Hydrogels. *Tissue Engineering Part A*. 2009;15:1343-52.
- [95] Mason MN, Arnold CA, Mahoney MJ. Entrapped Collagen Type 1 Promotes Differentiation of Embryonic Pancreatic Precursor Cells into Glucose-Responsive  $\beta$ -Cells When Cultured in Three-Dimensional PEG Hydrogels. *Tissue Engineering Part A*. 2009;15:3799-808.
- [96] Mason MN, Mahoney MJ. Inhibition of Gamma-Secretase Activity Promotes Differentiation of Embryonic Pancreatic Precursor Cells into Functional Islet-like Clusters in Poly(Ethylene Glycol) Hydrogel Culture. *Tissue Engineering Part A*. 2010;16:2593-603.
- [97] Lim F, Sun AM. Microencapsulated islets as bioartificial endocrine pancreas. *Science*. 1980;210:908-10.
- [98] Lucas-Clerc C, Massart C, Campion JP, Launois B, Nicol M. Long-term culture of human pancreatic islets in an extracellular matrix: morphological and metabolic effects. *Mol Cell Endocrinol*. 1993;94:9-20.
- [99] Brafman DA, Shah KD, Fellner T, Chien S, Willert K. Defining long-term maintenance conditions of human embryonic stem cells with arrayed cellular microenvironment technology. *Stem Cells Dev*. 2009;18:1141-54.
- [100] Flaim CJ, Teng D, Chien S, Bhatia SN. Combinatorial signaling microenvironments for studying stem cell fate. *Stem Cells Dev*. 2008;17:29-39.
- [101] Gilbert TW, Sellaro TL, Badylak SF. Decellularization of tissues and organs. *Biomaterials*. 2006;27:3675-83.
- [102] Thivolet CH, Chatelain P, Nicoloso H, Durand A, Bertrand J. Morphological and functional effects of extracellular matrix on pancreatic islet cell cultures. *Exp Cell Res*. 1985;159:313-22.
- [103] Zwolinski CM, Ellison KS, Depaola N, Thompson DM. Generation of cell-derived three dimensional extracellular matrix substrates from two dimensional endothelial cell cultures. *Tissue Eng Part C Methods*. 2011;17:589-95.
- [104] Tian XH, Xue WJ, Ding XM, Pang XL, Teng Y, Tian PX, et al. Small intestinal submucosa improves islet survival and function during in vitro culture. *World J Gastroenterol*. 2005;11:7378-83.

- [105] Woods EJ, Walsh CM, Sidner RA, Zieger MAJ, Lakey JRT, Ricordi C, et al. Improved in vitro function of islets using small intestinal submucosa. *Transplantation Proceedings*. 2004;36:1175-7.
- [106] De Carlo E, Baiguera S, Conconi MT, Vigolo S, Grandi C, Lora S, et al. Pancreatic acellular matrix supports islet survival and function in a synthetic tubular device: in vitro and in vivo studies. *Int J Mol Med*. 2010;25:195-202.
- [107] Mirmalek-Sani S-H, Orlando G, McQuilling JP, Pareta R, Mack DL, Salvatori M, et al. Porcine pancreas extracellular matrix as a platform for endocrine pancreas bioengineering. *Biomaterials*.
- [108] Ott HC, Matthiesen TS, Goh SK, Black LD, Kren SM, Netoff TI, et al. Perfusion-decellularized matrix: using nature's platform to engineer a bioartificial heart. *Nat Med*. 2008;14:213-21.
- [109] Robertson MJ, Dries-Devlin JL, Kren SM, Burchfield JS, Taylor DA. Optimizing recellularization of whole decellularized heart extracellular matrix. *PLoS One*. 2014;9:e90406.
- [110] Lu T-Y, Lin B, Kim J, Sullivan M, Tobita K, Salama G, et al. Repopulation of decellularized mouse heart with human induced pluripotent stem cell-derived cardiovascular progenitor cells. *Nat Commun*. 2013;4.
- [111] Petersen TH, Calle EA, Zhao L, Lee EJ, Gui L, Raredon MB, et al. Tissue-engineered lungs for in vivo implantation. *Science*. 2010;329:538-41.
- [112] Price AP, England KA, Matson AM, Blazar BR, Panoskaltsis-Mortari A. Development of a decellularized lung bioreactor system for bioengineering the lung: the matrix reloaded. *Tissue Eng Part A*. 2010;16:2581-91.
- [113] Daly AB, Wallis JM, Borg ZD, Bonvillain RW, Deng B, Ballif BA, et al. Initial binding and recellularization of decellularized mouse lung scaffolds with bone marrow-derived mesenchymal stromal cells. *Tissue Eng Part A*. 2012;18:1-16.
- [114] Bonvillain RW, Danchuk S, Sullivan DE, Betancourt AM, Semon JA, Eagle ME, et al. A nonhuman primate model of lung regeneration: detergent-mediated decellularization and initial in vitro recellularization with mesenchymal stem cells. *Tissue Eng Part A*. 2012;18:2437-52.
- [115] Uygun BE, Soto-Gutierrez A, Yagi H, Izamis M-L, Guzzardi MA, Shulman C, et al. Organ reengineering through development of a transplantable recellularized liver graft using decellularized liver matrix. *Nature medicine*. 2010;16:814-20.
- [116] Baptista PM, Siddiqui MM, Lozier G, Rodriguez SR, Atala A, Soker S. The use of whole organ decellularization for the generation of a vascularized liver organoid. *Hepatology*. 2011;53:604-17.

- [117] Soto-Gutierrez A, Zhang L, Medberry C, Fukumitsu K, Faulk D, Jiang H, et al. A whole-organ regenerative medicine approach for liver replacement. *Tissue Eng Part C Methods*. 2011;17:677-86.
- [118] Song JJ, Guyette JP, Gilpin SE, Gonzalez G, Vacanti JP, Ott HC. Regeneration and experimental orthotopic transplantation of a bioengineered kidney. *Nat Med*. 2013.
- [119] Guyette JP, Gilpin SE, Charest JM, Tapias LF, Ren X, Ott HC. Perfusion decellularization of whole organs. *Nat Protocols*. 2014;9:1451-68.
- [120] Lu TY, Lin B, Kim J, Sullivan M, Tobita K, Salama G, et al. Repopulation of decellularized mouse heart with human induced pluripotent stem cell-derived cardiovascular progenitor cells. *Nat Commun*. 2013;4:2307.
- [121] Ott HC, Clippinger B, Conrad C, Schuetz C, Pomerantseva I, Ikonomou L, et al. Regeneration and orthotopic transplantation of a bioartificial lung. *Nat Med*. 2010;16:927-33.
- [122] Lawrence BJ, Devarapalli M, Madihally SV. Flow dynamics in bioreactors containing tissue engineering scaffolds. *Biotechnol Bioeng*. 2009;102:935-47.
- [123] Khalpey Z, Qu N, Hemphill C, Louis AV, Ferng AS, Son TG, et al. Rapid Porcine Lung Decellularization Using a Novel Organ Regenerative Control Acquisition Bioreactor. *ASAIO Journal*. 2015;61:71-7.
- [124] Chang EI, Bonillas RG, El-ftesi S, Chang EI, Ceradini DJ, Vial IN, et al. Tissue engineering using autologous microcirculatory beds as vascularized bioscaffolds. *The FASEB Journal*. 2009;23:906-15.
- [125] Uzarski JS, Bijonowski BM, Wang B, Ward HH, Wandinger-Ness A, Miller WM, et al. Dual-purpose bioreactors to monitor non-invasive physical and biochemical markers of kidney and liver scaffold recellularization. *Tissue Eng Part C Methods*. 2015.
- [126] Nahmias Y, Kramvis Y, Barbe L, Casali M, Berthiaume F, Yarmush ML. A novel formulation of oxygen-carrying matrix enhances liver-specific function of cultured hepatocytes. *The FASEB Journal*. 2006;20:2531-3.
- [127] Stendahl JC, Kaufman DB, Stupp SI. Extracellular matrix in pancreatic islets: relevance to scaffold design and transplantation. *Cell Transplant*. 2009;18:1-12.
- [128] Vaithilingam V, Tuch BE. Islet transplantation and encapsulation: an update on recent developments. *Rev Diabet Stud*. 2011;8:51-67.
- [129] Brown BN, Barnes CA, Kasick RT, Michel R, Gilbert TW, Beer-Stolz D, et al. Surface characterization of extracellular matrix scaffolds. *Biomaterials*. 2010;31:428-37.
- [130] Sellaro TL, Ravindra AK, Stolz DB, Badylak SF. Maintenance of hepatic sinusoidal endothelial cell phenotype in vitro using organ-specific extracellular matrix scaffolds. *Tissue Eng*. 2007;13:2301-10.

- [131] Candiello J, Cole GJ, Halfter W. Age-dependent changes in the structure, composition and biophysical properties of a human basement membrane. *Matrix Biology*. 2010;29:402-10.
- [132] Tuch B, Gao S, Lees J. SCAFFOLDS TO SUPPORT ISLETS AND THE DIFFERENTIATION OF STEM CELLS AND PROGENITOR CELLS INTO INSULIN-SECRETING CELLS. *Current Medicinal Chemistry*. 2013;In press.
- [133] Wainwright JM, Czajka CA, Patel UB, Freytes DO, Tobita K, Gilbert TW, et al. Preparation of cardiac extracellular matrix from an intact porcine heart. *Tissue Eng Part C Methods*. 2010;16:525-32.
- [134] Remlinger NT, Wearden PD, Gilbert TW. Procedure for decellularization of porcine heart by retrograde coronary perfusion. *J Vis Exp*. 2012:e50059.
- [135] Ng SL, Narayanan K, Gao S, Wan AC. Lineage restricted progenitors for the repopulation of decellularized heart. *Biomaterials*. 2011;32:7571-80.
- [136] Uygun BE, Soto-Gutierrez A, Yagi H, Izamis ML, Guzzardi MA, Shulman C, et al. Organ reengineering through development of a transplantable recellularized liver graft using decellularized liver matrix. *Nat Med*. 2010;16:814-20.
- [137] Shupe T, Williams M, Brown A, Willenberg B, Petersen BE. Method for the decellularization of intact rat liver. *Organogenesis*. 2010;6:134-6.
- [138] Wallis JM, Borg ZD, Daly AB, Deng B, Ballif BA, Allen GB, et al. Comparative assessment of detergent-based protocols for mouse lung de-cellularization and re-cellularization. *Tissue Eng Part C Methods*. 2012;18:420-32.
- [139] Sullivan DC, Mirmalek-Sani SH, Deegan DB, Baptista PM, Aboushwareb T, Atala A, et al. Decellularization methods of porcine kidneys for whole organ engineering using a high-throughput system. *Biomaterials*. 2012;33:7756-64.
- [140] Ross EA, Williams MJ, Hamazaki T, Terada N, Clapp WL, Adin C, et al. Embryonic stem cells proliferate and differentiate when seeded into kidney scaffolds. *J Am Soc Nephrol*. 2009;20:2338-47.
- [141] Goh S-K, Bertera S, Banerjee I. Perfusion-Decellularization of Pancreatic Matrix – A Scaffold for Bio-Engineered Pancreas. *AICHE Annual Meeting*. Minneapolis, MN2011.
- [142] Goh S-K, Bertera S, Banerjee I. Perfusion-Decellularization of Pancreas as a Scaffold for the Differentiation of Human Embryonic Stem Cells into Insulin-Producing Cells. *ISSCR*. Yokohama, Japan2012.
- [143] Cukierman E, Pankov R, Stevens DR, Yamada KM. Taking Cell-Matrix Adhesions to the Third Dimension. *Science*. 2001;294:1708-12.

- [144] Goh S-K, Olsen P, Banerjee I. Extracellular Matrix Aggregates from Differentiating Embryoid Bodies as a Scaffold to Support ESC Proliferation and Differentiation. *PLoS One*. 2013;8:e61856.
- [145] Balasubramani M, Schreiber EM, Candiello J, Balasubramani GK, Kurtz J, Halfter W. Molecular interactions in the retinal basement membrane system: a proteomic approach. *Matrix Biol*. 2010;29:471-83.
- [146] Candiello J, Balasubramani M, Schreiber EM, Cole GJ, Mayer U, Halfter W, et al. Biomechanical properties of native basement membranes. *FEBS J*. 2007;274:2897-908.
- [147] Crapo PM, Gilbert TW, Badylak SF. An overview of tissue and whole organ decellularization processes. *Biomaterials*. 2011;32:3233-43.
- [148] Keane TJ, Londono R, Turner NJ, Badylak SF. Consequences of ineffective decellularization of biologic scaffolds on the host response. *Biomaterials*. 2012;33:1771-81.
- [149] Schuppig GT, Bonner-Weir S, Montana E, Kaiser N, Weir GC. Replication of adult pancreatic-beta cells cultured on bovine corneal endothelial cell extracellular matrix. *In Vitro Cell Dev Biol Anim*. 1993;29A:339-44.
- [150] Daoud J, Petropavlovskaja M, Rosenberg L, Tabrizian M. The effect of extracellular matrix components on the preservation of human islet function in vitro. *Biomaterials*. 2010;31:1676-82.
- [151] Wang RN, Rosenberg L. Maintenance of beta-cell function and survival following islet isolation requires re-establishment of the islet-matrix relationship. *J Endocrinol*. 1999;163:181-90.
- [152] Badylak SF, Taylor D, Uygun K. Whole-organ tissue engineering: decellularization and recellularization of three-dimensional matrix scaffolds. *Annu Rev Biomed Eng*. 2011;13:27-53.
- [153] Cortiella J, Niles J, Cantu A, Brettler A, Pham A, Vargas G, et al. Influence of acellular natural lung matrix on murine embryonic stem cell differentiation and tissue formation. *Tissue Eng Part A*. 2010;16:2565-80.
- [154] Shamis Y, Hasson E, Soroker A, Bassat E, Shimoni Y, Ziv T, et al. Organ-specific scaffolds for in vitro expansion, differentiation, and organization of primary lung cells. *Tissue Eng Part C Methods*. 2011;17:861-70.
- [155] Nakayama KH, Batchelder CA, Lee CI, Tarantal AF. Decellularized rhesus monkey kidney as a three-dimensional scaffold for renal tissue engineering. *Tissue Eng Part A*. 2010;16:2207-16.
- [156] Mauck RL, Baker BM, Nerurkar NL, Burdick JA, Li WJ, Tuan RS, et al. Engineering on the straight and narrow: the mechanics of nanofibrous assemblies for fiber-reinforced tissue regeneration. *Tissue Eng Part B Rev*. 2009;15:171-93.

- [157] Soto-Gutierrez A, Wertheim JA, Ott HC, Gilbert TW. Perspectives on whole-organ assembly: moving toward transplantation on demand. *J Clin Invest.* 2012;122:3817-23.
- [158] Nagata S, Hanayama R, Kawane K. Autoimmunity and the clearance of dead cells. *Cell.* 2010;140:619-30.
- [159] Brown BN, Valentin JE, Stewart-Akers AM, McCabe GP, Badylak SF. Macrophage phenotype and remodeling outcomes in response to biologic scaffolds with and without a cellular component. *Biomaterials.* 2009;30:1482-91.
- [160] Williams C, Liao J, Joyce EM, Wang B, Leach JB, Sacks MS, et al. Altered structural and mechanical properties in decellularized rabbit carotid arteries. *Acta Biomater.* 2009;5:993-1005.
- [161] Gratzer PF, Harrison RD, Woods T. Matrix alteration and not residual sodium dodecyl sulfate cytotoxicity affects the cellular repopulation of a decellularized matrix. *Tissue Eng.* 2006;12:2975-83.
- [162] Engler AJ, Sen S, Sweeney HL, Discher DE. Matrix elasticity directs stem cell lineage specification. *Cell.* 2006;126:677-89.
- [163] Discher DE, Janmey P, Wang YL. Tissue cells feel and respond to the stiffness of their substrate. *Science.* 2005;310:1139-43.
- [164] Wang Y, Cui CB, Yamauchi M, Miguez P, Roach M, Malavarca R, et al. Lineage restriction of human hepatic stem cells to mature fates is made efficient by tissue-specific biomatrix scaffolds. *Hepatology.* 2011;53:293-305.
- [165] Chun T-H, Hotary KB, Sabeh F, Saltiel AR, Allen ED, Weiss SJ. A Pericellular Collagenase Directs the 3-Dimensional Development of White Adipose Tissue. *Cell.* 2006;125:577-91.
- [166] Hotary KB, Allen ED, Brooks PC, Datta NS, Long MW, Weiss SJ. Membrane Type I Matrix Metalloproteinase Usurps Tumor Growth Control Imposed by the Three-Dimensional Extracellular Matrix. *Cell.* 2003;114:33-45.
- [167] Badylak SF, Freytes DO, Gilbert TW. Extracellular matrix as a biological scaffold material: Structure and function. *Acta Biomaterialia.* 2009;5:1-13.
- [168] Girard ED, Jensen TJ, Vadasz SD, Blanchette AE, Zhang F, Moncada C, et al. Automated procedure for biomimetic de-cellularized lung scaffold supporting alveolar epithelial transdifferentiation. *Biomaterials.* 2013;34:10043-55.
- [169] Price AP, Godin LM, Domek A, Cotter T, D'Cunha J, Taylor DA, et al. Automated decellularization of intact, human-sized lungs for tissue engineering. *Tissue Eng Part C Methods.* 2015;21:94-103.

- [170] Charest JM, Okamoto T, Kitano K, Yasuda A, Gilpin SE, Mathisen DJ, et al. Design and validation of a clinical-scale bioreactor for long-term isolated lung culture. *Biomaterials*. 2015;52:79-87.
- [171] Bijonowski BM, Miller WM, Wertheim JA. Bioreactor design for perfusion-based, highly-vascularized organ regeneration. *Curr Opin Chem Eng*. 2013;2:32-40.
- [172] Panoskaltsis-Mortari A. Bioreactor Development for Lung Tissue Engineering. *Curr Transplant Rep*. 2015;2:90-7.
- [173] Rennert RC, Sorkin M, Wong VW, Gurtner GC. Organ-level tissue engineering using bioreactor systems and stem cells: implications for transplant surgery. *Curr Stem Cell Res Ther*. 2014;9:2-9.
- [174] Ross EA, Abrahamson DR, St John P, Clapp WL, Williams MJ, Terada N, et al. Mouse stem cells seeded into decellularized rat kidney scaffolds endothelialize and remodel basement membranes. *Organogenesis*. 2012;8:49-55.
- [175] Scarritt ME, Bonvillain RW, Burkett BJ, Wang G, Glotser EY, Zhang Q, et al. Hypertensive Rat Lungs Retain Hallmarks of Vascular Disease upon Decellularization but Support the Growth of Mesenchymal Stem Cells. *Tissue Engineering Part A*. 2014;20:1426-43.
- [176] Ng SLJ, Narayanan K, Gao S, Wan ACA. Lineage restricted progenitors for the repopulation of decellularized heart. *Biomaterials*. 2011;32:7571-80.
- [177] Bonvillain RW, Scarritt ME, Pashos NC, Mayeux JP, Meshberger CL, Betancourt AM, et al. Nonhuman primate lung decellularization and recellularization using a specialized large-organ bioreactor. *J Vis Exp*. 2013:e50825.
- [178] Task K, Jaramillo M, Banerjee I. Population based model of human embryonic stem cell (hESC) differentiation during endoderm induction. *PLoS One*. 2012;7:e32975.
- [179] Mathew S, Jaramillo M, Zhang X, Zhang LA, Soto-Gutierrez A, Banerjee I. Analysis of alternative signaling pathways of endoderm induction of human embryonic stem cells identifies context specific differences. *BMC Syst Biol*. 2012;6:154.
- [180] Calle EA, Petersen TH, Niklason LE. Procedure for lung engineering. *J Vis Exp*. 2011.
- [181] Frisch SM, Francis H. Disruption of epithelial cell-matrix interactions induces apoptosis. *J Cell Biol*. 1994;124:619-26.
- [182] Bernard MP, Chu ML, Myers JC, Ramirez F, Eikenberry EF, Prockop DJ. Nucleotide sequences of complementary deoxyribonucleic acids for the pro alpha 1 chain of human type I procollagen. Statistical evaluation of structures that are conserved during evolution. *Biochemistry*. 1983;22:5213-23.
- [183] Brown NH. Extracellular matrix in development: insights from mechanisms conserved between invertebrates and vertebrates. *Cold Spring Harb Perspect Biol*. 2011;3.

- [184] Jensen J. Gene regulatory factors in pancreatic development. *Dev Dyn*. 2004;229:176-200.
- [185] Petersen TH, Calle EA, Colehour MB, Niklason LE. Bioreactor for the long-term culture of lung tissue. *Cell Transplant*. 2011;20:1117-26.
- [186] Greggio C, De Franceschi F, Figueiredo-Larsen M, Gobaa S, Ranga A, Semb H, et al. Artificial three-dimensional niches deconstruct pancreas development in vitro. *Development*. 2013;140:4452-62.
- [187] Akhyari P, Aubin H, Gwanmesia P, Barth M, Hoffmann S, Huelsmann J, et al. The quest for an optimized protocol for whole-heart decellularization: a comparison of three popular and a novel decellularization technique and their diverse effects on crucial extracellular matrix qualities. *Tissue Eng Part C Methods*. 2011;17:915-26.
- [188] Momtahan N, Sukavaneshvar S, Roeder BL, Cook AD. Strategies and Processes to Decellularize and Recellularize Hearts to Generate Functional Organs and Reduce the Risk of Thrombosis. *Tissue Eng Part B Rev*. 2014.
- [189] Momtahan N, Poornejad N, Struk JA, Castleton AA, Herrod BJ, Vance BR, et al. Automation of Pressure Control Improves Whole Porcine Heart Decellularization. *Tissue Eng Part C Methods*. 2015.
- [190] Park H, Berzin I, De Luis J, Vunjak-Novakovic G. Evaluation of silicone tubing toxicity using tobacco BY2 culture. *In Vitro CellDevBiol-Plant*. 2005;41:555-60.
- [191] Titmarsh D, Hidalgo A, Turner J, Wolvetang E, Cooper-White J. Optimization of flowrate for expansion of human embryonic stem cells in perfusion microbioreactors. *Biotechnology and Bioengineering*. 2011;108:2894-904.
- [192] Fridley K, Kinney M, McDevitt T. Hydrodynamic modulation of pluripotent stem cells. *Stem Cell Res Ther*. 2012;3:1-9.
- [193] Ricordi C, Fraker C, Szust J, Al-Abdullah I, Poggioli R, Kirlew T, et al. Improved human islet isolation outcome from marginal donors following addition of oxygenated perfluorocarbon to the cold-storage solution. *Transplantation*. 2003;75:1524-7.
- [194] Moser PT, Ott HC. Recellularization of organs: what is the future for solid organ transplantation? *Current Opinion in Organ Transplantation*. 2014;19:603-9.
- [195] Gilpin SE, Ren X, Okamoto T, Guyette JP, Mou H, Rajagopal J, et al. Enhanced lung epithelial specification of human induced pluripotent stem cells on decellularized lung matrix. *Ann Thorac Surg*. 2014;98:1721-9; discussion 9.
- [196] Shojaie S, Ermini L, Ackerley C, Wang J, Chin S, Yeganeh B, et al. Acellular lung scaffolds direct differentiation of endoderm to functional airway epithelial cells: requirement of matrix-bound HS proteoglycans. *Stem Cell Reports*. 2015;4:419-30.

- [197] Welsher K, Sherlock SP, Dai H. Deep-tissue anatomical imaging of mice using carbon nanotube fluorophores in the second near-infrared window. *Proceedings of the National Academy of Sciences*. 2011;108:8943-8.
- [198] Ren X, Tapias LF, Jank BJ, Mathisen DJ, Lanuti M, Ott HC. Ex vivo non-invasive assessment of cell viability and proliferation in bio-engineered whole organ constructs. *Biomaterials*. 2015;52:103-12.
- [199] Maidhof R, Tandon N, Lee EJ, Luo J, Duan Y, Yeager K, et al. Biomimetic perfusion and electrical stimulation applied in concert improved the assembly of engineered cardiac tissue. *Journal of tissue engineering and regenerative medicine*. 2012;6:e12-e23.
- [200] Tandon N, Marsano A, Cannizzaro C, Voldman J, Vunjak-Novakovic G. Design of electrical stimulation bioreactors for cardiac tissue engineering. *Conf Proc IEEE Eng Med Biol Soc*. 2008;2008:3594-7.
- [201] Ghaedi M, Calle EA, Mendez JJ, Gard AL, Balestrini J, Booth A, et al. Human iPS cell-derived alveolar epithelium repopulates lung extracellular matrix. *J Clin Invest*. 2013;123:4950-62.
- [202] Ren X, Moser PT, Gilpin SE, Okamoto T, Wu T, Tapias LF, et al. Engineering pulmonary vasculature in decellularized rat and human lungs. *Nat Biotech*. 2015.
- [203] Bonandrini B, Figliuzzi M, Papadimou E, Morigi M, Perico N, Casiraghi F, et al. Recellularization of well-preserved acellular kidney scaffold using embryonic stem cells. *Tissue Eng Part A*. 2014;20:1486-98.
- [204] Bhatti SS, Kumar L, Dinda AK, Dawar R. Prognostic value of bone marrow angiogenesis in multiple myeloma: use of light microscopy as well as computerized image analyzer in the assessment of microvessel density and total vascular area in multiple myeloma and its correlation with various clinical, histological, and laboratory parameters. *Am J Hematol*. 2006;81:649-56.
- [205] Carpentier G. ImageJ contribution: Angiogenesis Analyzer.: *ImageJ news*; 2012.
- [206] Cai J, Yu C, Liu Y, Chen S, Guo Y, Yong J, et al. Generation of homogeneous PDX1(+) pancreatic progenitors from human ES cell-derived endoderm cells. *J Mol Cell Biol*. 2010;2:50-60.
- [207] Johannesson M, Stahlberg A, Ameri J, Sand FW, Norrman K, Semb H. FGF4 and retinoic acid direct differentiation of hESCs into PDX1-expressing foregut endoderm in a time- and concentration-dependent manner. *PLoS One*. 2009;4:e4794.
- [208] Hosoya M. Preparation of pancreatic beta-cells from human iPS cells with small molecules. *Islets*. 2012;4:249-52.
- [209] Chen S, Borowiak M, Fox JL, Maehr R, Osafune K, Davidow L, et al. A small molecule that directs differentiation of human ESCs into the pancreatic lineage. *Nat Chem Biol*. 2009;5:258-65.

- [210] Wu KL, Gannon M, Peshavaria M, Offield MF, Henderson E, Ray M, et al. Hepatocyte nuclear factor 3beta is involved in pancreatic beta-cell-specific transcription of the pdx-1 gene. *Mol Cell Biol.* 1997;17:6002-13.
- [211] Cockell M, Stolarczyk D, Frutiger S, Hughes GJ, Hagenbuchle O, Wellauer PK. Binding sites for hepatocyte nuclear factor 3 beta or 3 gamma and pancreas transcription factor 1 are required for efficient expression of the gene encoding pancreatic alpha-amylase. *Mol Cell Biol.* 1995;15:1933-41.
- [212] Murtaugh LC, Stanger BZ, Kwan KM, Melton DA. Notch signaling controls multiple steps of pancreatic differentiation. *Proc Natl Acad Sci U S A.* 2003;100:14920-5.
- [213] Apelqvist A, Li H, Sommer L, Beatus P, Anderson DJ, Honjo T, et al. Notch signalling controls pancreatic cell differentiation. *Nature.* 1999;400:877-81.
- [214] Wang X, Ye K. Three-dimensional differentiation of embryonic stem cells into islet-like insulin-producing clusters. *Tissue Eng Part A.* 2009;15:1941-52.
- [215] Brereton HC, Carvell MJ, Asare-Anane H, Roberts G, Christie MR, Persaud SJ, et al. Homotypic cell contact enhances insulin but not glucagon secretion. *Biochem Biophys Res Commun.* 2006;344:995-1000.
- [216] Jaques F, Jousset H, Tomas A, Prost AL, Wollheim CB, Irminger JC, et al. Dual effect of cell-cell contact disruption on cytosolic calcium and insulin secretion. *Endocrinology.* 2008;149:2494-505.
- [217] Rouwkema J, Rivron NC, van Blitterswijk CA. Vascularization in tissue engineering. *Trends Biotechnol.* 2008;26:434-41.
- [218] Hoganson DM, Pryor HI, 2nd, Spool ID, Burns OH, Gilmore JR, Vacanti JP. Principles of biomimetic vascular network design applied to a tissue-engineered liver scaffold. *Tissue Eng Part A.* 2010;16:1469-77.
- [219] Nostro MC, Keller G. Generation of beta cells from human pluripotent stem cells: Potential for regenerative medicine. *Semin Cell Dev Biol.* 2012;23:701-10.
- [220] Teitelman G, Alpert S, Polak JM, Martinez A, Hanahan D. Precursor cells of mouse endocrine pancreas coexpress insulin, glucagon and the neuronal proteins tyrosine hydroxylase and neuropeptide Y, but not pancreatic polypeptide. *Development.* 1993;118:1031-9.
- [221] Watanabe K, Ueno M, Kamiya D, Nishiyama A, Matsumura M, Wataya T, et al. A ROCK inhibitor permits survival of dissociated human embryonic stem cells. *Nat Biotech.* 2007;25:681-6.
- [222] Chen G, Hou Z, Gulbranson DR, Thomson JA. Actin-myosin contractility is responsible for the reduced viability of dissociated human embryonic stem cells. *Cell Stem Cell.* 2010;7:240-8.

- [223] Nakayama KH, Lee CC, Batchelder CA, Tarantal AF. Tissue specificity of decellularized rhesus monkey kidney and lung scaffolds. *PLoS One*. 2013;8:e64134.
- [224] McGuire RF, Bissell DM, Boyles J, Roll FJ. Role of extracellular matrix in regulating fenestrations of sinusoidal endothelial cells isolated from normal rat liver. *Hepatology*. 1992;15:989-97.
- [225] Shapiro AM, Ricordi C, Hering BJ, Auchincloss H, Lindblad R, Robertson RP, et al. International trial of the Edmonton protocol for islet transplantation. *N Engl J Med*. 2006;355:1318-30.
- [226] Willenberg BJ, Oca-Cossio J, Cai Y, Brown AR, Clapp WL, Abrahamson DR, et al. Repurposed biological scaffolds: kidney to pancreas. *Organogenesis*. 2015;11:47-57.
- [227] Sionov RV, Finesilver G, Sapozhnikov L, Soroker A, Zlotkin-Rivkin E, Saad Y, et al. Beta cells secrete significant and regulated levels of insulin for long periods when seeded onto acellular micro-scaffolds. *Tissue Eng Part A*. 2015.
- [228] Ghazalli N, Mahdavi A, Feng T, Jin L, Kozlowski MT, Hsu J, et al. Postnatal Pancreas of Mice Contains Tripotent Progenitors Capable of Giving Rise to Duct, Acinar, and Endocrine Cells In Vitro. *Stem Cells Dev*. 2015;24:1995-2008.
- [229] Fitzpatrick LE, McDevitt TC. Cell-derived matrices for tissue engineering and regenerative medicine applications(1.). *Biomater Sci*. 2015;3:12-24.
- [230] Ziolkowski AF, Popp SK, Freeman C, Parish CR, Simeonovic CJ. Heparan sulfate and heparanase play key roles in mouse beta cell survival and autoimmune diabetes. *J Clin Invest*. 2012;122:132-41.
- [231] Rozario T, DeSimone DW. The extracellular matrix in development and morphogenesis: a dynamic view. *Dev Biol*. 2010;341:126-40.
- [232] Watt FM, Huck WT. Role of the extracellular matrix in regulating stem cell fate. *Nat Rev Mol Cell Biol*. 2013;14:467-73.
- [233] Kadota Y, Yagi H, Inomata K, Matsubara K, Hibi T, Abe Y, et al. Mesenchymal stem cells support hepatocyte function in engineered liver grafts. *Organogenesis*. 2014;10:268-77.
- [234] Barakat O, Abbasi S, Rodriguez G, Rios J, Wood RP, Ozaki C, et al. Use of decellularized porcine liver for engineering humanized liver organ. *J Surg Res*. 2012;173:e11-25.
- [235] Scarritt ME, Pashos NC, Bunnell BA. A review of cellularization strategies for tissue engineering of whole organs. *Front Bioeng Biotechnol*. 2015;3:43.
- [236] Jaramillo M, Banerjee I. Endothelial cell co-culture mediates maturation of human embryonic stem cell to pancreatic insulin producing cells in a directed differentiation approach. *J Vis Exp*. 2012.

- [237] Banerjee I, Sharma N, Yarmush M. Impact of co-culture on pancreatic differentiation of embryonic stem cells. *J Tissue Eng Regen Med*. 2011;5:313-23.
- [238] Skardal A, Devarasetty M, Kang HW, Mead I, Bishop C, Shupe T, et al. A hydrogel bioink toolkit for mimicking native tissue biochemical and mechanical properties in bioprinted tissue constructs. *Acta Biomater*. 2015;25:24-34.
- [239] Macchiarini P, Jungebluth P, Go T, Asnaghi MA, Rees LE, Cogan TA, et al. Clinical transplantation of a tissue-engineered airway. *Lancet*. 2008;372:2023-30.
- [240] Atala A, Bauer SB, Soker S, Yoo JJ, Retik AB. Tissue-engineered autologous bladders for patients needing cystoplasty. *Lancet*. 2006;367:1241-6.
- [241] Sicari BM, Rubin JP, Dearth CL, Wolf MT, Ambrosio F, Boninger M, et al. An acellular biologic scaffold promotes skeletal muscle formation in mice and humans with volumetric muscle loss. *Sci Transl Med*. 2014;6:234ra58.
- [242] Taylor-Weiner H, Schwarzbauer JE, Engler AJ. Defined extracellular matrix components are necessary for definitive endoderm induction. *Stem Cells*. 2013;31:2084-94.
- [243] Yang F, Cho SW, Son SM, Hudson SP, Bogatyrev S, Keung L, et al. Combinatorial extracellular matrices for human embryonic stem cell differentiation in 3D. *Biomacromolecules*. 2010;11:1909-14.
- [244] Flaim CJ, Chien S, Bhatia SN. An extracellular matrix microarray for probing cellular differentiation. *Nat Methods*. 2005;2:119-25.
- [245] Kuschel C, Steuer H, Maurer AN, Kanzok B, Stoop R, Angres B. Cell adhesion profiling using extracellular matrix protein microarrays. *Biotechniques*. 2006;40:523-31.
- [246] Reticker-Flynn NE, Malta DF, Winslow MM, Lamar JM, Xu MJ, Underhill GH, et al. A combinatorial extracellular matrix platform identifies cell-extracellular matrix interactions that correlate with metastasis. *Nat Commun*. 2012;3:1122.
- [247] LaBarge MA, Nelson CM, Villadsen R, Fridriksdottir A, Ruth JR, Stampfer MR, et al. Human mammary progenitor cell fate decisions are products of interactions with combinatorial microenvironments. *Integr Biol (Camb)*. 2009;1:70-9.
- [248] Fernandes TG, Kwon SJ, Bale SS, Lee MY, Diogo MM, Clark DS, et al. Three-dimensional cell culture microarray for high-throughput studies of stem cell fate. *Biotechnol Bioeng*. 2010;106:106-18.
- [249] Meli L, Barbosa HS, Hickey AM, Gasimli L, Nierode G, Diogo MM, et al. Three dimensional cellular microarray platform for human neural stem cell differentiation and toxicology. *Stem Cell Res*. 2014;13:36-47.
- [250] Gobaa S, Hoehnel S, Roccio M, Negro A, Kobel S, Lutolf MP. Artificial niche microarrays for probing single stem cell fate in high throughput. *Nat Methods*. 2011;8:949-55.

- [251] Dolatshahi-Pirouz A, Nikkhah M, Gaharwar AK, Hashmi B, Guermani E, Aliabadi H, et al. A combinatorial cell-laden gel microarray for inducing osteogenic differentiation of human mesenchymal stem cells. *Sci Rep*. 2014;4:3896.
- [252] Ranga A, Gobaa S, Okawa Y, Mosiewicz K, Negro A, Lutolf MP. 3D niche microarrays for systems-level analyses of cell fate. *Nat Commun*. 2014;5.
- [253] Seib FP, Muller K, Franke M, Grimmer M, Bornhauser M, Werner C. Engineered extracellular matrices modulate the expression profile and feeder properties of bone marrow-derived human multipotent mesenchymal stromal cells. *Tissue Eng Part A*. 2009;15:3161-71.
- [254] Hoshiba T, Chen G, Endo C, Maruyama H, Wakui M, Nemoto E, et al. Decellularized Extracellular Matrix as an In Vitro Model to Study the Comprehensive Roles of the ECM in Stem Cell Differentiation. *Stem Cells International*.
- [255] DeQuach JA, Mezzano V, Miglani A, Lange S, Keller GM, Sheikh F, et al. Simple and high yielding method for preparing tissue specific extracellular matrix coatings for cell culture. *PLoS One*. 2010;5:e13039.
- [256] Prewitz MC, Seib FP, von Bonin M, Friedrichs J, Stissel A, Niehage C, et al. Tightly anchored tissue-mimetic matrices as instructive stem cell microenvironments. *Nat Methods*. 2013;10:788-94.
- [257] Hoshiba T, Kawazoe N, Tateishi T, Chen G. Development of extracellular matrices mimicking stepwise adipogenesis of mesenchymal stem cells. *Adv Mater*. 2010;22:3042-7.
- [258] Jensen T, Roszell B, Zang F, Girard E, Matson A, Thrall R, et al. A rapid lung decellularization protocol supports embryonic stem cell differentiation in vitro and following implantation. *Tissue Eng Part C Methods*. 2012;18:632-46.
- [259] Oberwallner B, Brodarac A, Anic P, Saric T, Wassilew K, Neef K, et al. Human cardiac extracellular matrix supports myocardial lineage commitment of pluripotent stem cells. *Eur J Cardiothorac Surg*. 2015;47:416-25; discussion 25.
- [260] Dalby MJ, Gadegaard N, Oreffo RO. Harnessing nanotopography and integrin-matrix interactions to influence stem cell fate. *Nat Mater*. 2014;13:558-69.
- [261] Task K, D'Amore A, Singh S, Candiello J, Jaramillo M, Wagner WR, et al. Systems level approach reveals the correlation of endoderm differentiation of mouse embryonic stem cells with specific microstructural cues of fibrin gels. *J R Soc Interface*. 2014;11:20140009.
- [262] Lagenaur C, Lemmon V. An L1-like molecule, the 8D9 antigen, is a potent substrate for neurite extension. *Proceedings of the National Academy of Sciences of the United States of America*. 1987;84:7753-7.
- [263] Kunjukunju S, Roy A, Ramanathan M, Lee B, Candiello JE, Kumta PN. A layer-by-layer approach to natural polymer-derived bioactive coatings on magnesium alloys. *Acta Biomater*. 2013;9:8690-703.

- [264] Uriel S, Labay E, Francis-Sedlak M, Moya ML, Weichselbaum RR, Ervin N, et al. Extraction and assembly of tissue-derived gels for cell culture and tissue engineering. *Tissue Eng Part C Methods*. 2009;15:309-21.
- [265] Halfter W, Candiello J, Hu H, Zhang P, Schreiber E, Balasubramani M. Protein composition and biomechanical properties of in vivo-derived basement membranes. *Cell Adh Migr*. 2013;7:64-71.
- [266] Lin H, Yang G, Tan J, Tuan RS. Influence of decellularized matrix derived from human mesenchymal stem cells on their proliferation, migration and multi-lineage differentiation potential. *Biomaterials*. 2012;33:4480-9.
- [267] Candiello JE, Jaramillo M, Goh SK, Banerjee I. Role of substrates in diabetes therapy: stem cell differentiation and islet transplantation. *Crit Rev Biomed Eng*. 2011;39:535-55.
- [268] Albelda SM, Buck CA. Integrins and other cell adhesion molecules. *FASEB J*. 1990;4:2868-80.
- [269] Danen EH, Sonnenberg A. Integrins in regulation of tissue development and function. *J Pathol*. 2003;200:471-80.
- [270] Li X, Zhang X, Zhao S, Wang J, Liu G, Du Y. Micro-scaffold array chip for upgrading cell-based high-throughput drug testing to 3D using benchtop equipment. *Lab Chip*. 2014;14:471-81.
- [271] Koyama Y, Norose-Toyoda K, Hirano S, Kobayashi M, Ebihara T, Someki I, et al. Type I collagen is a non-adhesive extracellular matrix for macrophages. *Arch Histol Cytol*. 2000;63:71-9.
- [272] Wilson JL, Najia MA, Saeed R, McDevitt TC. Alginate encapsulation parameters influence the differentiation of microencapsulated embryonic stem cell aggregates. *Biotechnol Bioeng*. 2014;111:618-31.
- [273] Bio-rad Laboratories LSG. 3rd edition ed.
- [274] Qiu G-M, Zhu B-K, Xu Y-Y.  $\alpha$ -Amylase immobilized by Fe<sub>3</sub>O<sub>4</sub>/poly(styrene-co-maleic anhydride) magnetic composite microspheres: Preparation and characterization. *Journal of Applied Polymer Science*. 2005;95:328-35.
- [275] QiuGuangMing. Study on Synthesis of Poly(Styrene-co-Maleic Anhydride) and Their Functionalization for Membranes an [PhD Thesis]: Zhejiang University; 2006.
- [276] John B, Ricart B, Tait Wojno ED, Harris TH, Randall LM, Christian DA, et al. Analysis of behavior and trafficking of dendritic cells within the brain during toxoplasmic encephalitis. *PLoS Pathog*. 2011;7:e1002246.

- [277] Vasudeva K, Andersen K, Zeyzus-Johns B, Hitchens TK, Patel SK, Balducci A, et al. Imaging neuroinflammation in vivo in a neuropathic pain rat model with near-infrared fluorescence and (1)(9)F magnetic resonance. *PLoS One*. 2014;9:e90589.
- [278] Guilak F, Cohen DM, Estes BT, Gimble JM, Liedtke W, Chen CS. Control of stem cell fate by physical interactions with the extracellular matrix. *Cell Stem Cell*. 2009;5:17-26.
- [279] Kleinman HK, Martin GR. Matrigel: basement membrane matrix with biological activity. *Semin Cancer Biol*. 2005;15:378-86.
- [280] Halfter W, Monnier C, Muller D, Oertle P, Uechi G, Balasubramani M, et al. The bi-functional organization of human basement membranes. *PLoS One*. 2013;8:e67660.
- [281] Kingsmore SF. Multiplexed protein measurement: technologies and applications of protein and antibody arrays. *Nat Rev Drug Discov*. 2006;5:310-20.
- [282] Nie Z, Kumacheva E. Patterning surfaces with functional polymers. *Nat Mater*. 2008;7:277-90.
- [283] Hoffman GR, Moerke NJ, Hsia M, Shamu CE, Blenis J. A High-Throughput, Cell-Based Screening Method for siRNA and Small Molecule Inhibitors of mTORC1 Signaling Using the In Cell Western Technique. *Assay and Drug Development Technologies*. 2010;8:186-99.
- [284] Cirulli V, Beattie GM, Klier G, Ellisman M, Ricordi C, Quaranta V, et al. Expression and Function of  $\alpha(v)\beta(3)$  and  $\alpha(v)\beta(5)$  Integrins in the Developing Pancreas: Roles in the Adhesion and Migration of Putative Endocrine Progenitor Cells. *The Journal of Cell Biology*. 2000;150:1445-60.
- [285] George EL, Baldwin HS, Hynes RO. Fibronectins are essential for heart and blood vessel morphogenesis but are dispensable for initial specification of precursor cells. *Blood*. 1997;90:3073-81.
- [286] Pelletier AJ, Kunicki T, Quaranta V. Activation of the integrin alpha v beta 3 involves a discrete cation-binding site that regulates conformation. *J Biol Chem*. 1996;271:1364-70.
- [287] Kraehenbuehl TP, Langer R, Ferreira LS. Three-dimensional biomaterials for the study of human pluripotent stem cells. *Nat Methods*. 2011;8:731-6.
- [288] Discher DE, Janmey P, Wang Y-l. Tissue Cells Feel and Respond to the Stiffness of Their Substrate. *Science*. 2005;310:1139-43.
- [289] Wang Y, Cui C-B, Yamauchi M, Miguez P, Roach M, Malavarca R, et al. Lineage restriction of human hepatic stem cells to mature fates is made efficient by tissue-specific biomatrix scaffolds. *Hepatology*. 2011;53:293-305.
- [290] Meivar-Levy I, Ferber S. New organs from our own tissues: liver-to-pancreas transdifferentiation. *Trends in Endocrinology & Metabolism*. 14:460-6.

- [291] Nikolova G, Jabs N, Konstantinova I, Domogatskaya A, Tryggvason K, Sorokin L, et al. The Vascular Basement Membrane: A Niche for Insulin Gene Expression and  $\beta$  Cell Proliferation. *Developmental Cell*. 2006;10:397-405.
- [292] Comoglio PM, Boccaccio C, Trusolino L. Interactions between growth factor receptors and adhesion molecules: breaking the rules. *Curr Opin Cell Biol*. 2003;15:565-71.
- [293] Morrison SJ, Spradling AC. Stem cells and niches: mechanisms that promote stem cell maintenance throughout life. *Cell*. 2008;132:598-611.
- [294] Hynes RO. Integrins: Bidirectional, Allosteric Signaling Machines. *Cell*. 2002;110:673-87.
- [295] Meredith JE, Jr., Winitz S, Lewis JM, Hess S, Ren XD, Renshaw MW, et al. The regulation of growth and intracellular signaling by integrins. *Endocr Rev*. 1996;17:207-20.
- [296] Gattazzo F, Urciuolo A, Bonaldo P. Extracellular matrix: a dynamic microenvironment for stem cell niche. *Biochim Biophys Acta*. 2014;1840:2506-19.